NOTICE

The quality of this microfiche is heavily dependent upon the quality of the original thesis submitted for microfilming. Every effort has been made to ensure the highest quality of reproduction possible.

If pages are missing, contact the university which granted the degree.

Some pages may have indistinct print especially if the original pages were typed with a poor typewriter ribbon or if the university sent us a poor photocopy.

Previously copyrighted materials (journal articles, published tests, etc.) are not filmed.

Reproduction in full or in part of this film is governed by the Canadian Copyright Act, R.S.C. 1970, c. C-30. Please read the authorization forms which accompany this thesis.

THIS DISSERTATION
HAS BEEN MICROFILMED
EXACTLY AS RECEIVED

AVIS

La qualité de cette microfiche dépend grandement de la qualité de la thèse soumise au microfilmage. Nous avons tout fait pour assurer une qualité supérieure de reproduction.

S'il manque des pages, veuillez communiquer avec l'université qui a conféré le grade.

La qualité d'impression de certaines pages peut laisser à désirer, surtout si les pages originales ont été dactylographiées à l'aide d'un ruban usé ou si l'université nous a fait parvenir une photocopie de mauvaise qualité.

Les documents qui font déjà l'objet d'un droit d'auteur (articles de revue, examens publiés, etc.) ne sont pas microfilmés.

La reproduction, même partielle, de ce microfilm est soumise à la Loi canadienne sur le droit d'auteur, SRC 1970, c. C-30. Veuillez prendre connaissance des formules d'autorisation qui accompagnent cette thèse.

LA THÈSE A ÉTÉ
MICROFILMÉE TELLE QUE
NOUS L'AVONS REÇUE

UNIVERSITÉ D'OTTAWA
UNIVERSITY OF OTTAWA

REACTION DYNAMICS OF A+BC SYSTEMS

by

Khay-Gie Tan, Dipl.Chem.

A thesis submitted to the School of Graduate Studies
in partial fulfillment of the requirements for the
degree of Ph.D. in Chemistry.

UNIVERSITY OF OTTAWA
OTTAWA, CANADA, 1976

To my Parents

and my Teachers

PREFACE

This thesis is concerned with the fundamental concepts of molecular reaction dynamics and the development of a systematical method of investigation of simple chemical rate processes. A special effort has been made to understand the significance of individual parameters on the outcome of the reaction, on a microscopic scale. Parts of the work discussed in this thesis have been published:

(1) J. S. Wright, K. G. Tan, K. J. Laidler, and J.E. Hulse, Chem. Phys. Lett., 30, 200 (1975);

(2) J. S. Wright, K. G. Tan, and K. J. Laidler, J. Chem. Phys., 64, 970 (1976);

(3) J. S. Wright and K. G. Tan, J. Chem. Phys., received 1 July (1976);

(4) K. J. Laidler, K. G. Tan, and J. S. Wright, Chem. Phys. Lett., received 28 September (1976).

ACKNOWLEDGMENTS

The author expresses his most sincere gratitude to his supervisors, Professor K. J. Laidler and Professor J.S. Wright, for their direction, encouragement, patience and understanding, throughout the course of this work. It has been a great privilege and a valuable experience to carry out this program under their guidance. Thanks are also due to the teaching staff of the University of Ottawa, for many stimulating courses, seminars and discussions,and to the Computer Centres of the University of Ottawa and Carleton University for the use of their facilities. It is a great pleasure to acknowledge the friendship and moral support received from my fellow graduate students, post doctoral fellows, the support staff of the Chemistry Department, and the Indonesian community in Ottawa. Special thanks are due to Mrs. E. Szabo, Mr. Karl Dietrich and Mr. I.T. Lie for the preparation of the drawings in this thesis and for programming assistance. Fellowships awarded by the National Research Council of Canada are gratefully acknowledged.

Finally I wish to thank my immediate relatives and friends, who made all this become possible.

TABLE OF CONTENTS

LIST OF FIGURES

LIST OF TABLES

ABSTRACT

Systematic quasi-classical trajectory calculations are carried out in a study of the collinear $H+H_2$ reaction on the Shavitt, Stevens, Minn and Karplus (SSMK) surface, for a range of relative translational energies between 0 and 2.0 eV. At a constant vibrational energy and phase angle, the trajectories divide in continuous regions of alternating reactivity, the boundaries of which are marked by maxima of trajectory times and product vibrational energies. These reactivity bands shift continuously with the initial phase angle, as demonstrated by means of linear and polar reactivity plots. This band continuity property allows the determination of accurate total and specific reaction probabilities, with relatively few trajectory calculations. The observed dependence of the outcome of trajectories on the initial conditions is analyzed and discussed in terms of the motion of a single particle, sliding over a potential-energy surface, and many generalizations are made to characterize this dependence. The study is then extended to the collision of X+HX on the collinear SSMK surface, for masses X = 1.008(H), 2.014(D), 3.016(T), and 10.000. Except for a high-energy reactive region, the results obtained with other mass combinations are very similar to the H+HH results. The total reactivity maps, threshold energies and product vibrational-energy distributions show patterns which are related to the skew angle of the potential-energy surface model, which is also responsible for a high-energy cut-off in H+HH reactivity and the existence of second reactive regions

for the other mass combinations. The results are interpreted in terms of single and multiple collisions.

The method is then extended to coplanar H+HH reactions on the Yates-Lester (YL) surface. Preliminary results show that the reactivity bands persist in these higher-dimensional calculations, but that the results are generally more complicated than for the collinear cases. The influence of additional 2-D parameters is investigated separately by extensive calculations for the rotationless case. Total reactivity maps are obtained as a function of the initial translational energies and other initial parameters, allowing the evaluation of total reaction probabilities, reaction cross sections,and the determination of the dependence of the reaction probability on individual parameters. The results are interpreted in terms of a skewed potential-energy hypersurface model, the collinear orientational effect, and the generalizations of the collinear studies.

The origin of the reactivity bands is then investigated with the help of simple models and the vibrational adiabaticity principle. A satisfactory qualitative agreement is obtained with a simple surface representing a rectilinear cut of the true potential-energy surface, on which a platform had been added to allow for zero-point energy normal to the reaction path. More realistic models of greater quantitative predictive power should include curvilinear reaction paths and take into account the skew angle and geometry of the transition state region.

CHAPTER 1: INTRODUCTION

1.1 Molecular Reaction Dynamics.

Molecular reaction dynamics is a rapidly developing field, concerned with the elucidation of the details of chemical rate processes at a molecular level. In suitably designed experiments, specific rate constants are measured as a function of the energy states of the reactants. Theoretical considerations then serve to relate these experimental results to atomic and molecular collision processes. Excellent reviews of the present state of the art have been published[1-12,117]. They demonstrate the breadth of the field, and its explosive development in recent years.

The rate of an elementary chemical reaction, e.g.

$$A + B \longrightarrow X + Y, \qquad (1)$$

is proportional to the concentrations of the reactants:

$$v = - d[A]/dt = k [A][B]. \qquad (2).$$

The temperature dependence of the rate constant was established empirically by Arrhenius[13]:

$$k = A \exp(-E'/RT). \qquad (3).$$

The reaction is considered to occur through collisions between the reactants, leading to the interpretation of the pre-exponential factor A as a collision number[14,15]. The experimental activation energy E' then represents the energy barrier for effective encounters leading to reaction[13,16].

In practice, the macroscopic measurables in eqs. (2) and (3) are averagings over all possible internal states and molecular properties. For the most complicated systems, only statistical theories[17,18] can lead to successful quantitative interpretations, with present-day dynamical techniques. However, such methods usually obscure details of the elementary processes.

In gas-phase reactions, at sufficiently reduced pressures, the collisions between individual atoms and molecules need only be considered. From the detailed understanding of such elementary processes, the macroscopic kinetic properties of the gas can be deduced. Vice-versa, inferences can be made about the molecular interaction from a consideration of the experimental results. This two-way relationship is demonstrated in Fig.1[19,20]. Intermolecular potentials are calculated from the electrostatic interactions of electrons and nuclei according to quantum-mechanical theories[21]. The resulting potential-energy function or hypersurface[1-3] determines the dynamical behavior of the nuclei according to the Born-Oppenheimer approximation, with the assumption of a single electronic state. The macroscopic rate properties can then be calculated directly by use of statistical methods[22]. However, the details of molecular collision processes can only be obtained from dynamical studies. This involves the solution of Schroedinger's equation for nuclear motion[21] (quantum dynamics), or of Hamilton's equations of motion[23] (classical mechanics) for a large number of initial conditions. As indicated by the

Figure 1

Theories of reaction rates.

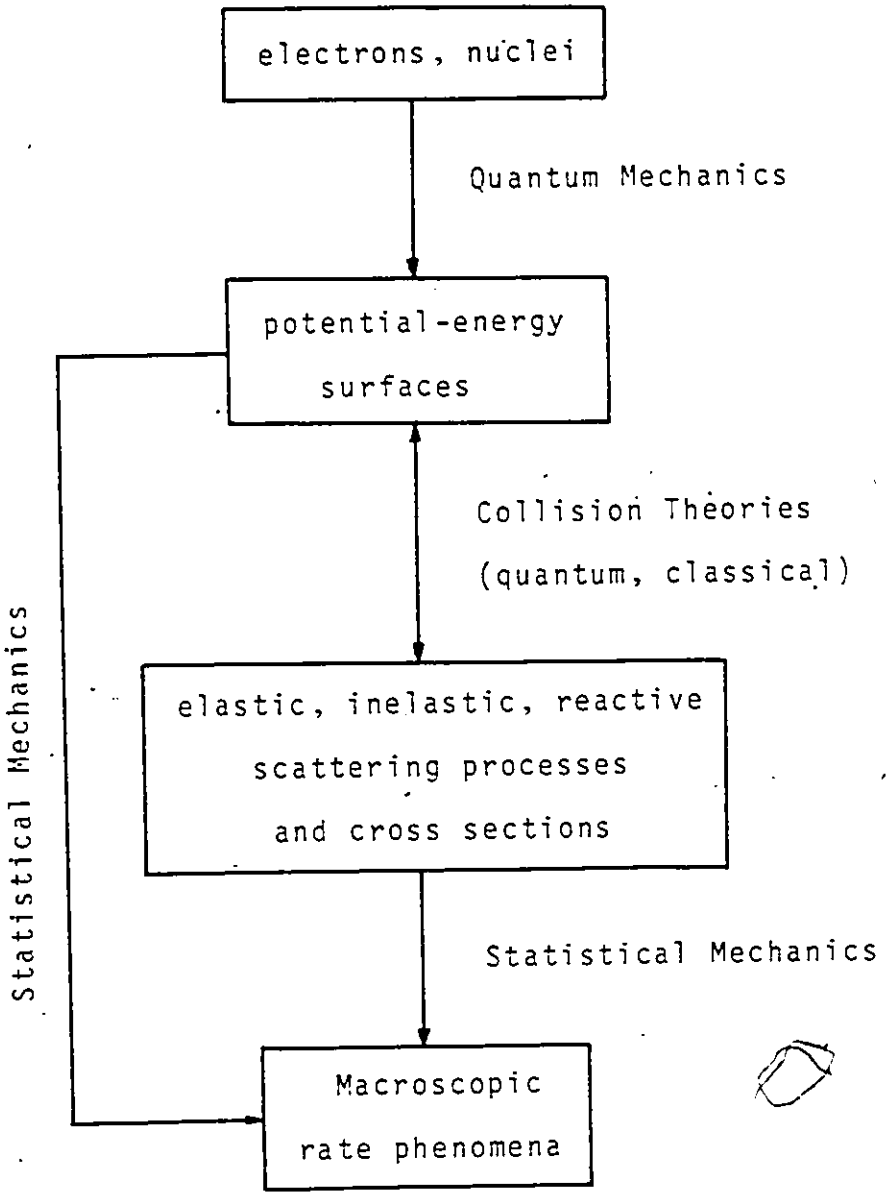
electrons, nuclei
Quantum Mechanics
potential-energy surfaces
Collision Theories (quantum, classical)
elastic, inelastic, reactive scattering processes and cross sections
Statistical Mechanics
Macroscopic rate phenomena
Statistical Mechanics

double-headed arrow in Fig.1, this is a reversible process, allowing the construction of potential-energy surfaces from the results of accurate scattering experiments. Classical mechanics is generally adequate to account for the observed scattering phenomena, but sometimes quantum-dynamical treatments are necessary to explain the finer details of such processes, and to evaluate the reliability of the potential-energy surfaces and molecular collision theories involved. The final derivation of macroscopic rate properties from molecular cross sections and specific rate constants is a statistical-mechanical problem.

1.2 Brief Historical Review.

In 1926 Schroedinger[24] showed that the quantum-mechanical problem of determining electronic interactions can, in principle, be solved. The first approximate solution of this kind was obtained in 1927 by Heitler and London[25] for the H_2 molecule. The treatment was extended by London[26] in 1929 to the H_3 system. In 1931 Eyring and Polanyi[27] modified the London equation to obtain the first workable semi-empirical surface for the $H+H_2$ reaction. The few early attempts to calculate trajectories on this surface were laborious[28] since the non-linear differential equations of motion could not be solved analytically. Most of the work was therefore restricted to qualitative speculations about the dynamical effects of various characteristic surface and reaction parameters on the basis of "thought trajectories"[29].

As an aid for such studies, a potential-energy surface model was developed, on which marbles could be rolled to simulate collinear collisions [27-30]. The results of these purely deductive efforts were of outstanding significance. Much of the groundwork for present-day theoretical treatments was laid by Eyring, Polanyi and coworkers[17,18,27-30] between 1931 and 1939. Experimental work was also initiated in 1935 by von Hartel and Polanyi[31], who studied the $Na+CH_3I$ reaction by monitoring the sodium flame.

In the meantime, an alternative statistical approach to rate theory was developed, based on an early suggestion of Marcelin[32]. The activated-complex theory, as formulated by Eyring, Polanyi, Wigner, and others (cf. Refs. 1 and 2), is still one of the most reliable and certainly the simplest of quantitative rate theories. Statistical theories, however, cannot provide certain detailed information, such as product energy distributions, specific rate constants, etc.

The real breakthrough in molecular reaction dynamics had to await the advent of advanced instrumental technology, including high-speed digital computers. In 1954 the first successful molecular-beam experiments were started by Bull and Moon[33], and in 1955 they were improved upon by Taylor and Datz[34]. Later, kinetic absorption spectroscopy[35] and infrared chemiluminescence measurements[36] were developed as powerful alternative methods. Continuous improvements to these techniques now allow the determination of microscopic details of elementary

gas-phase processes other than the early alkali-metal reactions. The latest developments include highly specific energy-state selectors and very sensitive detectors for molecular beams, and the use of laser technology in the spectroscopic methods.

Meanwhile, the use of digital computers led to a better understanding of molecular collision theories. In 1958 Wall, Hiller and Mazur[37] started the first extensive classical trajectory calculations for the collinear $H+H_2$ system. Around the same time, ab-initio calculations of H_3 potential-energy surfaces were also begun (see Ref.2 for an extensive review). These calculations were then extended to increasingly complicated systems and dynamical treatments, on a wide variety of ab-initio and semi-empirical surfaces. At the present time, chemically accurate potential-energy functions for collinear $H+H_2$ have been reported[38,39], and full three-dimensional quantum-dynamical calculations for this reaction have also been carried out[40,41,118]

The rapid accumulation of experimental and theoretical information has diversified the field of molecular dynamics into such specialized disciplines as scattering processes (elastic, inelastic, reactive); dynamical methods (classical, semi-classical, quantum-mechanical); statistical and heuristic theories; potential-energy surfaces (ab-initio, semi-empirical, parametric); energy-transfer processes, chemically excited states and chemical lasers; simplified reaction models, etc. The nature of the data obtained from these studies has become richer in detail, reflecting the attempts to bring theory and experiment into closer correspondence.

1.3 Perspective of the Thesis.

The first computer calculations for collinear $H+H_2$[37] were basically carried out in a systematic way. Most later work has relied on the random generation of initial conditions (Monte Carlo methods)[11,42,43], to reduce the amount of computation. Such methods seemed particularly necessary in higher-dimensional studies, where the number of degrees of freedom is very large. Statistical treatments of this kind usually result in the loss of detailed information on the outcome of individual collisions as a function of the initial parameters. Since the physical measurables of earlier experiments were macroscopic properties, details of this kind were not needed. As experimental techniques improved, the time and energy resolution of the instruments increased, and microscopic details of elementary reaction steps are now slowly becoming available.

Meanwhile, the calculations were extended to other chemical systems, for which only parametric or semi-empirical surfaces are available. The systematic variation of surface and system parameters was started as early as 1936[44,62] and yielded valuable insight into the dependence of reaction probabilities on such parameters. Polanyi and co-workers[45-47] carried out extensive calculations on a variety of reactions and surfaces, using semi-systematic techniques[45], as well as Monte Carlo methods[46,47]. As a result of such calculations, a classification was achieved in terms of the reaction types (endothermic and exothermic), surface types (attractive, repulsive), mass combinations (L+LL,

L+HH, H+LH, etc.; L = light, H = heavy atom), and reaction mechanisms (stripping, rebound, spectator stripping, harpooning). These investigations aided in the interpretation of experimental results and in the qualitative prediction of the behavior of new systems. Complete systematic studies of collinear collisions have also been reported[48-54], usually in relation to quantum-mechanical or semi-classical treatments. They yield much more information about individual collision processes, but require more computer time than the Monte Carlo calculations. They are therefore unsuitable for extension to higher dimensions.

The $H+H_2$ system, for which the most accurate computational results are available, has been the testing ground for new theoretical methods and models. Examples are the extensive comparisons of results obtained with different surfaces, and computational methods, for this reaction[1-19]. The general trend in all these investigations is to start with the simplest case and to gradually increase the sophistication of the treatment. Since the simpler calculations require far less computer time, reliable extrapolation methods to more complicated cases are constantly being explored. Marcus[55] classifies such methods as approximations which rely heavily on generalizations of dynamical behavior. For example, semi-classical theories[56,57] can account for essentially all quantum effects, using classical trajectory data as input. Other, much cruder, approximations include extrapolations of collinear and coplanar results to higher dimensions, the vibrational adiabaticity assumption,

and other simple reaction models.

In accordance with these general trends, the purpose of the present thesis was to seek a more systematic approach toward the acquisition of accurate classical results with a limited number of trajectory calculations. By varying the free reaction parameters one at a time, the attempt was made to determine the influence of the initial conditions on the outcome of the trajectories. The investigation was restricted to the $H+H_2$ system and some of its isotopic variations.

The remainder of this thesis is organized in a chronological order, the later studies being logical extensions of the earlier ones. In Chapter 2 a general introduction to collinear calculations and a detailed description of the general methods of investigation are given. Calculations on the Shavitt, Stevens, Minn and Karplus (SSMK) surface[38] are then presented for the collinear $H+H_2$ reaction. This particular choice represents the simplest case study, using the most accurate potential-energy surface available at the time this work was begun. The calculations are generally restricted to reactant molecules initially in their zero-point energy (ZPE) vibrational levels. Only two initial parameters, the vibrational phase angle and the relative translational energy had to be varied. In Chapter 3 a simple extension of the study to include symmetric mass combinations X+HX, with X taken as various real and fictitious isotopes of H, is presented and discussed. Such an extension corresponds in principle to a systematic variation of one additional parameter,

the skew angle (cf.Sec.2.2), although changes in ZPE and the vibrational constants have to be taken into account for a complete analysis. The same surface, computer program and methods of calculation were used in all collinear studies. At the end of Chapter 3 a general discussion of the implications of these studies is presented, and a comparison to the work of others is made. In Chapter 4 a far more complicated extension to the coplanar $H+H_2$ reaction is discussed. At the present time, the most accurate potential-energy surface for collinear $H+H_2$ is the one obtained by Liu[39]. Liu's results have been generalized to three dimensions by Yates and Lester[58], by the use of a Porter-Karplus type of function[59]. The three-dimensional (3-D) trajectory program of Muckerman[60] was modified to allow a 2-D study of the $H+H_2$ reaction, with the use of the Yates-Lester (YL) hypersurface and systematic selection of initial parameter values. Preliminary computations with J=5 (J is the reactant rotational quantum number) were essential in establishing the reliability of the program, and in the development of general methods of investigation. An extensive study of the initially rotationless case (J=0) was then undertaken to determine the influence of two new parameters, the orientation angle θ and the impact parameter b. The vibrational phase angle ϕ and the relative translational energy T_t were varied as in the 1-D case, basically retaining the method developed earlier.

Because of the accumulation of data which remained to be analyzed, the quasi-classical trajectory calculations were

halted. Attempts were made to generalize a particularly consistent relationship, observed between some final and initial reaction parameters. Such a generalization was aimed at the reduction of computational requirements, and at a better understanding of the nature of the dynamics of molecular collisions. The development of some simple models to achieve this purpose is discussed in Chapter 5. It was hoped that ultimately qualitative, or even semi-quantitative, predictions might be made from the consideration of such basic parameters as the barrier height, the skew angle, the reaction coordinate, rotational and vibrational constants, and energies.

CHAPTER 2: COLLINEAR CALCULATIONS

2.1 Introduction.

In quasi-classical calculations, the reactant molecules are initially restricted to quantum-mechanically allowed vibrational and rotational actions, p_{vib} and p_{rot} ( ). The initial vibrational energy (E_v^o) must therefore have a minimum value corresponding to the zero-point energy (ZPE) of vibration. In collinear calculations no rotation is allowed.

The first computer calculations of classical (E_v^o=0) and quasi-classical (v=0,1) trajectories were carried out by Wall, Hiller and Mazur[37] for the collinear $H+H_2$ reaction, using the London-Eyring-Polanyi surface[27]. The collision time was shown to be a complicated banded function of the total energy, in which some continuous reactive and unreactive bands could be observed, bounded by maxima and minima in time. For v=0, a consistent shift of the bands with the initial vibrational phase angle was also shown. Wall et al.[37] were more interested in obtaining reaction probabilities, and later[61] introduced a pseudo-random method for 3-D calculations. However, only 6 of the 700 trajectories were found to be reactive, so that no significant conclusions were reached. Wall and Porter[62] then returned to classical collinear calculations (E_v^o=0), and investigated the effects of the variation of mass combinations and of the parametric Wall-Porter surfaces[63]. The results of Wall, Hiller and Mazur[37,61] can now be attributed to the

deficiency of the London-Eyring-Polanyi (LEP) surface[27], which had a potential-energy well on top of the barrier. Porter and Karplus[59] constructed a semi-empirical surface, based on the modification of the LEP treatment[27] by Sato[64]. Using this surface and a Monte Carlo method, Karplus, Porter and Sharma[65] were then able to obtain the first 3-D reaction cross sections for $H+H_2$, $D+H_2$ and $T+H_2$ reactions. This started the era of quasi-classical Monte Carlo calculations[11,42,43].

Recent systematic investigations[49-54] revealed that the variation of the initial vibrational phase angle at constant energy results in the observation of only a few regions of continuous reactivity or non-reactivity, bounded by high values of the product vibrational energy. Such features were obscured in the Monte Carlo treatments, and suggested some interesting possibilities for future systematic investigations.

A preliminary study by Hulse[66] was based on the original method of Wall et al.[37] in which the initial relative translational energy was varied at a constant phase angle. For the more realistic SSMK surface[38] the banded behavior of the reaction time was again observed, but in a much simpler form, showing a few regions of alternating reactivity, marked by isolated time peaks. It was therefore decided to carry out a full systematic investigation of the collinear $H+H_2$ reaction on the SSMK surface, to gain a better understanding of molecular collision processes, and to explore the possibilities of such an approach. It was realized that the detailed study of the dependence of final parameters on the initial conditions could lead to accurate e-

results with reasonable amounts of trajectory calculations, only if a reliable method of interpolation could be found.

Many alternative systematical methods, along such lines as phase-space theory[67], geometrical analysis[68], and classical wave-mechanical treatments[69], were at one time being considered. Since such methods would invariably involve some degree of approximation, they were soon dismissed in favor of exact quasi-classical trajectory calculations.

2.2 Description of the System.

The collinear three-particle system is fully described by two interatomic distances and the position of the center-of-mass of the system ($\overline{ABC}$) in space. Denoting the atoms A, B and C, from left to right, on the x axis of the laboratory frame:

$$r_{AB} = x_B - x_A, \tag{4}$$

$$r_{BC} = x_C - x_B, \tag{5}$$

$$x_{\overline{ABC}} = (m_A x_A + m_B x_B + m_C x_C)/M, \tag{6}$$

where m_i is the mass of atom i, $M = m_A+m_B+m_C$, and the third atomic distance is always equal to the sum of the other two:

$$r_{AC} = x_C - x_A = r_{AB} + r_{BC}. \tag{7}$$

The kinetic energy of the system is

$$T_{lab} = \tfrac{1}{2}(m_A\dot{x}_A^2 + m_B\dot{x}_B^2 + m_C\dot{x}_C^2), \tag{8}$$

where the dots above the variables denote their time derivatives.

A more complete description of the reaction is given in Fig.2, where three different configurations of the system are considered. When the atom-molecule distance is very large, the motion can be separated into a translational and a vibrational mode, characterized by different coordinates (R_i,r_i) and by different reduced masses (μ_{it},μ_{iv}). The subscripts i denote the configurations (a and c), and t and v stand for translation and vibration respectively. The transformation formula relating the coordinates of a and c has been given by Rankin and Miller[70], and the conjugate momenta and kinetic energies associated with the different modes of motion are[65,70]:

$$p_i = \mu_{it} \dot{R}_i \quad ; \; p_i = \mu_{iv} \dot{r}_i \; ; \tag{9}$$

$$T_{it} = \tfrac{1}{2}\mu_{it} p_i^2 \quad ; \; T_{iv} = \tfrac{1}{2}\mu_{iv} p_i^2 . \tag{10}$$

When the atoms are closer together, as in configuration b, a strong coupling occurs between translation and vibration. The analytical treatment by Marcus[71] shows that the kinetic energies of the normal modes of motion can be continuously evaluated along the reaction path, by the use of normal coordinates and force constants. For the present purposes it suffices to state that the translational and vibrational modes of motion are gradually converted into the asymmetric (A) and symmetric (S) stretching vibrations of the transition state[1], i.e. the kinetic energies at $r_{AB}=r_{BC}$ can be written as:

$$T_{bt} = T_A \quad ; \; T_{bv} = T_S . \tag{11}$$

Figure 2

Description of collinear A+BC reactions.

State	Reactants	Transition state	Products
Configuration, (i)	A + B-C, (a)	A·····B····C, (b)	A-B + C, (c)
Condition	$r_{AB} > r_{BC}$	$r_{AB} \simeq r_{BC}$	$r_{AB} < r_{BC}$
Translation:	A relative to $\overline{BC}$	asymmetric	C relative to $\overline{AB}$
coordinate R_i	$R_{A,BC}=r_{AB}+\frac{m_C}{m_B+m_C} r_{BC}$	stretching	$R_{AB,C}=r_{BC}+\frac{m_A}{m_A+m_B} r_{AB}$
reduced mass μ_{it}	$\mu_{A,BC}=M^{-1}m_A(m_B+m_C)$	mode	$\mu_{AB,C}=M^{-1}m_C(m_A+m_B)$
Vibration:	B relative to C	symmetric	A relative to B
coordinate r_i	r_{BC}	stretching	r_{AB}
reduced mass μ_{iv}	$\mu_{BC}=m_Bm_C/(m_B+m_C)$	mode	$\mu_{AB}= m_Am_B/(m_A+m_B)$

$\overline{BC}$ is the center of mass of B-C

$\overline{AB}$ is the center of mass of A-B

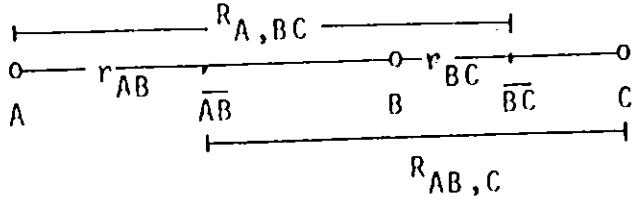

In a center-of-mass coordinate frame, the motion of $\overline{ABC}$ can be neglected, and $T_{\overline{ABC}} = \frac{1}{2}M\dot{x}^2_{\overline{ABC}}$ is subtracted out of eq. (8), to yield the center-of-mass total kinetic energy:

$$T = T_{lab} - T_{\overline{ABC}} = T_{it} + T_{iv}; \quad (i=a,b,c). \tag{12}$$

Such a simplification is possible, since the collision process is governed by the interatomic potential, which is a function of the interatomic distances only, i.e. for collinear processes:

$$V = V(r_{AB}, r_{BC}). \tag{13}$$

The three-particle problem can be represented by the motion of a single particle of reduced mass over the three-dimensional surface (13), if the kinetic energy expression (12) can be written without cross terms as[1,27,72]:

$$T = \tfrac{1}{2}\mu(\dot{x}^2 + \dot{y}^2), \tag{14}$$

A particularly illuminating and convenient method to achieve this purpose is to assume $\mu=1$, and to make use of the relative coordinates (R_i, r_i)[72]. It is easily seen that for i=a, eqs.(10) and (12) are transformed into (14) when:

$$x = \mu^{\frac{1}{2}}_{A,BC} R_{A,BC} \quad ; \quad y = \mu^{\frac{1}{2}}_{BC} r_{BC}. \tag{15}$$

For i=c, the corresponding expressions would be

$$x' = \mu^{\frac{1}{2}}_{AB,C} R_{AB,C} \quad ; \quad y' = \mu^{\frac{1}{2}}_{AB} r_{AB}, \tag{16}$$

so that apparently two different coordinate systems must be used. Unification is achieved in terms of r_{AB} and r_{BC}, for which eq.(12) is unchanged for different configurations:

$$T = \tfrac{1}{2}\mu_{A,BC}\dot{r}^2_{AB} + (m_A m_C/M)\dot{r}_{AB}\dot{r}_{BC} + \tfrac{1}{2}\mu_{AB,C}\dot{r}^2_{BC}. \tag{17}$$

It was shown[1,27] that by introducing a parameter ξ, one possible transformation of (17) into (14) would yield

$$x = \mu_{A,BC}^{\frac{1}{2}} r_{AB} + \mu_{AB,C}^{\frac{1}{2}} r_{BC} \sin(\xi), \tag{18}$$

$$y = \mu_{AB,C}^{\frac{1}{2}} r_{BC} \cos(\xi), \tag{19}$$

$$\sin(\xi) = [m_A m_C / \{(m_A+m_B)(m_B+m_C)\}]^{\frac{1}{2}}. \tag{20}$$

It is significant that eq.(20) can also be obtained by comparing (18) to (15), and that a comparison of (19) to (15) yields

$$\cos(\xi) = (\mu_{BC}/\mu_{AB,C})^{\frac{1}{2}} = (\mu_{AB}/\mu_{A,BC})^{\frac{1}{2}}. \tag{21}$$

This shows that the (x,y), (x',y'), (R_i,r_i), and (r_{AB},r_{BC}) coordinate systems can be correlated by an appropriate skewing and scaling of the axes. The relationships are graphically represented in Fig.3a, where the parameter ξ is seen to be a skew angle for the (r_{AB},r_{BC}) axes (solid lines), and a rotational angle for the (x',y') coordinates (dashed-dotted lines), with respect to the (x,y) coordinate system. The coordinates have a common origin O, and the corresponding coordinates of a point P are also shown, where the thin solid, dashed and dashed-dotted lines again pertain to the (r_{AB},r_{BC}), (x,y), and (x',y') coordinate systems respectively.

The potential energy surface (13) can thus be plotted in such a coordinate system, as shown in Fig.3b, where the curves represent equipotential contours of the surface. For the symmetric X+HX systems studied in the present work $m_A=m_C$, and the R_i, r_i axes need not be scaled, if the reduced mass of the single particle representing the system is taken as $\mu = \mu_{A,BC} = \mu_{AB,C}$.

Figure 3

(a) Skewed and scaled coordinates:

——— (r_{AB}, r_{BC});

----- $(x,y) = (R_{A,BC}, r_{BC})$;

----- $(x',y') = (R_{AB,C}, r_{AB})$

(b) Potential-energy surface model for symmetric X+HX reactions. a = reactant, b = transition state, c = product region. $\cos\xi = \mu_{AB}^{\frac{1}{2}}/\mu_{AB,C}^{\frac{1}{2}} = \mu_{BC}^{\frac{1}{2}}/\mu_{A,BC}^{\frac{1}{2}}$.

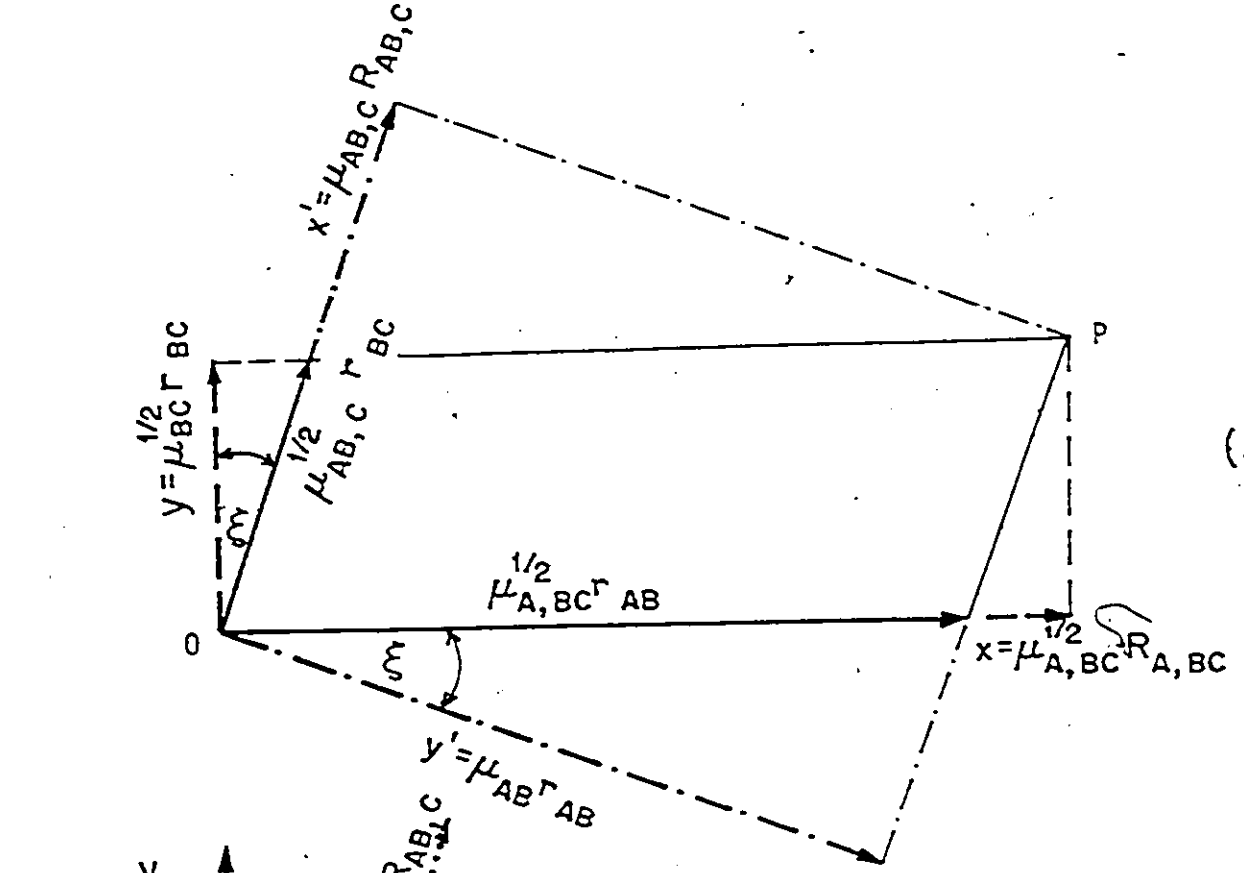
$x' = \mu_{AB,C} R_{AB,C}$
P
$y = \mu_{BC}^{1/2} r_{BC}$
$\mu_{AB,C}^{1/2} r_{BC}$
ξ
0
$\mu_{A,BC}^{1/2} r_{AB}$
$x = \mu_{A,BC}^{1/2} R_{A,BC}$
$y' = \mu_{AB} r_{AB}$

(a)

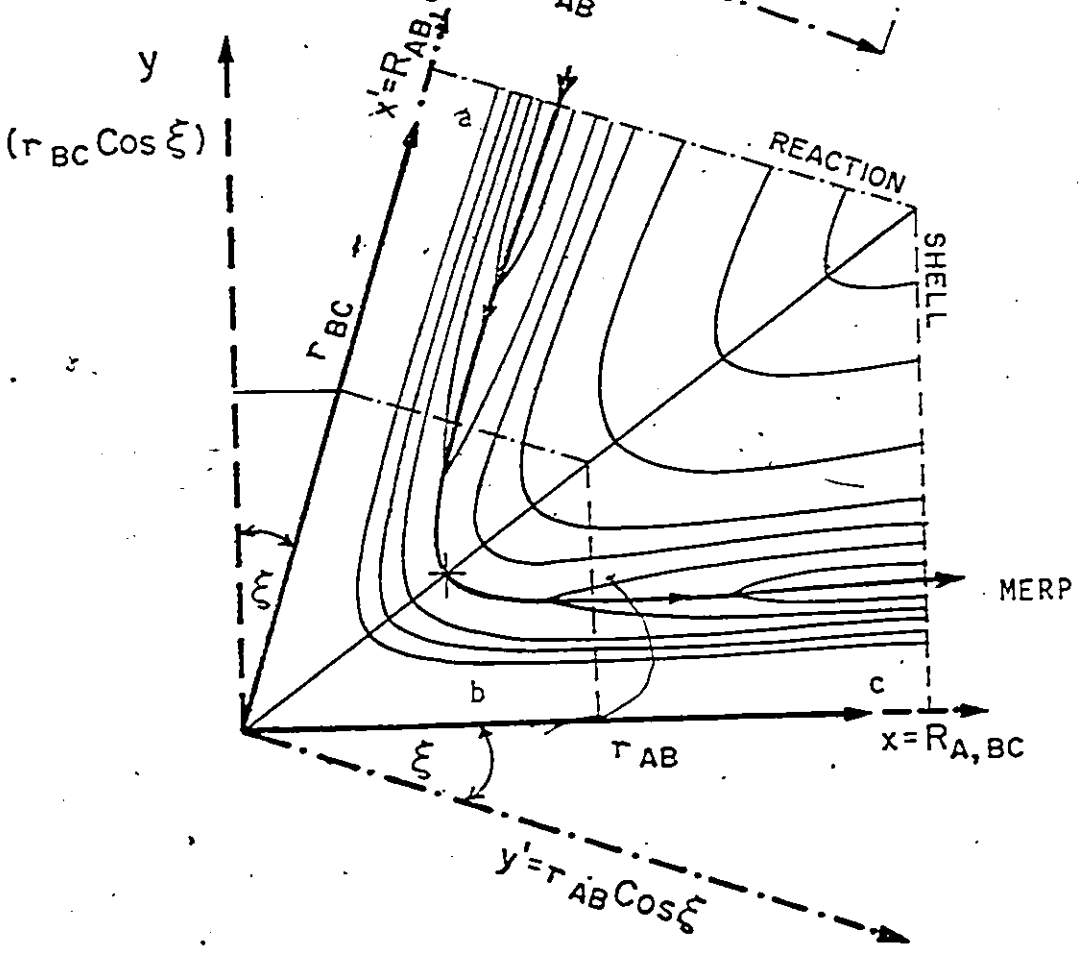
y
$(r_{BC} \cos \xi)$
$x' = R_{AB,C}$
a
REACTION
SHELL
r_{BC}
ξ
MERP
b
c
r_{AB}
$x = R_{A,BC}$
$y' = r_{AB} \cos \xi$

(b)

This skewed potential-energy surface model, formerly used to simulate collinear trajectories[27-30], has remained a most powerful interpretive tool. For reactions X+HX, as in Fig.3b, the surface is totally symmetric about the "dividing line", which represents $r_{AB}=r_{BC}$ (thin solid line). The energetically most economic pathway for reaction is indicated as the minimum-energy reaction path (MERP, heavy solid curve). It follows the bottom of the reactant valley (a), crosses the energy barrier at the saddle point (+), and follows the path of steepest descent into the product valley (c). The true reaction coordinate[73], followed by actual trajectories, is an oscillating path across the surface, and is dependent on all initial conditions. It is more conveniently represented[71] by the vibrationally averaged reaction path (VARP, not shown), which is a function of the initial translational energy only. The "reaction shell" is defined along R_i= constant lines, and limits the region in which the trajectories are simulated. It has to be large enough to assume negligible interaction between atom and molecule, but small enough to reduce the computer time to within economical limits. Because R_i= constant, and if no atom-molecule interaction is present, the energy profile along the reaction shell represents the vibrational potential of the diatomic molecule. The "complex shell" defines the region where the atom-molecule interactions are so large, that a clear distinction between separate entities and modes of motion can no longer be made. It is convenient to locate the complex shell at a point where the

MERP just begins to curve, indicating the start of vibration-translation coupling. The region within the complex shell represents the activated state. At the saddle point, the symmetric stretch occurs along the dividing line, and the asymmetric stretch takes place along a line perpendicular to it.

2.3. Internal Coordinates and Equations of Motion.

The explicit form of the classical equations of motion used is that given by Wall and Porter[62]. The Hamiltonian or total energy is the sum of the kinetic and potential energy terms, which are expressed in terms of generalized coordinates and canonical conjugate momenta[23]:

$$H = T(p_1,p_2) + V(q_1,q_2). \tag{22}$$

The internal coordinates are the interatomic distances

$$q_1 = r_{AB} = x_B - x_A, \tag{23}$$

$$q_2 = r_{BC} = x_C - x_B, \tag{24}$$

and the kinetic energy term is evaluated by performing a point contact transformation[23] ($p_i = \sum_j p_j(\partial q_j/\partial Q_i)$):

$$p_{x_A} = m_A\dot{x}_A = -p_1, \tag{25}$$

$$p_{x_B} = m_B\dot{x}_B = p_1 - p_2, \tag{26}$$

$$p_{x_C} = m_C\dot{x}_C = p_2, \tag{27}$$

and substituting the results in eq.(8):

$$T = \tfrac{1}{2}p_1^2/\mu_{AB} - p_1p_2/m_B + \tfrac{1}{2}p_2^2/\mu_{BC}. \tag{28}$$

The canonical Hamiltonian equations of motion are[23]:

$$\dot{q}_i = \partial T/\partial p_i; \qquad \dot{p}_i = -\partial V/\partial q_i; \tag{29}$$

so that from eq.(28):

$$\dot{q}_1 = p_1/\mu_{AB} - p_2/m_B; \quad \dot{q}_2 = p_2/\mu_{BC} - p_1/m_b. \tag{30}$$

The translational and vibrational kinetic-energy terms can be directly obtained from eqs.(10) and (30), together with the definitions of the coordinates and reduced masses in Fig.2. A more informative procedure involves the determination of the conjugate momenta from eq.(30), or more conveniently from eq.(17) through another canonical equation[23] ($p_i = \partial T/\partial \dot{q}_i$):

$$p_1 = \mu_{A,BC}\dot{q}_1 + (m_A m_C/M)\dot{q}_2 = \mu_{A,BC}\dot{R}_{A,BC} = p_a;$$
$$p_2 = \mu_{AB,C}\dot{R}_{AB,C} = p_c. \tag{31}$$

It is then clear, that p_1 and p_2 are not associated with the motions of A relative to B, and of B relative to C, as might have been expected since $q_1 = r_{AB}$ and $q_2 = r_{BC}$. Instead, p_1 and p_2 are identical to the relative translational momenta of configurations a (A relative to $\overline{BC}$) and c (C relative to $\overline{AB}$). From eqs.(10) and (31) follow:

$$T_{at} = \tfrac{1}{2}p_1^2/\mu_{A,BC}; \qquad T_{ct} = \tfrac{1}{2}p_2^2/\mu_{AB,C}; \tag{32}$$

and with eq.(30):

$$T_{av} = \tfrac{1}{2}\mu_{BC}\dot{r}_{BC}^2 = \tfrac{1}{2}\mu_{BC}(-p_1/m_B + p_2/\mu_{BC})^2;$$
$$T_{cv} = \tfrac{1}{2}\mu_{AB}(p_1/\mu_{AB} - p_2/m_B)^2. \tag{33}$$

The expressions derived by Wall and Porter[62] are identical to eqs.(32) and (33) after some rearrangements.

2.4 The SSMK Surface.

Shavitt, Stevens, Minn and Karplus[38a] completed two sets of ab-initio calculations of the H_3 potential energy. First a set of six optimized basis functions (1s, 1s' on each atom) was used, but better results were obtained with a 15-orbital basis set (1s,1s',$2p_x$,$2p_y$,$2p_z$ on each nucleus). The H_2 energy was only about 3 kcal/mole above the true energy, and a barrier height of 0.477 eV was obtained for the collinear geometry. The calculated points were fitted by analytical expressions:

$$E_{H_2} = \exp(-Ar_{BC}) \sum_{0}^{8} (C_i r_{BC}^i) \quad \text{(a.u.)}, \tag{34}$$

$$E_{H_3} = E_{H_2} - 0.5 + \exp\{-\alpha(r_{AB}+r_{BC})\} \sum_{i=0}^{6} \sum_{j=0}^{6-i} (C_{ij} r_{AB}^j r_{BC}^i). \tag{35}$$

for collinear geometries and $r_{AB} \geq r_{BC}$. The values of the optimized parameters A, C_i, α, C_{ij}, as published and corrected by Shavitt et al.[38], are listed in Table I. The analytical fit to the ab-initio points is satisfactory in the neighborhood of the MERP, and a slightly higher barrier height of 0.493 eV is obtained. The correct limit, $E_{H_3} = E_{H_2} + 0.5$ a.u., is reached when $r_{AB} \to \infty$, but an examination of eq.(34) revealed that $E_{H_2} \to 0$ instead of -1 for dissociated H+H ($r_{BC} \to \infty$)[74]. This causes large errors near the H+H+H limit, in regions which are fortunately irrelevant to the present study. A more serious consequence is that the dissociation energy D_e is then ca. 27.21 eV higher than the reported ab-initio value of -4.61 eV. The latter value is therefore used in the calculation of vibrational energies.

H_2 (10 orbitals) cf. eq. (34)	H_3 (15 orbitals) cf. eq. (35)			
$A = 1.32$ au.$^{-1}$	$\alpha = 1.2180$ au.$^{-1}$			
i C_i	i j C_{ij}	i j C_{ij}	i j C_{ij}	
0 2.881106	0 0 20.6782	1 2 8.5460058	3 0 -80.772167	
1 -8.6064101	0 1 -3.5326727	1 3 0.45704353	3 1 9.0971615	
2 4.6016784	0 2 3.8209212	1 4 -0.1196757	3 2 6.1798531	
3 -2.3976518	0 3 -2.7667995	1 5 -0.078315251	3 3 -1.4533685	
4 -0.42034964	0 4 0.53396417	2 0 103.11613	4 0 32.350972	
5 0.54761616	0 5 -0.034958722	2 1 -1.9957114	4 1 -8.8025261	
6 -0.2462333	0 6 0.0056669712	2 2 -8.5296565	4 2 1.0203549	
7 0.046039649	1 0 -61.744419	2 3 -0.63722732	5 0 -4.5584173	
8 -0.004368049	1 1 -9.8121584	2 4 0.55209208	5 1 0.5386946	
			6 0 0.17204175	

Table I: Optimized coefficients for the analytical SSMK potential-energy funttion.

Ab-initio points were also calculated for non-linear geometries, by Shavitt et al.[38a], but only the collinear results were fitted by an analytical function. The results show that the collinear geometry is clearly the energetically most favored configuration. This is also evident from the positive value for the force constant of the bending vibrations (A_b) at the saddle point. In Table II some of the SSMK surface parameters are shown in comparison to the Liu[39] and Yates-Lester[58] surface characteristics, and to some experimental values[75]. The H_2 parameters are the Morse parameters[76] D_e(dissociation energy), r_e (equilibrium distance) and β (exponential factor), where the ab-initio value for D_e (see above) is taken, and where β has been calculated from the reported force-constant of the H_2 vibration. E_c is the calculated energy for H_2; the experimental value is the true non-relativistic value obtained from spectroscopic data. The saddle-point parameters are for the collinear geometry; r_{sp} is the interatomic separation at the saddle point ($r_{AB}=r_{BC}$); A_S, A_A and A_b are the force constants for the symmetric, asymmetric and bending modes, and are rough measures of the width of the reaction channel, the width of the barrier, and the stability of the collinear geometry respectively; E_a is the height of the barrier relative to $H+H_2$ (E_c - 0.5). The agreement between the three surfaces and the experimental values is quite close, indicating that the surfaces are very realistic and very similar to one another. More detailed comparison of the surfaces have shown that they generally parallel each other[39,58].

Table II. Characteristics of the SSMK, YL and Liu surfaces.

	SSMK	YL	Liu	Exp.[a]
H_2 parameters:				
D_e/eV	4.6147	4.7270	4.7281	4.747
r_e/a.u.	1.4018	1.4063	1.4014	1.401
β/a.u.	1.0303	1.037	1.0250	
E_c/a.u.	-1.1696	—	-1.1737	-1.1744
Collinear saddle point:				
r_{sp}/a.u.	1.764	1.742	1.757	1.658
A_S/a.u.	0.31	0.32	0.32	—
A_A/a.u.	-0.061	-0.071	-0.058	—
A_b/a.u.	0.024	0.03	—	—
E_a/eV	0.477	0.4254	0.425	0.425

[a] cf. Ref. 38b and 75.

Explanation of the symbols used:

D_e, r_e, and β are Morse parameters[75,79] (dissociation energy, equilibrium separation and exponential factor).

E_c is the computed energy of H_2; the experimental value is the true, nonrelativistic value obtained from spectroscopic data.

r_{sp} is the internuclear separation at the saddle point.

A_S, A_A and A_b are force constants of the transition state (symmetric, asymmetric and bending).

E_a is the height of the barrier relative to $H+H_2$ (E_c-0.5).

Fig.4 shows a contour map of the SSMK surface, which is seen to be very well behaved in the region of interest in this study. The contours are very smooth compared to earlier semi-empirical and parametric surfaces[2,27,59,63,64], as has been shown in in Refs.2 and 38. The contours are almost perfectly parallel outside the range (2.610 Å) shown in the original paper[38], and the MERP shows appreciable curvature only at very small atom-molecule distances ($r_{AB}, r_{BC} < 1.5$ Å). The energy profile along the MERP starts to dip below the minimum energy of the separated reactants near $r_{AB} = 7$ Å, and reaches a minimum at $r_{AB} = 3.5$ Å. This shallow well of depth 0.0089 eV may represent the true van der Waals interaction of the reactants, but may also be an artifact of the analytical fit[38a]. Slight discrepancies are observed if trajectories are started with initial atom-molecule separations less than 7 Å to achieve sufficiently reduced computational times. These discrepancies, however, are caused by slight oscillations in the MERP in the region $2.6 < r_{AB} < \infty$, rather than by the presence of this dip. The most acceptable results would be obtained by locating the reaction shell through the true minimum of the surface, where the MERP is essentially rectilinear, and where pure vibrational trajectories would remain translationless. Examination of the potential-energy profiles taken along cuts perpendicular to the MERP (Fig.1, Ref.38a) indicates that the reaction shell can still be moved much closer to the saddle point, without serious coupling of vibration and translation taking place.

Figure 4

Contour map of the SSMK surface.

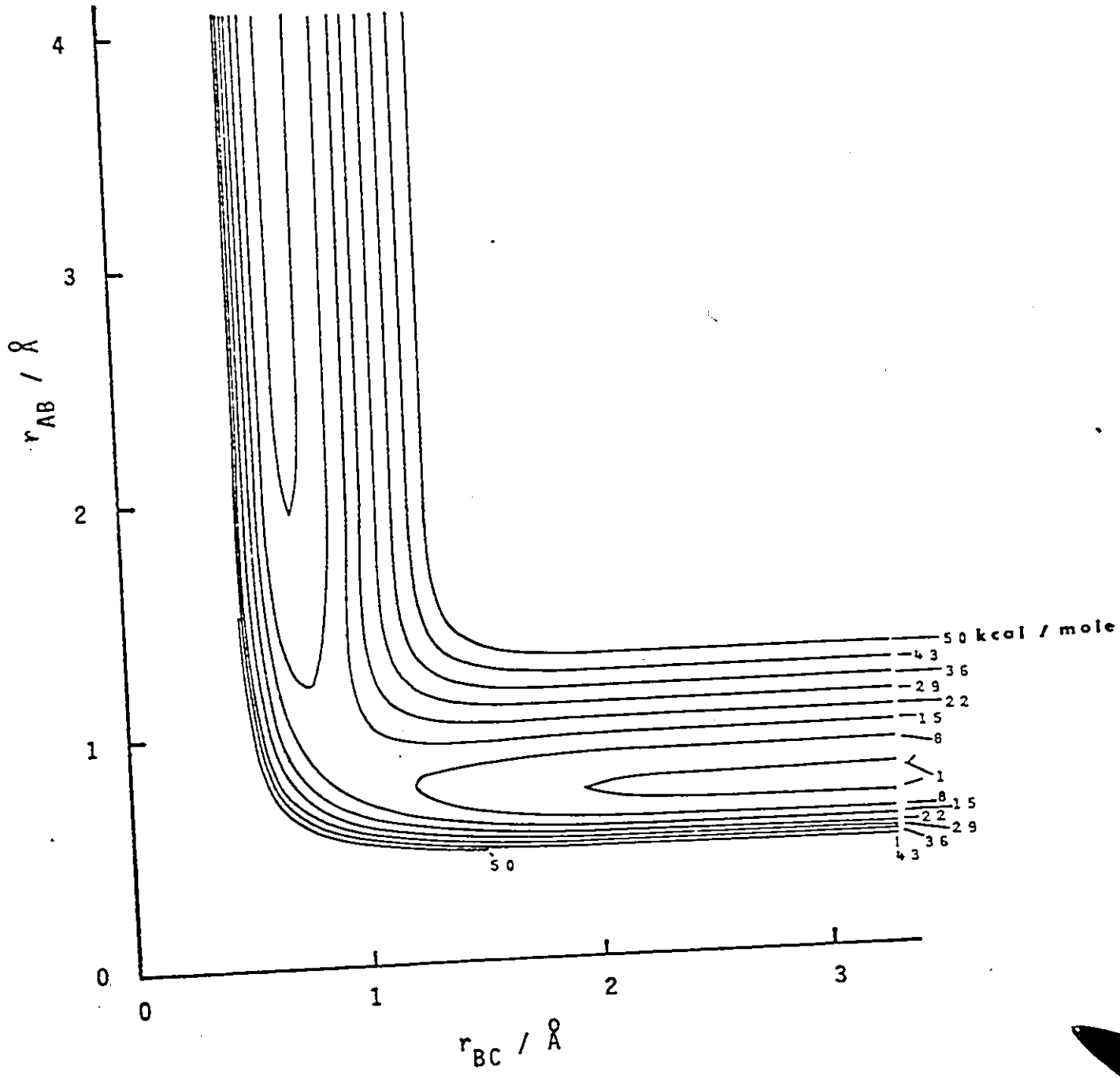
4
3
2
1
0
0
1
2
3
r_{AB} / Å
r_{BC} / Å
50 kcal / mole
43
36
29
22
15
8
1
8
15
22
29
36
43
50

2.5 Methods of Calculation.

2.5.1 General Restrictions.

The initial conditions were varied within the limits set by the following restrictions:

a. E_v^o = ZPE. The reactant molecule always started out with v=0, i.e. with the zero-point energy (ZPE) appropriate to the SSMK anharmonic oscillator. The vibrational energies were calculated from the spectroscopic formulae, for a Morse oscillator[76]:

$$\begin{aligned} E_v &= \omega_e(v+\tfrac{1}{2}) - \omega_e x_e(v+\tfrac{1}{2})^2 && \text{cm}^{-1}, \\ \omega_e &= (2\pi c)^{-1}(\underline{k}/\mu)^{\frac{1}{2}} && \text{cm}^{-1}, \\ \omega_e x_e &= \omega_e^2/(4D_e) && \text{cm}^{-1}, \end{aligned} \qquad (36)$$

where c is the speed of light, μ is the reduced mass of the molecule, and $\underline{k}$ and D_e are the H_2 force constant and dissociation energy obtained from the ab-initio SSMK results[38], and where all constants have been converted into the appropriate units. The results of these calculations are listed in Table III, together with the cut-offs for the quantization of product vibration, amplitudes and half-periods of vibration, and the reduced masses of the HX molecules, corresponding to the first two series of calculations (see below).

b. ρ^o = constant. Three series of calculations (I,II,III) were carried out with different "reaction shell radii" (ρ^o), which are schematically illustrated in Fig.5. The trajectories were first started with r_{AB}^o=5.0 Å (line I'), and terminated when r_{AB} or r_{AC} exceeded 5.5 Å (reaction shell I in Fig.5).

Table III. Data characteristic of the HX oscillators.

	HH	HD	HT	H-10
E_0/eV	0.2686	0.2331	0.2200	0.2000
E_1/eV	0.7816	0.6812	0.6438	0.5868
E_2/eV	1.2624	1.1051	1.0461	0.9558
E_3/eV	1.7109	1.5048	1.4270	1.3071
E_4/eV	2.1273	1.8804	1.7863	1.6407
E_5/eV	2.5115	2.2319	2.1242	1.9565
E'_0/eV $\leq$	0.5251	0.4571	0.4319	0.3934
E'_1/eV $\leq$	1.022	0.8931	0.8450	0.7713
E'_2/eV $\leq$	1.487	1.305	1.237	1.131
E'_3/eV $\leq$	1.919	1.693	1.607	1.474
E'_4/eV $\leq$	2.319	2.056	1.955	1.799
r_l/Å	0.6349	0.6412	0.6444	0.6483
r_r/Å	0.8838	0.872	0.868	0.8618
$\tau_l \times 10^{16}$/s	32.32	37.67	40.09	44.46
$\tau_r \times 10^{16}$/s	45.54	51.76	54.71	59.74
μ/a.m.u.	0.5	0.6702	0.7545	0.9157

Figure 5

Definition of the reaction shells used in calculations I, II and III. The initial vibrational phase angles are also shown in this schematic diagram.

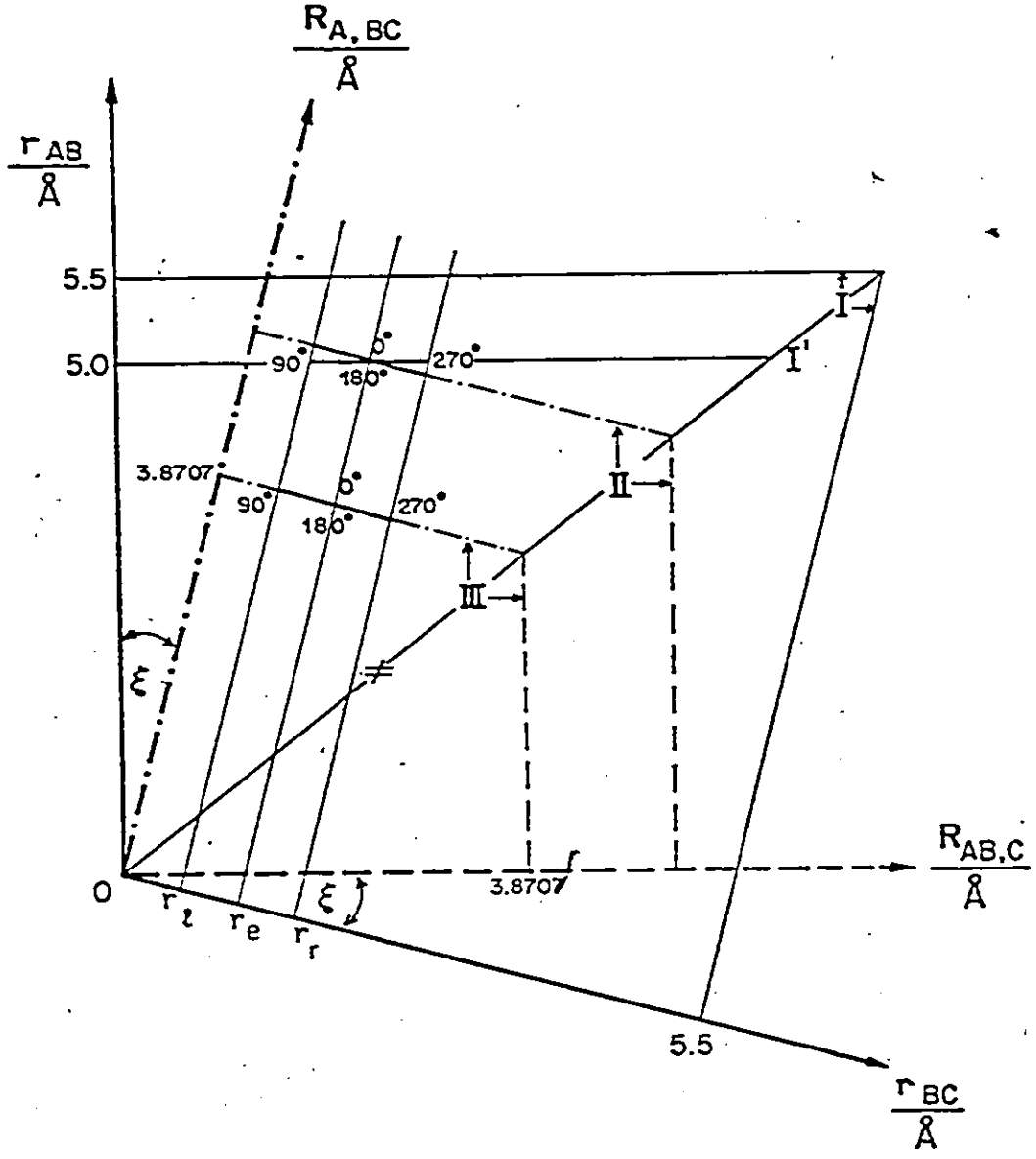
$R_{A,BC}$ Å
r_{AB} Å
5.5
5.0
90°
0°
180°
270°
I
I'
3.8707
II
III
ξ
≠
0
r_l
r_e
r_r
ξ
3.8707
$R_{AB,C}$ Å
5.5
r_{BC} Å

The second series of calculations were performed with reaction shell II ($\rho^o = R^o_{A,BC} = 5.3714$ Å, passing through $r_{AB} = 5.0$, $r_{BC} = r_e$). This is the proper reaction shell, as defined in Sec. 2.2. The potential-energy profile along it is the vibrational potential of the reactant molecule, which has a minimum value $V_{ref} = 0.00$ eV, when $r_{BC} = r_e = 0.7427$ Å.

A third set of calculations corresponded to the choice of the more accurate reaction shell discussed in Sec.2.4, passing through the true minimum of the surface ($r_{AB} = 3.5$ Å, $r_{BC} = r_e = 0.7414$ Å, $V_{ref} = -0.009$ eV) for $H+H_2$, or close to it ($\rho^o = R^o_{A,BC} = 3.8707$ Å) for other mass combinations.

Aside from defining the reaction shells, Fig.5 was also used to show the choice of the initial phase angles (ϕ^o), and to indicate that for clarity the y and y' axes can serve as a separate scale for r_{AB} and r_{BC}, since for a particular mass combination $\cos(\xi)$ = constant. Finally, the reaction time t^R is defined as the time spent within the reaction shell.

c. $\underline{T^o_t = T^{thld.}_t \rightarrow T^{max}_t}$. The initial translational energy was varied within a range beyond which no reaction is observed. The lower limit is defined by the reactive threshold, $T^{thld.}_t$, which occurred at 0.35 ± 0.01 eV for all cases. The upper limit is the cut-off energy T^{max}_t, which was encountered below 2.2 eV, except for T+HT where it could not be observed.

d. $\underline{\phi^o = 0^o \rightarrow 360^o}$. The vibrational phase angle ϕ^o is defined according to the following extrema: $r^o_{BC} = r_e$, contracting (0^o); $r^o_{BC} = r_1$, minimum (90^o); $r^o_{BC} = r_e$, expanding (180^o); $r^o_{BC} = r_r$, maximum (270^o); as shown in Fig.5.

2.5.2 The Vibrational Phase Distribution.

The energy profile along the reaction shell determines the vibrational motion of the reactant molecule, whereas the energy profile normal to it strictly pertains to translational motion, as long as the atom-molecule distance is large enough. Thus, a non-zero value for V_{ref} (minimum potential of vibration relative to $H+H_2$) would mean that this value has to be included in the initial relative translational energy:

$$E_t^o = T_t^o + V_{ref}. \qquad (37)$$

V_{ref} is generally much smaller than the finest energy resolution used in the calculations, and is therefore not included in the values of T_t^o discussed in this thesis. More problematic is the fact that the vibrational potential is quite anharmonic, and that it varies with the choice of the reaction shell. For accurate calculations, in which the vibrational phase is to be varied exhaustively, an appropriate phase distribution must be obtained prior to the actual trajectory calculations. This problem can be solved by a variety of methods. A simple approximation, used by many workers[49-52], is to consider the relative-translational and angular-vibrational velocities ($\dot{R}_{A,BC}$ and $\dot{\phi}$) as constants of motion, outside the reaction shell. A uniform phase angle distribution is then obtained:

$$F(\phi)d\phi = (\tau/2\pi)d\phi, \qquad (38)$$

where τ is the classical period of vibration. A shift $\Delta\phi$ is then directly related to a displacement $\Delta R_{A,BC} = \Delta\phi(\dot{R}_{A,BC}/\dot{\phi})$, through

the common variable time. The trajectories are then always started at a single phase angle ϕ^o, but at a pre-calculated distance ($0 \leq \Delta R_{A,BC} \leq R_{A,BC}$) outside the reaction shell (ρ^o), to vary the phase angle at ρ^o. Hence, only the knowledge of E_v^o, τ, and r_e is required, since ϕ^o can be chosen such that $r_{BC}^o = r_e$, where $T_v^o = E_v^o$. Another possibility is to choose r_{BC}^o as one of the turning points of vibration, where $T_v^o = 0$. Then, V_{ref} and r_e must be determined from the MERP, or by solving

$$\partial V(\rho^o, r_{BC})/\partial r_{BC} = 0, \tag{39}$$

and the turning points are obtained by solving

$$V(\rho^o, r_{BC}) - V_{ref}(\rho^o, r_e) - E_v^o = 0, \tag{40}$$

e.g. using Newton's method[65,77]. For realistic calculations, several additional requirements must be fulfilled. The correct definition of the reaction shell (Sec.2.2) requires that the potential energy in eqs.(39) and (40) is expressed as $V(R_{A,BC}, r_{BC})$. The vibrational period and energies should further correspond to the appropriate values, calculated from the surface parameters, and the vibrational potentials must be constant outside the reaction shell. From the insight gained in the course of the present investigations, this method can now be considered quite accurate. For realistic surfaces the vibrational constants will correspond closely to spectroscopically determined values, and the vibrational adiabaticity principle[71] can be strictly applied up to distances close to the transition state[78]. Further, the outcome of trajectory calculations, especially when averaged to

obtain the total reaction probability, is very insensitive to slight variations in the inital values of vibrational parameters. Evidence to this extent was not available at the start of the present work. The method was also deemed less suitable for a systematic study, where the explicit anharmonic distribution of the vibrational phase over the r_{BC} coordinate was to be taken into consideration.

The following method was therefore developed independently. A translationless trajectory is calculated at the reaction shell, with E_v^o = ZPE and $r_{BC}^o = r_e$, which were determined as described above. This computation allows the simultaneous evaluation of all other necessary vibrational parameters (amplitudes, half-periods, energy profile, oscillator path). It was then discovered, rather empirically, that the anharmonic oscillation can be quite accurately described by the "double harmonic approximation":

$$r_{BC} = r_e - A_i \sin(\phi_i), \tag{41}$$

$$\phi_i = \phi_i^0 + (\pi/\tau_i)\Delta t_i, \tag{42}$$

where i=l (compression phase, $0 \leq \phi_l \leq \pi$), or i=r (extension phase, $\pi \leq \phi_r \leq 2\pi$); A_i and τ_i are the computed amplitudes and half-periods of vibration; Δt_i is the time elapsed since the latest passage through the equilibrium position with $\phi_l^0=0$, $\phi_r^0=\pi$. Table IV shows that the displacements $x_i=r_{BC}-r_e$ of the actual SSMK oscillator are closely reproduced by the values x_i' computed from (41) and (42), and that the path of the oscillator in coordinate space ($R_{A,BC}$, r_{BC}) adheres closely to the reaction shell II, but is moving away from it slowly as time increases.

Table IV. The Double Harmonic Approximation.

$t \times 10^{16}/s$	$r_{BC}/\AA$	$R_{A,BC}/\AA$	$x_i/\AA$	ϕ_i/deg.	$x'_i/\AA$
0.	0.7427	5.37135	0.0000	0.000	0.0000
4.	0.7029	5.37135	-0.0398	22.291	-0.0408
8.	0.6882	5.37135	-0.0745	44.582	-0.0756
12.	0.6441	5.37135	-0.0986	66.873	-0.0990
16.15	0.6350	5.37135	-0.1077	90.000	-0.1077
32.30	0.7427	5.3713	0.0000	180.000	0.0000
36.	0.7797	5.3712	0.0370	194.605	0.0356
40.	0.8162	5.3712	0.0735	210.395	0.0714
44.	0.8460	5.3710	0.1036	226.184	0.1019
48.	0.8683	5.3710	0.1256	241.974	0.1246
52.	0.8809	5.3710	0.1382	257.763	0.1380
55.10	0.8839	5.3710	0.1412	270.000	0.1412
77.90	0.7423	5.3704	-0.0004	360.000	0.0000

The advantage of the double harmonic approximation is that it provides a simple formula correlating r_{BC} and time in quite a realistic way, considering that the largest discrepancies, occurring near 0^o and 180^o, disappear when averaged over the extension and compression phases. This is permissible, since the approximation primarily serves as a measure of the time spent by the system within a particular range of its vibrational phase. The actual vibrational momentum at a particular r_{BC}^o value is determined in an accurate fashion by use of eq.(49) below.

A more accurate but rather complicated method would be to fit the vibrational-energy profile at the reaction shell by a Morse function[76]:

$$V_v = V(\rho^o, r_{BC}) - V_{ref}$$
$$= D_e[\exp\{-2\beta(r_{BC}-r_e)\} - 2\exp\{-\beta(r_{BC}-r_e)\}]. \quad (43)$$

The ZPE is again determined according to eq.(36), with

$$\underline{k} = (d^2V_v/dr_{BC}^2)_{r_{BC}=r_e} = 2D_e\beta^2. \quad (44)$$

Rankin and Miller[70] have derived analytical expressions from the Morse equation, correlating ϕ and r_{BC} in terms of action-angle variables. Recently, it was also pointed out[79] that a uniform phase distribution (38) can be accurately generated if the trajectories are always started on the reaction shell with constant ϕ^o, by introducing the relative translational energy T_t^o only after a pre-determined period $\Delta t = \tau\Delta\phi/2\pi$. An improved procedure for sampling the vibrational phase has been given by Porter, Raff and Miller[116].

2.5.3 Initial and Final States.

Of the four semi-independent variables q_1, q_2, P_1, P_2, conditions a and b of Sec.2.5.1 constrain the initial values p_2^o and q_1^o respectively. The initial values chosen for the true independent variables (T_t^o and ϕ^o) further determine those of the coordinates and momenta. Summarizing the relationships in proper order of evaluation:

$$q_2^o = r_{BC}^o = r_e - A_i \sin(\phi_i^o);\ (i=1,r); \tag{45}$$

$$q_1^o = r_{AB}^o = \rho^o - q_2^o m_C/(m_B+m_C); \tag{46}$$

$$p_1^o = -(2T_t^o \mu_{A,BC})^{\frac{1}{2}}; \tag{47}$$

$$T_v^o = E_v^o - V_v^o = ZPE - V(q_1^o, q_2^o) + V_{ref}; \tag{48}$$

$$p_2^o = \pm (2T_v^o \mu_{BC})^{\frac{1}{2}} + m_B \mu_{BC} p_1^o, \tag{49}$$

where $\pm$ is the sign of $\dot{r}_{BC}$ in accordance with the definition of the phase angles (cf.Fig.5 and Sec.2.5.2).

The final kinetic-energy terms are determined from eqs. (32) and (33), and the product vibrational energy, $E_n' = T_v' + V' - V_{ref}$, converges to a stable value as the system leaves one of the valleys. Quantization of product vibration is achieved according to the mean-value method[51-54], by assigning the product quantum number n an integral value v, such that

$$\tfrac{1}{2}(E_v + E_{v-1}) \leq E_n' \leq \tfrac{1}{2}(E_{v+1} + E_v), \tag{50}$$

where the values E_v are obtained from eq.(36), and are listed with the cut-off values for E_n' in Table III.

2.5.4 The Computer Program.

The original program was written by Hulse, Jackson and Wright[66,73], and was modified to allow the systematic variation of the phase angle and different mass combinations. It was also abbreviated and optimized to reduce computer time and storage requirements, and adapted to the IBM/OS-360 system. FORTRAN listings of the basic program are given in Appendix I, with the input and output data for a sample calculation. Options include the use of an internal CPU timer, punched and/or printed output after NPRINT iterations, on-line and graphical trajectory plots, back integration, etc. Calculations were performed on the IBM/OS-360 (batch) and XEROX Sigma 9 (time-sharing) systems. The program was written in the double-precision mode, and is briefly outlined below.

The computations are started by generating the initial values of the coordinates and momenta according to eqs.(45) to (49), within the MAIN program. The potential energy is evaluated in SUBROUTINE POTIN from eqs.(34) and (35). The equations of motion are numerically integrated in SUBROUTINE DBASH, by use of an Adams-Bashforth fourth-order predictor-corrector method, with a three-step Runge-Kutta start-up, and a fixed step size[80]. The time derivatives of the coordinates and momenta are calculated in SUBROUTINE DERIVE, according to eqs.(29) and (30), where:

$$\frac{\partial V}{\partial r_{AB}} = \exp\{-\alpha(r_{AB}+r_{BC})\}\Big[\sum_{i=1}^{6}\Big\{\sum_{j=0}^{6-i}(jC_{ij}r_{AB}^{j-1}r_{BC}^{i})\Big\} - \sum_{i=0}^{6}\Big\{\sum_{j=0}^{6-i}(C_{ij}r_{AB}^{j}r_{BC}^{i})\Big\}\Big], \qquad (51)$$

$$\frac{\partial V}{\partial r_{BC}} = \exp(-Ar_{BC})\Big[\sum_{i=1}^{8}\{iC_i r_{BC}^{i-1} - A\sum_{i=0}^{8}(C_i r_{BC}^{i})\}\Big] + \exp\{-\alpha(r_{AB}+r_{BC})\}\Big[\sum_{i=1}^{6}\{\sum_{j=0}^{6-i}(iC_{ij} r_{AB}^{j} r_{BC}^{i-1})\} - \sum_{i=0}^{6}\{\sum_{j=0}^{6-i}(C_{ij} r_{AB}^{j} r_{BC}^{i})\}\Big]. \quad (52)$$

In these equations and others related to the SSMK function, e.g. eqs.(34)and (35), the convention $r_{AB} \geq r_{BC}$ is used. Thus, $r_{AB}=q_1$, $r_{BC}=q_2$ for configuration a, and $r_{AB}=q_2$, $r_{BC}=q_1$ for c. The evaluation of product vibrational energy has been described in Sec.2.5.3, and also takes the product configuration (a or c) into account, through the definition of the reaction channel, $\chi=0$ (unreactive, configuration a), $\chi=1$ (reactive, configuration c). At the end of each trajectory, the final parameters are printed out. These include the final coordinates and momenta, the reaction time t^R, the reaction channel χ, the total energy H, the potential energy V', the kinetic energies T', T'_t and T'_v, and the vibrational energy E'_n. The computations require ca. 2.5 CPU seconds per 100 iterative steps.

2.6 Collinear $H+H_2$, Results and Discussion.

2.6.1 Reactivity bands at $\phi^o = 0^o$.

The final parameters t^R, χ, and E'_n were selected for analysis. The general method of investigation was to hold ϕ^o constant and to vary the translational energy T_t^o systematically. Graphical methods were then used to record the results and to analyze the data obtained. The details of the method will be described below.

The results of the first series of calculations at $\phi^o=0^o$, with E_v^o=ZPE, r_{AB}^o=5.0 Å, and $r_{BC}^o=r_e$=0.7427 Å are plotted in Fig.6 as a function of T_t^o. At "low" energy resolution (ΔT_t^o=0.02 eV) there is a definite separation into reactive (R) and unreactive (U) regions, as shown in the upper part of the figure. Thus, no reaction occurs until the threshold is reached, and several regions of alternating reactivity are then observed between 0.36-0.60 eV (R), 0.62-0.68 eV (U), 0.70-1.04 eV (R), 1.06-2.0 eV (U). This is the clearest demonstration of what are termed reactivity bands, which are similar to the regions of "direct" reactivity reported in the literature[49-53]. When the resolution is increased to determine the location of the band boundaries to within 0.005 eV, it becomes apparent that except for an "anomalous peak" at 0.44 eV, a peculiar rise near 1.8 eV, and the splitting of the peaks near 0.68 and 1.04 eV, the time peaks accurately mark the boundaries between R and U regions. Such an observation was also made by Duff and Truhlar[53] in terms of increased complex life-times, and can be seen in the original work of Wall et al.[37].

In Fig.6, a close parallel exists between the reaction time (solid line) and product vibrational energy (dashed line). This is easily understood from the conservation of the total energy: if E_n' is large, less translational energy is available for the separation of the products, and the system spends a longer time t^R within the reaction shell. However, the E_n' peaks are not quite as sharp as the t^R peaks, and do not coincide as closely with the band edges.

Figure 6

Results for collinear $H+H_2$, $\phi_I^o = 0^o$. The reaction probability, reaction time and product vibrational energy are shown as a function of the initial relative translational energy.

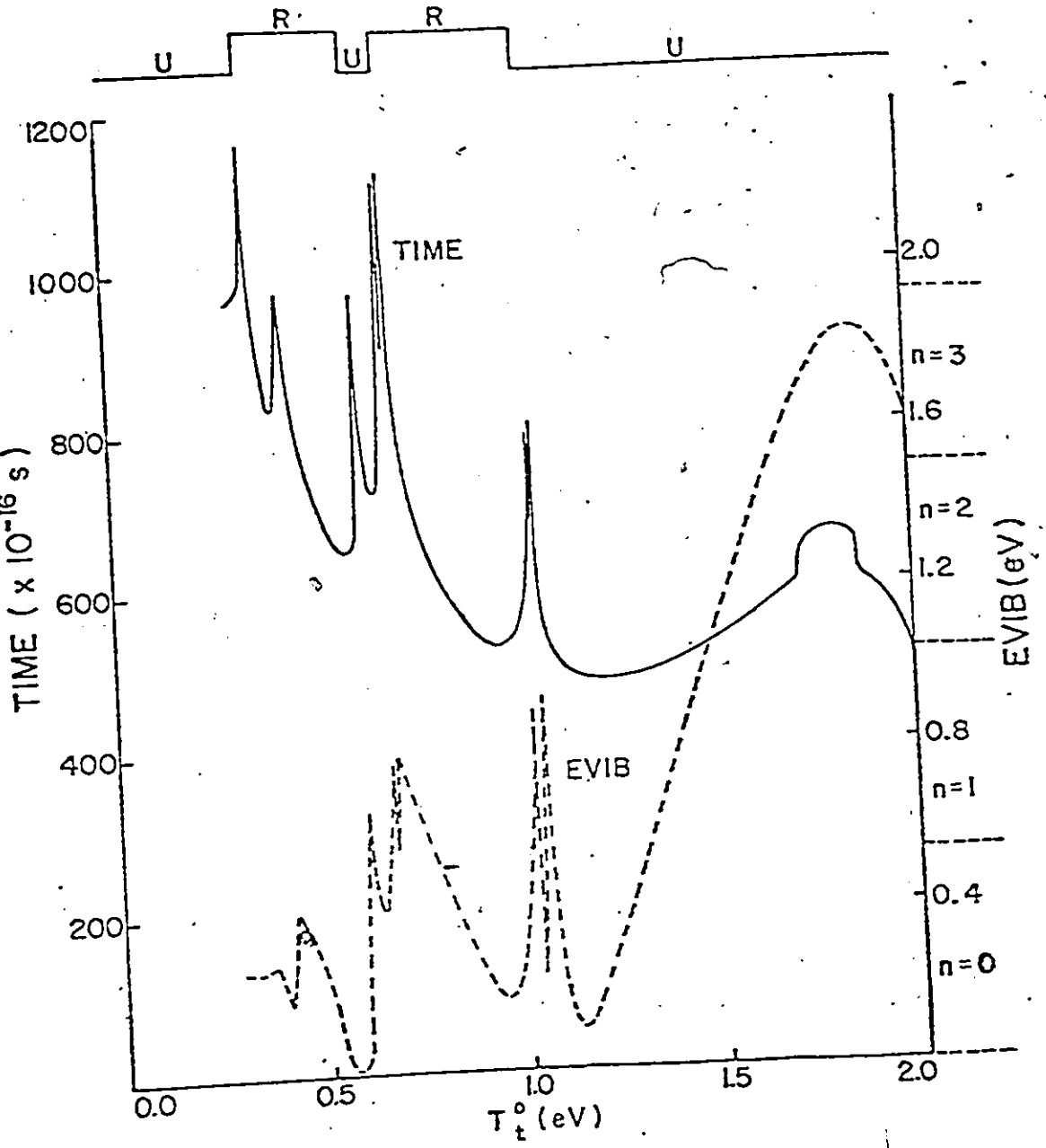
U
R
U
R
U
TIME
EVIB
TIME (x 10^-16 s)
EVIB (eV)
1200
1000
800
600
400
200
2.0
1.6
1.2
0.8
0.4
n=3
n=2
n=1
n=0
0.0
0.5
1.0
1.5
2.0
T°t (eV)

For the purposes of the present study, the behavior of the time curve (preferred to that of E_n') allows the prediction of where a band boundary may occur. The energy resolution is then increased in the region of a time peak, to determine the break points more accurately[49-51].

The simplicity of the results is quite surprising, in that only two relatively narrow reactive bands are observed over the wide range of energy studied (0-2.0 eV), and in that such a close correspondence between t^R and E_n' is found. A scan at higher energies (up to 10 eV) did not reveal any other reactivity bands or structures in the t^R and E_n' curves, which is also surprising as an increase in reactivity would be expected with increasing energy, from a consideration of eq.(3).

The reaction time (left-hand scale) indicates that no long-lived collision complexes are formed, since the increase in t^R near the band boundaries can be attributed to the increase of E_n' (right-hand scale) in the same regions. The product quantum number n, as determined from the procedure outlined in Sec.2.5.3, is also shown on the right hand side of the figure, and reaches a maximum (n=3) near 1.8 eV, dropping down again to n=0 at higher energies, but steadily increasing again at very high energies (> 7 eV) to approach the dissociation limit beyond 10 eV.

A number of intriguing questions remained to be answered about the dynamic behavior at the band edges and anomalous time peaks, and about the mechanisms of product vibrational excitation, occurring at these locations.

2.6.2 Individual Trajectories.

Trajectory plots[37] and time vs. distance diagrams[65] were helpful in understanding the specific features of the results obtained. Fig.7a shows a reactive trajectory at the threshold (0.347 eV), where the product has essentially its ZPE. This is related to the fact that the trajectory is symmetric[53,54]. The system crosses the dividing line along the direction of the H_3 asymmetric stretch, slightly above the saddle point (+). Considering the barrier height (E_a=0.493 eV) and the ZPE (0.269 eV), the results of various other workers[48,49,51-54,65] are confirmed, in that the contribution of vibrational energy to motion over the barrier is ca. 50%.

Classically, product energies less than ZPE are allowed. Fig.7b shows the trajectory at 0.56 eV, where the product has essentially no vibrational energy. This is of interest in the determination of the optimum crossing point of the dividing line for translational excitation of the product. The direction of motion is still predominantly along the asymmetric stretch, but the crossing point is now closer than the saddle point to the origin, typical of the "bobsled effect"[62,71] and the location of the centrifugal barrier[54,71]. More generally, product vibrational excitation is closely related to the energy content of the symmetric stretching mode, if the centrifugal potential is also taken into account[54,71,81]. The effective potential curve for vibration is then shifted closer to the origin, with a minimum located at the point where the VARP crosses the dividing

line (centrifugal barrier location)[54,81,82]. The trajectories in Fig.7a,b both have little kinetic energy along the symmetric stretch, but the one at 0.347 eV (Fig.7a) crosses at a point of higher effective vibrational potential, which results in product vibrational energy. Both trajectories do not undergo reflections on the highly curved parts of the reaction channel in the transition state region ("corner-cutting"[43]), so that no excessive translation-vibration energy transfer occurs, and the vibrational energy of the products is directly related to the energy content of the symmetric stretch.

Fig.7c shows the a trajectory near the end of the anomalous rise in t^R at 1.8 eV. The system crosses the dividing line with a large amount of excess translational energy, characterized by a direction almost perpendicular to r_{BC}. It therefore spends little time on the product side of the surface, and is reflected by the steep repulsive wall ("brick wall effect"[62]), back into the reactant valley. It recrosses the dividing line, before it loses most of its kinetic energy by climbing the embankment separating the reactant and product valleys. Hence, there is a considerable build-up of potential energy, which is released in the vibrational mode as the system backs down into the reactant valley. The peculiar shape of the discontinuity near 1.8 eV (Fig. 6) can now be related to the high vibrational content of the "products". When n=3 the system leaves the reaction shell in a direction almost parallel to it (Fig.7c), so that a slight change in T_t^θ can cause an increase or decrease in reaction time by nearly half a vibrational period.

Figure 7.

Typical trajectories for collinear $H+H_2$, $\phi_I^o = 0^o$, resulting in different product vibrational excitation. (a) Adiabatic trajectory at the reactive threshold, (b) "optimum" trajectory in the middle of a reactive band, (c) unreactive trajectory near anomalous peak.

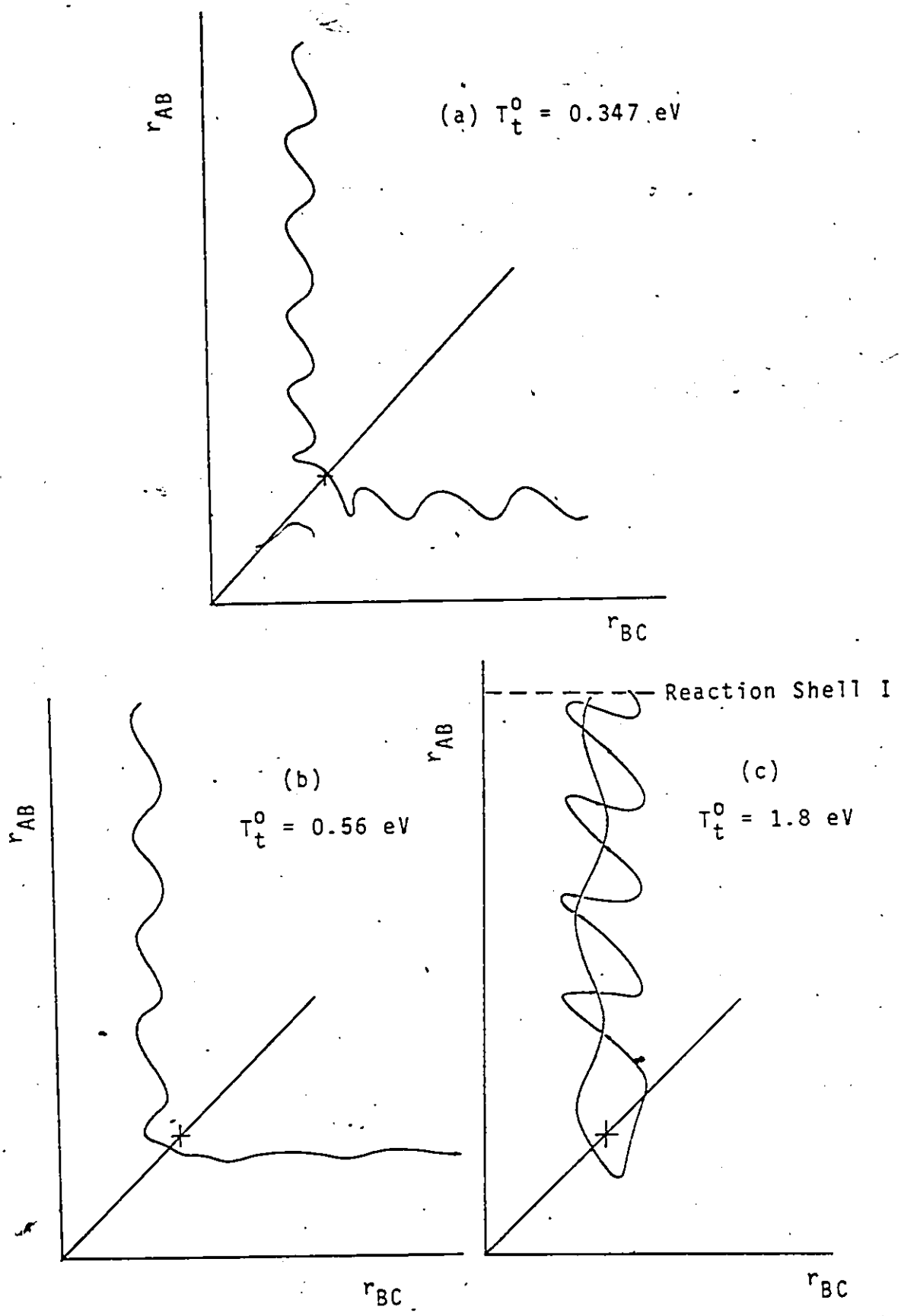
(a) T_t^o = 0.347 eV
r_{AB}
r_{BC}
(b)
T_t^o = 0.56 eV
r_{AB}
r_{BC}
Reaction Shell I
(c)
T_t^o = 1.8 eV
r_{AB}
r_{BC}

To obtain a better understanding of the dynamic behavior when a band boundary is crossed, attention is focussed on the band edge at 0.61 eV, where a single time peak is observed (cf.Fig.6). Trajectories before, at, and after the reactive to unreactive (R→U) transition are shown in Fig.8a-c, where the reaction path is followed by "snapshots" of the mass-point moving on a skewed 3-D plot of the SSMK surface[73], at time intervals of 10^{-15}s. Fig.8a shows that the trajectory at 0.59 eV is reactive and nearly symmetric, therefore resulting in product energy, slightly less than the ZPE. However, it is of a different type than the trajectories shown in Figs.7a,b, in that it is reflected several times in the transition state region, before clearing the bend and entering the product valley. It can therefore be classified as a "corner-hitting" trajectory, as opposed to corner cutting described above. More generally, corner-hitting is associated with most of the motion in the transition-state region directed along the symmetric stretch, but not necessarily with high product vibrational energy. Reflections on points of high curvature[71,81] promote the energy flow between normal modes of motion, so that the system "loses its memory" about its energy content in the symmetric stretch, by undergoing one or more reflections after crossing the dividing line, but before entering the linear part of the product valley. The reactive trajectory in Fig.8b (0.61 eV) is an even more extreme example of corner hitting, typical of trajectories at band boundaries. It is first

reflected on the slightly curved portion of the embankment (reactant side), to a point of high curvature on the steep wall, near the dividing line (product side). It then travels along the ridge separating the reactants from the products, as if in doubt which side to stay on. It eventually remains on the product side, and climbs the embankment along the dividing line, to end up with high product vibration, and consequently with an increase in reaction time (see Sec.2.6.1).

The unreactive trajectory at 0.63 eV (Fig.8c) is reflected even further down the curved part of the embankment, and as a result it hits the steep wall nearly perpendicularly. It is then reflected on almost an identical path, back into the reactant valley. (To aid in following the trajectory, the reflected path is indicated by open circles.) The prediction of product vibrational energy should again be related to the location and direction of motion at the re-crossing point, but is complicated by the subsequent reflection on a curved portion of the embankment.

From the discussion of Figs.7 and 8 it is clear that the local direction of motion at the dividing line determines the attributes of the products (reactive or unreactive, high or low vibrational energy, long or short reaction times), if no complications in terms of subsequent reflections on curved contours occur. For reactive $H+H_2$ trajectories, complex behavior (including multiple crossings of the dividing line) only occurs in the vicinity of band edges (cf.Refs.53,54,70 and the next section).

Figure 8

Trajectories on a skewed 3-D plot of the SSMK surface for collinear $H+H_2$, $\phi_I^o = 0^o$, before (a), at (b), and after (c) a band boundary. In (a) and (b) the reactants enter at the right and exit at the left. In (c) the reflected trajectory appears as open circles.

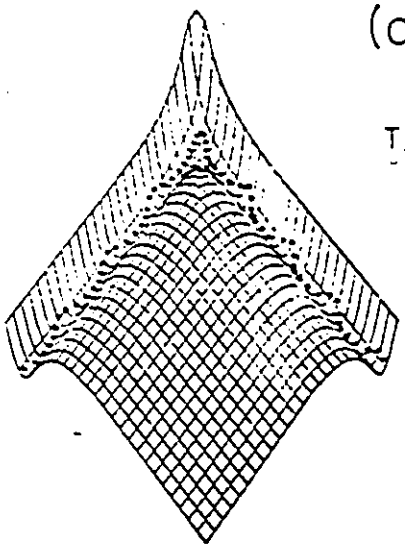

(a)

T_t^o = 0.59 eV

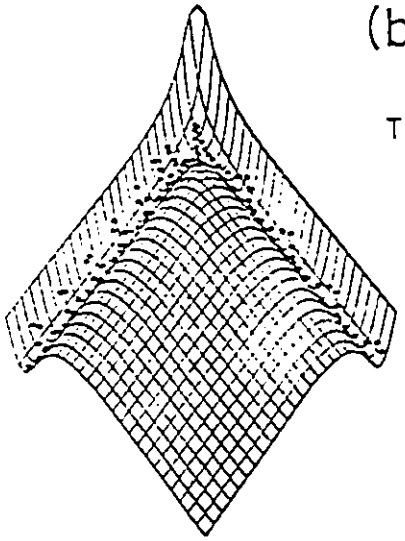

(b)

T_t^o = 0.61 eV

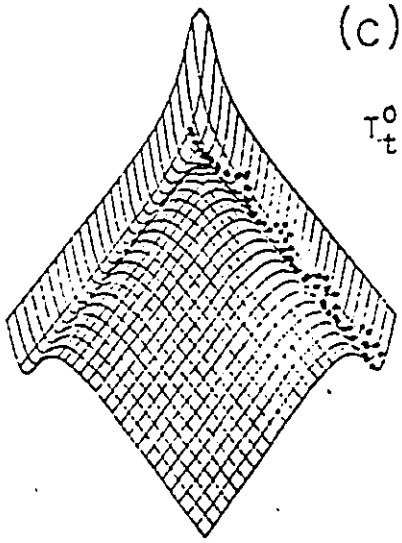

(c)

T_t^o = 0.63 eV

2.6.3 Statistical Regions.

The splitting of the peaks near 0.68 and 1.04 eV (Fig.6) is due to "statistical" behavior of the trajectories within a narrow range near some band edges[51-54,71,83]. This is apparent when these regions are studied under higher resolution. Fig.9 is a magnification of the region near 0.68 eV with an energy resolution of 0.0002 eV. There is now a subdivision into many reactive and unreactive bands, and a definite coincidence of the time peaks with the band edges. Again, a close parallel exists between the t^R and E_n' curves (not shown) and, typically, about half the trajectories are reactive within a region which is ca. 0.01 eV wide. This behavior has been termed statistical in previous studies[53,71] and has been treated accordingly, as opposed to direct scattering where the individual trajectories are completely defined.

Figs.10a-d show some trajectories at 0.6844,0.6848,0.6852 and 0.6856 eV, demonstrating the complexity that can occur, and the totally different outcome of the collisions that can be obtained with slight variations (0.0004 eV) of T_t^o, in these statistical regions. Thus, within the narrow range of 0.0016 eV (Figs.10a-d), reactive and unreactive trajectories with very different product vibrational energies can be observed. Multiple collisions (multiple crossings of the dividing line) frequently occur, resulting in short-lived collision complex formation[84]. This result has also been specifically associated with the

Figure 9

Fine structure of band boundary,

at $\phi_I^o = 0^o$, $T_t^o = 0.68$ eV.

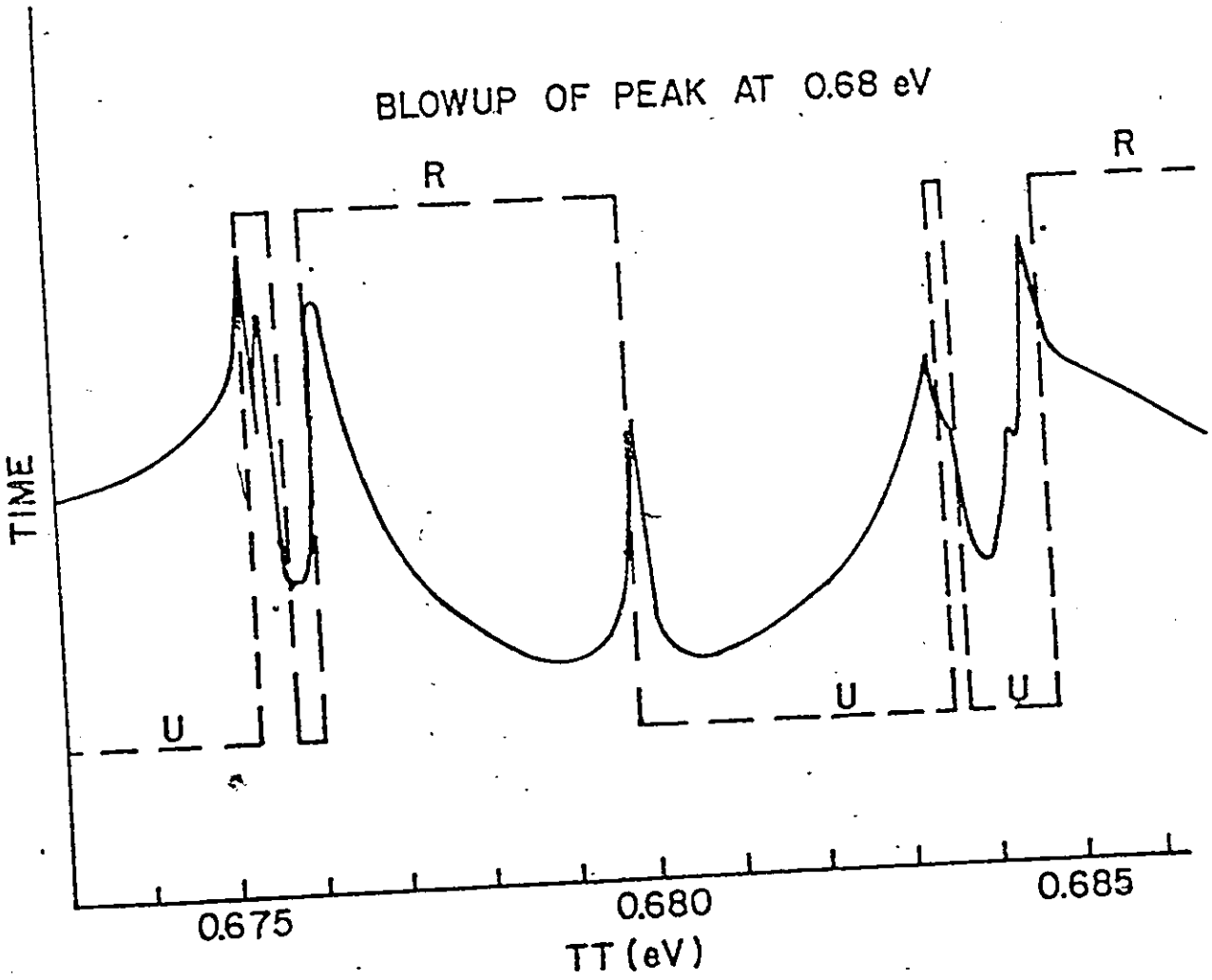
BLOWUP OF PEAK AT 0.68 eV
R
R
U
U
U
TIME
0.675
0.680
0.685
TT (eV)

Figure 10

Typical complex trajectories in the statistical region at $\phi^o=0^o$, $T_t^o=0.68$ eV.

(a)

T_t^o=0.6844 eV

(b)

T_t^o=0.6848 eV

(c)

T_t^o=0.6852 eV

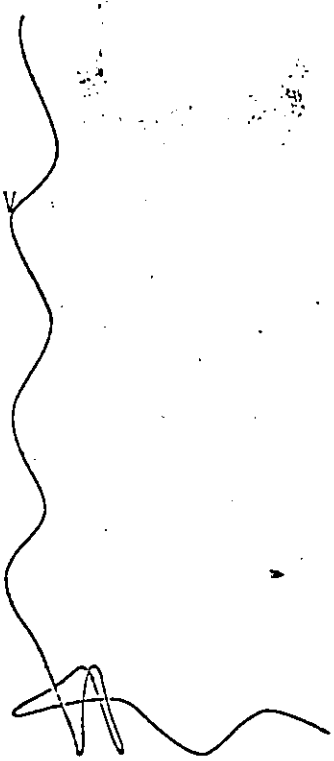

(d)

T_t^o=0.6856 eV

behavior in statistical regions, by several other workers[53,71,83]. Complex formation is generally discussed in analogy to nuclear physics, in terms of quasi-bound states or resonances[19,53-57,70,71,81,83-85]. The trajectories in Figs.10a-c are seen to execute several vibrations in the product region, but are then turned back to recross the dividing line. Pechukas and McLafferty[86], and Rankin and Miller[70] suggest that such behavior is related to roughness of the surface contours near the transition state. For $H+H_2$ the general behavior, expected for reactive $H+H_2$ trajectories, is as shown in Fig.10d, where once the dividing line is crossed the trajectory will continue to stay on the product side[68,86]. Figs.10a-c indicate that even for the extremely well-behaved SSMK surface the dynamic behavior of $H+H_2$ is unpredictable and multiple collisions can occur, if reflections in the region of highest curvature are involved (typical of extreme corner-hitting at band edges). It is therefore understandable that more complicated behavior and wider statistical regions are observed for the Wall-Porter surfaces[51,53], where the surface contours are bent around the transition state[63]. For the LEP surface, an actual well exists on top of the barrier[27], and the results of trajectory calculations on this surface[37] can be interpreted in terms of one large statistical region.

2.6.4. Variations of the Phase Angle.

By setting E_v^o = ZPE, r_{AB}^o = 5.0 Å and varying T_t^o at diferent ϕ^o values, the band behavior as a function of ϕ^o and T_t^o can be

followed. The results of these calculations can be conveniently presented in the form of composite plots, such as Fig.11a-h, where the t^R curves for eight different phase angles are shown, and where the reactive and unreactive regions are indicated by solid and dashed lines respectively. The individual t^R curves were generally obtained by using an energy resolution of 0.04 eV over the whole T_t^o range, and 0.01 eV near the time peaks. The thin lines used to interconnect the time peaks in Fig.11 demonstrate the continuous shift of the time peaks and the reactivity bands with ϕ^o. In fact, this continuity extends beyond a single 360^o interval. Thus, the anomalous peak at (0^o,0.43 eV) is clearly related to the opening of an unreactive band at (180^o,0.49 eV). The reactive to unreactive (R→U) edge of this band becomes the peak at (0^o,0.61 eV), which subsequently shifts to (180^o,0.75 eV), (0^o,1.041 eV), (180^o,1.36 eV), and finally ends up in the other anomalous rise near (0^o,1.8 eV). In this way, time peaks at all ϕ^o are either directly or indirectly related to the presence of a band boundary. With increasing ϕ^o, the anomalous peaks correspond to the beginning of an unreactive band, or the termination of a reactive band. A similar continuity is shown in Fig.12a-h for the product vibrational energy E_n'. The generalizations for $\phi^o=0^o$ are thus observed to apply for all phase angles:

a. Separations into reactive and unreactive bands occur.

b. The band edges are accurately marked by time peaks.

c. A close parallel exists between t^R and E_n' curves.

d. Statistical regions occasionally occur at the band edges.

Figure 11

Reaction time at various phase angles. Solid lines indicate reactive, dashed lines indicate unreactive trajectories. The thin solid lines interconnect the time peaks and show how the bands vary with ϕ_I^{σ}.

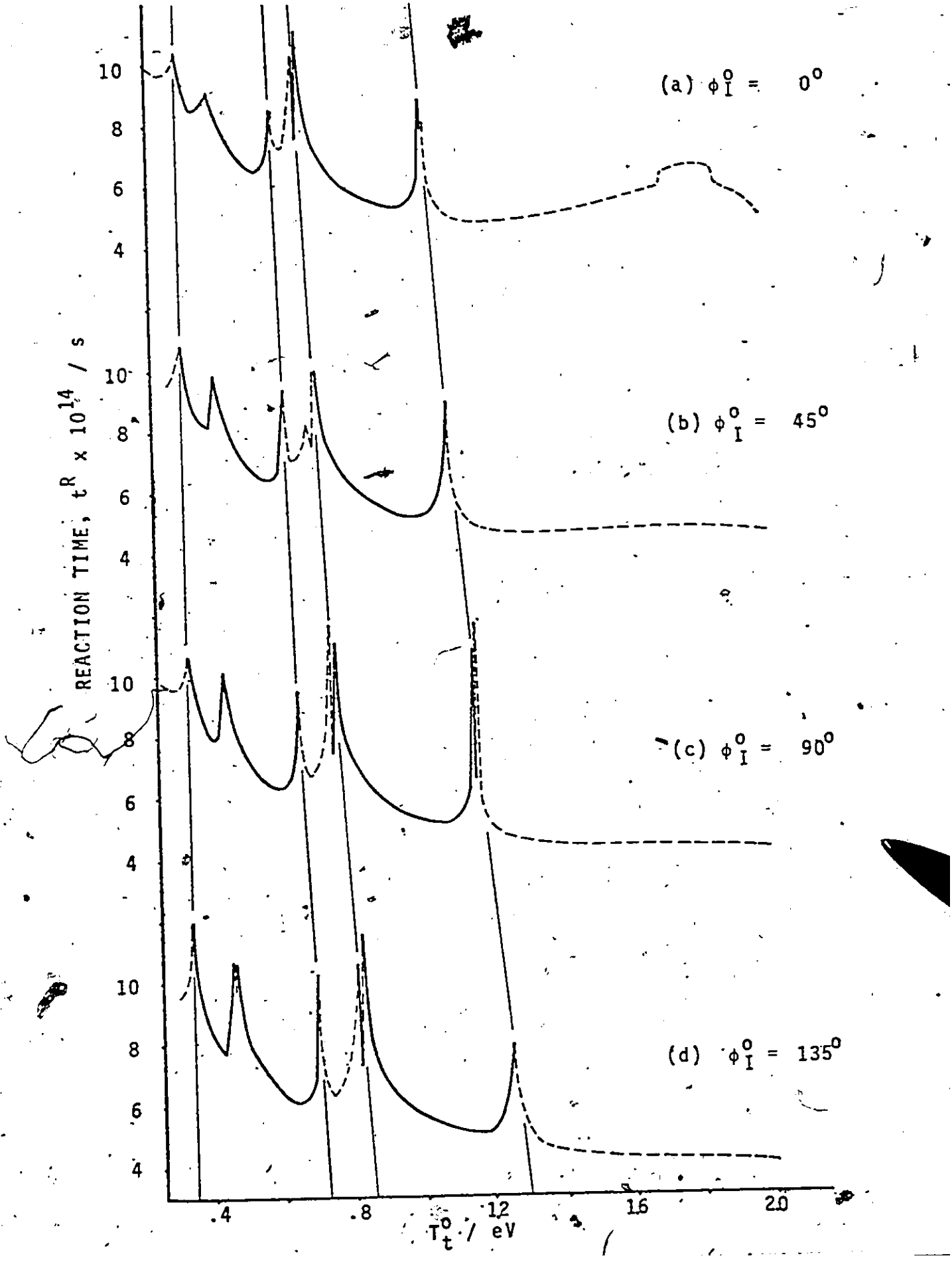
(a) ϕ_I^o = 0°
(b) ϕ_I^o = 45°
(c) ϕ_I^o = 90°
(d) ϕ_I^o = 135°
REACTION TIME, $t^R \times 10^{14}$ / s
10
8
6
4
.4
.8
1.2
1.6
2.0
T_t^o / eV

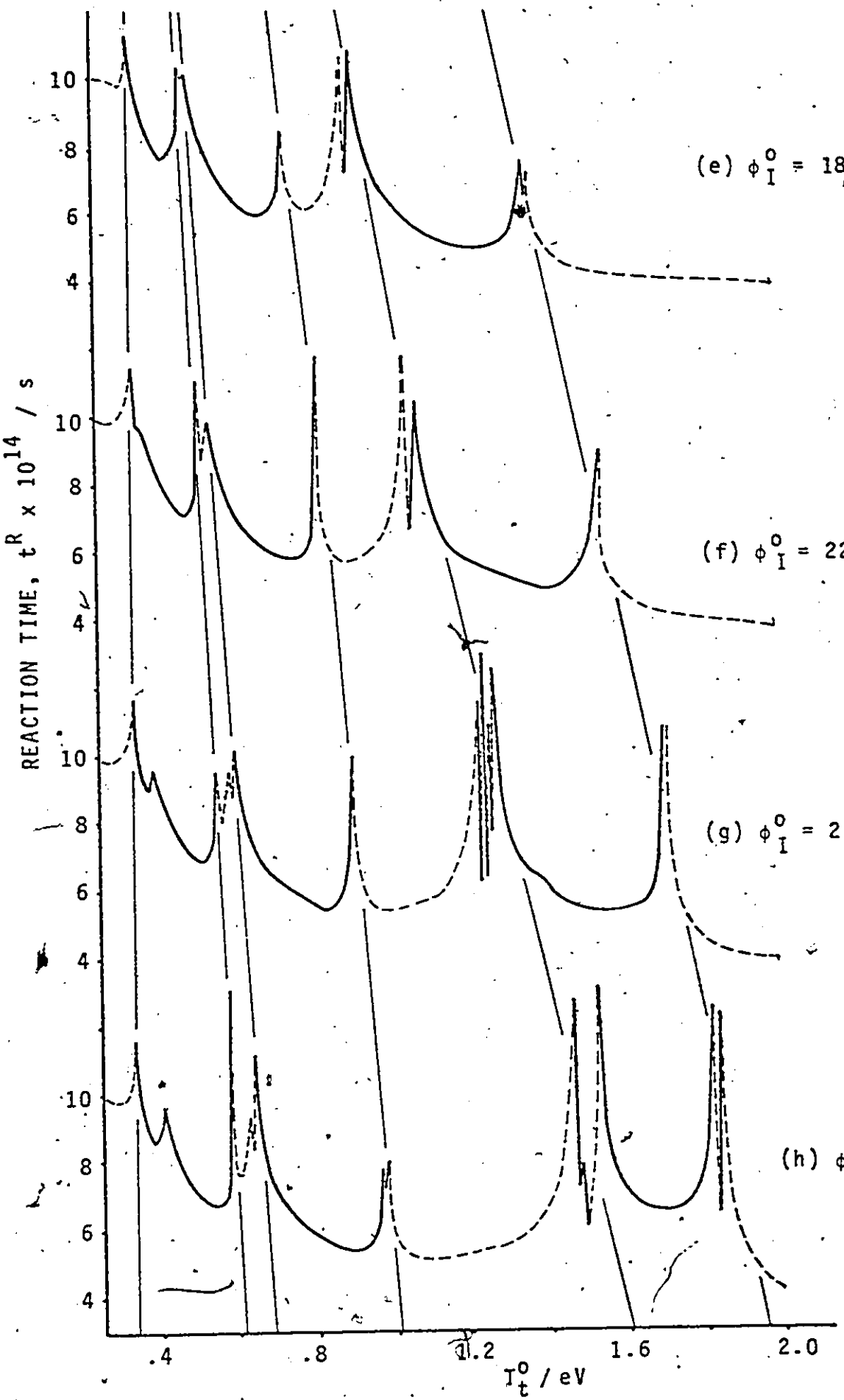
REACTION TIME, $t^R \times 10^{14}$ / s
10
8
6
4
(e) $\phi_I^o = 180^o$
(f) $\phi_I^o = 225^o$
(g) $\phi_I^o = 270^o$
(h) $\phi_I^o = 315^o$
.4
.8
1.2
1.6
2.0
T_t^o / eV

Figure 12

Product vibrational energy at various phase angles. Dashed lines interconnect the peaks to show the continuity with ϕ_I^o.

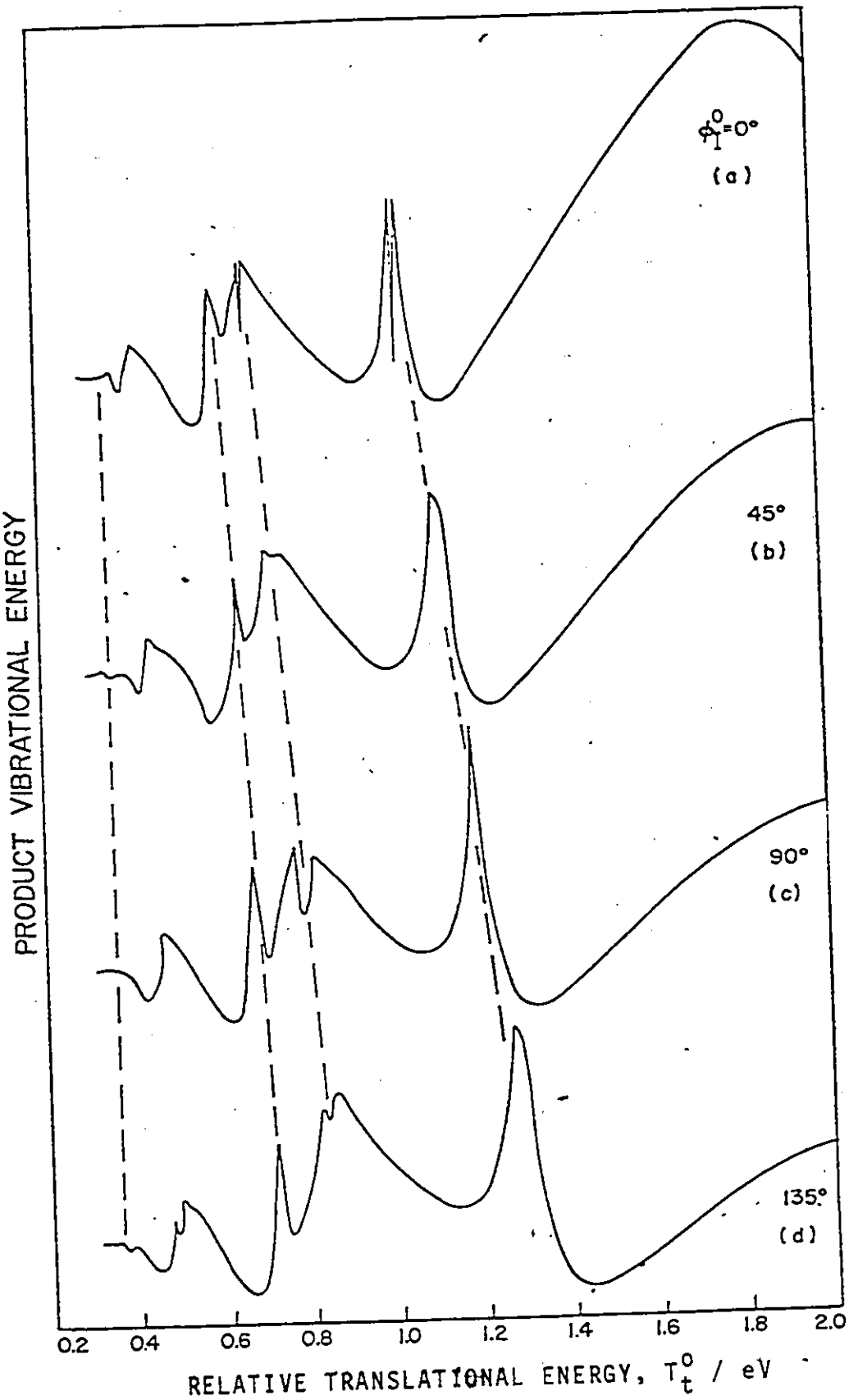
ϕ_I^o=0°
(a)
45°
(b)
90°
(c)
135°
(d)
PRODUCT VIBRATIONAL ENERGY
0.2
0.4
0.6
0.8
1.0
1.2
1.4
1.6
1.8
2.0
RELATIVE TRANSLATIONAL ENERGY, T_t^o / eV

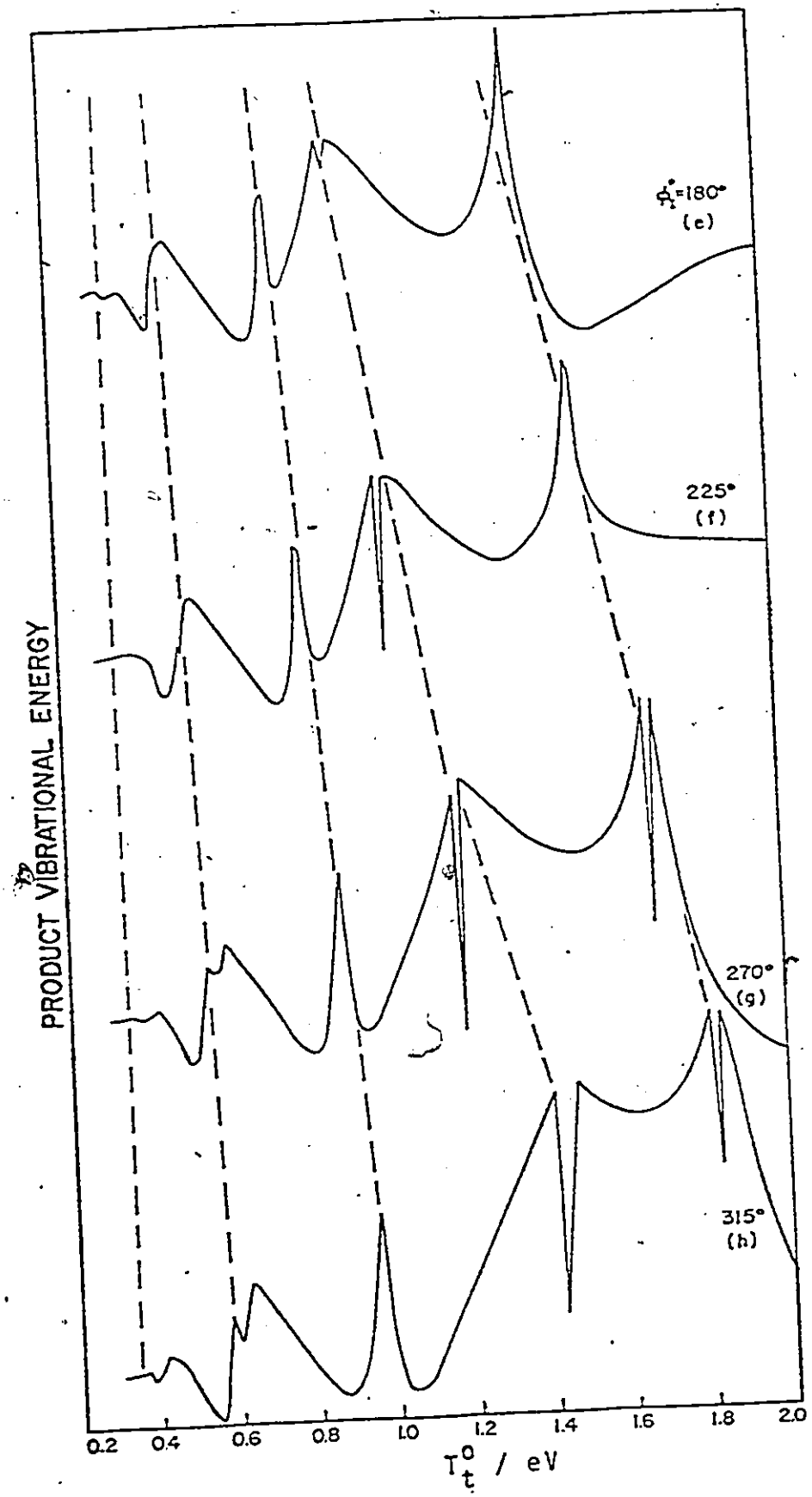
PRODUCT VIBRATIONAL ENERGY
ϕ_r°=180°
(e)
225°
(f)
270°
(g)
315°
(h)
0.2
0.4
0.6
0.8
1.0
1.2
1.4
1.6
1.8
2.0
T_t^o / eV

e. A reactive threshold occurs at 0.35 ± 0.01 eV, and a high-energy cut-off is always observed.

In addition, the generalizations about individual trajectories and statistical regions also apply, together with the further observations:

f. Except for the reactive threshold, all features of the final parameters shift to higher T_t^o values with increasing ϕ^o, in a continuous and cyclic manner.

g. The t^R and E_n' curves retain their characteristic shapes at all phase angles; corresponding peaks are easily recognizable from phase angle to phase angle.

H. The statistical regions tend to broaden at higher energies, but never exceed 0.06 eV.

These generalizations have important practical significance: each individual trajectory contributes to the precise location of the breakpoints in reactivity, reaction time and product vibration. Thus, the determination of the band boundaries at a particular ϕ^o is aided by following the t^R curve obtained with a rough T_t^o grid, and increasing the resolution near suspected discontinuities only. Further, the band continuity property allows the prediction of the location of time peaks and possible band boundaries, at many phase angles, once the time peaks have been accurately established at one particular ϕ^o. Resolution may then be directly increased in these suspected areas. This allows a very precise picture of the total reaction probability to be obtained with relatively few trajectory calculations; the accuracy of the results is limited only by the width of the statistical regions.

2.6.5 Reaction probabilities.

For purposes of obtaining the reaction probabilities, only the location of the band boundaries as a function of ϕ^o and T_t^o need be considered. The reaction probability as a function of T_t^o can be written as

$$p_{OT}^R(T_t^o) = p^R(\phi^o, T_t^o)\ F(\phi^o)\ d\phi^o, \qquad (53)$$

where the subscript OT indicates that all transitions from reactants in the zeroth vibrational energy level to products in all vibrational levels are considered; the superscript R denotes that only reactive transitions are of interest. The individual reaction probability p^R is unity, if a trajectory at a particular (ϕ^o, T_t^o) is reactive; otherwise it is zero. The probability distribution function $F(\phi^o)d\phi^o$ reflects the probability of encountering the reactant molecule between the phase angles ϕ^o and $\phi^o + d\phi^o$ at the reaction shell, and is directly proportional to the time spent by a translationless system within this interval $d\phi^o$. For the double harmonic approximation, eq.(42) can be written in differential form, yielding

$$F(\phi_i^o)d\phi_i^o = dt = \frac{\tau_i}{\pi}\, d\phi_i^o \qquad (54).$$

A particularly simple method to evaluate eq.(53) is to use a graphical procedure. Fig.13a shows a map of the reactive regions as a function of ϕ^o and T_t^o, where the location of the band edges has been taken through the center of the statistical regions, and where the ϕ^o axis has been scaled to reflect eq.(54). The

subscript I has been used to denote that the phase angles ϕ_I^o correspond to the choice of reaction shell I (see Fig.5 and further discussions below). Considering the explicit form of the probability distribution function (54) and the definition of the individual reaction probabilities $p^R(\phi^o, T_t^o) = 0,1$ as described above, eq.(53) can be written as

$$P_{OT}^R = (\pi\tau)^{-1}(\tau_l \Delta\phi_l^R + \tau_r \Delta\phi_r^R) \qquad (55),$$

where $\Delta\phi_i$ (i=l,r) is the width of the reactive region in terms of initial phase angles in the different (compression and extension) intervals. Since the ϕ axis in Fig.13a has been scaled proportional to τ_i, the total width of the reactive regions at one particular T_t^o value corresponds directly to the right-hand side of eq.(55) multiplied by the length of the ϕ axis. Hence, the reaction probability can be obtained by direct graphical summation, yielding the solid curve in Fig.13b (QC_{SSMK}). This result is compared to the exact quantum-mechanical (EQ^*) and quasi-classical (QC^*) results of Bowman and Kuppermann[52], obtained from a Wall-Porter type of fit[63] to the scaled SSMK surface[38b]. The latter curves (dashed and dotted lines) were shifted towards higher T_t[87] to adjust for the lower barrier height of 0.424 eV[38b,88]. Although the EQ^* results seem to be rather well reproduced, the dip in the probability curve near 0.65 eV, related to the position of the first unreactive band, is an artifact of the erroneous choice of the reaction shell I. As is evident from Sec.2.2 and confirmed by the results of translationless trajectories

Figure 13

(a) Plot of reactive (shaded) and unreactive regions as a function of ϕ^o and T_t^o.
(b) Total reaction probability P_{OT}^R obtained by graphical summation from (a). EQ^* and QC^* are the quantum and classical results of Bowman and Kuppermann[52].

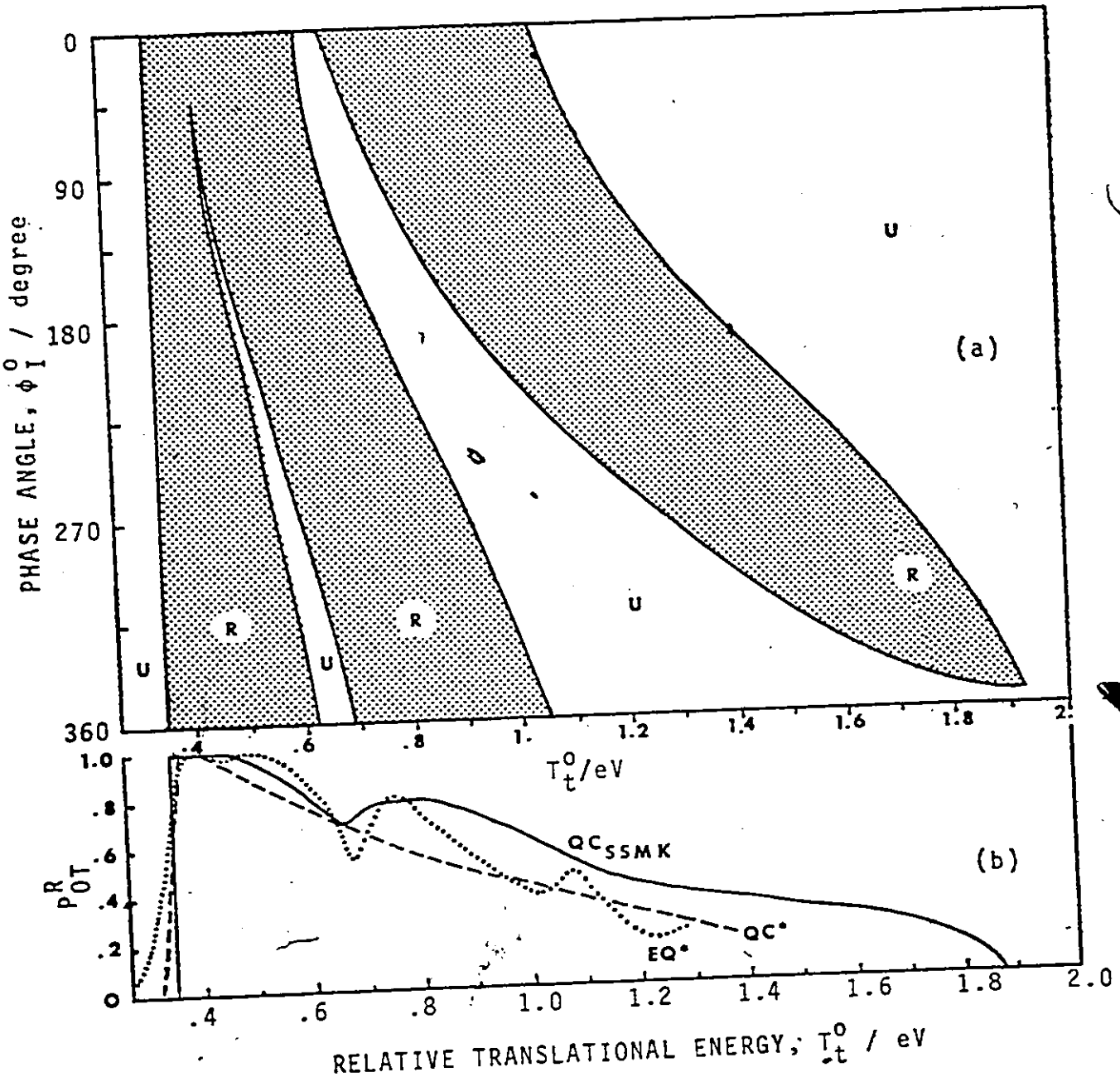
PHASE ANGLE, ϕ_I^o / degree
0
90
180
270
360
U
R
U
R
U
U
R
(a)
.4
.6
.8
1.
1.2
1.4
1.6
1.8
2.
T_t^o/eV
p_{OT}^R
1.0
.8
.6
.4
.2
0
QC_{SSMK}
QC*
EQ*
(b)
.4
.6
.8
1.0
1.2
1.4
1.6
1.8
2.0
RELATIVE TRANSLATIONAL ENERGY, T_t^o / eV

(see Table IV), pure vibrational motion does affect r_{AB} but not $R_{A,BC}$. Hence the probability distribution function (54) is valid only for $R^o_{A,BC}$ = constant. In a second series of calculations, reaction shell II ($R^o_{A,BC}$= 5.3714 Å, see Fig.5) was used. The detailed results of these calculations have been published[89], and differ appreciably only with respect to the linear ϕ^ovs. T^o_t plot and the P^R_{OT} curve, which are shown in Fig.14a and b. The dashed lateral lines in Fig.14a indicate that identical results can directly be obtained from the earlier calculations by evaluating the shift $\Delta\phi = \phi^o_{II} - \phi^o_I$ from the displacement $\Delta R_{A,BC}$ between the reaction shells I and II, as discussed in Sec.2.5.2, following eq.(38). This involves the computation of the displacement $\Delta R_{A,BC}$ at various phase angles and the evaluation of the phase shifts $\Delta\phi$ as a function of ϕ^o and T^o_t. No additional trajectories need then be calculated, since the relationships between phase angles ϕ^o_{II} on reaction shell II and phase angles ϕ_I on reaction shell I are established as a function of T^o_t, and the positions of band boundaries at ϕ^o_I, T^o_t determine the location of these band edges at ϕ^o_{II}, T^o_t. In Fig.14b the corrected P^R_{OT} curve for the SSMK surface (solid line), obtained from Fig.14a, is again compared to the QC^* and EQ^* curves[52]. The QC_{SSMK} curve now shows no oscillations characteristic of the quantum results (the dip has largely disappeared), and is more reactive compared to QC^*.

From the above discussion, it is clear that from now on a correct representation of the results should be given in terms

Figure 14

(a) Reactivity map for collinear $H+H_2$ with a proper choice of the reaction shell (II). The dashed lines show the relation between ϕ_I^o and ϕ_{II}^o.

(b) The correct total reaction probability, obtained by graphical summation from (a), compared to the EQ* and QC* results of Bowman and Kuppermann[52].

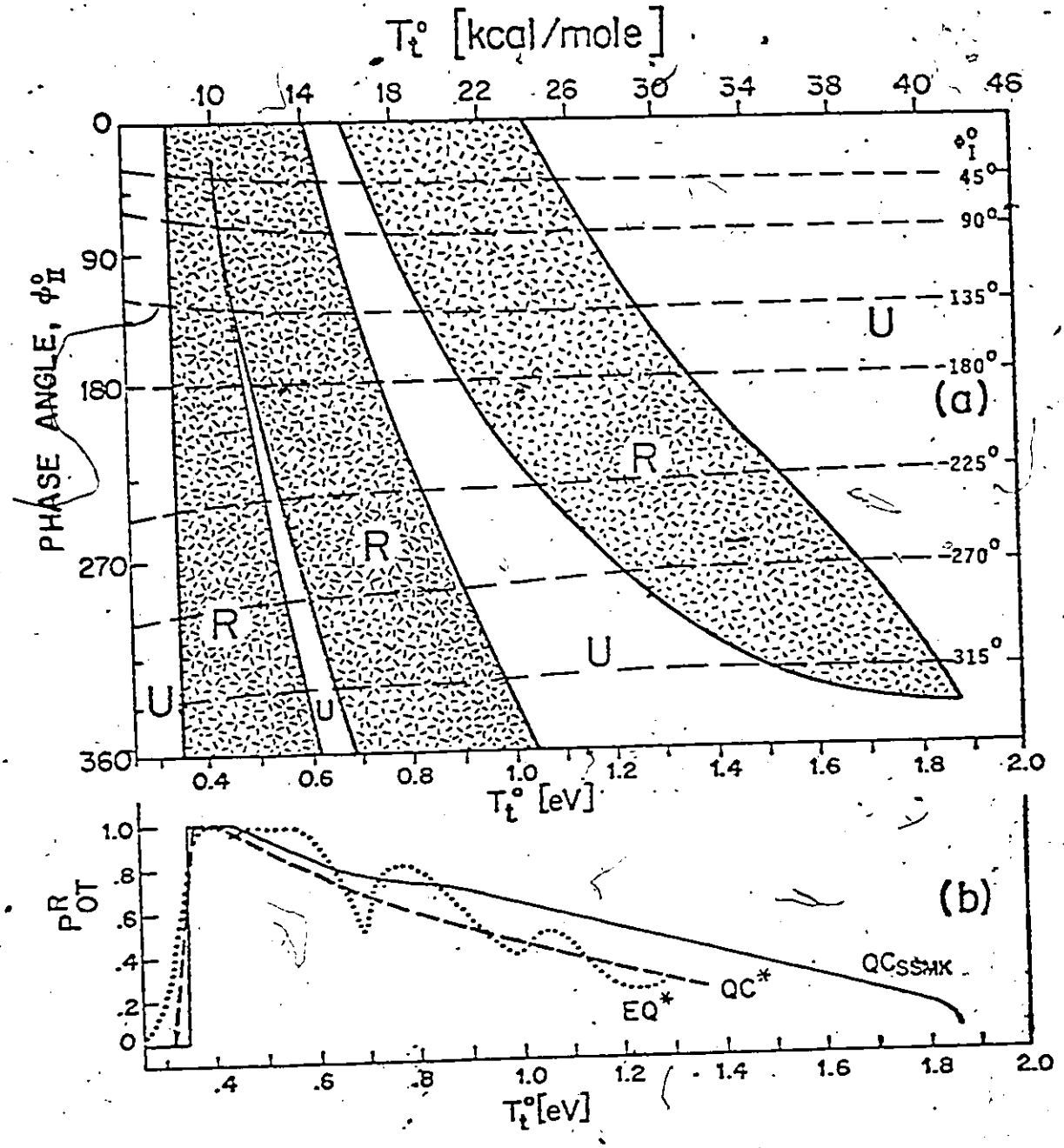
T_t° [kcal/mole]
10
14
18
22
26
30
34
38
40
46
0
90
180
270
360
PHASE ANGLE, ϕ_{II}°
ϕ_I°
45°
90°
135°
180°
225°
270°
315°
U
R
U
R
U
R
U
(a)
0.4
0.6
0.8
1.0
1.2
1.4
1.6
1.8
2.0
T_t° [eV]
P_{OT}^R
1.0
.8
.6
.4
.2
0
QC*
EQ*
QCSSMK
(b)
.4
.6
.8
1.0
1.2
1.4
1.6
1.8
2.0
T_t°[eV]

of ϕ_{II} rather than ϕ_I. The results of calculations with the "accurate" reaction shell III have also been published[90] and will be discussed in Chapter 3, in connection with other mass combinations. The t^R and E'_n curves (Figs.11 and 12) are still valid representations of correct results of the present investigation, although they no longer correspond to constant ϕ^o_{II}, except for $\phi^o_I = \phi^o_{II} = 0^o, 180^o$ (see Figs.5 and 14a). Similar to the band-boundary positions, the specific product attributes (t^R and E'_n) can be directly transformed to different choices of the reaction shell, by establishing the relationships of the corresponding phase angles as a function of T_t.

In Figs.13a and 14a, the continuity of the reactivity bands with ϕ^o and T^o_t is effectively demonstrated. The cyclic character of this band-continuity property is more evident in the polar plot shown in Fig.15. The angular and radial variables are ϕ^o_{II} and T^o_t respectively and the band boundaries were again taken through the center of the statistical regions. For all ϕ^o_{II}, the reactive threshold occurs at 0.35 $\pm$ 0.01 eV (inner circle). An unreactive band opens up at approximately (100^o,0.45 eV) and forms a continuously widening spiral. The reactive branch of the spiral (shaded) terminates near (340^o,1.85 eV). Most of the high-energy region beyond 1.5 eV is unreactive, thus contributing to the decrease of reaction probability observed in Fig.14b.

Specific reaction probabilities P^R_{On} may be obtained by specifying a product vibrational quantum number n as outlined in Sec. 2.5.3. The additional information is collected in the rather complicated band plot shown in Fig.16a. In this figure,

Figure 15

Polar plot of the total reactivity. Shaded region is reactive. Radial coordinate=T_t^o (eV); angular coordinate=ϕ_{II}^o (degrees).

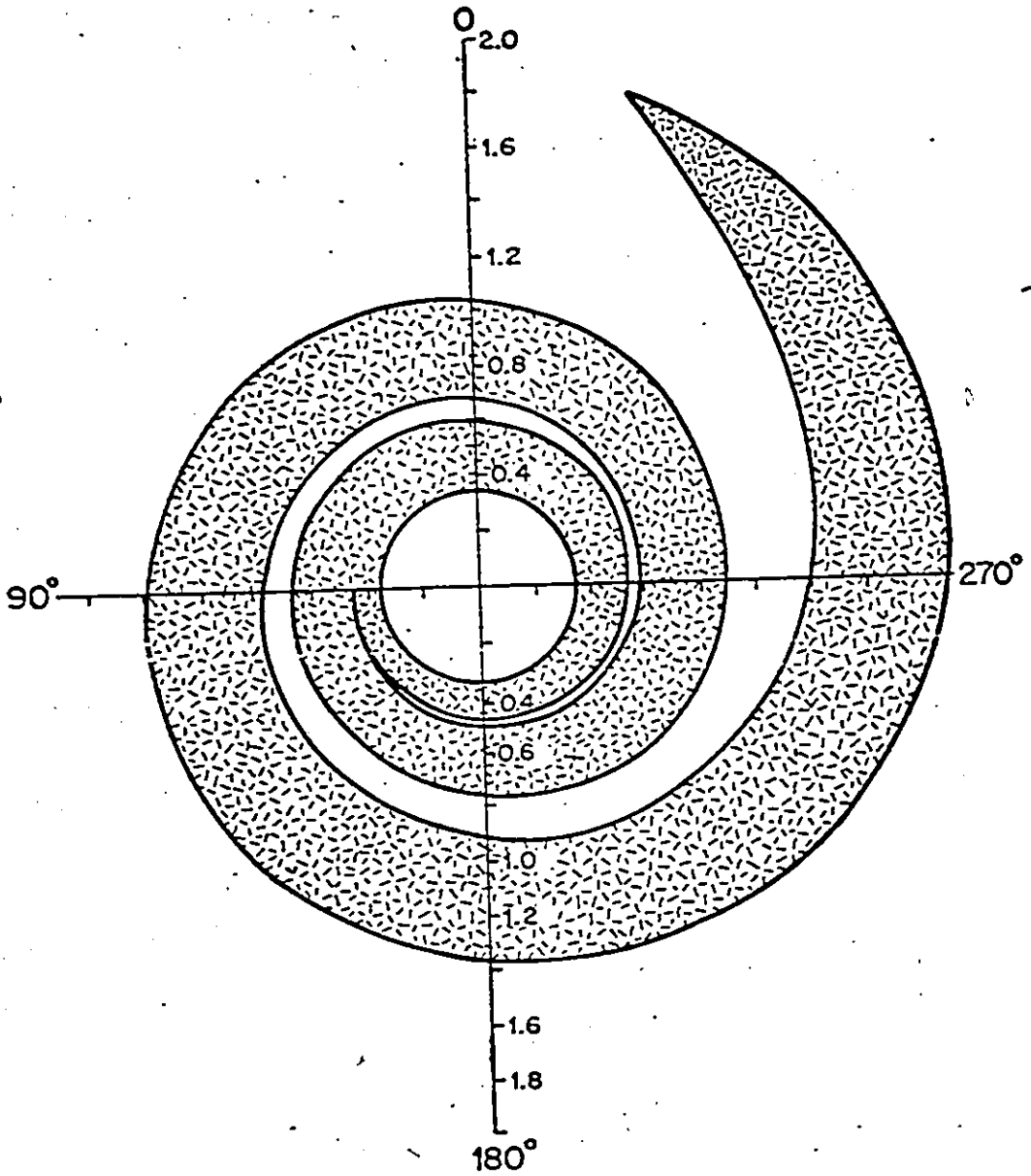
0
2.0
1.6
1.2
0.8
0.4
90°
270°
0.4
0.6
1.0
1.2
1.6
1.8
180°

region U_i indicates an unreactive region with product in the i^{th} vibrational state, and similarily for R_i (shaded). An attempt has also been made to indicate the width of the statistical regions at the band edges (dark shading). In these regions the trajectories are considered to be distributed uniformly over all available U_i, R_i states[53,71]; the highest possible i is thereby determined from the adjacent direct scattering regions. From this map, the continuity of product vibrational energy in both R, U regions is evident. Fig.16b shows the specific reaction probability P_{00}^R for the SSMK surface, along with the corresponding EO^* and QC^* curves[52]. Direct graphical summation of the widths of the R_0 regions in Fig.16a was carried out to obtain this result. The QC_{SSMK} curve is again more reactive than the QC^* curve, and averages the quantum oscillations. This is also true for the P_{01}^R curve shown in Fig.16c. The P_{02}^R curve for the SSMK surface is also shown in this figure. The energy thresholds associated with the opening up of specific product vibrational levels are indicated in these Figs.16b and c by arrows labeled T_n[52] on the ordinate axis. In general, the thresholds correspond closely to the expected values:

$$T_n = T_t^{thld} + (E_n - E_0).$$

To summarize, the SSMK surface gives results comparable to those of previous calculations on a similar surface[52,88]; the QC_{SSMK} curves average the quantum results, and are somewhat more reactive than the QC^* curves, although generally parallel to the latter.

Figure 16

(a) Vibrationally quantized reactive (R_i) and unreactive (U_i) regions, with product in the i^{th} vibrational box.

(b) P_{00}^{R} reaction probabilities,

(c) P_{0i}^{R} reaction probabilities.

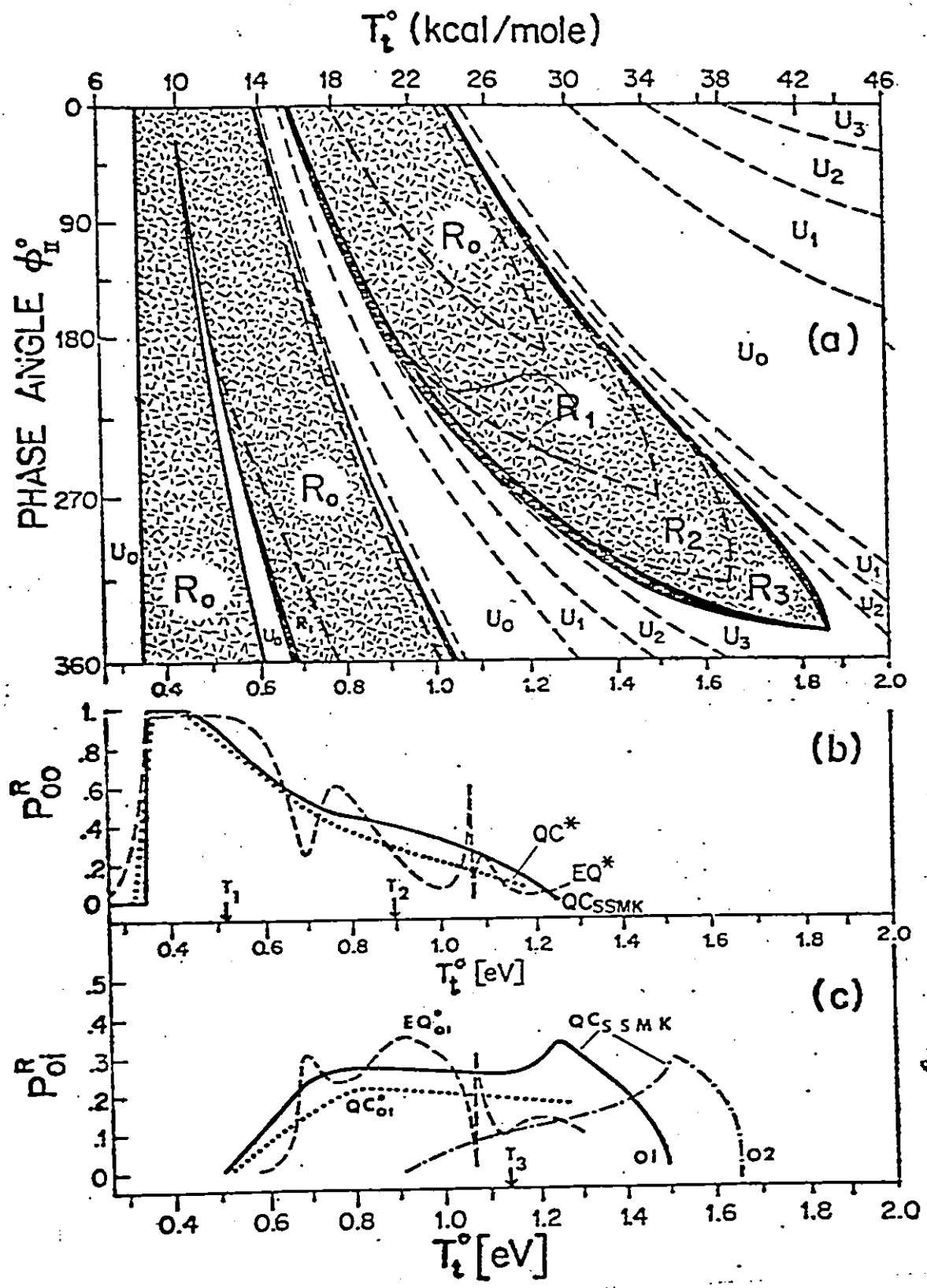
T_t° (kcal/mole)
6 10 14 18 22 26 30 34 38 42 46
PHASE ANGLE ϕ_{II}°
0 90 180 270 360
R_0
R_1
R_2
R_3
U_0
U_1
U_2
U_3
(a)
0.4 0.6 0.8 1.0 1.2 1.4 1.6 1.8 2.0
P_{00}^R
0 .2 .4 .6 .8 1
(b)
QC*
EQ*
QC_{SSMK}
T_1
T_2
T_t° [eV]
P_{01}^R
0 .1 .2 .3 .4 .5
(c)
EQ_{01}^*
QC_{SSMK}
QC_{01}^*
T_3
01
02
T_t° [eV]

2.6.6 Discussion.

The results of the collinear trajectory calculations for the $H+H_2$ reaction were shown to be of remarkable simple form, when reactivity bands and the structure of the final parameter curves are considered. Except for the statistical regions, the outcome of individual trajectories with varying initial parameters seems to be very predictable, once the results for a few phase angles have been obtained. The coincidence of the band edges with t^R peaks, the otherwise smooth and quite predictable behavior of the t^R curves, and the band continuity property with increasing phase angle have allowed the reduction of the calculations to fewer trajectories than required in other 1-D systematical and Monte Carlo methods of the same accuracy. It was thus possible to cover a wider range of energies with a finer resolution, than in other detailed studies[48-54], and this led to the observation of the high energy cut-off in reactivity which is related to the quasi-classical brick-wall effect, and of many other, previously reported features, such as the high product-vibrational energy near band edges, statistical regions and complex behavior within these regions, etc. Most of these features have been successfully interpreted, or made plausible, from examinations of the individual trajectories. The most important phenomena, the existence of reactivity bands and their continuity with the variation of the phase angle, remain to be discussed.

From skewed trajectory plots, e.g. Fig.8, it is seen that

the trajectories along the approach coordinate (reactant valley) have a distinct wave form, which appears to be very regular up to regions close to the transition state. The wavelength of these reactant waves increases with increasing T_t^o, but the amplitudes are constant, since they depend on the initial vibrational energy which is always equal to the ZPE. The orthogonal trajectory plots (Figs.7 and 10) also show these features, but here the wave form seems distorted since the system cannot be represented by a single particle in this coordinate system. The products also show a wave form, but with a large variety of amplitudes. It is therefore appropriate to speak of a reactant channel of constant width, up to the transition-state region, and of a reactant wave, the wavelength and phase of which depend on the initial conditions (T_t^o and ϕ^o). Such regular behavior and generalizations of the type made in the discussion of the trajectory plots, lead to the intriguing possibility that a priori predictions might be made about reaction probabilities and energy transfer phenomena, from considerations of the initial conditions and local features of the surface near the transition state. It seems quite natural that reactivity bands should occur, and that the behavior of the t^R and E_n' curves is so smooth within the reactive and unreactive bands, because the variation of T_t^o will gradually change the reactant wavelength, and no sudden changes can occur unless a corner hitting trajectory is generated. These ideas will be pursued more quantitatively in Chapter 5, where the shift of the bands with ϕ^o is explained, and a complete discussion of the collinear case is given at the end of Chapter 3.

CHAPTER 3: COLLINEAR X + HX

3.1 Introduction.

The collinear $H+H_2$ study was extended to include mass combinations of the symmetric type Heavy + Light-Heavy, where the light atom is hydrogen and the heavy atoms are actual or hypothetical isotopes of hydrogen. The effect of changing the mass combination is equivalent to a variation of the skew-angle of the potential-energy surface model (see Sec.2.2), and of the characteristics of vibrational motion of the reactant molecule (ZPE, amplitudes, vibrational period). The variation of reactant vibrational energy could have been more conveniently studied by staying with the $H+H_2$ reaction. However, more drastic changes in dynamical behavior are expected for different mass combinations, due to differences in kinetic energy transfer as predicted from simple models[45-47,68,91-93]. For Heavy + Light-Heavy mass combinations, an area of interest to previous workers has been the possibility of vibrational relaxation through reactive collisions[94-97].

Although unsymmetric mass combinations X+HY are generally easier to study experimentally, the symmetric cases X+HX are of greater advantage in systematic trajectory calculations. Thus, the scaling factor for the coordinate axes can be neglected (see Sec.2.2), the reverse reactions need not be considered separately, and the equations of motion assume a simpler, symmetric form. Moreover, the results could be expected to be of general validity and easily extended to include unsymmetric reactions.

3.2 Methods of Calculation.

As in the $H+H_2$ study, three series of calculations were performed with different sets of initial conditions, specified in Sec.2.5.1. In the first two series of calculations (I and II) the hypothetical masses 2.0, 3.0 and 10.0 a.m.u. were chosen to represent X. In series III a switch was made to the actual isotopes of mass 2.014 (D) and 3.016 (T), while the hypothetical mass 10.0 a.m.u. was retained. The potential-energy surface, computer program and methods of calculation were identical to those discussed in the previous chapter. The generalizations of Chapter 2 also apply for this part of the study. In particular the correlation between the three series of calculations, as discussed in Sec.2.6.5, established that the results are essentially identical, indicating that the slight mass differences D-(2.0), T-(3.0) had negligible effect on the final reaction probabilities. Free use of the results of all three calculations is therefore made; the symbol ϕ_i^o (i=I,II,III) will indicate which results are refered to, and the cases studied will be labeled H+HH, D+HD, T+HT, and 10+H-10. The specific initial conditions are characterized by the parameters for vibrational motion (A_i, τ_i, and ZPE), and by the reaction shell radius (ρ^o), the equilibrium distance at the reaction shell (r_e^o), and the potential energy at this point (V_{ref}). These parameters were summarized for series I and II in Table III (Sec.2.5.1). For series III, they are listed together with the skew angle (ξ), the reduced mass ($\mu_{A,BC}$) and the integration step size (Δt) in

Table V. For $H+H_2$ the reaction shell III was chosen to pass through the absolute minimum of the surface; for the other cases it passes nearby. The values of r_{BC}, V_{ref}, A_i and τ_i are markedly dependent on the exact location of the reaction shell (compare to Table II). The vibrational energies are calculated from eq.(40), using the published surface constants[38], and are therefore independent of the choice of the reaction shell. (The slight differences in mass D-(2.0), T-(3.0) introduce negligible variations in the ZPE.) The skew angle is calculated from eq.(21) and is again unaffected by slight mass differences. Integration step sizes were 2.0×10^{-16}s except for I0+H-10 where it was increased to 2.5×10^{-16}s to retain a good balance between accuracy and computer time. In general, the total energy H was well conserved, averaging a constancy of 2 parts in 10^4. The accuracy increases with increasing mass X, but decreases with increasing T_t^o. At a band edge larger fluctuations in H occur, up to an order of magnitude larger than for stable trajectories. The largest round-off errors occur at the turning points of the trajectories, especially when large changes in velocity are involved.

3.3. Results and Discussion.

3.3.1 Reaction Times.

The reaction channel, reaction time, and product vibrational energy were again obtained as a function of T_t^o at various ϕ^o. The

Table V. Data Characteristic of X+HX on Reaction Shell III[a].

	H+HH	D+HD	T+HT	10+H-10
r^{o}_{AB}/Å	3.5000	3.3768	3.3153	3.1976
r^{o}_{BC}/Å	0.7414	0.7411	0.7410	0.7408
V_{ref}/eV	-4.62358	-4.62355	-4.62339	-4.62277
A_l/Å	0.1066	0.1000	0.0975	0.0934
A_r/Å	0.1399	0.1289	0.1246	0.1180
τ_r/τ_l	1.406	1.382	1.371	1.341
ZPE/eV	0.2686	0.2331	0.2200	0.2000
E'_0/eV $\leq$	0.5251	0.4571	0.4319	0.3934
E'_1/eV $\leq$	1.022	0.8931	0.8450	0.7713
E'_2/eV $\leq$	1.487	1.305	1.237	1.131
E'_3/eV $\leq$	1.919	1.693	1.607	1.474
E'_4/eV $\leq$	2.319	2.056	1.955	1.799
ξ/deg.	30.0	41.8	48.5	65.3
$\Delta t \times 10^{16}$/s	2.0	2.0	2.0	2.5
$\mu_{A,BC}$/a.m.u.	.672	1.2086	1.7239	5.2399

[a] ρ^{o} = 3.8707 Å, see Sec.2.5.1.

same kind of behavior as for the H+HH reaction (Sec.2.6.4) was observed. Fig.17a-d shows the reaction time for D+HD as a function of T_t^o. Except for a compression along the T_t^o axis, the general features of this plot are nearly identical to those shown in Fig.11a-h for H+HH. Thus for $\phi_I^o = 0^o$ and D+HD (H+HH), regions of alternating reactivity are found at 0.35-0.52 (0.35 -0.61) (R), 0.52-0.60 (0.61-0.69) (U), 0.60-0.79 (0.69-1.04) (R), 0.79- 2.0 (1.04- 2.0) (U), and anomalous irregularities occur at 0.39 (0.43) and 1.17 (1.8) eV. The reactive thresholds coincide at 0.35 eV, but different cut-off energies are observed at 0.79 (1.04) eV. Viewed in this light, the results for T+HT, shown in Fig.18a-d, can be recognized as a further contraction of the bands towards low T_t^o, and a new reactive band appearing at high energies. Figs.19a-d for 10+H-10, which seem very complicated at first glance, can then be understood as a continuation of this contraction pattern. The low-energy bands have been crowded very closely together, and many high-energy bands have appeared in the range between 0.5 and 2.0 eV. In view of these results, it seemed highly probable that high-energy reactive regions exist for H+HH and D+HD. The H+HH reaction was investigated up to 20 eV without any indication of high-energy reactivity, but a scan along $\phi_I^o = 0^o$ did reveal the beginning of a reactive band at 4.45 eV for D+HD extending beyond 10 eV. These results are summarized in Table VI, from which the contraction pattern is also evident for the high-energy reactive regions. Thus, no cut-off energies are observed for D+HD and T+HT, but for 10+H-10 no reactivity is observed at any ϕ_I^o beyond 2.2 eV.

Figure 17

Reaction times for D+HD at various ϕ_I^o.

——— reactive; ------- unreactive.

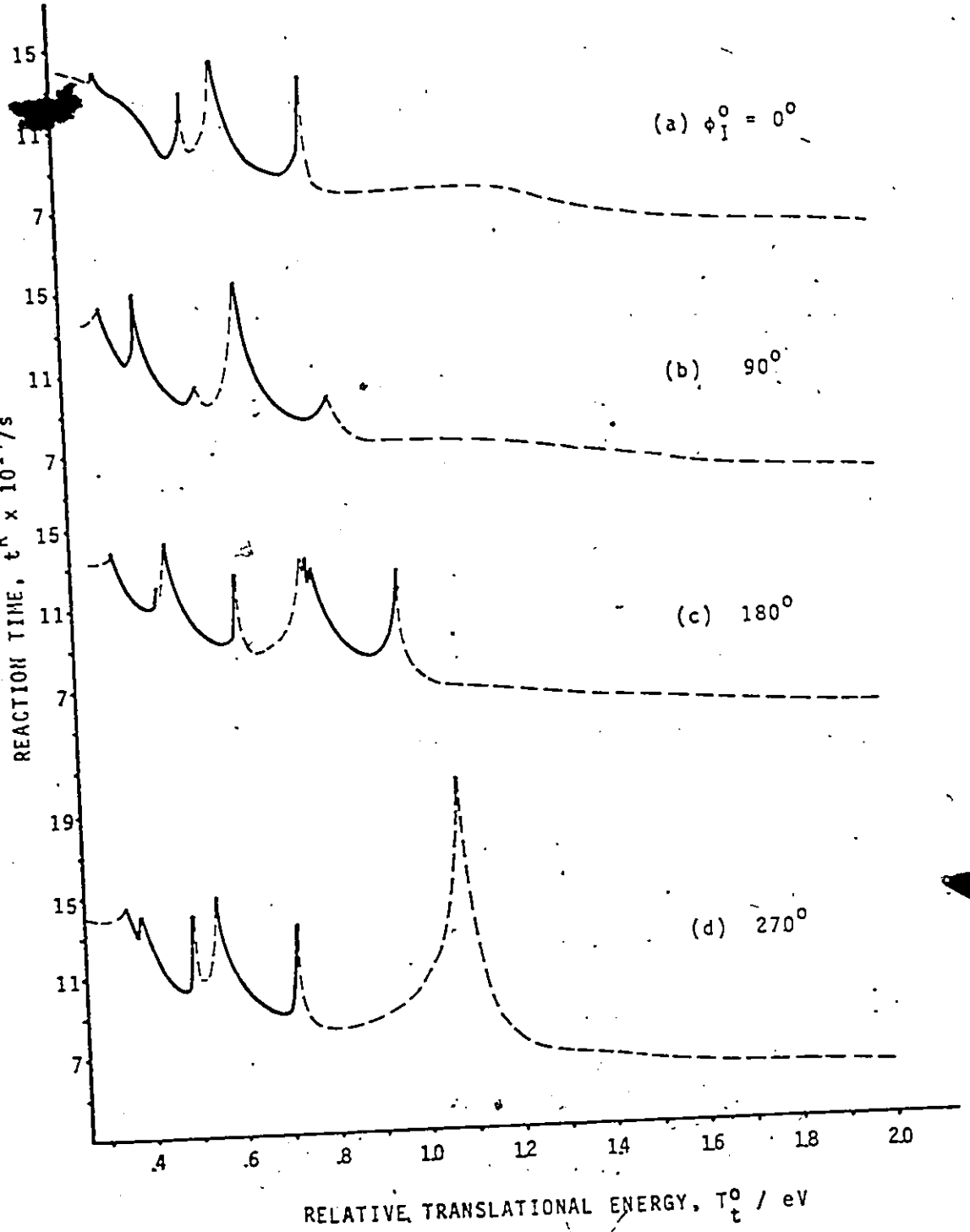
15
11
7
(a) $\phi_I^o = 0^o$
15
11
7
(b) 90°
15
11
7
(c) 180°
19
15
11
7
(d) 270°
REACTION TIME, $t^R \times 10^{14}$/s
.4
.6
.8
1.0
1.2
1.4
1.6
1.8
2.0
RELATIVE TRANSLATIONAL ENERGY, T_t^o / eV

Figure 18.

Reaction times for T+HT at various ϕ_I^o.

——— reactive; ------- unreactive.

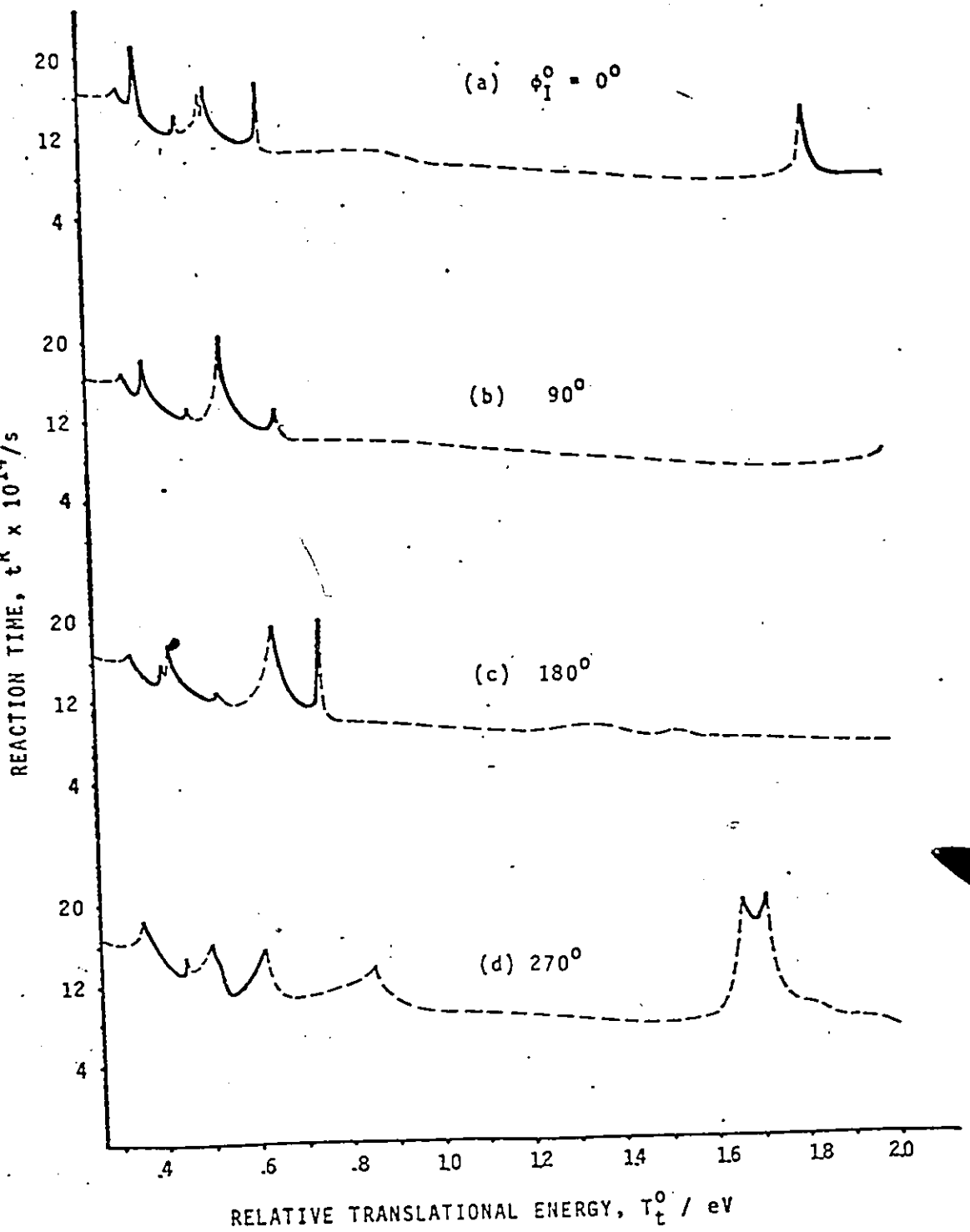
(a) $\phi_I^o = 0^o$
(b) 90^o
(c) 180^o
(d) 270^o
20
12
4
REACTION TIME, $t^R \times 10^{14}$/s
.4
.6
.8
1.0
1.2
1.4
1.6
1.8
2.0
RELATIVE TRANSLATIONAL ENERGY, T_t^o / eV

Figure 19

Reaction times for 10+H-10 at various ϕ_I^o.

——— reactive; ------- unreactive.

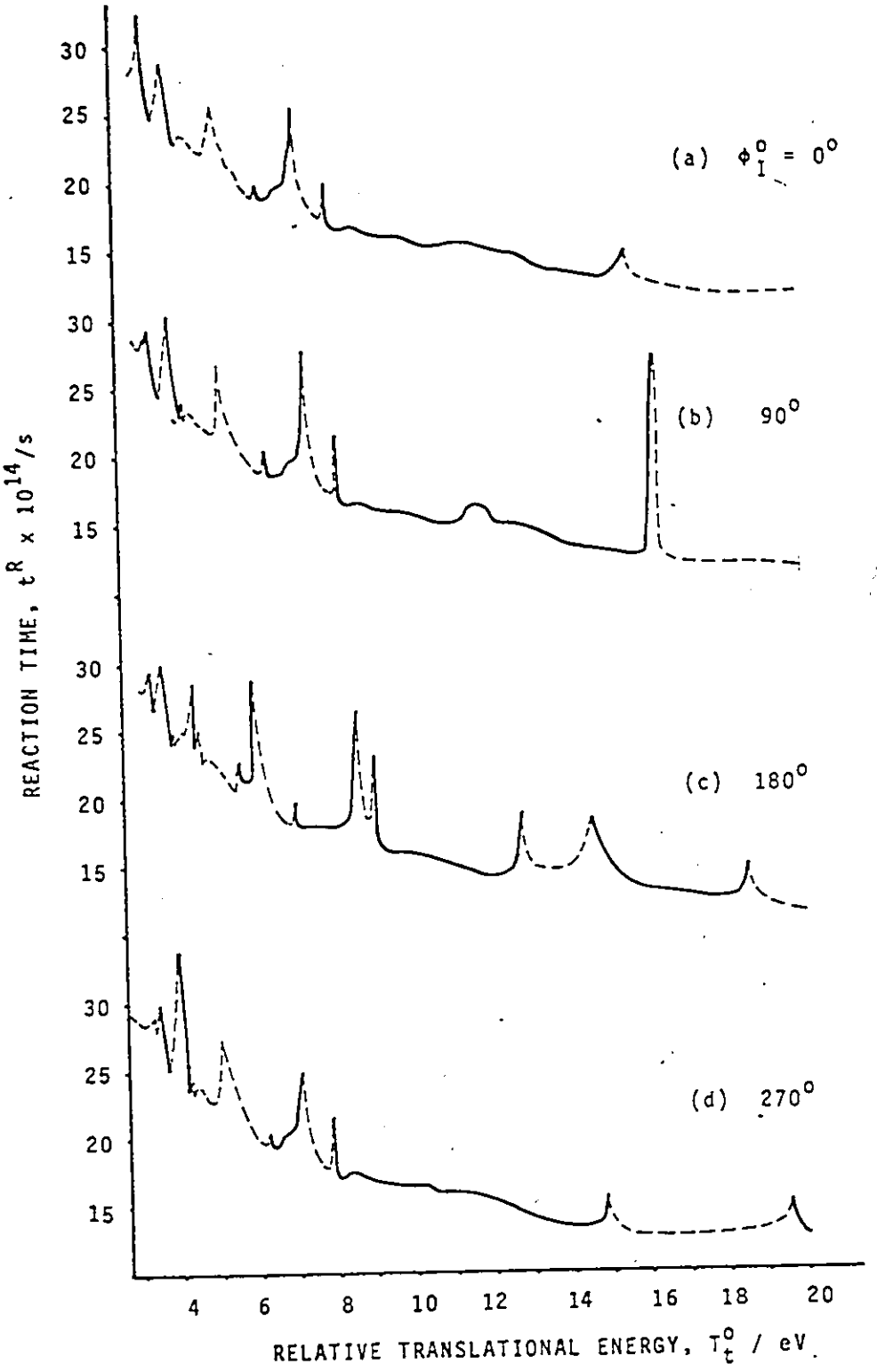
(a) $\phi_I^o = 0^o$
(b) 90^o
(c) 180^o
(d) 270^o
REACTION TIME, $t^R \times 10^{14}$/s
RELATIVE TRANSLATIONAL ENERGY, T_t^o / eV
30
25
20
15
4
6
8
10
12
14
16
18
20

Table VI. Reactivity bands for X+HX at $\phi_I^o = 0^o$.

	R	U	R	U	R	U	R
H + H-H	0.35-0.61	0.61-0.69	0.69-1.04	1.04- 20.	-	-	-
D + H-D	0.35-0.52	0.52-0.60	0.60-0.79	0.79-4.45	4.45- 10.	-	-
T + H-T	0.35-0.47	0.47-0.53	0.53-0.65	0.65-1.83	1.83-2.36	2.36-2.60	2.60- 10.
10 + H-10	0.34-0.36	0.36-0.39	0.39-0.42	0.42-0.63	0.63-0.73	0.73-0.81	0.81-1.57

3.3.2 Reaction Probabilities.

The total reaction probability P^R_{0T} may be obtained by the method described in Sec.2.6.5. Fig.20a shows the linear ϕ^o_{III} vs. T^o_t band plot for H+HH. The results for this series of calculations assume a particularly simple form, in which fewer reactivity bands are present in the linear band plots. This can be understood from the dashed correction lines, shown in Fig.20a correlating $\phi^o_{II} = 0^o$ to ϕ^o_{III} as a function of T^o_t. The correction lines for other ϕ^o_{II} are parallel to the one shown, since the distance between reaction shells II and III is the same for all phase angles: $\Delta R_{A,BC} = \rho^o_{II} - \rho^o_{III} = 1.5$ Å (see also Fig.6 where reaction shells II and III are parallel to each other). In Fig.20a the correction line for $\phi^o_{II} = 0^o$ starts at $\phi^o_{III} = 360^o$, $T^o_t = 0.34$ eV, crosses the threshold near 350^o, 0.35 and the first (R→U)-boundary at 200^o, 0.62 eV. This indicates that in a ϕ^o_{II} vs. T^o_t bandplot, the first reactive region at 0^o should extend from 0.35-0.62 eV. From Fig.14a, it is seen that this is indeed the case. Following the correction line in Fig. 20a to the end near 295^o, 2.0 eV, the results for $\phi^o_{II} = \phi^o_I = 0^o$ (see also Table VI) are faithfully reproduced. With many such correction lines for many phase angles ϕ^o_{II} drawn in Fig.20a, all parallel to one another, the complete Fig. 14a is reproduced. The effect of transforming Fig.20a into Fig.14a, using such correction lines, will be to extend the plot along the ϕ^o_{II} axis, yielding narrower reactivity bands but extending over a longer ϕ^o range at constant T^o_t. The fact that the correction lines at all ϕ^o_{II} are parallel will automatically lead to identical reaction probability curves,

which are indeed observed (compare Fig.20b to the QC_{SSMK} curve in Fig.14b). This verifies that the correct probability distribution has been used[98], since the outcome is independent of the choice of the reaction shell. It also shows that the relative and angular velocities (cf. Sec.2.5.2) can be considered to be constants of motion outside the reaction shell. The switch to the smaller reaction shell radius (II→III) therefore not only reduces the computer time, while increasing the accuracy (cf. Sec.2.2), but also simplifies the form of the band plots. This is also true for the higher mass combinations, the results of which are shown in Figs. 21 to 23 in the form of ϕ^o_{III} vs. T^o_t and $P^R_{OT}(T^o_t)$ plots. The correction lines for $\phi^o_{II} = 0^o$ are also shown to simplify the correlation of these diagrams to the t^R vs. T^o_t curves of Figs.17 to 19.

Fig.21a shows that the results obtained for D+HD are very similar in shape to those for H+HH (Fig.20a), but the total reactivity (area of the shaded regions) has dropped considerably because of the shrinkage of the bands along the T^o_t axis. This is also reflected in the probability curve in Fig.21b, which like the H+HH curve (Fig.20b) rises steeply at the threshold to a value of 1.0, but then drops off more rapidly to reach zero at 1.1 eV. For T+HT, the results again reflect the consistently shrinking pattern, when the appearance of the band at high energies is ignored.(Fig.22a,b). Again the same general shape of the low-energy bands is evident, although they have become much thinner, and the probability curve still shows the same behavior

Figure 20

(a) Linear reactivity map for collinear $H+H_2$ as a function of ϕ^o_{III} and T^o_t. The correction lines (dashed) relate $\phi^o_{II}=0^o$ to ϕ^o_{III}, and parallel correction lines can be drawn for other ϕ^o_{II}.

(b) Total reaction probability obtained by graphical summation from (a) is identical to P^R_{OT} (OC_{SSMK}) in Fig.14b.

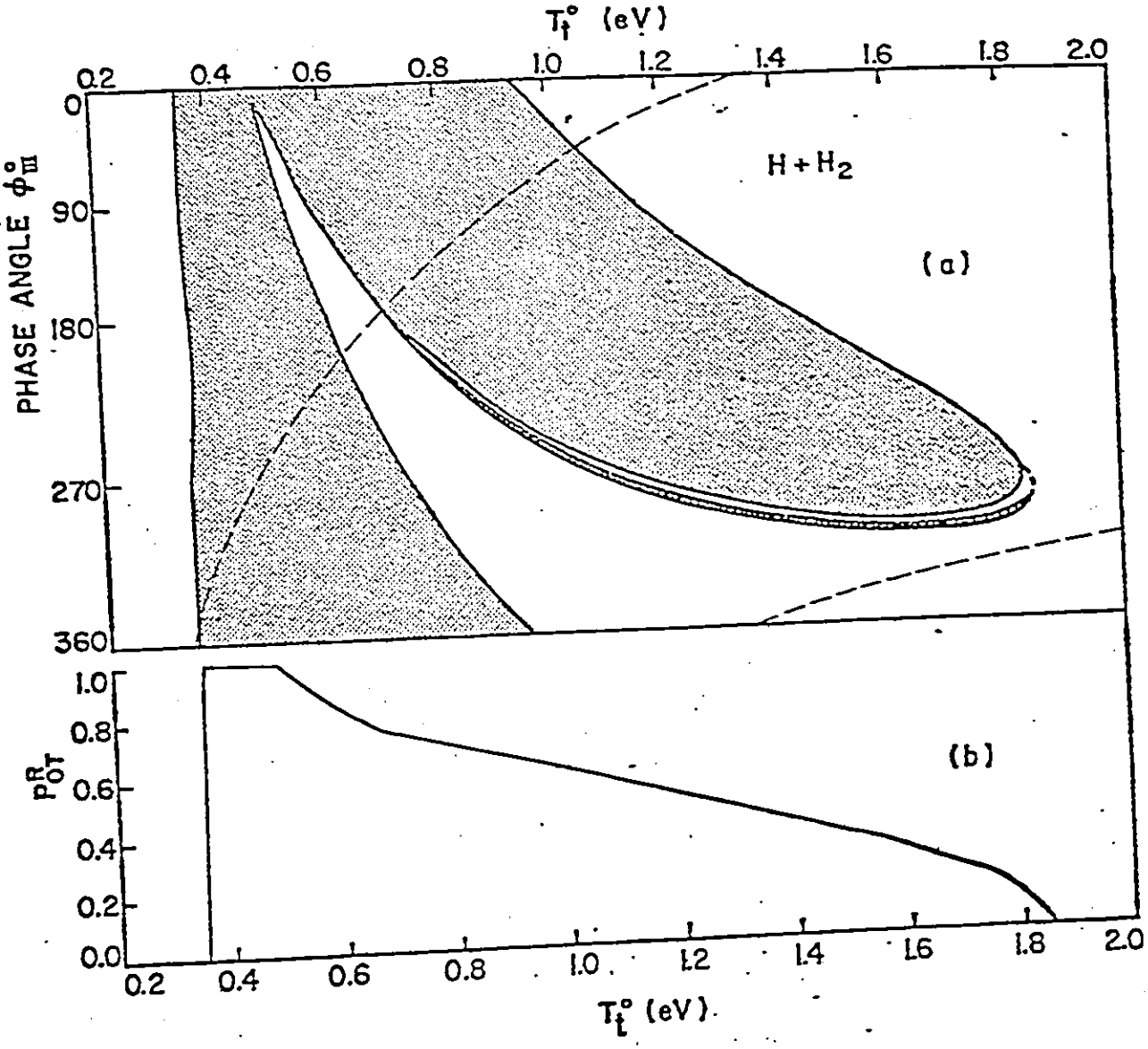
T_i° (eV)
0.2
0.4
0.6
0.8
1.0
1.2
1.4
1.6
1.8
2.0
PHASE ANGLE ϕ_{III}°
0
90
180
270
360
$H + H_2$
(a)
P_{OT}^R
1.0
0.8
0.6
0.4
0.2
0.0
(b)
T_i° (eV)

Figure 21

(a) Reactivity map for collinear D+HD (III).

(b) Total reaction probability curve.

(------) $\phi_{II}^{o} = 0^{o}$.

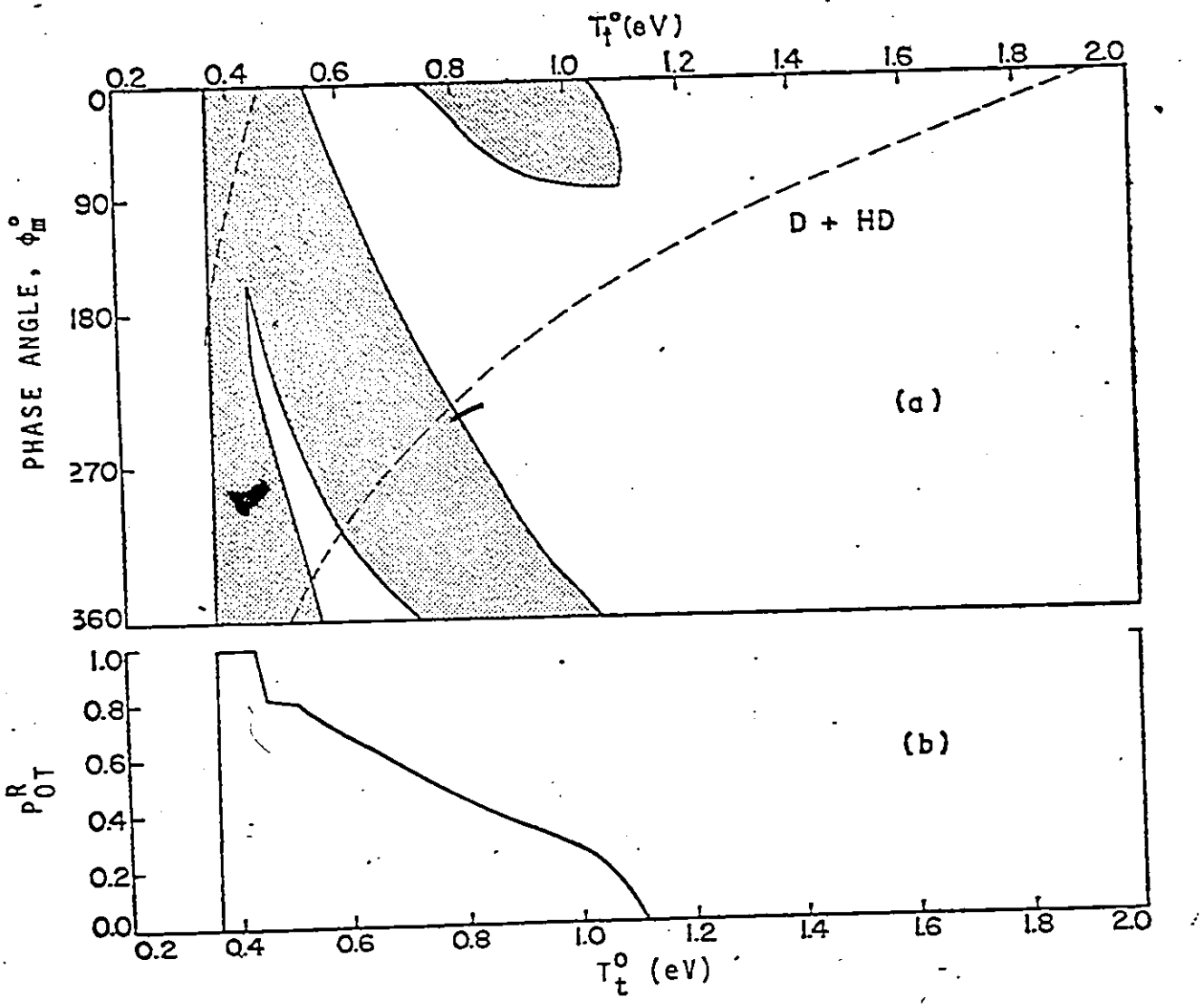
T_t^o(eV)
0.2
0.4
0.6
0.8
1.0
1.2
1.4
1.6
1.8
2.0
0
90
180
270
360
PHASE ANGLE, ϕ_m^o
D + HD
(a)
1.0
0.8
0.6
0.4
0.2
0.0
P_{OT}^R
(b)
T_t^o (eV)

Figure 22

(a) Reactivity map for collinear T+HT (III).

(b) Total reaction probability curve.

(------) $\phi_{II}^{o}=0^{o}$.

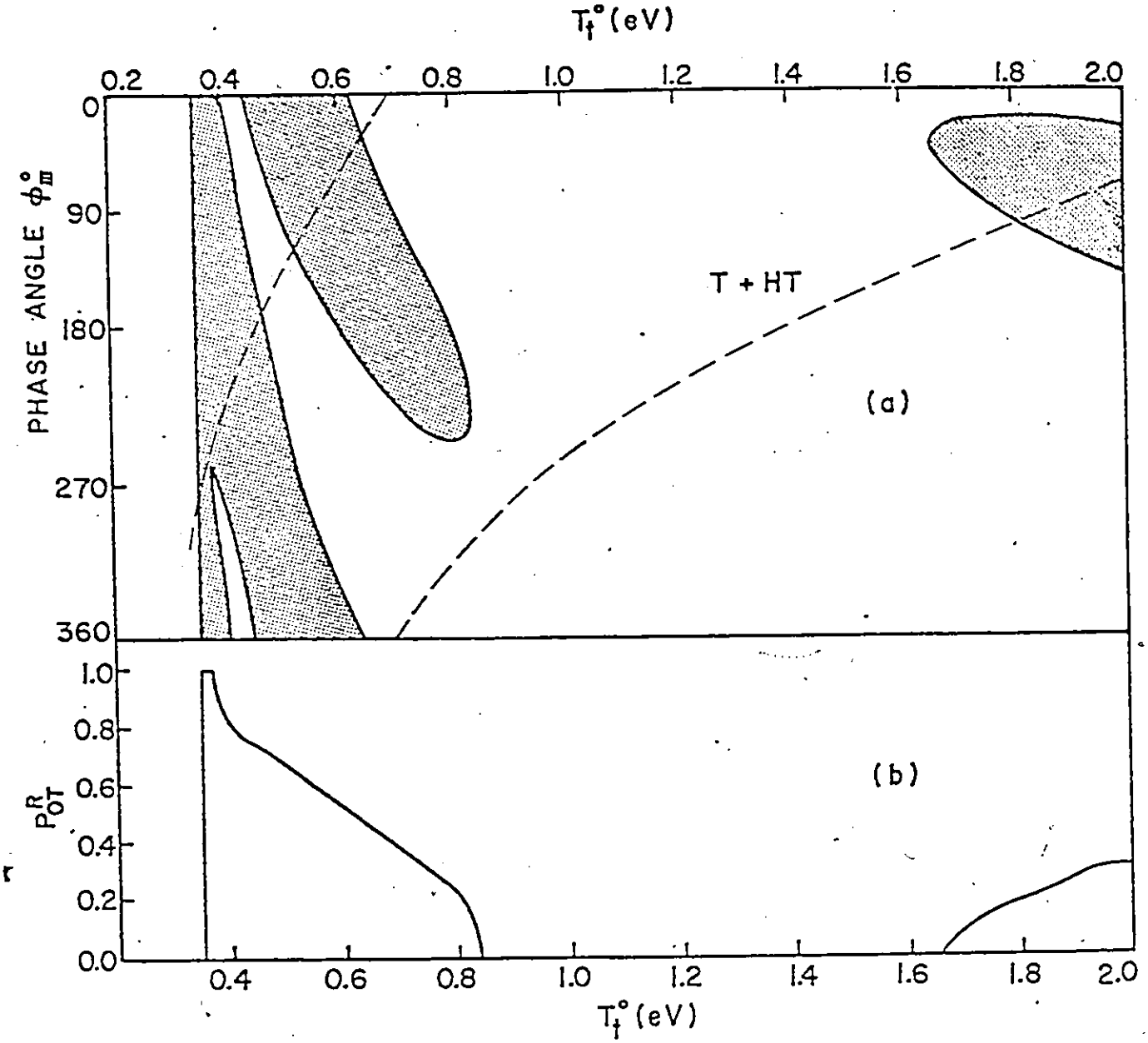
T_f° (eV)
0.2
0.4
0.6
0.8
1.0
1.2
1.4
1.6
1.8
2.0
PHASE ANGLE ϕ_m°
0
90
180
270
360
T + HT
(a)
P_{OT}^R
1.0
0.8
0.6
0.4
0.2
0.0
(b)
T_f° (eV)

Figure 23

(a) Reactivity map for collinear 10+H-10.

(b) Total reaction probability curve.

(------) $\phi_{II}^{o}=0^{o}$.

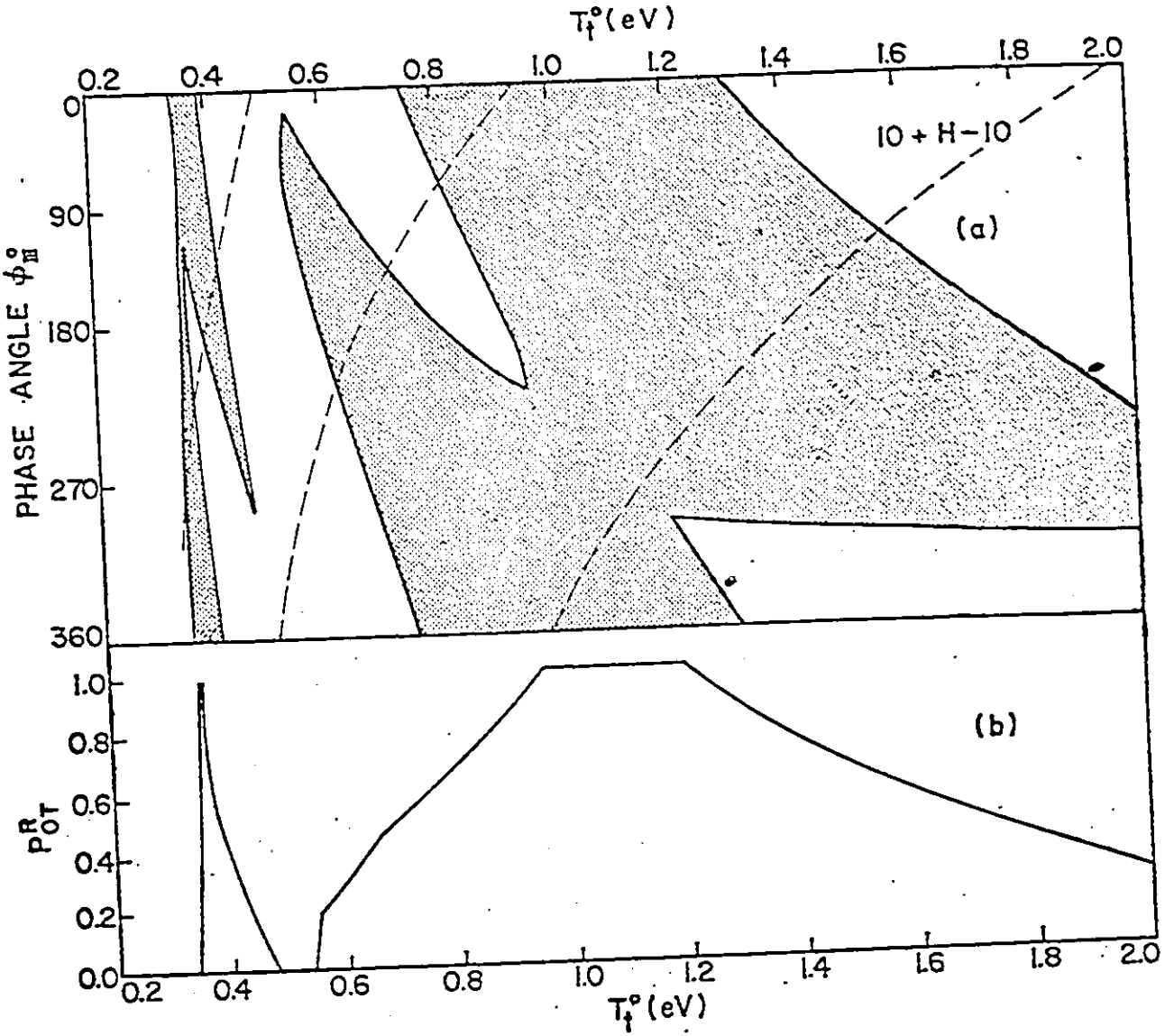
T_i° (eV)
0.2
0.4
0.6
0.8
1.0
1.2
1.4
1.6
1.8
2.0
0
90
180
270
360
PHASE ANGLE ϕ_m°
10 + H − 10
(a)
1.0
0.8
0.6
0.4
0.2
0.0
P_{OT}^R
(b)
T_i° (eV)

as was noted above for D+HD, with an even faster decline to zero. The high energy reactive band then introduces a remarkable phenomenon, in that the reaction probability is zero over a wide range (0.85-1.68 eV), and then starts to increase again at higher energy. Under experimental conditions such a behavior could be explained by two different reaction mechanisms, e.g. rebound at low energies and stripping at higher energies[99]. In collinear processes, the collision is always head-on, so that a purely dynamical effect must account for this peculiar behavior. For 10+H-10 in Fig.23, the region of zero reaction probability persists, but over a much narrower range (0.48-0.53 eV). The low energy bands have also narrowed considerably. The correction lines are much steeper in slope than for the previous cases (this is because the relative velocity of the 10+H-10 system is very small at a given energy); they indicate the complicated form of the results obtained with the larger reaction shell II, narrowing the low energy bands even further, and giving rise to many more bands at high energy (see Fig.19). The reaction probability curve (Fig.23b) shows two distinct reactive regions, separated by the narrow range of zero reaction probability. The first (low energy) region is clearly related by shape to the "first" reactive regions of the previous cases. The second reactive region is now for the first time presented in more or less complete form. It is seen that it gradually rises to reach total reactivity (P_{0T}^{R}=1.0) at 0.95 eV, but drops down again at 1.2 eV to gradually reach zero by 2.2 eV (not shown). As in the previous case, this is a truly remarkable behavior, never encountered before in such explicit

form in the literature on quasi-classical calculations. Since the shrinking pattern with increasing mass of X is so consistent, the same effect can be predicted to occur for collinear X+HX, with X between 4 and 9.

The results can be summarized more conveniently, as in Fig. 24a-d, where polar reactivity plots for the different mass combinations are shown. Owing to the continuity of the bands, the reactive regions (shaded) assume a characteristic spiral form for all mass combinations. Furthermore, there is a striking relationship between the individual plots. Where the pattern for H+HH is rotated and compressed, it becomes almost identical with the pattern for D+HD. Further compression and rotation generates the inner T+HT spiral, and a continuation of this procedure will yield the narrow inner spiral for 10+H-10. The outer reactive spiral, the beginning of which first appears for T+HT, was also detected at very high energies (>4.45 eV) for D+HD, and dominates the picture for 10+H-10. Symmetric mass combinations X+HX, with X between T and 10, are expected to show increasing portions of the outer spiral in the range below 2.0 eV.

Another feature common to all mass combinations, at all phase angles, is the threshold occurring at 0.35±0.01 eV (inner circle). Since the ZPE differs by 0.07 eV between HH and H-10, this constancy of threshold energy is a surprising result. A more general and quantitative discussion of this phenomenon will be given in Sec.3.4.3 C.

Finally, the band continuity property and familiarity with the

Figure 24

Polar reactivity maps for collinear X+HX. The radial coordinate=T_t^o (eV); the angular coordinate= ϕ_{III}^o (degrees).
(a) H+HH, (b) D+HD, (c) T+HT, (d) 10+H-10.

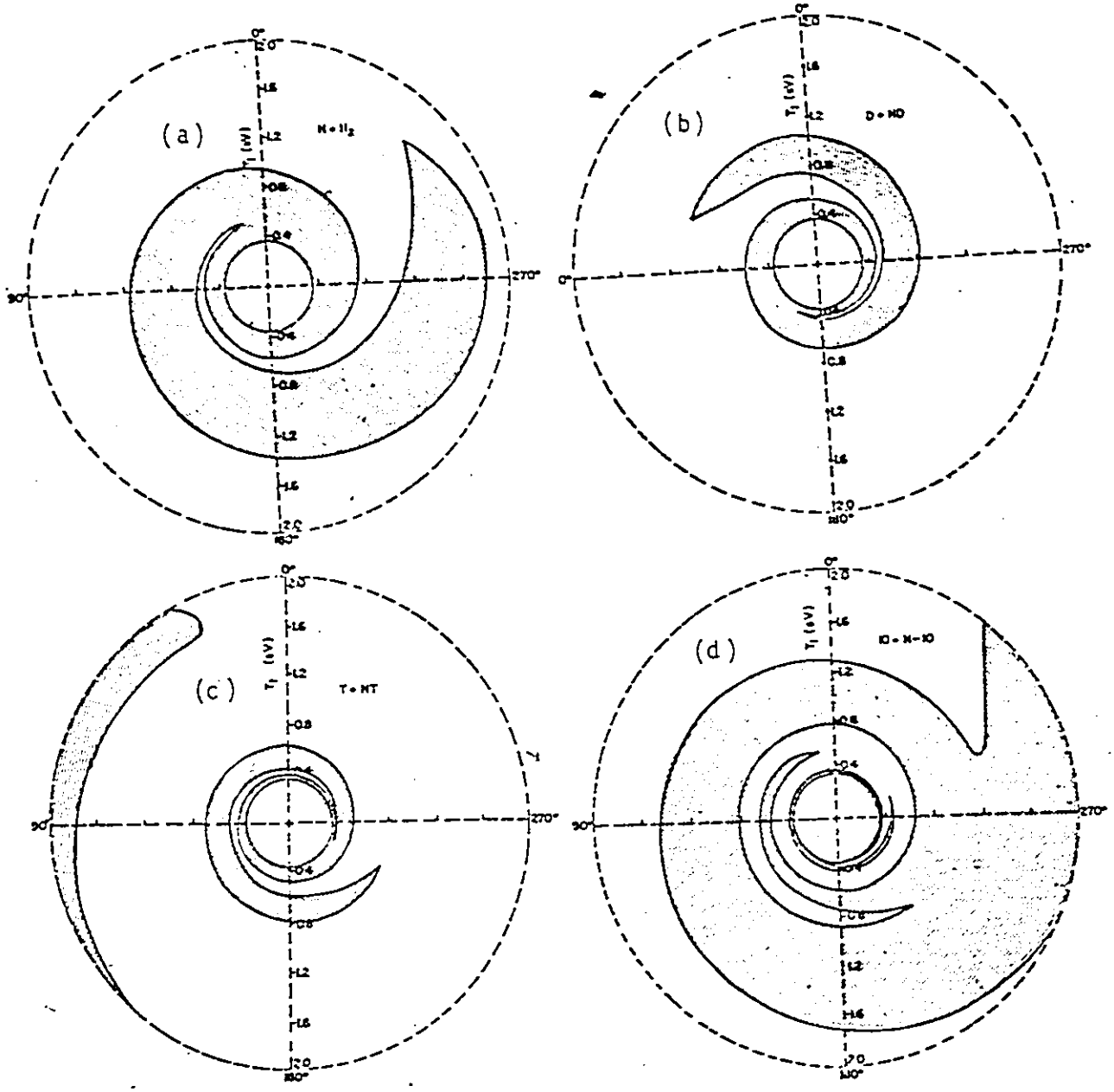
(a)
N + H2
(b)
D + HD
(c)
T + HT
(d)
10 + N-10

method allowed the determination of the reaction probability with an absolutely minimum amount of trajectory calculations. Basically, a complete scan of only four phase angles ($\phi^o = 0^o$, $90^o, 180^o, 270^o$) is sufficient, initially with a resolution of 0.05 eV from 0.3 - 2.0 eV, increasing the resolution near the time peaks until all (R,U) boundaries are defined to within 0.01 eV. A rough ϕ^o vs. T_t^o plot is obtained at this stage. For further refinements, calculations can be concentrated near the suspected locations of the band boundaries at intermediate phase angles ($45^o, 135^o, 225^o, 315^o$), which can usually be predicted to within 0.05 eV, and near the ends of reactive spirals. If the product vibrational energy is to be studied quantitatively, e.g. to determine specific reaction probabilities P_{On}^R or energy distributions (see next section), complete scans at eight phase angles will suffice. In this way, Figs.20-22 were each generated from about 400 data points. Fig.23, with its narrow reactive and unreactive branches, required about twice as many points. The total reaction probability, shown in Figs.20b-23b, is estimated to be known to at least $\pm$ 0.02 probability units. The compression of the bands with increasing mass X also causes the statistical regions to decrease in width.

3.3.3 Product Vibrational-Energy Distributions.

The product vibrational energies are not shown, since they are found to vary in the same way as the reaction times, also in the second reactive regions. In fact, all the generalizations made in Sec.2.6.5 fully apply. No specific reaction probabilities

were calculated, but product vibrational-energy distributions were examined instead. According to the method of Fong and Diestler[51], the fraction of the total energy H, which was converted into product vibrational energy, is defined as

$$f_{vib} = \bar{E}_{vib}/H \tag{56}$$

with

$$\bar{E}_{vib} = N_R^{-1} \sum_i E_n'(i) \tag{57}$$

where $\bar{E}_{vib}$ is the mean product vibrational energy, N_R is the number of reactive trajectories at a given T_t, and $E_n'(i)$ is the product vibrational energy at the i^{th} discrete phase angle. In this case no use of continuity was made, since a single number is sought to characterize $E_n'(i)$, and many graphical interpolations would have to be made to determine E_n' accurately as a function of ϕ^o at many T_t^o. Since continuity of the bands has allowed the use of only eight phase angles at each T_t^o, N_R will be a small number ($0 \leq N_R \leq 8$) and f_{vib} will be a crude measure, so that only trends will be significant. Fig.25 shows a plot of f_{vib} vs. T_t^o for all mass combinations; discontinuous segments represent unreactive regions. In spite of the approximate nature of f_{vib} as measured here, clear trends are evident in the plot:

a. In the first reactive regions, at increasing collision energies, the fraction of total energy channeled into product vibration increases.

b. The f_{vib} curves of the first reactive regions are clearly related to each other by a compression along both axes for heavier mass combinations.

Figure 25

Fraction of total energy which is product vibrational energy (f_{vib}) over the range of T_t^o values. (——) $H+H_2$, (----) D+HD, (·····) T+HT, (·-·-·-) 10+H-10. Discontinuous segments: unreactive.

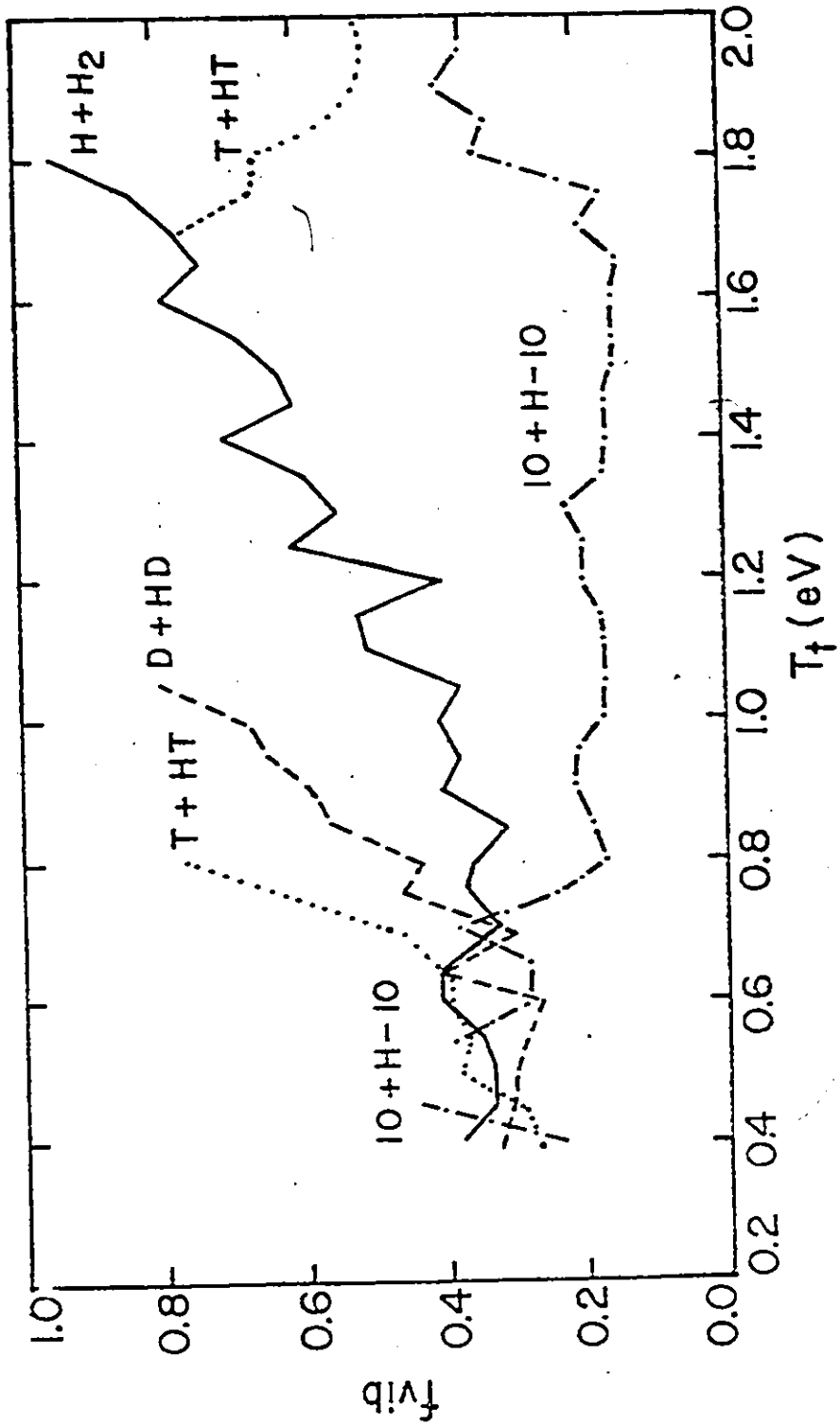
H+H2
T+HT
D+HD
T+HT
IO+H-IO
IO+H-IO
fvib
Tt (eV)
0.0
0.2
0.4
0.6
0.8
1.0
0.2
0.4
0.6
0.8
1.0
1.2
1.4
1.6
1.8
2.0

Figure 26

f_{vib} as a function of T_t^o for $H+H_2$ and $T+HT$, assuming vibrational adiabaticity for all reactive trajectories.

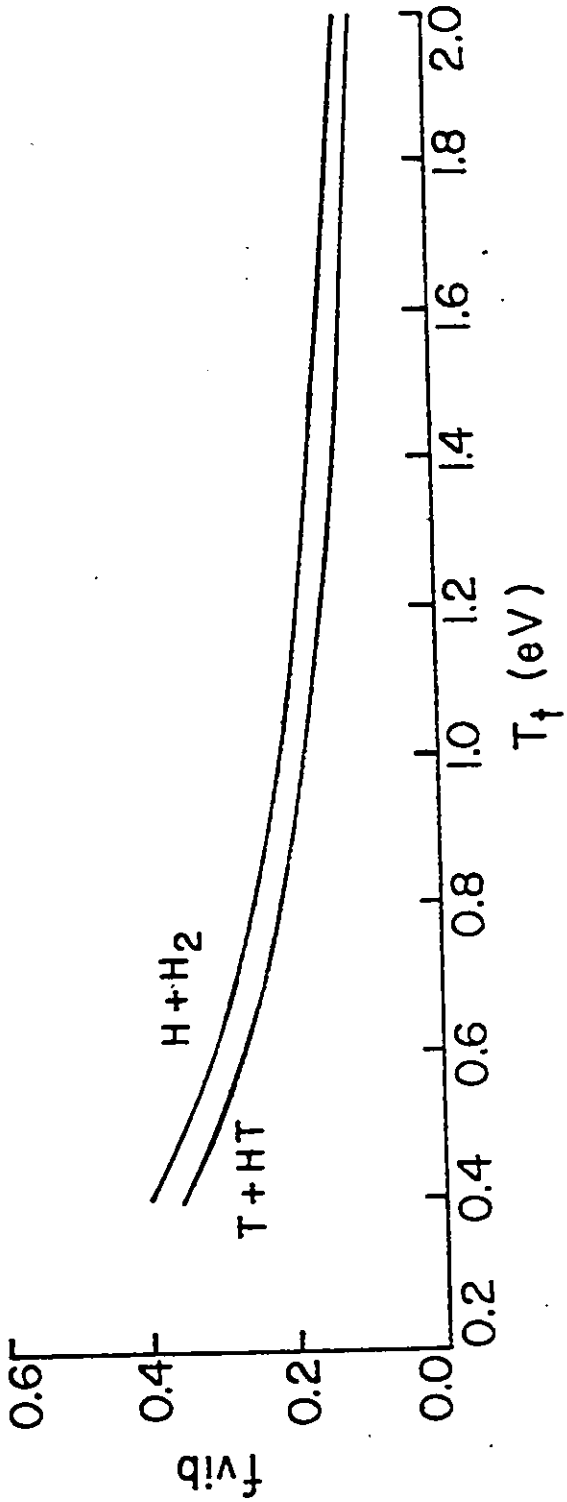
fvib
0.0
0.2
0.4
0.6
0.2
0.4
0.6
0.8
1.0
1.2
1.4
1.6
1.8
2.0
T_t (eV)
H+H2
T+HT

c. In the second reactive regions (T+HT and 10+H-10), f_{vib} initially decreases with increasing T_t^o, and for 10+H-10 it remains relatively constant over a wide range (0.8-1.8 eV), increasing again at high energies.

In analyzing these results account must be taken of the fact that only relative fractions and not absolute values of energies are being considered. If the reactive trajectories were strictly vibrationally adiabatic, with product n = 0 (reactants always start out with ZPE), the appearance of the $f_{vib}^{ad.}$ plot would be as shown in Fig.26 for H+HH and T+HT only. Since the product vibrational energy remains fixed at the ZPE, and the total energy increases ($H = T_t^o + ZPE$), $f_{vib}^{ad.}$ is a smoothly decreasing function of T_t^o. Fig.25 shows that this behavior holds for H+HH and D+HD only for a narrow region above threshold (0.2 eV). This statistical adiabatic behavior has often been observed[11,54,71,81], and is closely associated with the fact that at low energies near the threshold the vibrationally averaged reaction path (VARP, see Sec.2.2) coincides closely with the minimum-energy reaction path (MERP). At higher energies, the behavior mentioned in conclusion a takes over, and it is striking that for H+HH, at energies near the end of the first reactive region, almost complete conversion of excess energy into product vibration is achieved ($f_{vib} \approx$ 0.95). This unusual amount of product excitation was not seen in the study of Fong and Diestler[51], owing to their restriction to a narrower energy range (about 1 eV above threshold for various Wall-Porter type surfaces). Wall and Porter[62], who studied many collinear mass combinations on a variety of surfaces up to 2.2 eV,

report f_{vib} values as high as 0.65 for H+HH with initially vibrationless reactants. The trend observed in conclusion a can be understood from the generalizations made in Sec.2.6.2. At low energies, the VARP coincides closely with the MERP and rounds the bend connecting reactant and product valleys cleanly. On the average, reactant vibrational energy is thus continuously converted into the symmetric stretch of the transition state and into product vibration, without much conversion of translational into vibrational energy. At higher energies, the VARP strikes the steep repulsive wall facing the reactant valley at increasingly perpendicular angles, with larger amounts of excess reactant translational energy converted into product vibration. Further, the product vibrational energy is at a maximum near the band edges, as a consequence of corner-hitting trajectories, which are especially effective in the conversion of reactant energy into product vibration. Towards the ends of the reactive regions, only few reactive trajectories are observed over the whole ϕ^o range, all occurring near a band edge. It is therefore reasonable to assume, that the maximum f_{vib} values at the end of the first reactive regions (see Fig.26) reflect the minimum amount of product translational energy possible. By the principle of microscopic reversibility the absolute minimum of product translational energy should be equal to the reactive threshold for the reverse reaction, i.e. with reactants starting out with E_n'. Wall et al.[37] and Smith and Wood[100] have shown the decrease of the reactive threshold

with increasing reactant vibrational energy. The observations made in conclusion b can then be understood as follows. The contraction of the first reactive regions along the T_t^o axis with heavier mass combinations simply reflects the contraction pattern of the reactivity bands mentioned in the preceding sections. This contraction indicates that the brick wall effect (see Sec.2.6.2) is encountered earlier (at lower T_t^o) for the heavier mass combinations. The light atom B in the middle is more easily pushed towards the end atom C by heavier incoming masses A. The VARP is therefore expected to strike the steep repulsive wall perpendicularly at much lower energies than for the lighter mass combinations (this is also related to the skew angle of the potential-energy surface model). The corresponding decrease in the maximum values for f_{vib} is then related to the cut-off energies and maximum E_n' values for the different cases. For H+HH the cut-off energy is $T_t^{max} < 1.8$ eV, and the products can be excited to the third vibrational level. The threshold for the reverse reaction is expected to be very small[100] $T_t^{thld.}(v=3) < 0.1$ eV. Theoretically, the following maximum values are expected: $E_n' = H - T_t^{thld.}(v=3) > 2.07 - 0.1 = 1.97$ eV and $f_{vib}(max) = E_n'/H > 0.95$. For the other extreme case, 10+H10, the cut-off occurs at 0.45 eV with products still in their lowest vibrational level. Hence, $E_n'(max) = 0.65-0.35 = 0.3$ eV, and $f_{vib}(max) = 0.46$, which was indeed observed. Similarly, the maximum f_{vib} values for D+HD and T+HT are consistent with the excitation of the products to the first vibrational level, and

a threshold for the reverse reaction of $T_t^{thld.}(v=1) \simeq 0.23$ eV. The behavior of f_{vib} in the second reactive regions (conclusion c) can also be understood qualitatively, by associating high product vibrational energy with the band edges, and the beginning and end of the reactive region to few reactive trajectories near a band edge. Thus, the f_{vib} curve for 10+H-10 in Fig.25 shows almost perfect adiabatic behavior in the middle of the second reactive region, and higher values towards the extremities of this region (0.5-0.8 eV and 1.8-2.0 eV). This is consistent with the picture presented in Fig.23a, where the reactive trajectories are, on the average quite far away from the band edges, except where narrow reactive regions are found near 0.6 and 2.0 eV. For T+HT only the beginning of the second reactive region is shown in Fig.25, but again higher f_{vib} is found near the very edge of this region.

3.3.4 The Role of Multiple Collisions.

A more satisfying explanation of the different nature of the second reactive region is provided by an analysis of typical trajectories in various energy regions. Using T+HT as an example, two reactive trajectories are shown in Fig.27. The one shown in Fig.27a is typical of the first reactive region, where similar to the H+HH case, all the reactive trajectories are direct in the sense that they cross the dividing line once only (statistical regions have disappeared because of the contraction pattern). All generalizations of Sec.2.6.2 therefore apply to the first reactive regions. The trajectory in Fig.27a shows a corner-

cutting behavior, and ends up with high product vibration (f_{vib} = 0.63), because the local direction of motion at the crossing point is far from optimum. Fig.27b shows a trajectory typical of the second reactive region, where the dividing line is crossed exactly three times. The complex behavior, where the dividing line is crossed in a normal fashion (first collision), but where the reflection on the steep repulsive wall occurs in a direction towards decreasing r_{BC}, has been observed for H+HH in high energy regions beyond the cut-off, but never to such an extent that the repulsive wall is again hit, within the transition state region, on the reactant side, to result in yet another crossing of the dividing line. As in the discussion of the contraction pattern (conclusion b, preceding section), this phenomenon can be related to the kinematic mass effect and the skew angle of the surface. According to Mahan[68], multiple collisions on a hard sphere potential-energy surface model are predicted to occur when the angle between the coordinate axes is less than 51^{o} ($\xi > 39^{o}$). For H+HH ($\xi = 30^{o}$) this condition is not met, explaining the absence of a second reactive region. D+HD is a marginal case ($\xi = 41.8^{o}$) and, as noted earlier, does show a broad reactive region above 4.45 eV. Multiple collisions are clearly very important for T+HT ($\xi = 45.8^{o}$) and especially for 10+H10 ($\xi = 65.3^{o}$), explaining the complicated banding observed in Fig.23a and 24d.

The trends in product vibrational energy can also be explained in this way. Fig.27b shows why the product of a high-energy multiple collision for T+HT may have low vibrational

Figure 27

(a) Typical direct trajectory for T+HT in the first reactive region.

(b) Typical trajectory for T+HT in the second reactive region, showing a triple crossing of the reactant-product dividing line. The location of the saddle point is indicated by *.

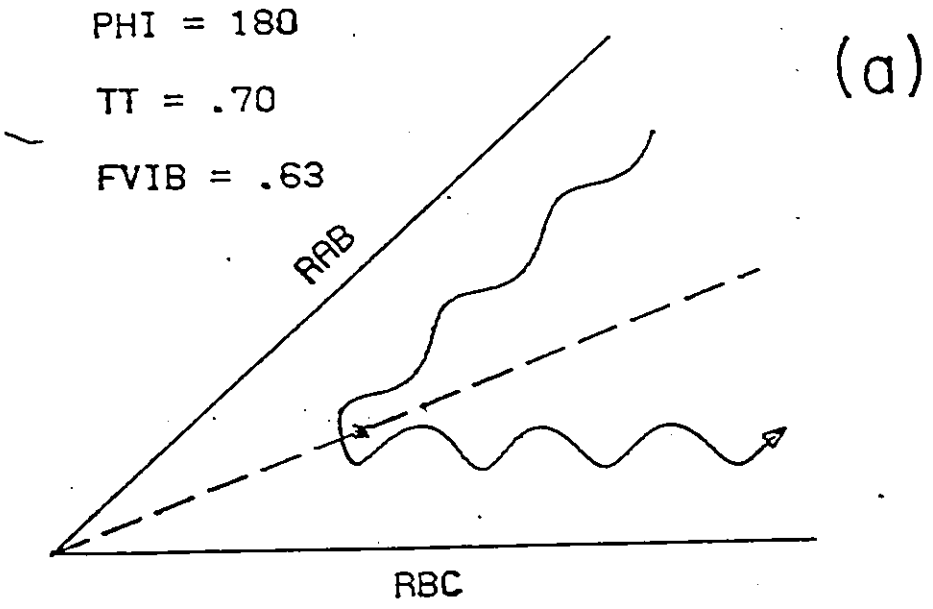

(a)

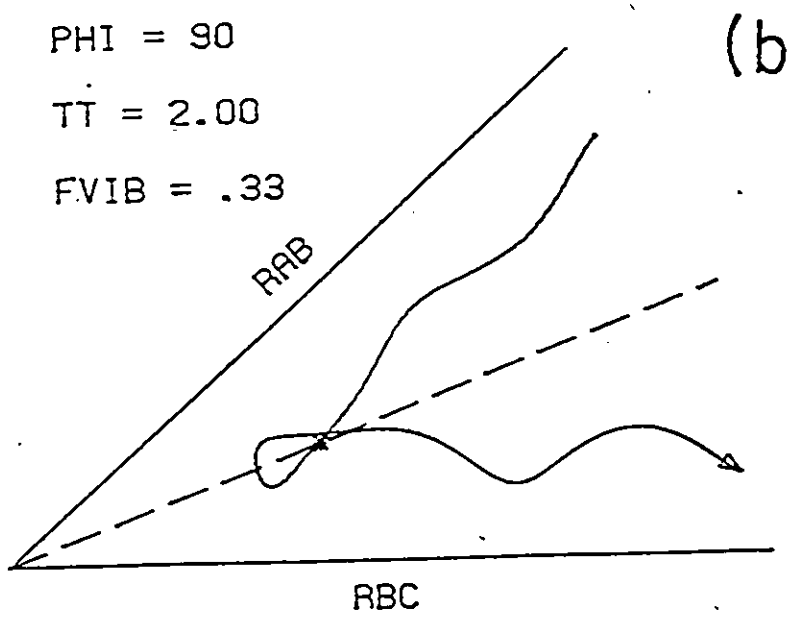

(b)

energy. As the system makes its second rebound and aims towards the product, it is nearly optimally oriented along the product channel, but crosses at a point of high effective vibrational energy (see Sec.2.6.2, and Refs.54,71,81,82), ending up with product vibrational energy in excess of the ZPE. However, since the total energy is quite high (2.22 eV) for this trajectory, f_{vib} assumes a small value(0.33). Towards the edge of the reactive region, the trajectories cross the dividing line at a location and in a direction further away from the optimum, resulting in an increase of f_{vib}. Towards the middle of the second reactive region, the opposite is true, and the trajectories will become nearly symmetrical, explaining the adiabatic behavior observed in Fig.25 for the 10+H-10 case.

3.4 General Discussion.

3.4.1 Band Continuity.

It is significant that although most of the important observations have frequently been mentioned in the literature, the continuity of reactivity bands has never been clearly demonstrated or used to obtain reaction probabilities. Thus, Wall et al.[37] did not clearly establish the existence of the reactivity bands, and their P^R_{OT} curve was obtained by simple numerical averaging of the fraction of reactive trajectories over small energy ranges. Later systematic investigations[48-54] relied on the assumption of strict vibrational adiabaticity outside the reaction shell to generate the initial phase angle

distribution (see Sec.2.5.2). As a consequence ϕ^o was varied at constant T_t^o. The use of action-angle variables in semi-classical studies also leads to this method of variation. Under such conditions a separation into two bands (R,U) is observed for some surfaces and at some energies[51]. This is easily understood from the band plot shown in Fig.14a. At some energies only a single R band is encountered (e.g. at 0.4 eV), at others large statistical regions occur. Most workers[48-54] have noted high values of n at the band edges and have used this feature to determine the location of the band boundaries more precisely. The detection of band continuity, however, eluded them, most probably because of their method of varying ϕ^o at constant T_t^o. Thus, judging from the Figs.1-6 of Ref.53, the curves of the product vibrational energy and the complex lifetime as a function of ϕ^o are of indefinite shape, seldom showing pronounced peaks, and are difficult to correlate at different T_t^o. This is also due to the fact that the ϕ^o range is cyclic ($0 \rightarrow 2\pi$), so that the absolute position of the peaks cannot be determined when different plots (at different T_t^o) are compared. When the final parameters are plotted as a function of T_t^o, as in the present work, a totally different picture is obtained. The many t^R and E_n' peaks are sharp and often have a characteristic, easily recognizable shape. The positions of the peaks are further measured on an absolute scale (T_t^o), and correspond accurately to the locations of the band edges. There can be no ambiguity in arriving at the correct shifting pattern using Figs. 11,12,17-19 to generate the band plots.

3.4.2 The Efficiency of the Method.

As stated in Secs.2.6.4 and 3.3.3, the band continuity has an important practical significance. To give some quantitative estimate of the economies possible by the present approach, a comparison is made to the work of Fong and Diestler[51], which is typical of other systematic quasi-classical studies. These authors show that up to 100 trajectories may be required at one energy to obtain a precision of 1% in the reaction probability. The use of 40 trajectories (20 for a rough grid, 20 for a more precise determination of the break points) led to an estimated error of 2.5-5.0%. An energy grid spaced at 0.02 eV intervals between 0.3 and 2.0 eV (the same range and resolution used in Sec.2.6) would thus require ca. 8500 trajectories to attain a precision in the reaction probability curve comparable to that obtained in the present work from ca. 800 trajectories (8 phase angles, 85 energies, estimated 1.0% precision). Subsequent calculations have shown (see Sec.3.3.3) that for a variety of mass combinations, 400-600 trajectories generally suffice to attain the 2% precision level, except in the case of a highly complicated band structure, where up to 1000 trajectories may be required. It is therefore clear that the systematic determination of R,U bands also has several distinct advantages over the Monte Carlo selection of initial conditions (at least in 1-D calculations):

a. Band boundaries can be efficiently located with the help of the t^R and E_n' peaks and a very predictable shift of these peaks with ϕ^o.

b. Once a rough map has been obtained, calculations can be concentrated near the band boundaries, resulting in a high precision with relatively few trajectories.

c. A total rather than statistical picture is then obtained. Thus, the outcomes of all possible trajectories are known in detail, except in the statistical regions, which are small.

d. With no further trajectory calculations, the results can be converted to different reaction shells and vibrational phase distributions, without losing track of the detailed correspondence between the various initial and final parameters.

e. Such detailed information can further be used, e.g. for semi-classical studies and for the development of simple models to allow further reductions of computational requirements.

f. The total picture obtained extends beyond a single case to other mass combinations. Kinematic mass effects can be understood in terms of different behavior in different energy-regions. Similarly, the influence of surface parameters might be better understood if comparison was made in terms of energy bands rather than probability curves.

3.4.3 Reaction Probabilities.

The results obtained in the present study seem to agree very well with the results of other workers. Thus for $H+H_2$, the only case in which extensive comparisons to calculations on similar surfaces and similar methods can be made, the salient

features of other reaction probability curves are quite well reproduced (see Sec.2.6.5). Of the other reactions studied, only T+HT can be compared to the results of Wall and Porter[62], who observed a slightly higher reaction threshold and a lower cut-off energy relative to the H+HH reaction. These results were obtained with initially non-vibrating reactants, and are quite consistent with the observations made in the present study (see Sec.3.3.3 and Subsection C below). In principle, rate constants can be calculated from the P_{OT}^{R} curves, according to well established methods[43,49,65,88]. However, 1-D rate constants are quite meaningless, unless comparison is made to transition state theory (also in 1-D)[49,88] to determine the convergence of the different methods. For H+HH, this convergence has been often established, also for the higher dimensional cases[38b,65,83,88,99]. The comparison to experimental results would involve a highly questionable extrapolation from 1-D to 3-D.

The emphasis in the discussion of this work will therefore center on a comparison of the gross structure of the probability curves, the effective thresholds for reaction, and the degree of vibrational excitation of the products, to other classical, semi-classical and quantum-mechanical results.

A. Sensitivity to Potential-Energy Surface Parameters.

Wall and Porter[62] first carried out extensive series of classical calculations for collinear $H+H_2$ and isotopic analogues on systematically varied parametric Wall-Porter (WP)[63] surfaces. Of these, the second (WP2) surface comes closest to the SSMK

surface; the next best WP6 surface, with a larger symmetric-stretch force constant, was chosen to investigate the effect of different mass combinations. Their calculations were carried out with vibrationless reactants. They related the bobsled effect to an effective activation energy, which is in excess of the barrier height. The existence of cut-off energies was related to the brick-wall effect. These reactivity bounds were further shown to depend on the surface geometry and the skew angle, as was the product vibrational energy. No indication of long-lived collision complexes was found, and no quantitative correlations were made.

Later, Fong and Diestler[51] performed similar calculations for collinear $H+H_2$, also on a series of WP-type surfaces (FD) for which quantum-mechanical results were also available[101]. Their third surface (FD3) was identical to WP2 with a dissociation energy of 100 kcal/mole and a barrier height of 12.8 kcal/mole. They investigated the variations of the barrier height, the curvature (and position) of the MERP, and the slope and the width of the potential barrier along the MERP, always comparing the results to those of quantum-mechanical calculations. The following conclusions were arrived at:

1. For both the quantum and classical calculations, the effective threshold of reaction is directly related to the barrier height and inversely to its width along the MERP.
2. f_{vib} decreases with increasing barrier height, but depends very weakly on the curvature of the reaction path and on the slope and width of the barrier along the MERP.

3. The agreement between quantum and classical results is generally poor, but is much improved for higher barrier surfaces.
4. Effective classical thresholds are higher than the corresponding quantum-mechanical thresholds.
5. Specific quantum effects (tunneling, oscillations in the probability curves) are not predicted by purely classical calculations.
6. On the average the classical results agree with the quantum results, in the sense that the quantum results oscillate around the classical ones as a function of energy.

In general all these conclusions are substantiated by the work of many others[48-50,52-54,81,83,88]. These generalizations can therefore serve as an aid in making more meaningful comparisons between results obtained with different potential-energy surfaces. Table VII summarizes most of the work done on the H+HH reaction and some of its isotopic analogues (first column). The next entries specify the surfaces used, in terms of the original type and specific modifications; the numbers indicate the barrier heights. The third, subdivided column lists the methods used, including characteristic data for the generation of the initial conditions (ρ^o, J, v, T_t^o,ϕ^o), and the two last columns give the final results and references respectively. Since most of the work has been carried out with surfaces which generally parallel each other, but which differ in barrier height, conclusion 1 allows a simple shift of the probability curves along the energy axis to compensate

Table VII. Summary of Relevant Studies.

System:	Surface: (E_a/eV)	Details of Calculations: method:	ρ^o/Å	T_t^o/eV	E_v^o/eV	$F(\phi^o)$	Results reported:	Ref.
1-D, H+HH	LEP (0.48)	C,QC,systematic	r_{AC}=5.0	0-0.7	0,0.27, 0.81	?	t^R, P_{OT}^R	37
1-D, H+HH, T+DH, T+HD, H+TH, T+HT.	LEPS/WP (0.61)	C, systematic	r_{AB}=2.5	0-2.2	0	-	$T_t^{thld.}$, f_{vib}, T_t^{max}.	62
3-D H+HH, T+HH, D+HH.	LEPS/PK (0.40)	QC, Monte Carlo	$R_{A,BC}$= 4.233	0-1.35	0.27	uniform.	S^R(J=0-5), P^R, k.	65
1-D, H+HH, D+DD, D+HH, H+DD.	LEPS/W (0.367)	QM,QC systematic	$R_{A,BC}$= 8.0	0-0.5	0.27	uniform	P_{OT}^R, k.	49
1-D, H+HH.	LEPS/WP 0,0.28, 0.56.	QM,QC, systematic	$R_{A,BC}$= 2.4	0-1.0	0.27	uniform.	P_{OT}^R, f_{vib}.	51
1-D, H+HH.	LEPS/W 0.367	QC, systematic	r_{AB}=5.0	0-1.2	0.27	C,QM, harmonic	P_{OT}^R	48

continued.....

Table VII. (continued).

System:	Surface: (E_a/eV)	Details of Calculations: method:	$\rho^o/\mathring{A}$	T_t^o/eV	E_v^o/eV	$F(\phi^o)$	Results reported:	Ref.
1-D, H+H_2.	PK/SSMK (0.424)	QC,SC, systematic	$R_{A,BC}$= 2.43	0-1.3	0.27, 0.785	uniform	P_{ij}^R, k.	52
1-D, H+HH.	WP (0.56)	QC,SC, systematic	$R_{A,BC}$= 2.4	0-1.0	0.27	uniform	P_{ij}^R final parameters	53
1-D, 2-D, H+HH,	PK (0.4)	QC (VA), systematic	$R_{A,BC}$= 2.4	0-1.0	0.27	harmonic	P_{OT}^R, final parameters	54
1-D, H+HH, D+HD, T+HT, 10+H10.	SSMK (0.477)	QC, systematic	$R_{A,BC}$= 5.37, 3.87.	0-2.0	0.27	double harmonic	P_{OT}^R, P_{Oi}^R, final parameters.	present work

C = Classical;
QC = Quasi-Classical;
QM = Quantum-Mechanical
VA = Vibrational Adiabaticity Assumption.

LEP = London-Eyring-Polanyi;
LEPS = LEP-Sato;
WP = Wall-Porter;
PK = Porter-Karplus;
W = Weston

P_{ij}^R = reaction probability (i j); S^R = reaction cross section; k = rate constant.

for this difference. Conclusion 2 could not be properly evaluated in the present work, but the results shown in Figs.14b and 16b are certainly in good agreement with conclusions 3 to 6. The higher reactivity obtained for the SSMK surface compared to the quasi-classical results of Bowman and Kuppermann[52] can be explained by the assumption that when the barrier is lowered to the scaled SSMK surface[38b,52,88], the reaction channel is also made narrower, so that the system would have more difficulty rounding the bend to the product side.

Fig.28a shows the same QC_{SSMK} curve of Fig.14b, compared to the results obtained by Careless and Hyatt[48] on an LEPS type surface, and by Fong and Diestler[51] on the WP2 (FD3) surface. The latter results (dashed and dotted lines) have been shifted along the T_t^o axis to reflect the differing barrier heights of 8.44 and 12.8 kcal/mole. The LEPS and SSMK results agree well, but now the WP surface is seen to be too reactive. This is again related to the fact that the WP surface has a wider reaction channel, as indicated by a lower force constant of the symmetric stretch. The oscillation in the LEPS curve reflects the choice of a classical harmonic phase distribution. A similar effect was obtained for the SSMK surface as shown in Fig.28b. The harmonic curve in this figure (dotted line) was obtained by rescaling the ϕ^o axis of the band plots to a single linear scale, and seems to fit the quantum curve[52] (dashed line) in a better way. Careless and Hyatt[48] also showed that the use of a quantum distribution function can lead to an even more oscillatory behavior of the

Figure 28

(a) Comparison of quasiclassical reaction probabilities P_{OT}^{R} on different surfaces: WP = Wall-Porter surface #2 = Fong-Diestler surface #3[51]; LEPS = Weston's surface[48].
(b) The effect of vibrational distribution function on P_{OT}^{R}.

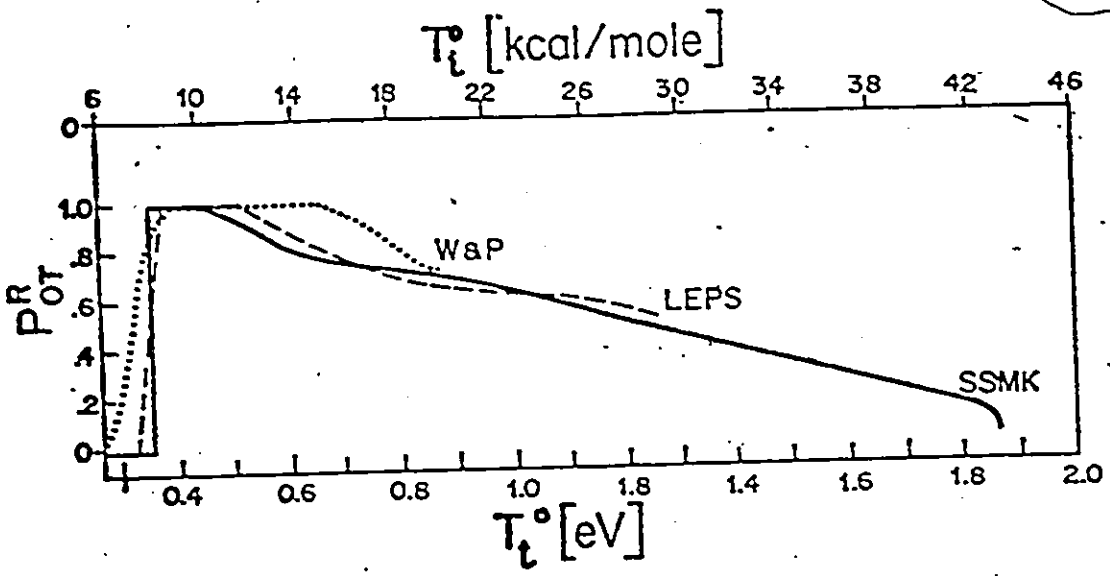
T_t° [kcal/mole]
6 10 14 18 22 26 30 34 38 42 46
0 1.0 .8 .6 .4 .2 0
P_{OT}^R
W&P
LEPS
SSMK
0.4 0.6 0.8 1.0 1.8 1.4 1.6 1.8 2.0
T_t° [eV]

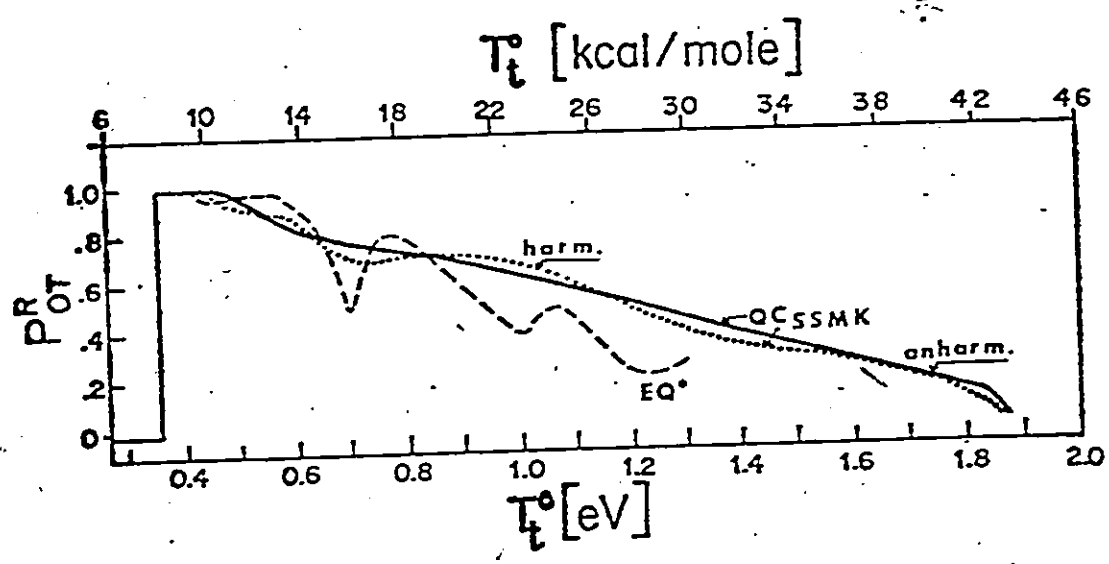
T_t° [kcal/mole]
6 10 14 18 22 26 30 34 38 42 46
1.0 .8 .6 .4 .2 0
P_{OT}^R
harm.
QCSSMK
anharm.
EQ°
0.4 0.6 0.8 1.0 1.2 1.4 1.6 1.8 2.0
T_t° [eV]

probability curves. However, Bowman et al.[98] proved that only the classical anharmonic distribution function is (correctly) independent of the choice of the reaction shell and therefore the only physically acceptable one. The present work has confirmed this, and has also shown that the improper choice of the reaction shell also introduces artificial oscillations in the probability curve (see Fig.13b).

The geometry of the potential-energy surface can also be changed in a systematic way by varying the mass combinations. The variation of total reactivity with the skew angle can qualitatively be understood[62,100], in that as the coordinate axes approach each other, the system should have more difficulty rounding the sharp bend at the saddle point to reach the product valley. At the same time,however, a different reaction mechanism becomes increasingly possible, in which the system uses the sharp corner to cross the transition state in a complex way (multiple collisions). Fortunately, the present investigation has shown that the regions in which these different mechanisms take place are distinctly separated from each other by an energy range where the reaction probability is zero. It was thus possible to study the influence of the skew angle on the reaction probability in an uncomplicated way. The first reactive region, where direct reaction takes place, is seen to decrease in size with increasing mass X, as was predicted by Wall and Porter[62]. This contraction was shown to occur in a very regular and predictable manner, characteristic features of dynamic behavior, reactivity bands and probability curves being completely retained in the process. The second reactive region,

where multiple collisions occur, also shows a quite regular behavior with increasing mass combination, but seems definitely more complicated than the first reactive region. Thus, it seems to grow in size from D+HD to T+HT, but shows a high-energy cut-off for 10+H10. At the same time it consistently shifts towards lower energy regions with increasing mass X, being barely visible for T+HT below 2.0 eV, but dominating the total reactivity for 10+H10, which now becomes the most reactive of all the systems studied in this energy range. The possibility of multiple collisions has been correctly predicted by Mahan[68] on the basis of a hard-sphere potential-energy surface model, and the work of Smith and Wood[100] suggests that it is enhanced by the availability of higher reactant vibrational energy, so that a similar second reactive region can be expected for $H+H_2$ ($v \geq 1$). The main significance of these findings is that it has shown that the potential-energy surface model is quite capable of taking kinematic effects into account, and that potentially very interesting systems can be found for experimental studies, by simple extrapolation of the results of this investigation. However, the persistence of the bands and their effects on the reaction probability are by no means certain for the more realistic higher dimensional cases, and must yet be completely investigated.

B. Oscillations in the Quantum Results.

The important differences between classical and quantum reaction probability curves are mainly centered around the reaction thresholds ("tunneling") and the thresholds for the vibrational excitation of the products[52,81,83,88] (resonances).

Tunneling is generally defined as quantum mechanical leakage through a potential energy barrier, caused by finite values for the quantum mechanical wave function beyond classically allowed limits. Wu and Levine[81] show that tunneling in this sense does not occur to a significant extent. Quantum-mechanical reaction thresholds are generally observed at energies in excess of the barrier height, although significantly lower than the corresponding classical thresholds. They attribute this difference to purely dynamical effects, caused by quantum-mechanically forbidden transfers of translational energy vibrational mode in the transition state region, making less energy available (classically) to cross the barrier. On the other hand, semi-classical studies generally account for tunneling corrections by taking into account classically forbidden processes, by means of complex valued classical trajectories[102]. The treatment by Truhlar and Kuppermann[103] further shows that the calculations of tunneling corrections normally applied to transition state theory results are not very reliable, and that exact calculations in higher dimensions (taking into account the curvature of the reaction path, the bending energy of the activated complex and the change of the vibrational potential along the MERP) are as yet impossible to achieve. In view of these results, the most reliable method to account for dynamical tunneling (i.e. in the sense of dynamically forbidden processes) seems to be the semi-classical method[102], which successfully relates quasi-classical results to quantum-mechanical ones.

Semi-classical studies not only provide good results in accounting for essentially all quantum effects, on the basis of purely classical considerations, but also provide a better understanding of the origin and significance of the differences between classical and quantum mechanics. In Miller's[56] and Marcus's[57] theories interferences of real and complex valued classical trajectories which are "stationary" (exactly fulfill quantum mechanical boundary conditions) are considered to give rise to these quantum effects. The oscillations in the probability curves were interpreted in terms of the formation of quasi-bound states (complexes of short lifetimes)[19,20,52,53,81,83-85], which in analogy to nuclear physics, were thought to give rise to resonances, a term meaning enhanced (or reduced) reactivity over narrow ranges of incident energy. Classically, such collision complexes were observed to be formed in statistical regions[53,70] and an important contribution by Stine and Marcus[83] showed that interferences of such complex trajectories with the normally observed stationary trajectories (direct trajectories), can account for the observed oscillations in quantum mechanical probability curves. These examples illustrate how reliable results incorporating important quantum effects can be obtained via the more accessible method of classical trajectory calculations, if a complete and detailed picture of the classical results in all ϕ^o, T_t^o space is available. The present method provides such information in an optimal way, by making use of the band continuity property. The results obtained indicate that the behavior of the statistical regions can also be treated on a more accurate and detailed basis,

by making use of the band continuity property on a more microscopic scale (see Sec.2.6.3), so that the results of the present study can directly be extended to semi-classical investigations without many more computational requirements.

C. The Reaction Threshold.

The reaction probability at the threshold in all cases was observed (see Figs.20b-23b) to approximate the classical "step function" behavior, predicted by Karplus et al.[65] for reactions restricted to small impact parameters (extreme case: collinear collisions where the impact parameter is zero). Fong and Diestler[51] showed that the shape of the probability curve is dependent on the barrier height, and its shape along the MERP. A steep rise to a value of 1.0, as observed in the present studies, was predicted for a barrier of medium height and gentle slope along the reaction path, characteristic for the SSMK surface. Mortensen[49] further observes that the closer the masses of the reactant atom and molecule, the steeper the classical probability curve rises at the threshold. Wall and Porter note for vibrationless reactants[62] the increase of the threshold with increasing skew angle, but Smith and Wood[100] observe the opposite effect for reactants with v=1,2. All these and many more qualitative generalizations can be understood from a consideration of the potential-energy surface model and the roles of vibrational and translational energies in the crossing of the barrier.

First, vibrationless trajectories are considered at low translational energies near the threshold. They travel along

the VARP which closely coincides with the MERP. The results of Wall and Porter[62] show that even at the threshold a bobsled effect is detected, so that the effective threshold is higher than the barrier. It is further remarkable that the smallest deviations from the MERP (lowest thresholds) are observed for surfaces which resemble the SSMK surface most (WP2 and WP6). The bobsled effect has been related to a centrifugal potential[54, 71,81,82] which is dependent on the curvature of the reaction path. It is therefore no surprise that the heavier mass combinations, associated with larger skew angles and larger curvatures of the reaction path, give rise to higher thresholds, when no reactant vibration is available.

Now reactants having ZPE are considered on a surface with a gradual slope along the MERP, such as the SSMK surface. A typical threshold trajectory (Fig.7a) shows that in order to cross to the product side, the VARP does not have to reach the dividing line itself. Rather it has to reach a point at which subsequent vibrational motion can bring the system over the ridge along the dividing line, quite far from the actual saddle point. On a gradual sloping barrier, trajectories within a narrow energy region will spend a long time in just the right location along the reaction path for such an optimum crossing to take place. This is because they gradually lose their translational energy, so that their motion near the zenith along the MERP is extremely slow. It is therefore not surprising that the probability curve rises so abruptly at the threshold for the SSMK surface, and that an even steeper rise is expected for heavier mass combinations

whose translational motion is slowed down much more than their vibrational motion, because of the different reduced masses for translation ($\mu_{A,BC}$) and vibration (μ_{BC}).

Finally, attention should be focussed on the constancy of the threshold energy for all the mass combinations (Sec.3.3.2). A qualitative explanation of this invariance can be given in terms of skewed coordinates as in the discussion by Smith and Wood[100]: The skew angle for the r_{AB},r_{BC} coordinate axes range from 30^o for H+HH to 65.3^o for 10+H-10. The effectiveness of the ZPE in promoting reaction becomes greater as the skew angle ξ increases, since then the momentum vector of vibrational energy becomes more parallel to the direction of optimum crossing of the saddle point. In Fig.29 the reactant vibrational momentum p_o is resolved into components along the symmetric and asymmetric stretch at the saddle point. It is seen that with increasing ξ more of the ZPE becomes available for motion along p_A, which is effective in bringing the system over the barrier:

$$p_A = p_o \cos(45^o - \tfrac{1}{2}\xi). \tag{58}$$

Since the vectors p_i are proportional to the square roots of the corresponding energies, the fraction of reactant vibrational energy contributing to motion across the barrier must be

$$E_{eff} = E_v^o \cos^2(45^o - \tfrac{1}{2}\xi). \tag{59}$$

Table VIII shows that the values for E_{eff} are indeed nearly constant for different mass combinations, despite the large differences in ZPE, as larger fractions of E_o become available.

Figure 29

The contribution of initial vibrational momentum (p_o) to motion along the asymmetric stretch (p_A).

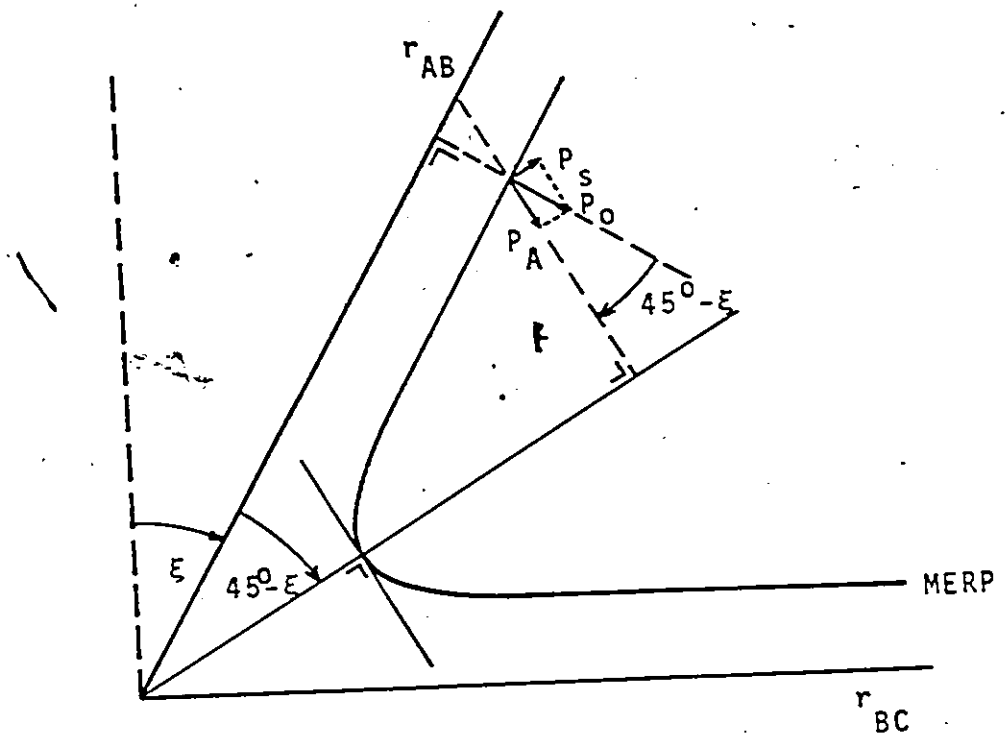
r_{AB}
P_s
P_o
P_A
$45^o-\xi$
ξ
$45^o-\xi$
MERP
r_{BC}

Table VIII. Effective vibrational energies.

	Skew angle	ZPE/eV	E_{eff}/eV cf.eq.(59)	$(T_t^{thld.} + E_{eff.})$ / eV
H+HH	30^o	0.2686	0.2015	0.5485
D+HD	41.8^o	0.2331	0.1942	0.5442
T+HT	48.5^o	0.2200	0.1924	0.5424
10+H10	65.3^o	0.2000	0.1909	0.5400

3.4.4 Significance of the Collinear Studies

The most important aspect of the study has been the development of the method and the attempts to interpret many old and new observations with the help of additional information yielded by the method. Thus, a better insight has been gained into many aspects of dynamical behavior on potential-energy surfaces, especially on the relationship between various initial and final trajectory parameters. A very consistent picture has emerged and many useful generalizations have been made.

The method has opened up new territory, which can be further explored in a number of ways. Investigations on other symmetric and unsymmetric analogues of the H+HH reaction have been carried out[104] in 1-D. Such studies can lead to a better evaluation of the results, conclusions and generalizations obtained in the present work. The suitability of the method in connection with semi-classical studies has also been mentioned.

For comparison to experimental results and to obtain chemically more significant information, however, the usefulness of the present approach in higher dimensional studies must first be established. It is possible that in a higher dimensionality the banding effects in reactivity will completely disappear, or that no simple correlation of initial and final parameters is possible because of the additional degrees of freedom.

As should be clear from the previous discussions, an important emphasis in this work, aside from developing an alternative to Monte Carlo methods and understanding the dynamics of collisions, is to develop more reliable predictive faculties.

CHAPTER 4:- COPLANAR CALCULATIONS

4.1. Introduction.

The extension of the study from linear to planar collisions brings it much closer to reality, since rotational motions and off-center collisions can then be accounted for. Trajectory calculations have been extended to higher dimensionalities by Karplus, Porter and Sharma[65], who obtained the first theoretical 3-D cross sections for $H+H_2$ and some of its isotopic variations. Since the extension involves an extremely large increase of computational work with every additional degree of freedom, the only practical method has been the random sampling of initial conditions. Polanyi and coworkers[45-47] have carried out extensive higher-dimensional calculations on a wide variety of reactions and diagnostic potential-energy surfaces. Most often a semi-systematical method was used[45], in which some parameters were varied systematically according to the random distributions expected under 2-D or 3-D conditions. Some Monte Carlo studies were also carried out, modified by "stratified and importance sampling"[46] techniques.

The present investigation examines the possibilities of extending the systematic method developed for some collinear X+HX reactions (Chapters 2 and 3), to coplanar systems. It was of interest to determine the band continuity property as a function of additional 2-D parameters and to examine to what extent the band behavior would influence the shape of reactive

cross sections. It is quite possible that many of the earlier generalizations will have to be modified in 2-D. The results of Karplus et al.[65] do not indicate any banding effects in the reactive cross sections. Pattengill and Polanyi[93] note that multiple collisions for Heavy + Light-Heavy mass combinations are of lesser importance in 3-D, and White and Thompson[95] show that rotational motion is responsible for these secondary encounters. An important contribution by Malcolme-Lawes[99] also shows that at high energies the lateral attack of the molecule can become more effective than an axial approach. With the present study, a better understanding of these phenomena is again sought. By following the outcome of every individual trajectory as a function of each initial parameter, the cause of the observed behavior might become clearer.

4.2. Description of the System.

The relative or center-of-mass coordinate system used by Karplus et al.[65] and their definition of initial and final parameters are particularly convenient for the treatment of higher dimensional collisions. The coplanar A+BC system is restricted to lie on the (x,y) plane, with $\overline{BC}$ (center-of-mass of BC) at the origin and the translational momentum vector p_t initially parallel to the positive direction of the y-axis. This is shown in Fig.30, where the directions of the positive vibrational (p_v) and rotational momenta (p_r) are also defined. Initially A is located on the reaction shell ($R^o_{A,BC} = \rho^o$).

Figure 30

The 2-D coordinate system, in which the positive directions of rotation (p_r), vibration (p_v), orientation (θ) and of the impact parameter (b) are indicated. The direction of the generalized coordinate vectors are also defined, as well as the scattering quadrants (γ). The angle η is a measure of collinearity, not employed in the definition of the system, but useful in the analysis of the results.

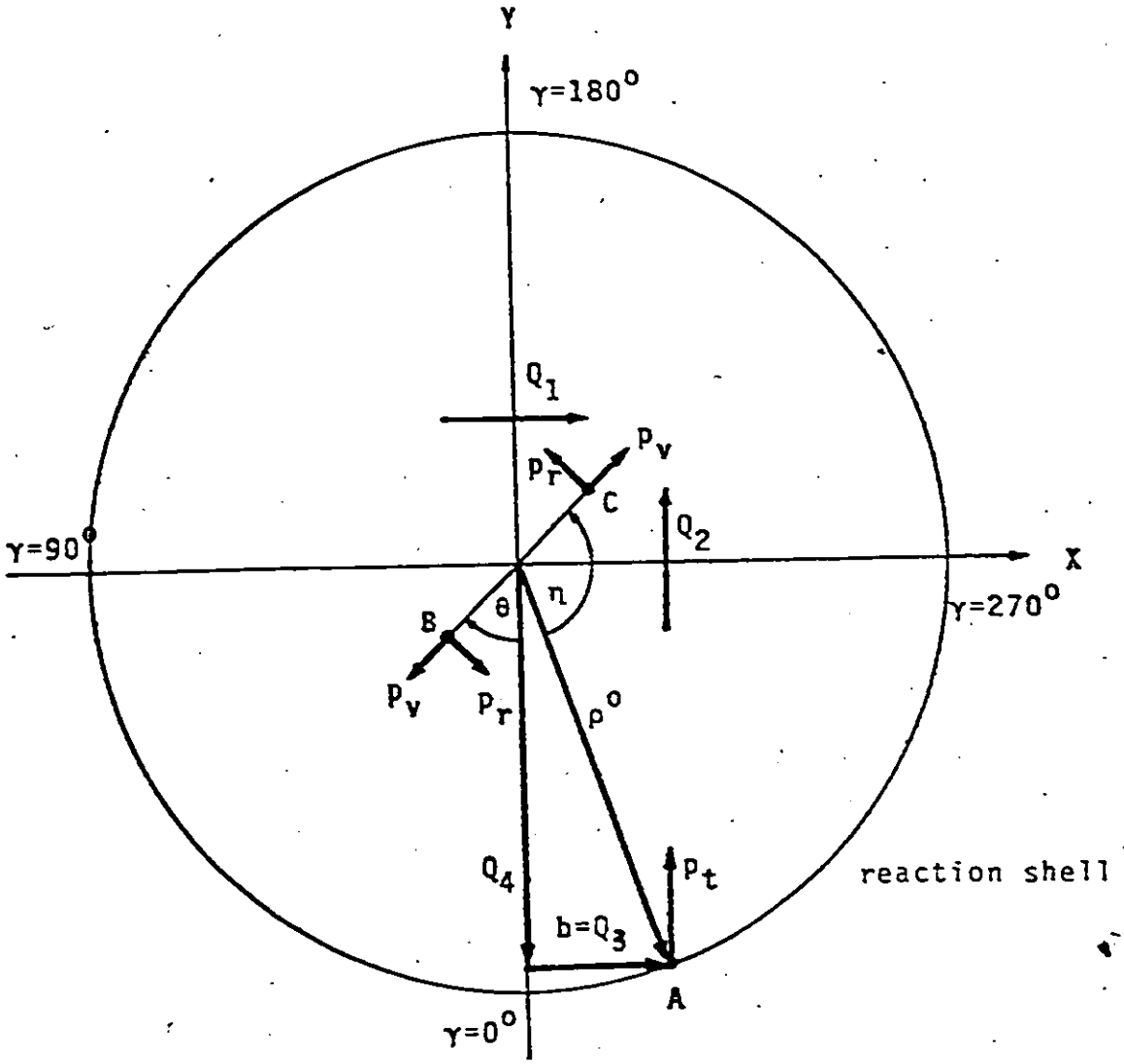
Y
γ=180°
Q1
pv
pr
C
Q2
γ=90°
X
η
θ
B
γ=270°
pv
pr
ρ°
Q4
pt
reaction shell
b=Q3
A
γ=0°

Two additional positional parameters complete the description of the system. These are the impact parameter (b) and the orientation angle (θ), the positive directions of which are also indicated in Fig.30.

The generalized coordinates are so chosen as to make a mobile of the system[63,68], i.e. as the components of $R_{A,BC}$ and r_{BC} along the x and y directions:

$$\left.\begin{aligned} Q_1 &= x_C - x_B \\ Q_2 &= y_C - y_B \end{aligned}\right\} \qquad (60)$$

$$\left.\begin{aligned} Q_3 &= x_A - (m_B x_B + m_C x_C)/(m_B + m_C) = x_A \\ Q_4 &= y_A - (m_B y_B + m_C y_C)/(m_B + m_C) = y_A \end{aligned}\right\} \qquad (61)$$

where the reduction of (61) reflects the choice of $\overline{BC}$ as the origin of the Cartesian coordinate system. It is further more convenient to carry out the derivation of the equations in terms of positional vectors, defining:

$$\begin{aligned} r_{ij} &= \left[(x_j - x_i)^2 + (y_j - y_i)^2\right]^{\frac{1}{2}} \\ &= (x_{ij}^2 + y_{ij}^2)^{\frac{1}{2}} \quad ; (i,j = A,B,C) \end{aligned} \qquad (62)$$

Since x and y are orthogonal, the equations in terms of x_{ij} and y_{ij} will have exactly the same form as the ones derived for r_{ij}. Thus,

$$r_{BC} = (Q_1^2 + Q_2^2)^{\frac{1}{2}} \qquad (63)$$

$$R_{A,BC} = r_{AB} + \frac{m_C}{m_B + m_C} r_{BC} = (Q_3^2 + Q_4^2)^{\frac{1}{2}} \qquad (64)$$

As shown in Sec.2.2 and Ref.65, the equations of motion are then obtained in a particularly simple form:

$$\left.\begin{aligned} p_t &= p_{A,BC} = \mu_{A,BC}\dot{R}_{A,BC} \\ p_{int} &= p_{BC} = \mu_{BC}\dot{r}_{BC} \\ T &= T_t + T_{int} = \tfrac{1}{2}p^2_{A,BC}/\mu_{A,BC} + \tfrac{1}{2}p^2_{BC}/\mu_{BC} \end{aligned}\right\} \quad (65)$$

For higher dimensional cases, the potential-energy hypersurface is usually a function of the interatomic distances, i.e. $V = V(r_{AB}, r_{BC}, r_{AC})$. The time derivatives of the conjugate momenta must therefore be obtained as

$$\dot{p}_{A,BC} = -\frac{\partial V}{\partial R_{A,BC}} \quad (66)$$
$$= -\frac{\partial V}{\partial r_{AB}}\frac{\partial r_{AB}}{\partial R_{A,BC}} + \frac{\partial V}{\partial r_{BC}}\frac{\partial r_{BC}}{\partial R_{A,BC}} + \frac{\partial V}{\partial r_{AC}}\frac{\partial r_{AC}}{\partial R_{A,BC}}$$

and

$$\dot{p}_{BC} = -\frac{\partial V}{\partial r_{BC}} \quad (67)$$
$$= -\frac{\partial V}{\partial r_{AB}}\frac{\partial r_{AB}}{\partial r_{BC}} + \frac{\partial V}{\partial r_{BC}} + \frac{\partial V}{\partial r_{AC}}\frac{\partial r_{AC}}{\partial r_{BC}}$$

To evaluate these relationships, eqs.(60) and (61) are used together with (62), to obtain:

$$r_{AB} = \{(\frac{m_C}{m_B+m_C}Q_1 + Q_3)^2 + (\frac{m_C}{m_B+m_C}Q_2 + Q_4)^2\}^{\frac{1}{2}} \quad (68)$$

$$r_{AC} = \{(\frac{m_C}{m_B+m_C}Q_1 - Q_3)^2 + (\frac{m_C}{m_B+m_C}Q_2 - Q_4)^2\}^{\frac{1}{2}} \quad (69)$$

and together with (63):

$$\left.\begin{aligned}
\frac{\partial r_{AB}}{\partial Q_i} &= \frac{m_C}{m_B+m_C}\left(\frac{m_C}{m_B+m_C}\,Q_i + Q_{i+2}\right)/r_{AB} \\
\frac{\partial r_{BC}}{\partial Q_i} &= Q_i/r_{BC} \\
\frac{\partial r_{AC}}{\partial Q_i} &= \frac{m_B}{m_B+m_C}\left(\frac{m_B}{m_B+m_C}\,Q_i - Q_{i+2}\right)/r_{AC}
\end{aligned}\right\} \quad (70)$$

$$(i=1,2)$$

$$\left.\begin{aligned}
\frac{\partial r_{AB}}{\partial Q_i} &= \left(\frac{m_C}{m_B+m_C}\,Q_{i-2} + Q_i\right)/r_{AB} \\
\frac{\partial r_{BC}}{\partial Q_i} &= 0 \\
\frac{\partial r_{AC}}{\partial Q_i} &= \left(\frac{m_C}{m_B+m_C}\,Q_{i-2} - Q_i\right)/r_{AC}
\end{aligned}\right\} \quad (71)$$

$$(i=3,4)$$

In terms of the generalized coordinates and momenta, i.e. the components of r_{BC} and $R_{A,BC}$ along the x and y axes, the necessary set of Hamilton's equations of motion is thus:

$$\left.\begin{aligned}
H &= T + V(r_{AB}, r_{BC}, r_{AC}) \\
T &= T_t + T_{int} \\
&= \tfrac{1}{2}(P_3^2 + P_4^2)/\mu_{A,BC} + \tfrac{1}{2}(P_1^2 + P_2^2)/\mu_{BC}
\end{aligned}\right\} \quad (72)$$

$$\left.\begin{aligned}
\dot{Q}_i &= P_i/\mu_{BC} \;;\; (i=1,2) \\
\dot{Q}_i &= P_i/\mu_{A,BC} \;;\; (1=3,4)
\end{aligned}\right\} \quad (73)$$

$$\left.\begin{aligned}
\dot{P}_i &= -\left(\frac{\partial V}{\partial r_{AB}}\frac{\partial r_{AB}}{\partial Q_i} + \frac{\partial V}{\partial r_{BC}}\frac{\partial r_{BC}}{\partial Q_i} + \frac{\partial V}{\partial r_{AC}}\frac{\partial r_{AC}}{\partial Q_i}\right); \quad (i=1,2) \\
\dot{P}_i &= -\left(\frac{\partial V}{\partial r_{AB}}\frac{\partial r_{AB}}{\partial Q_i} + \frac{\partial V}{\partial r_{AC}}\frac{\partial r_{AC}}{\partial Q_i}\right); \quad (i=3,4)
\end{aligned}\right\} \quad (74)$$

The integration of eqs.(73) and (74) will then yield coplanar

trajectories which automatically satisfy the boundary conditions of the conservation of total energy and total angular momentum. The total angular momentum (ω_T) is the sum of the internal (ω_{int}) and orbital angular momenta (ω_{orb}), which initially have the values:

$$\omega_T = \omega_{int} + \omega_{orb} = p_r r_{BC} + p_t b. \qquad (75)$$

The coplanar A+BC reaction can produce four different product configurations (a-d), characterized by the reaction channel $\chi=0-\pi$, and different coordinates and momenta for different modes of motion, as shown in Fig.31. At the end of every trajectory, the internal energy of the two particle-system having the shortest interatomic distance r_{ij} is determined from an extension of eq.(65):

$$E'_{int} = \tfrac{1}{2}\mu_{ij}\dot{r}_{ij}^2 \quad ; \ (r_{ij} < r_{ik}, r_{jk}) \qquad (76)$$

For product configurations a (no reaction) and d (dissociation), the original set of generalized coordinates and momenta (R_a, r_a, P_a, p_a) can be used to evaluate the final parameters. Otherwise, a transformation to the appropriate coordinates is similar to the one given by Rankin and Miller[70]:

$$\left.\begin{aligned} \begin{pmatrix} R_b \\ r_b \end{pmatrix} &= \begin{pmatrix} -\dfrac{m_A}{m_A+m_C} & -\dfrac{m_C M}{(m_A+m_B)(m_B+m_C)} \\ -1 & \dfrac{m_B}{m_B+m_C} \end{pmatrix} \begin{pmatrix} R_a \\ r_a \end{pmatrix} \\ \begin{pmatrix} R_c \\ r_c \end{pmatrix} &= \begin{pmatrix} -\dfrac{m_A}{m_A+m_B} & \dfrac{m_B M}{(m_A+m_C)(m_B+m_C)} \\ 1 & \dfrac{m_C}{m_B+m_C} \end{pmatrix} \begin{pmatrix} R_a \\ r_a \end{pmatrix} \end{aligned}\right\} \qquad (77)$$

Figure 31

Possible product configurations in coplanar reactions, and the corresponding coordinates.

i	Configuration:	Conditions:	X	R_i	$P_i = P_t$	r_i	$p_i = p_{int}$
a	A + B-C	$r_{BC}<r_{AB}, r_{AC}$ $E_{BC} < D_e$	0	$R_{A,BC}$	$P_{A,BC}=\mu_{A,BC}\dot{R}_{A,BC}$	r_{BC}	$p_{BC}=\mu_{BC}\dot{r}_{BC}$
b	A-C + B	$r_{AC}<r_{AB}, r_{BC}$ $E_{AC} < D_e$	2	$R_{AC,B}$	$P_{AC,B}=\mu_{AC,B}\dot{R}_{AC,B}$	r_{AC}	$p_{AC}=\mu_{AC}\dot{r}_{AC}$
c	A-B + C	$r_{AB}<r_{AC}; r_{BC}$ $E_{AB} < D_e$	1	$R_{AB,C}$	$P_{AB,C}=\mu_{AB,C}\dot{R}_{AB,C}$	r_{AB}	$p_{AB}=\mu_{AB}\dot{r}_{AB}$
d	A + B + C	$r_{ij}<r_{ik}, r_{jk}$ $E_{ij} > D_e$	3	$R_{A,BC}$	$P_{A,BC}$	r_{BC}	p_{BC}

b:

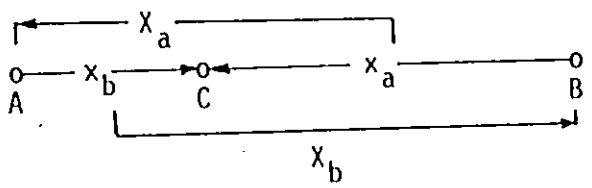

c:

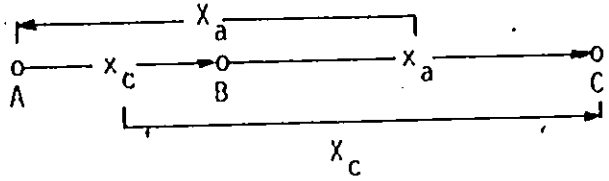

These relationships follow from the definitions of the directions of the positional vectors (R_i, r_i), shown in Fig.31 for typical configurations b and c, in terms of their components along the x-axis (X_i, x_i). The directions of the original coordinates (R_a, r_a) have already been defined in eqs.(61) and (60) respectively.

4.3. The Vibrating Rotator.

In the preceding section the rotational and vibrational kinetic energy terms were collectively treated as internal kinetic energy, pertaining to motion of B and C relative to their center-of-mass $\overline{BC}$. The fact is that these two motions are strongly coupled through the flexibility of the BC bond. Thus, rotational motion causes centrifugal forces to influence the vibrational motion, and vibration causes changes in the moment of inertia ($I_{BC} = \mu_{BC} r_{BC}^2$) to influence the rotation. Initially, at large $R_{A,BC}$, or more generally, at large atom-molecule separations, the total internal energy is a constant, depending only on the rotational and vibrational quantum numbers v and J[65,76]:

$$E_{v,J} = \sum_{1}^{3} \{g_i (v+\tfrac{1}{2})^i + \sum_{1}^{3} f_{ij} (v+\tfrac{1}{2})^{j-1} [J(J+1)]^i\} \quad (78)$$

where the coefficients g_i and f_{ij} are obtained from spectroscopic measurements[105], and the 3rd-order approximations, indicated by the indices of the sums, are very accurate. The problem now is to separate the vibrational and rotational terms, and to express these as a function of the molecular distance r_{BC}. In general the internal energy can be written as:

$$E_{v,J} = T_r + T_v + V_{int}, \tag{79}$$

where in analogy to the collinear case (Sec.2.5.3)

$$V_{int} = V(r_{AB},r_{BC},r_{AC}) - V_{ref}(\rho^o,r_e). \tag{80}$$

Here, V_{ref} is the minimum energy at the reaction shell, and should ideally ($R_{A,BC} \to \infty$) be independent the initial orientation of the molecule relative to the translational vector p_t. In the actual case V_{ref} is slightly dependent on b and θ, and must be determined separately for different (b,θ) combinations. The equilibrium separation r_e is taken to be the distance r_{BC} at the reaction shell, for which the potential energy is a minimum (V_{ref}). This distance does not depend on b and θ for the Yates and Lester surface, but does not correspond to the equilibrium separation of the vibrating rotator[76].

The rotational energy can then be approximated by the expression for the rigid rotator[76]:

$$T_r = \frac{\hbar^2}{2\mu_{BC}r_{BC}^2} J(J+1), \tag{81}$$

and the internal potential energy can be expressed as a Morse function (cf. eq.(43)):

$$V_{int}(r_{BC}) = D_e\exp(-\beta\,(r_{BC}-r_e)\{\exp(-\beta\,(r_{BC}-r_e)-2\}. \tag{82}$$

The kinetic vibrational energy term is then determined:

$$T_v(r_{BC}) = E_{v,J} - T_r(r_{BC}) - V_{int}(r_{BC}), \tag{83}$$

and the momenta p_r and p_v can be calculated from

$$p_i = \pm\,(2\mu_{BC}T_i)^{\frac{1}{2}}\ ;\ (i=r,v). \tag{84}$$

The methods of generating the initial vibrational phase distribution are similar to the ones mentioned in the 1-D case (Sec.2.5.2). The system can again be started from outside the reaction shell, always at one of its vibrational turning points, which are characterized by $T_v = 0$ and can be determined[65] by solving eq.(85) for $r_{BC} = r_l, r_r$:

$$E_{v,J} - T_r(r_{BC}) - V_{int}(r_{BC}) = 0 \qquad (85)$$

The initial conditions can again be calculated as in Sec.2.5.2 (eq.(38) and the paragraph following it), using spectroscopic values for the vibrational period τ.

The method used in the present work is based on the computation of a translationless trajectory at the reaction shell, starting from the equilibrium position r_e, with $E_{v,J}$ as obtained from eq.(78). In Fig.32 the vibrational paths for $H+H_2$ on the Yates and Lester[58] (YL) surface are shown in coordinate-time space for v=0, J=0,2,5. By taking into account the different vibrational amplitudes and periods of vibration, obtained from the translationless trajectories and listed in Table IX, the double harmonic approximation,(dashed lines in Fig.32) is found to be of sufficient accuracy. The more accurate methods[70,79,116] mentioned in Sec.2.5.2 can in principle also be used.

4.4 Initial and Final Values.

The generalized coordinates and momenta are initialized by a particular choice of initial values for T_t, ϕ, b, θ, J, with v = 0 and $R^o_{A,BC} = \rho^o = 4.0$ Å at every trajectory. Using the double harmonic approximation, r_{BC} is determined by:

Figure 32

The vibrational path of the H_2 vibrating rotator, corresponding to the Yates-Lester surface, in coordinate-time space, for J= 0,2,5. (———) actual path; (------) path generated by the double harmonic approximation.

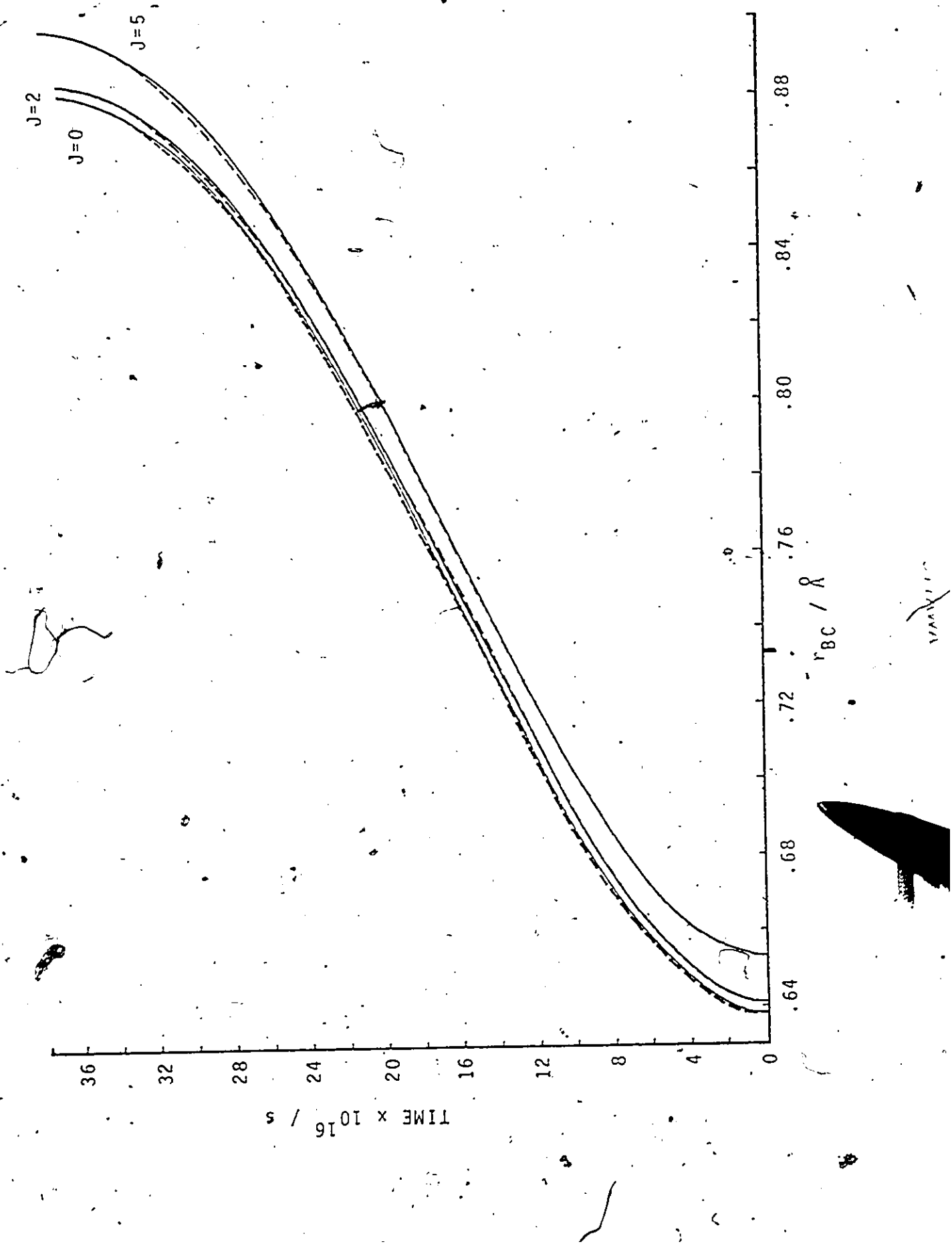
J=5
J=2
J=0
.88
.84
.80
.76
.72
.68
.64
$-r_{BC}$ / Å
0
4
8
12
16
20
24
28
32
36
TIME x 10^{16} / s

Table IX. Characteristics of the H_2 vibrating rotator (v=0)

J	E_{int}/eV	r_l/a.u.	A_l/a.u.	$\tau_l x10^{16}$/s	r_r/a.u.	A_r/a.u.	$\tau_r x10^{16}$/s
0	0.269	1.207	0.199	15.85	1.660	0.254	21.65
2	0.313	1.213	-0.193	15.35	1.667	0.261	22.45
5	0.485	1.235	0.171	14.58	1.692	0.286	23.70

$$r^o_{BC} = r_e - A_i(J)\sin(\phi^o_i) \; ; \quad (i=1,r) \tag{86}$$

where the notation $A_i(J)$ is used to indicate that the amplitudes are significantly dependent on J only, if v is held constant as in the present work. $T^o_r(r^o_{BC})$, $V^o_{int}(r^o_{BC})$, and $T^o_v(r^o_{BC})$ can then be calculated using the procedure outlined in the preceding section, yielding p^o_v and p^o_r with eq.(84). In accordance with Fig.3, the coordinates will take on the following initial values:

$$\begin{aligned}
Q^o_1 &= r^o_{BC}\sin(\theta^o) \\
Q^o_2 &= r^o_{BC}\cos(\theta^o) \\
Q^o_3 &= b \\
Q^o_4 &= -(\rho^{o\,2} - b^2)^{\frac{1}{2}} \\
p^o_1 &= -p^o_r\cos(\theta^o) + p^o_v\sin(\theta^o) \\
p^o_2 &= p^o_r\sin(\theta^o) + p^o_v\cos(\theta^o) \\
p^o_3 &= 0 \\
p^o_4 &= p^o_t = (2\mu_{A,BC}T^o_t)^{\frac{1}{2}}
\end{aligned} \tag{87}$$

As stated in Sec.4.2, the evaluation of the final parameters is dependent on the product configuration. Thus, the internal angular momentum can be obtained from the generalized form of eq.(75), written as a vector cross product:

$$\omega_{int} = [p_i \times r_i] \quad ; (i=a,b,c). \tag{88}$$

The total angular momentum is a constant of motion and can be evaluated in the original set of coordinates:

$$\omega_T = \omega_{int} + \omega_{orb} = [p_a \times r_a] + [P_a \times R_a]$$

$$= [p_i \times r_i] + [P_i \times R_i] \; ; \; (i=b,c). \qquad (89)$$

The scattering angle γ is originally[60,65] defined as the angle between the initial and final relative velocity vectors, and is evaluated in terms of the dot product of the vectors:

$$[\dot{R}_a^o . \dot{R}_i'] = |\dot{R}_a^o||\dot{R}_i'|\cos(\gamma)$$

$$= \dot{X}_a^o \dot{X}_i' + \dot{Y}_a^o \dot{Y}_i' \; ; \; (i=a,b,c). \qquad (90)$$

This procedure involves a rather complicated algorithm, since the initial relative velocity vector components $(\dot{X}_a^o, \dot{Y}_a^o)$ have to be stored and the final velocity vector $(\dot{R}_i')$ has to be computed from P_a' and p_a'. Since its absolute value $|\dot{R}_i'|$ is obtained from

$$|\dot{R}_i'| = (\dot{X}_i'^2 + \dot{Y}_i'^2)^{1/2}, \qquad (91)$$

its sign is lost in the process, and the direction of scattering is therefore not completely determined. A simpler alternative would be to directly use the initial and final translational momenta (P_a^o, P_i'); taking into account that P_a^o is parallel to the y axis, γ is directly determined from the components of P_i':

$$\tan(\gamma) = P_{ix}'/P_{iy}', \qquad (92)$$

so that information about the quadrant of scattering is retained.

The product vibrational and rotational energies are calculated according to the deconvolution method described by

Muckerman[60]. The equations for separate rotation and vibration are[76]:

$$J'(J'+1) = (\omega'_{int}/\hbar)^2 \tag{93}$$

$$\bar{E}'_r = J'(J'+1)\hbar^2/(2\mu_{ij}r_e^2) = J'(J'+1)B_e \tag{94}$$

$$\bar{E}'_v = E'_{int} - \bar{E}'_r \tag{95}$$

$$(v'+\tfrac{1}{2}) = \tfrac{1}{2}(\omega_e/\omega_e x_e) - \tfrac{1}{2}\{(\omega_e/\omega_e x_e)^2 - (4\bar{E}'_v/\omega_e x_e)\}^{\frac{1}{2}}, \tag{96}$$

where eq. (96) corresponds to eq.(36) for the anharmonic YL oscillator, with the parameters $\omega_e, \omega_e x_e$ determined from the surface constants D_e and β . $\bar{E}'_r$ and $\bar{E}'_v$ are approximate values for product rotational and vibrational energies, E'_{int} is obtained from eq.(76), and μ_{ij} is the corresponding reduced mass of the product molecule. Rotational-vibrational coupling is then taken into account by[60,76]:

$$B_v = B_e - (v+\tfrac{1}{2})\alpha_e \tag{97}$$

$$\alpha_e = 6\{(\omega_e x_e B_e^3)^{\frac{1}{2}} - B_e^3\}/\omega_e \tag{98}$$

$$D_v = 4B_e^3/\omega_e^2 + \beta_e(v+\tfrac{1}{2}) \tag{99}$$

$$E'_r = J'(J'+1)B_v - \{J'(J'+1)\}^2 D_v \tag{100}$$

$$E'_v = E'_{int} - E'_r, \tag{101}$$

where E'_r and E'_v are more accurate values for the product energies. The rotational constant β_e in eq. (99) is very small[76] and has

been neglected[60]. This is quite justified since the rotational constant D_v itself is a correction for the influence of the centrifugal force which is often neglected[76]. The influence of the vibrational motion is taken into account in B_v, which represents the averaged value of B_e over several periods of vibration ($\tau_{rot} >> \tau_{vib}$). Further refinement of the energies is achieved by substituting E'_v in place of $\bar{E}'_v$ into eq.(96), and recalculating more accurate values for E'_r and E'_v through eqs. (97)-(101) until convergence is obtained. The product quantum numbers are obtained by solving $J' \leq \{J'(J'+1)\}^{\frac{1}{2}}$ and $v' \leq v'+\frac{1}{2}$ for the largest integers.

4.5 Methods of Calculation.

The investigation was started by modifying the computer program for 3-D Monte Carlo calculations[60] to allow systematic calculations of coplanar $H+H_2$ on the YL potential-energy surface. The following restrictions on the limits of variation of the free variables were decided upon:

1. Initial vibration: $v = 0$; E_v^o = ZPE.
2. Initial rotation : $J = 0 - 5$.
3. Orientation : $\theta = 0 - 360^o$.
4. Impact parameter : $b = 0 - 2.0$ a.u.
5. Vibrational phase: $\phi = 0, 90, 180, 270^o$.
6. Translation : $T_t = 0 - 2.0$ eV.
7. Reaction shell : $\rho^o = 4.0$ Å.
8. Step size : $\Delta t = 2.\times10^{-16}$s.

These values were chosen on the basis of the work of Karplus et al.[65], who used similar values to restrictions 1-4, and the earlier 1-D calculations (Chapters 2 and 3), which indicated that reliable results can be obtained with restrictions 5-8.

In order to test the modified program and to determine the general effects of various new parameters on the dynamic behavior of the system, a preliminary run with $J=5, \theta^o=0^o, \phi^o=90^o$ was calculated. On the basis of the results of these calculations, it was then decided to first investigate the simplest case, J=0, where the influence of only two additional parameters (θ^o and b) could be established separately, and where a direct comparison to the 1-D results would be possible. The results of the preliminary calculations could then serve to evaluate the influence of J on the outcome of the trajectories.

For this part of the study the following method was used:

1. Starting with b = 0 a.u., $\theta^o = 0^o$ and $\phi^o = 0^o$, trajectories were calculated, T_t^o being varied from 0.2 to 2.0 eV with a step size of 0.05 eV.
2. The final parameters χ (reaction channel), t^R (reaction time), E'_{int}, E'_v, E'_J, v', J' (product energies and quantum numbers), and γ (scattering angle), were tabulated and plotted as a function of T_t^o.
3. Energy band boundaries were determined to within 0.01 eV by additional trajectory calculations in the neighborhood of the t^R peaks.
4. Similar calculations were then carried out for different phase angles, resulting in ϕ^o vs. T_t^o plots as familiar from

the 1-D calculations.

5. Next, b was varied in steps of 0.5 a.u., again completing a full cycle of ϕ^o values before proceding with the next b value. Maps of the band boundaries as a function of b and T_t^o were thus obtained at constant θ^o, J, ϕ^o.
6. When b = 2.0 a.u. very few trajectories lead to reaction, indicating that the maximum impact parameter[43,65], b_{max}, has almost been reached. A systematic variation of θ^o can then be started, by succesively repeating steps 1 to 5 at different θ^o values. A step size of 22.5° in θ^o was found necessary to obtain a rough θ^o vs. T_t^o map of the band edges, although sometimes $\Delta\theta^o = 30^o$ was sufficient.
7. Refinement of the maps was achieved by calculating individual trajectories with any combination of T_t^o, ϕ^o, b and θ^o values, deemed necessary to complete the exact determination of the band boundaries. A more complete and revealing picture is obtained by arranging corresponding maps in sequence, to reflect the variation of the patterns with additional parameters (composite maps).

4.6 The Potential-Energy Surface.

At the present time, the most accurate ab-initio surface for collinear $H+H_2$ is considered to be the one obtained by Liu[39], from a complete configuration-interaction study using a basis set of 27 σ-type, 15 π-type, and 6 δ-type functions for the collinear H_3 system. These calculations yielded a barrier height of 9.8 kcal/mole, and the energy of the hydrogen molecule was found to be only

0.48 kcal/mole above the true energy. The results were estimated to be accurate to ca. 0.3 kcal/mole and no worse than 0.8 kcal/mole, in the region near the MERP and in the range 1.0 a.u. $< r_{AB}, r_{BC} \leq 4.0$ a.u. As in the SSMK paper[38a], the ab-initio points were fitted to analytical expressions:

$$E_{H_2}(r_{BC}) = -1 + \exp(-\alpha r_{BC}) \sum_0^8 (a_i r_{BC}^i) \qquad (102)$$

$$E_{H_3}(r_{AB}, r_{BC}) = -1.5 + \{E_{H_2}(r_{AB}) + 1.\} + \{E_{H_2}(r_{BC}) + 1.\}$$
$$+ \exp\{-\gamma(r_{AB} + r_{BC})\} \sum_0^{14} \sum_0^7 c_{k-j,j} (r_{AB}^{k-j} r_{BC}^j + r_{AB}^j r_{BC}^{k-j}). \qquad (103)$$

The analytical surface generally parallels the SSMK function, but has a lower barrier (9.8 kcal/mole) and a saddle point closer to the origin (1.757 a.u.). When examined over a wider range of r_{AB}, r_{BC}, however, the analytical Liu function shows an incorrect qualitative behavior outside r = 2.5 Å[79a].

The Liu results have been generalized to three dimensions by Yates and Lester[58], using a Porter-Karplus (PK)[56] type of semi-empirical function. The PK treatment is a refinement of the LEPS approach[27,64], based on a more consistent quantum-mechanical formulation, and includes all overlap and multiple exchange integrals in a parametric form. Yates and Lester found that the best fit to the ab-initio points calculated by Liu could only be obtained by omission of the energy of the repulsive triplet state of H_2. The potential energy can then be expressed in terms of the Coulomb (Q_k), exchange (J_k), double exchange (J_{123}) and overlap (S_k) integrals, with k = 1 (AB), 2 (BC) and 3 (AC) denoting the diatomic contributions.

$$^1E_k = D_e\left[\exp\{-2\beta(r_k-r_e)\} - 2\exp\{-\beta(r_k-r_e)\}\right]$$

$$\zeta_k = 1 + \kappa\exp(-\lambda r_k)$$

$$S_k = (1 + \zeta_k r_k + \zeta_k r_k^2/3)\exp(-\zeta_k r_k)$$

$$Q_k = \tfrac{1}{2}(1 + S_k^2)\,^1E_k$$

$$J_k = Q_k + \Delta_k$$

$$\Delta_k = \delta S_k\{(1+1/r_l)\exp(-2r_l)+(1+1/r_m)\exp(-2r_m)\};$$

$$(k \neq l \neq m)$$

$$Q = Q_1 + Q_2 + Q_3$$

$$J_{123} = \varepsilon S_1 S_2 S_3$$

$$C_1 = (1-S_1S_2S_3)^2 - \tfrac{1}{2}\{(S_1^2-S_2^2)^2+(S_2^2-S_3^2)^2+(S_3^2-S_1^2)^2\}$$

$$C_2 = -(1-S_1S_2S_3)(Q-J_{123})$$

$$+ \tfrac{1}{2}\{(J_1-J_2)(S_1^2-S_2^2)+(J_2-J_3)(S_2^2-S_3^2)+(J_3-J_1)(S_3^2-S_1^2)\}$$

$$C_3 = (Q-J_{123})^2 - \tfrac{1}{2}\{(J_1-J_2)^2+(J_2-J_3)^2+(J_3-J_1)^2\}$$

$$V(r_{AB}, r_{BC}, r_{AC}) = -\{C_2+(C_2^2-C_1C_3)^{1/2}\}/C_1. \qquad (104)$$

The best fit was obtained with[58]:

D_e = 4.72703 eV

r_e = 1.40631 a.u.

β = 1.07366 a.u.

(Morse parameters)

δ = 58.25083 eV

ε = - 79.135565 eV

κ = 3.127965 a.u.

λ = 0.96131 a.u.

For the collinear $H+H_2$ geometry the hypersurface thus obtained typically differs from Liu's values by $\sim 0.05\%$. The agreement with the SSMK results[38a] is also very good, and even extends to non-linear geometries. The characteristics of this surface are listed in Table II (Sec.2.4), together with those of the SSMK and Liu surfaces, and are compared to experimental data.

The integration of the equations of motion requires the derivatives $\partial V/\partial r_k$ (k = AB,BC,AC). These can be obtained in analytical form[59], yielding:

$$\frac{d^1E_k}{dr_k} = -2\beta D_e\{\exp\{-2\beta(r_k-r_e)\}-\exp\{-\beta(r_k-r_e)\}$$

$$\frac{d\zeta_k}{dr_k} = -\lambda\kappa\exp(-\zeta r_k)$$

$$\frac{dS_k}{dr_k} = \left(\zeta_k+r_k\frac{d\zeta_k}{dr_k}+\frac{2}{3}\zeta_k^2 r_k+\frac{2}{3}\zeta_k r_k^2\frac{d\zeta_k}{dr_k}\right)\exp(-\zeta_k r_k)$$

$$-\left\{\zeta_k+r_k\frac{d\zeta_k}{dr_k}\right\}(1+\zeta_k r_k+\zeta_k^2 r_k^2/3)\exp(-\zeta_k r_k)$$

$$= -\frac{1}{3}\left\{\zeta_k+r_k\frac{d\zeta_k}{dr_k}\right\}(1+\zeta_k r_k)\zeta_k r_k\exp(-\zeta_k r_k)$$

$$\frac{dQ_k}{dr_k} = {}^1E_k S_k\frac{dS_k}{dr_k}+\tfrac{1}{2}(1+S_k^2)\frac{d^1E_k}{dr_k}$$

$$\frac{\partial J_{123}}{\partial r_k} = \varepsilon S_1 S_m\frac{dS_k}{dr_k}$$

$$\frac{\partial J_k}{\partial r_k} = \frac{dQ_k}{dr_k}+(2/S_k)\Delta_k\frac{dS_k}{dr_k}$$

$$\frac{\partial J_1}{\partial r_k} = -S_1^2\delta(2+2/r_k+1/r_k^2)\exp(-2r_k)$$

$$\frac{\partial C_1}{\partial r_k} = -2\left\{(1-S_1S_2S_3)S_1S_m\frac{dS_k}{dr_k} + \{(S_k^2-S_1^2)+(S_k^2-S_m^2)\}S_k\frac{dS_k}{dr_k}\right\}$$

$$\frac{\partial C_2}{\partial r_k} = (Q-J_{123})S_1S_m\frac{dS_k}{dr_k} - (1-S_1S_2S_3)\left\{\frac{dQ_k}{dr_k} - \frac{\partial J_{123}}{\partial r_k}\right\}$$
$$+ \left[(J_k-J_1)+(J_k-J_m)\right]S_k\frac{dS_k}{dr_k} + \tfrac{1}{2}\left\{(S_1^2-S_2^2)\left\{\frac{\partial J_1}{\partial r_k} - \frac{\partial J_2}{\partial r_k}\right\}\right.$$
$$\left. + (S_2^2-S_3^2)\left\{\frac{\partial J_2}{\partial r_k} - \frac{\partial J_3}{\partial r_k}\right\} + (S_3^2-S_1^2)\left\{\frac{\partial J_3}{\partial r_k} - \frac{\partial J_1}{\partial r_k}\right\}\right\}$$

$$\frac{\partial C_3}{\partial r_k} = 2(Q-J_{123})\left\{\frac{dQ_k}{dr_k} - \frac{\partial J_{123}}{\partial r_k}\right\} - (J_1-J_2)\left\{\frac{\partial J_1}{\partial r_k} - \frac{\partial J_2}{\partial r_k}\right\}$$
$$- (J_2-J_3)\left\{\frac{\partial J_2}{\partial r_k} - \frac{\partial J_3}{\partial r_k}\right\} - (J_3-J_1)\left\{\frac{\partial J_3}{\partial r_k} - \frac{\partial J_1}{\partial r_k}\right\}$$

$$\frac{\partial V}{\partial r_k} = \tfrac{1}{2}(C_2^2-C_1C_3)^{-\frac{1}{2}}\left\{V^2\frac{\partial C_1}{\partial r_k} + 2V\frac{\partial C_2}{\partial r_k} + \frac{\partial C_3}{\partial r_k}\right\}, \qquad (105)$$

where the last equation follows after some rearrangement of the more complicated expression initially obtained from the differentiation of eq. (104) with respect to C_1, C_2 and C_3. Porter and Karplus[59] have given similar expressions, but the elimination of their ^3E_k term and some serious misprints[59] necessitated a redetermination of all the derivatives.

In Fig.33 contour maps for different geometries (bending angle $\Gamma = 0^o, 30^o, 90^o$) are shown. It is apparent that the surface contours are very smooth and well behaved at all Γ, and that locations of the valleys and the saddle point do not shift appreciably with Γ. The behavior of the surface is very

Figure 33

Contour maps of the YL surface for various bending angles.

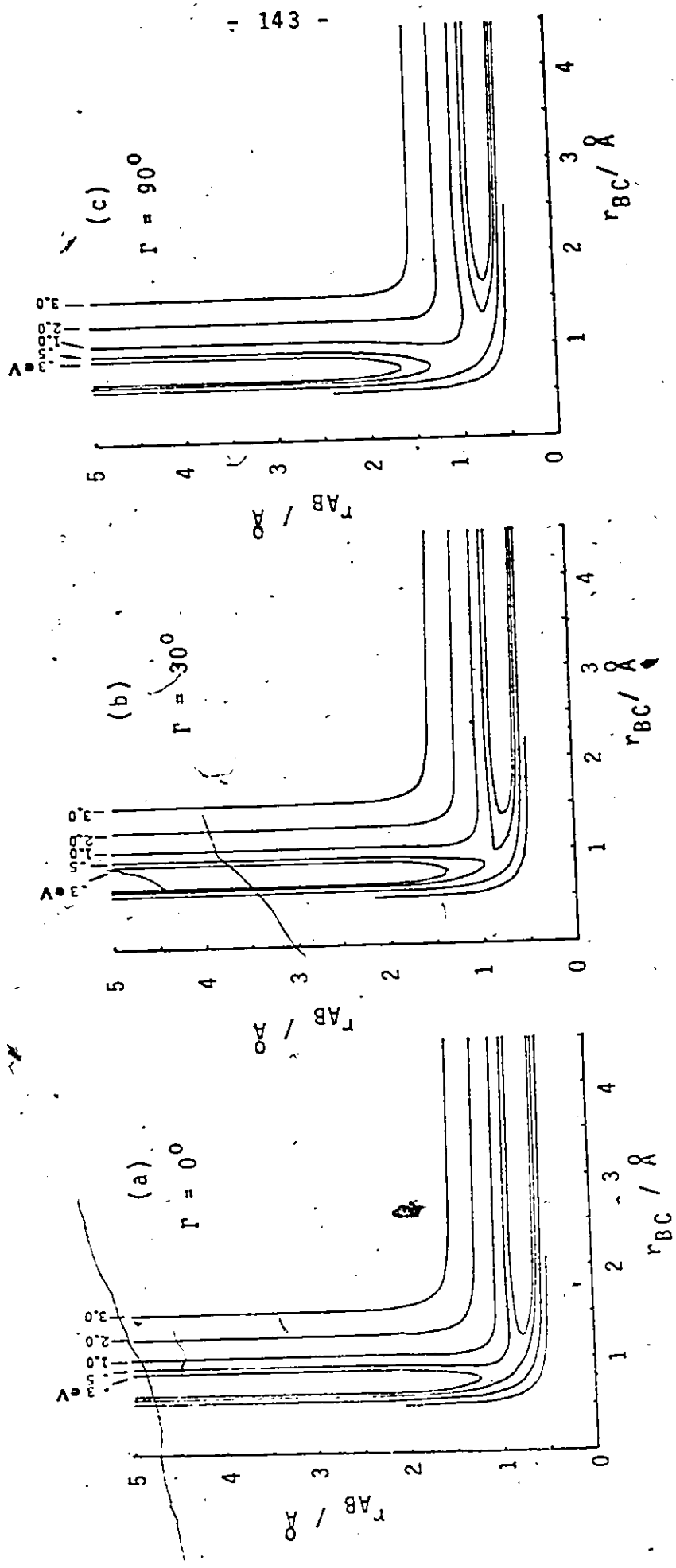
(a)
r = 0°
(b)
r = 30°
(c)
r = 90°
r_AB / Å
r_BC / Å
eV

similar to the SSMK results in many respects. A comparison of the energy profiles along the MERP at different Γ to the corresponding SSMK profiles is shown in Fig.1,Ref.58, and for the collinear geometry the MERP is almost perfectly parallel to the MERP of the SSMK surface, but is shifted nearer to the coordinate axes, as shown in Fig.1,Ref.39. It is also interesting to note that the YL function for collinear geometries has a van der Waals minimum at r_{AB}≈5.7a.u. of depth 0.0087 eV, similar to the one observed for the analytical SSMK surface[38a] (Sec.2.4).

4.7 The Computer Program.

The original computer program was obtained from the Quantum Chemistry Program Exchange (QCPE) and is briefly described in its catalog[60] under number 229 CLASTR. It was written by Muckerman[60], based on the formulation of Karplus, Porter and Sharma[65], appropriate for 3-D Monte Carlo calculations using generalized LEPS potential-energy functions. The program was first modified to allow a free choice of the initial parameter values and the use of the YL surface for $H+H_2$. The program was further abbreviated to adjust for the reduced number of parameters and equations of motion in 2-D, and the highly symmetric reaction ($H+H_2$). The integration routine was exchanged with the fourth-order predictor-corrector algorithm (see Sec.2.5.4), which allowed a greater precision using a larger time step and the double precision mode. Preliminary runs were calculated at this stage to determine the reliability

of the modified program. Further modifications then allowed the use of the double harmonic approximation (see Secs.2.5.2 and 4.3). The units used throughout the whole program were changed to eV for energies, a.u. (bohrs) for distances and a.m.u. for masses, in order to avoid frequent conversions within the program. The unit for time, 1 s = $1.8562336887 \times 10^{14}$ is then only needed for the numerical integration, Planck's constant $\hbar = h/2\pi = 0.1221806963$ being directly used in the correct units. The remaining conversion factors from degrees (input/output of angles) to radians (calculation) are stored in COMMON/CONST/ together with the value for $\hbar$, and are initialized in a BLOCK DATA statement (see Appendix II where the FORTRAN listings of the modified program are given). The reaction shell radius RHO and the atomic masses EM are read into the MAIN program together with program control parameters (HO = time step/10^{-16}s; NTOT = # of trajectories to be calculated; NPRINT, IE are output control parameters) and some pre-determined vibrating-rotator parameters (RLO,RHI are the turning points; NV,NJ are the quantum numbers; EOJ is the internal energy). The control options are explained by the comments in the listings and a table for the mnemonics used is also given in Appendix III. Next, mass ratios important for the calculation of energies and the transformation between several coordinate systems (see Secs. 4.2-4.4) are evaluated. These mass ratios are transmitted through a blank COMMON block, together with the Morse parameters (C = D_e, B = β, RO = r_e), generalized coordinates, momenta and time derivatives (Y(8),FF(8)), internal coordinates and potential-energy

derivatives (R(3),DD(3)), energies and momenta, initial and final parameters, and internal counters. Some of these parameters and other more specific constants are given initial values by a call to various initializing routines, e.g. the free parameters ϕ^o, θ^o, b are read from data cards in SUBROUTINE PARMIN, where r^o_{BC}, p^o_r, p^o_v are determined from $E^o_{v,J}$, T^o_r, V^o_{int} and T^o_v as described in Sec.4.3. These parameters remain constant for one batch of trajectory calculations. The remaining free parameter T^o_t is then read into the MAIN program for the first trajectory, and the generalized coordinates and momenta are assigned initial values according to eqs.(87) in SUBROUTINE PARMIN, ENTRY PARMO. Relative velocity vectors are calculated in SUBROUTINE ANGLIN, ENTRY ANGLST (initial relative velocity) and ENTRY ANGLE (final relative velocity and scattering angle); internal and total angular momenta in SUBROUTINE FMOM; internal and total energies in SUBROUTINE FENGIN, ENTRY FENGY; all according to the procedures described in Secs.4.2-4.4. The YL potential-energy function and its derivatives are evaluated in SUBROUTINE DFPOTI, ENTRY DERIVE(MM); MM = 1 if only the potential energy is required, MM = 2 otherwise; the potential energy of the diatomic molecule (with the shortest interatomic distance) is evaluated from the Morse equation in ENTRY FPOTN. The internal coordinates used in these calculations are determined from the generalized coordinates in SUBROUTINE RVECT.

The numerical integration of the equations of motion is controlled by SUBROUTINE MASTER, which calls on SUBROUTINE DBASH

to perform the actual integration. The values of the derivatives for the generalized coordinates and momenta are obtained from SUBROUTINE FSTART, ENTRY F which transforms the derivatives obtained from DERIVE according to eqs.(70) and (71). MASTER also controls various options for the output of the details of individual trajectories in the form of data files of the Cartesian coordinates as a function of reaction time, or of on-line time vs. distance diagrams; it further decides when a trajectory is terminated, what product configuration is formed, and whether back integration (ENTRY REMAST) should be performed. It then returns control to the main program, where the final parameters are calculated using the subroutines already mentioned above for the calculation of initial parameters. The results are then printed out before proceding to the next value of T_t^o. When one batch of trajectories at constant ϕ^o, θ^o, b has been calculated, these parameters can be changed by specifying a non-zero value for NTOT on the next data card, otherwise the program is automatically terminated.

4.8 Results and Discussion.

4.8.1 Preliminary Calculations.

At an early stage the partially modified program was tested by calculating a series of trajectories with v=0, J=5, ρ^o=4 Å, θ^o=0°, ϕ^o=90°, b = 0-2 a.u. and T_t^o = 5 - 25 kcal/mole. No routine was yet available to vary the phase angle, and no information had yet been gathered on the vibrating rotator. The trajectories were therefore always started at the inner turning point, where T_v^o = 0 and T_r^o was evaluated using eq.(81). Here, an error was made in assuming that the rotational motion would have negligible effect on the turning points of vibration. With $r_{BC}^o = r_1$ = 0.6385 Å and J = 5, T_r^o was determined to be 7.07 kcal/mole, yielding $E_{v,J} = V_{int} + T_r^o$ = 13.27 kcal/mole. At the end of the preliminary calculations a thorough check on the reliability of the results was made, and it was discovered that an evaluation of $E_{v,J}$ from eq.(78) and Stoicheff's data[105] yields the markedly different value of $E_{0,5}$ = 11.18 kcal/mole. A detailed analysis of this discrepancy then led to correct treatment of the vibrating rotator as discussed in Sec.4.3. Since the results of the preliminary calculations were found quite useful despite the error in the initial conditions, they will be briefly reported and discussed in this section.

The initial coordinates and momenta were evaluated from eqs.(86) and (87), and a time step of 2×10^{-16}s was used for the numerical integration. The total energy and the total

angular momentum were conserved to better than 0.01%. The back integration always yielded the initial coordinates and momenta to within 4 significant digits. The final parameters χ, t^R, E'_{int}, v', J' and γ were selected for analysis of the results.

Fig.34a-e shows a plot of these parameters against T_t^o for $b = 0$. The reaction channel χ is indicated as follows:

$\chi = 0$, no reaction, product A+BC : thin dashed line;

$\chi = 1$, reaction, product AB+C : heavy dashed dotted line;

$\chi = 2$, reaction, product AC+B : heavy solid line;

$\chi = 3$, dissociation; product A+B+C : not observed.

These were the first results obtained, and immediately some striking similarities to the 1-D results were observed. Above the threshold, regions of alternating reactivity occur between 0.41-0.43 eV (χ=2), 0.43-0.45 eV (χ=0), 0.45- 1.0 eV (χ=2). The boundaries of the reactivity bands are again clearly marked by peaks of reaction time and product internal energy, and an anomalous peak is observed at 0.91 eV. A rough parallel to the t^R and E'_n curves (a and b) is further noticeable for J' and (c and e), but the v' curve (d) seems very insensitive to the structure in the other parameters. The relative scales in parts b to d in the figure are misleading. In terms of energy, a difference of 1 in the quantum numbers would correspond to roughly 0.45 eV for v', and to around $J'^2 \times 0.08$ eV for J'. In subsequent calculations (see Sec.4.8.3) E'_v and E'_r were therefore selected as the final parameters of interest, instead of v' and J'. It is further observed that unreactive scattering takes place in

the backward hemisphere, and reactive scattering in the forward direction (Fig.34e; see also Fig.30 where the scattering quadrants are defined). Throughout the 2-D calculations, γ was determined from eq.(90), and the absolute direction of scattering, shown in Fig.34e, was subsequently obtained from eq.(92). Finally, it is of interest to note that only product AC+B (χ=2) was formed in the reactive regions. When the calculations were extended to higher energies, an unreactive band was found between 1.7-1.9 eV, followed by another reactive region in which χ=1 exclusively. This is shown in Fig.35a-e for b=0.435 a.u., where a larger range of energies is plotted. The first reactive region (χ=2) has decreased in size (0.45-1.1 eV), and the second reactive band (χ=1) has moved in to lower energies (1.34-2.0 eV). The results have assumed a very simple form: no bands within a band are observed, and no anomalous peaks occur. Again there is a striking similarity between the t^R and E'_{int} curves (a,b), a rough parallel to the J' and γ plots (c,e), and an insensitive behavior of v' (d). Such plots are in marked contrast to plots of the final parameters as a function of b at constant T_t^o (not shown), where the band edges are less clearly marked by irregularities in the curves which are now quite dissimilar to one another.

The final results are presented in the form of a rough b vs. T_t^o band plot, shown in Fig.36. The first reactive region (χ=2) decreases in width with increasing b, until it completely disappears near b=1.0 a.u. The second reactive region (χ=1), was not detected for high b values, but appears to extend beyond

Figure 34

Plots of the reaction time (a), product internal energy (b), rotational quantum number (c), vibrational quantum number (d), and scattering angle (e), as a function of T_t^o; (———) reactive; (-----) unreactive. $b = 0$ a.u., $J = 5$, $\theta^o = \phi^o = 0^o$.

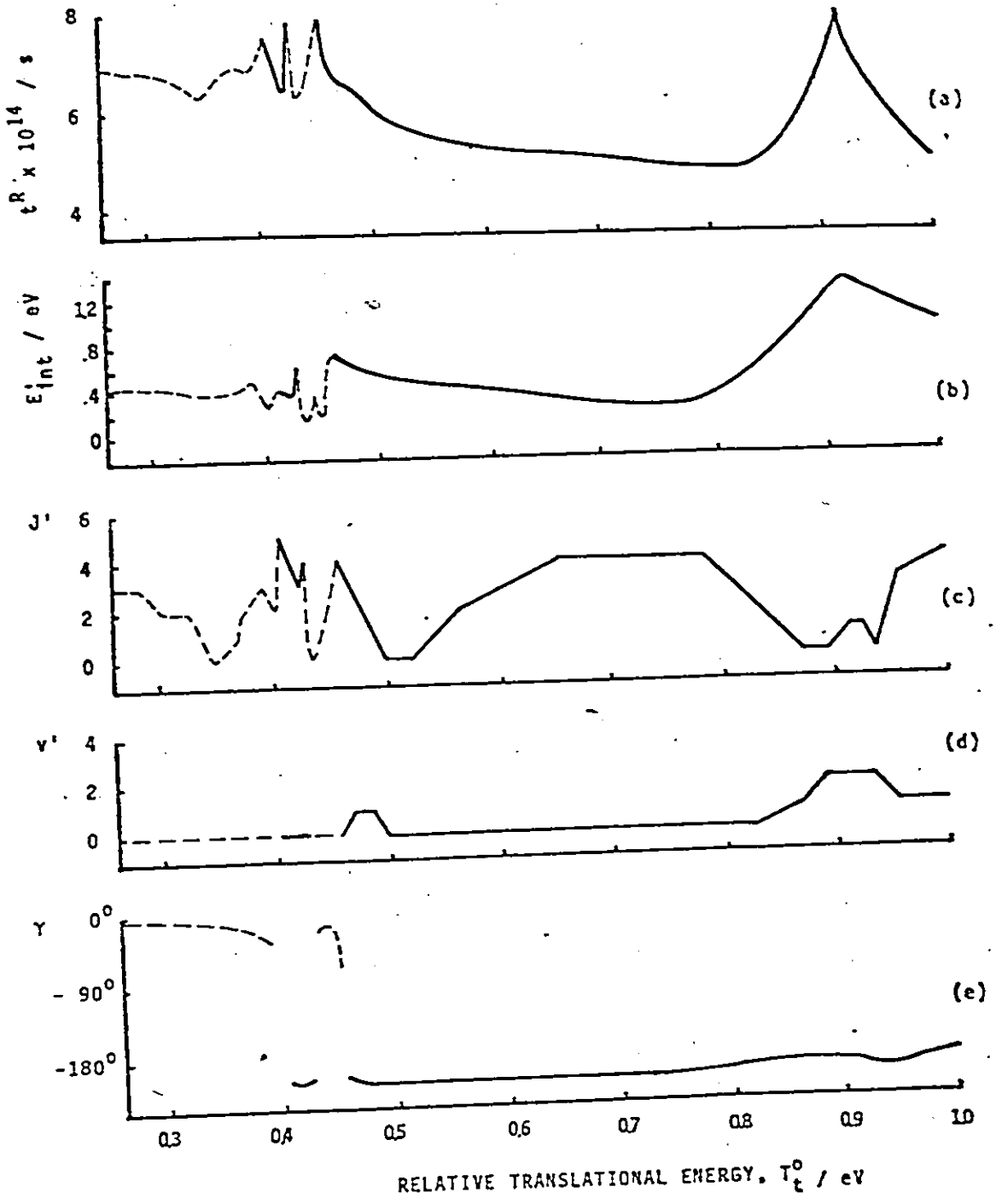
8
6
4
$k^R \times 10^{14}$ / s
(a)
12
.8
.4
0
ϵ'_{int} / eV
(b)
J'
6
4
2
0
(c)
v'
4
2
0
(d)
γ
0°
- 90°
-180°
(e)
0.3
0.4
0.5
0.6
0.7
0.8
0.9
1.0
RELATIVE TRANSLATIONAL ENERGY, T_t^o / eV

Figure 35

Plots similar to Fig.34, for J=5, b=0.435 a.u., $\theta^{o}=\phi^{o}=0^{o}$. (————) reactive, $\chi=2$, product AC+B; (-.-.-.-) reactive, product AB+C, $\chi=1$; (------) unreactive, product A+BC, $\chi=0$.

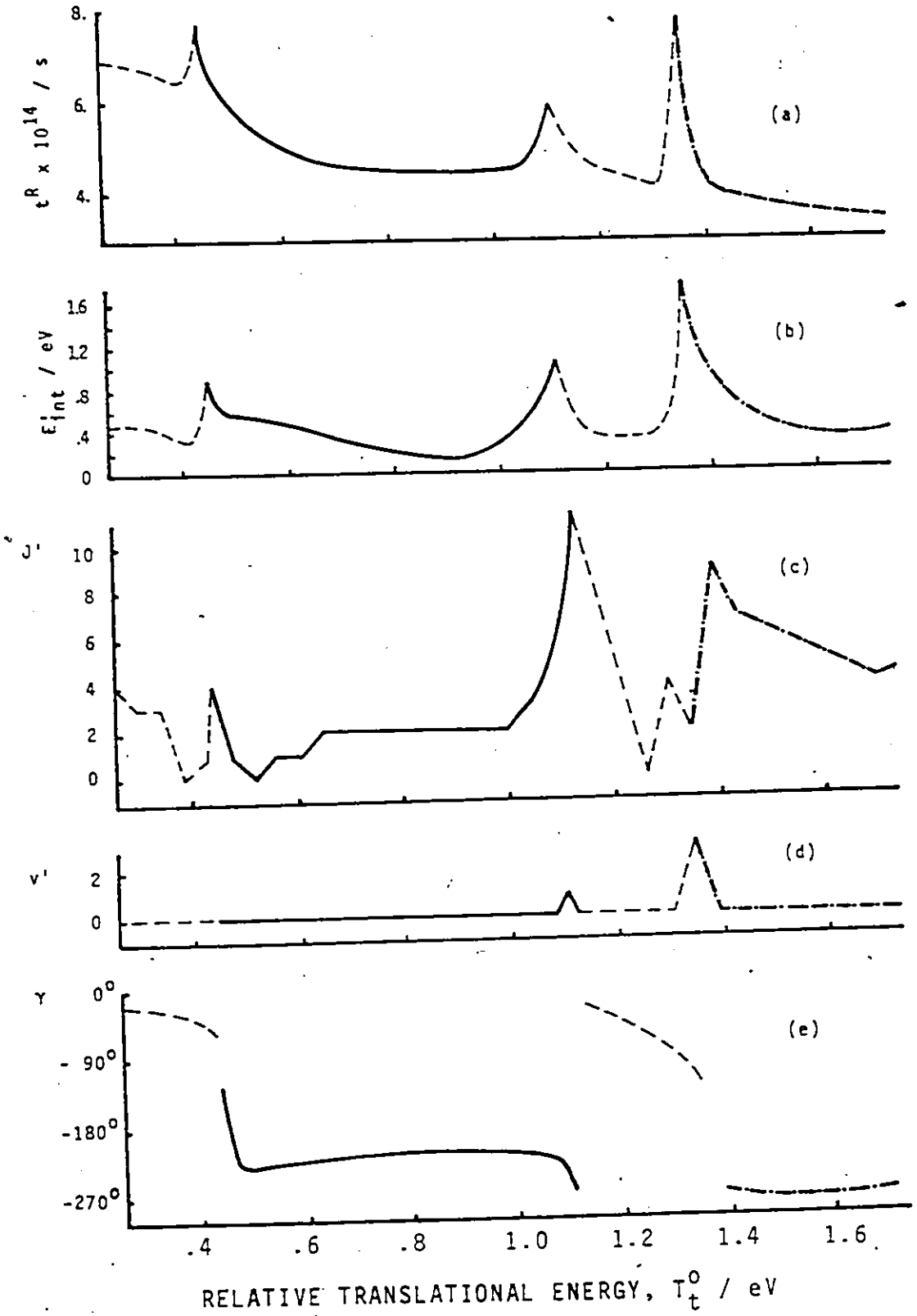
8.
6.
4.
$t^R \times 10^{14}$ / s
(a)
1.6
1.2
.8
.4
0
ϵ^i_{int} / eV
(b)
J'
10
8
6
4
2
0
(c)
v'
2
0
(d)
γ
0°
- 90°
-180°
-270°
(e)
.4
.6
.8
1.0
1.2
1.4
1.6
RELATIVE TRANSLATIONAL ENERGY, T^o_t / eV

Figure 36

Reactivity map for J=5, $\theta^{o}=\phi^{o}=0^{o}$, as a function of b and T_t^o. The reactive regions (shaded) represent different reaction channels.

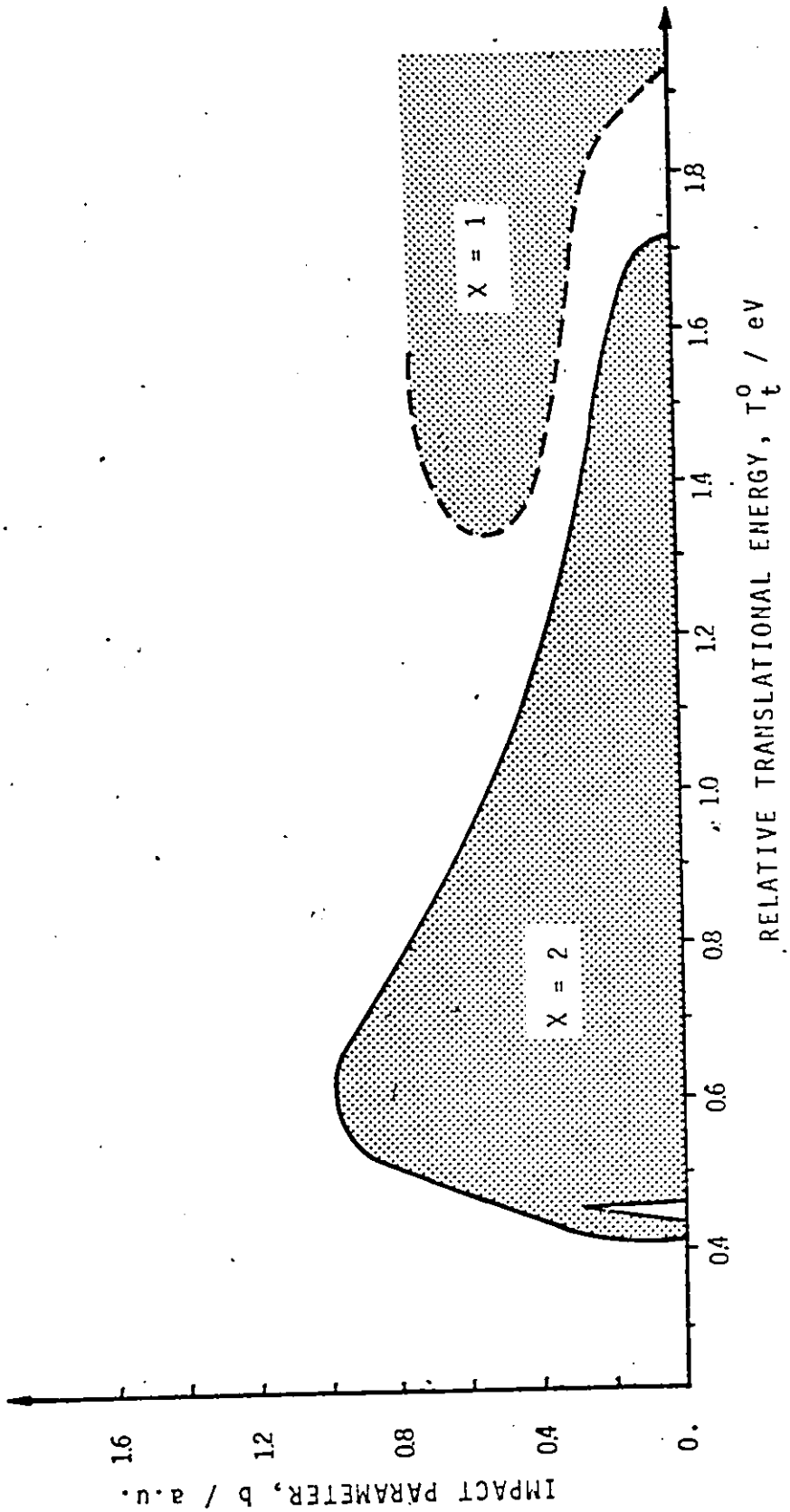
X = 1
X = 2
0.4
0.6
0.8
1.0
1.2
1.4
1.6
1.8
RELATIVE TRANSLATIONAL ENERGY, T_t^o / eV
0.
0.4
0.8
1.2
1.6
IMPACT PARAMETER, b / a.u.

4.0 eV at low impact parameters. The plot also shows that the maximum impact parameter[43,65] has the value of b_{max}= 1.0 a.u., which is about half the values reported by Karplus et al.[65], and by Yates and Lester[58], from 3-D Monte Carlo calculations. In order to evaluate the reliability of the results, an analysis of individual trajectories was made, and the interpretation various observations was attempted.

4.8.2 Analysis of the preliminary results.

A single three-dimensional potential-energy surface model can no longer be used to analyze 2-D trajectories, since the system cannot be characterized by a constant bending angle. Aside from elaborate computer animation techniques[106], time vs. distance diagrams[65] were found extremely informative. In Fig. 37a-f, some trajectories at b=0 and various T_t^o values are shown. The plotted distances are r_{AB}(dashed), r_{BC}(solid), r_{AC}(dashed-dotted), and the sum of the two shortest interatomic separations R (heavy solid line). In plot a, the threshold has almost been reached (T_t^o=0.398 eV; $T_t^{thld.}$=0.407 eV). The vibrational motion of the reactant molecule (BC) is represented by the uninterrupted r_{BC} wave. The translational motion causes r_{AB}, r_{BC}, and R to decrease as A approaches BC, and to subsequently increase again as the system does not make it over the (multidimensional) energy barrier. The rotational motion can be roughly represented by the angle η between the generalized coordinates ($\eta = \measuredangle r_i, R_i$; see Fig. 30). For a collinear configuration, $\eta = 0^o$, and R will equal the

Figure 37

Typical trajectories for J=5, b=0, $\theta^{o}=\phi^{o}=0^{o}$, at various T_t^o. The curves represent the interatomic distances as a function of time; the legend is given at the bottom of the figure.

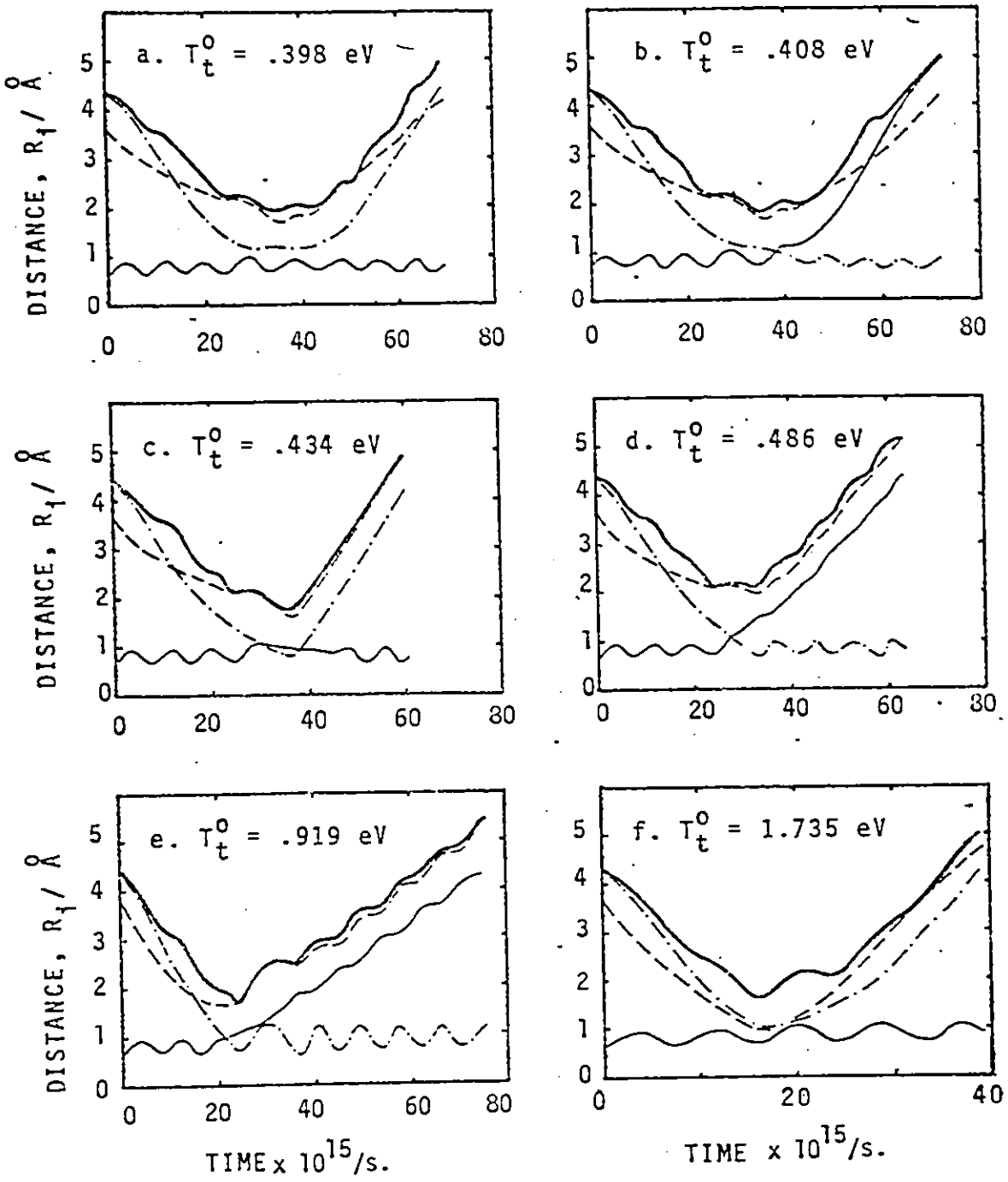
a. T_t^o = .398 eV
b. T_t^o = .408 eV
c. T_t^o = .434 eV
d. T_t^o = .486 eV
e. T_t^o = .919 eV
f. T_t^o = 1.735 eV
DISTANCE, R_1 / Å
TIME x 10^{15}/s.
Legend: —— r_{BC}; ----- r_{AB}; ----- r_{AC}; —— R.

largest interatomic distance, e.g. at the start of the trajectory $b=0, \theta^o=0^o$, hence $\eta=0^o$ and $R=r_{AB}+r_{BC}=r_{AC}$. When $\eta=90^o$ the two largest interatomic distances are equal. This is indicated by a crossing of the two "translatory" distances.

Using this information, the rotational period of the "undisturbed" reactant molecule (i.e. at large atom-molecule separations) can be estimated as $4\times150\times10^{-16}s = 600\times10^{-16}s$. This is longer than the rotational periods reported by Karplus et al.[65] and those obtained from spectroscopic formula[76], which predict values of $\tau_{rot}\simeq400\times10^{-16}s$ for truly undisturbed molecules with the same energy content. This can be interpreted as evidence of the early transfer of rotational to orbital angular momentum, where even as A approaches it is already deflected from its original direction of motion, at the expense of rotational energy of the reactant molecule. This also is related to the "reluctance" of the system to assume the $\eta=90^o$ configuration. The subsequent quarter turn to attain the collinear configuration ($R=r_{AC}+r_{BC}$) takes place in a much shorter time ($\sim100\times10^{-16}s$), but the atom-molecule distance has become too short to be able to assume undisturbed rotational motion. The point of closest interaction is difficult to define for an unreactive trajectory such as the one shown in Fig. 37a. However, it is seen that the system spends between 100 to $200\times10^{-16}s$ with all three atoms in close proximity. The vibrational motion of BC is slightly affected during this period and the collinear configuration is closely maintained. In fact, a slowing down of the rotational motion to a standstill and a subsequent reversal of the direction of rotation seems to

have taken place. This would agree with Marcus's theory[71,107] where initial rotation is transformed into the plane bending mode of the transition state in coplanar collisions, and where such reversals of rotational motion have been predicted and observed for low T_t^o and low total angular momentum. The atom and molecule then separate again, without having reacted, but with J'=2 in a reverse direction. This is therefore an example of a rotationally highly inelastic collision.

The subsequent trajectories (Fig.37b-e), at b=0 and with T_t^o increasing, show similar "undisturbed" rotational periods and the strong orientation effect at the period of close interaction. Plot b shows a reactive trajectory at the threshold. Reactivity is indicated by a single crossover of one of the translatory paths with the vibrational wave (r_{AC} and r_{BC} in this example). This trajectory is highly adiabatic, in that product is formed in the same vibrational and rotational states of the reactant. The next plot (c) shows a trajectory in the narrow unreactive region at low energies just above the threshold. It is more complex than typical 2-D (and 3-D[65]) unreactive trajectories, in that a double crossover occurred, indicating that reaction almost took place, but that the local directions of motion of the atoms, at the moment of closest approach, was unfavorable. Too much repulsive energy was buil up in the AC-entity of the transition state, so that A is bounced back again (2-D brick-wall effect). This is also an example of a highly (rotationally) inelastic collision, in which reactant rotational

energy was converted into repulsive potential energy, which is subsequently released totally in the product translational mode ($J'=0$). Fig.37d is typical of reactive trajectories in the broad reactive region ($\chi=2$), except for the fact that its translational energy was completely used up to climb the barrier and to halt the reactant rotational motion. As a consequence, no product rotational motion is observed ($J'=0$). At higher energies, the excess translational motion is converted into product rotational energy, as can be seen from Fig.34. The next trajectory (e) shows the behavior at the anomalous time peak in Fig.34, and indicates that reaction almost failed to occur. It is therefore reasonable to assume that the anomalous peak corresponds to the opening up of an unreactive region at slightly higher ϕ^o, just as in the 1-D cases, since it can be expected that under slightly less favorable conditions at the moment of closest interaction a double crossover similar to the one shown in Fig.37c might well have taken place. This trajectory is also highly non-adiabatic: reactant translational energy was totally used up to reverse the rotational motion and to excite the vibrational mode of the products to a high degree. Product translation is therefore very low, and a long reaction time results. The last trajectory shown for $b=0$ (f) is typical of the high-energy unreactive region separating the regions with $\chi=2$ and $\chi=1$. The time scale has been doubled in this plot, since the reaction times are very short at higher energies. In Figs.37b-e a trend can be observed, in which the crossover points of translational and vibrational

distances move towards shorter times as T_t^o increases, whereas the undisturbed rotational periods remain roughly constant. In plot f this trend has progressed to a point where the first $\eta=90^o$ configuration coincides with the expected crossover point, resulting in a highly unfavorable geometry at the moment of closest approach. It is seen that A cannot overcome the highly repulsive barrier to come within distances close enough for reactive interaction with either B or C. It is therefore turned back without even influencing the vibrational motion of the molecule appreciably. However, it must have interacted with the rotational motion to a considerable extent, since the first quarter turn of the molecule has been slowed down considerably. An extrapolation of these trends to higher energies explains the existence of the $\chi=1$ reactive region. At b=0, $\theta^o=0^o$, $\phi^o=90^o$ and $T_t^o>2$ eV, the B end of the molecule will always be closer to A so that product AB+C will be formed. The absence of a cut-off below 4 eV for this second reactive region must be due to the fact that the configuration at the distance of closest approach is no longer collinear, so that different behavior from the 1-D case must be expected.

In Fig.38a,b some trajectories at b=0.873 a.u. are shown for comparison to the previous case where b=0. Trajectory a is typical of the narrow (0.52-0.715 eV) reactive region with $\chi=2$. The collinear geometry is again favored at the moment of closest interaction (crossover point), but is kinematically unstable, since the excess translational energy is directed along a vector more perpendicular to the molecular axis of the collinear complex.

Figure 38

Time vs. Distance diagrams, similar to Fig. 37, for J=5, $\theta^{o}=\phi^{o}=0^{o}$, b=0.873 a.u.

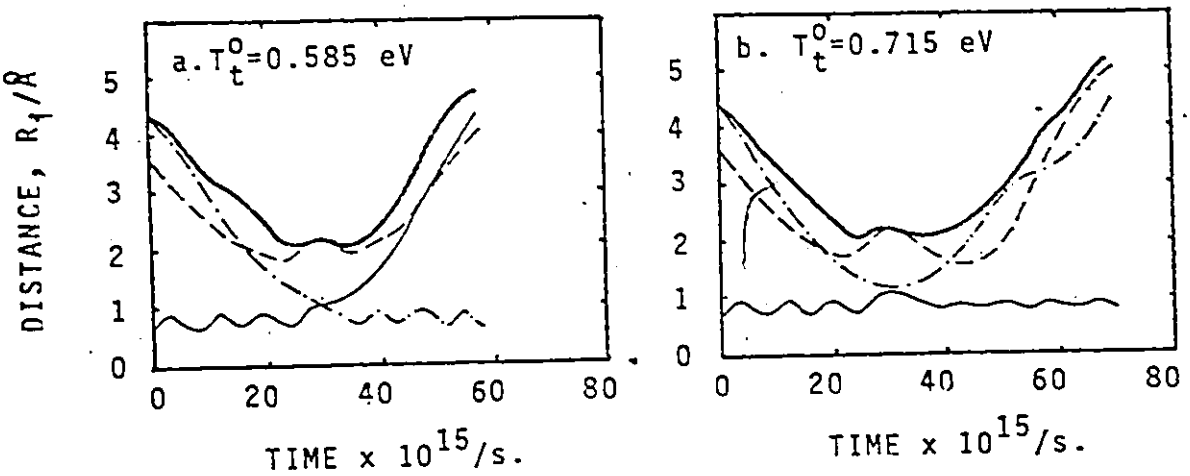
DISTANCE, $R_1/\AA$
a. T_t^o=0.585 eV
b. T_t^o=0.715 eV
0
1
2
3
4
5
0
20
40
60
80
TIME x 10^{15}/s.
TIME x 10^{15}/s.

The higher threshold (compared to b=0) can be understood from a consideration of the initial configuration of the system (see Fig.30, and imagine $\theta^o=0^o$). The direction of rotational motion causes A to be deflected towards the right (positive x-axis) on its approach coordinate (extension of p_t). Thus higher T_t^o is required to minimize the extent of this deflection and to bring A close enough to react with the molecule BC. The lower cut-off in reactivity could also be understood from this picture, in that it is apparent that B will spend more time closer to A, than in the b=0 case. Thus, B will still be closer than C to A, at relatively low T_t^o for high impact parameters. Fig.38b shows that this is not the whole picture. The $\pi=90^o$ configuration still occurs before the crossover, but is now so close in time to it, that the molecule has to increase its rotational velocity very much to achieve the collinear geometry at the (expected) crossover. It does not quite make it and as a consequence the A atom is reflected by the non-optimum barrier. The increased rotational motion is still evident in the products (J'=10).

Finally, the observed scattering angles (Sec.4.8.1) were also found to be consistent with the method of reasoning used above. Thus product (atom) scattering in a backward direction for unreactive trajectories and forward scattering in reactive collisions, indicate a rebound mechanism in all low energy, low impact parameter collisions. With increasing b and T_t^o, scattering in a more sideways direction ($\gamma=90^o,270^o$) is observed. A reactive stripping mechanism is never observed, except at very high T_t^o ($\sim$4 eV). Furthermore, with very few exceptions near band edges,

particle A is always scattered (reactively and unreactively) in the direction of the positive x-axis. In the above discussion, this was related to the direction of reactant rotation, and considerations of the conservation of total angular momentum.

The results of these preliminary calculations were thus found to be very acceptable despite the minor discrepancies with previously published results (the rotational period as determined above does not reflect the undisturbed vibrating rotator, and the maximum impact parameter was not really specified for J=5 in Refs.58 and 65). The major discrepancy in the internal energy was traced to a logical error, and led to detailed analysis of the vibrating rotator problem. The results were also quite encouraging in that the persistence of reactivity bands in 2-D was established, and that a good correlation between the final parameters was again detected. However, the influence of individual initial parameters on the outcome of the trajectories had not yet been established and seemed to be a more complicated problem than in the 1-D case. The program was therefore modified to take into account the correct evaluation of the initial rotational momentum. Translationless trajectories were calculated to determine the characteristics of the vibrating rotator, and the double harmonic approximation was again found to offer an adequate description of the vibrational motion. This solved the problem of introducing further modifications to the program, to allow the systematic variation of ϕ^o. Calculations were then started on the special case of J=0.

4.8.3 Results for J=0.

The basic method of investigation has been outlined in Sec. 4.5. As before, graphs were found to be the most convenient form in which the massive amount of data can be represented. The reactive regions are generally indicated by shaded areas, bounded by heavy solid (χ=1) or heavy dashed lines (χ=2).

A. Final Parameters.

For purposes of determining band boundaries, only the reaction times and the reaction channel need be recorded. The other parameters follow the behavior of the time curve quite closely, and can be presented for more detailed studies in the form shown in Fig.39a-e for the randomly selected case v=0, J=0, θ^o=0^o, b=0.5 a.u., ϕ^o=0^o. Here, alternating reactive bands are observed above the threshold: 0.29-0.515 (χ=1), 0.515-0.595 (χ=0), 0.595-1.07 (χ=1), 1.07- 2.0 eV (χ=0). This result is by no means typical. At other initial conditions total unreactivity or a single reactive region above the threshold can be observed, with several anomalous peaks in the time curve. Cut-off energies as found for this case (the last region stays unreactive beyond 3 eV) are generally observed only for the more collinear cases. Reactive regions with χ=2 are often found, but seldom together with χ=1 below 2.0 eV. The more general features in Fig.39 are the coincidence of the time peaks (a) with the band boundaries, and the relatively close parallel of the other parameter curves. The scattering angle γ has now been plotted in the form obtained from the computer output, i.e. in a range from 0^o to 90^o only.

Figure 39

Reaction time (a), scattering angle (b), internal energy (c), rotational energy (d), and vibrational energy (e) as a function of T_t^o for J=0, b=0.5 a.u., $\theta^o=\phi^o=0^o$. The product quantum numbers are also shown on the right-hand side of plots (d) and (e). (————) reactive, $\chi=1$, product AB+C; (-------) unreactive, $\chi=0$, product A+BC.

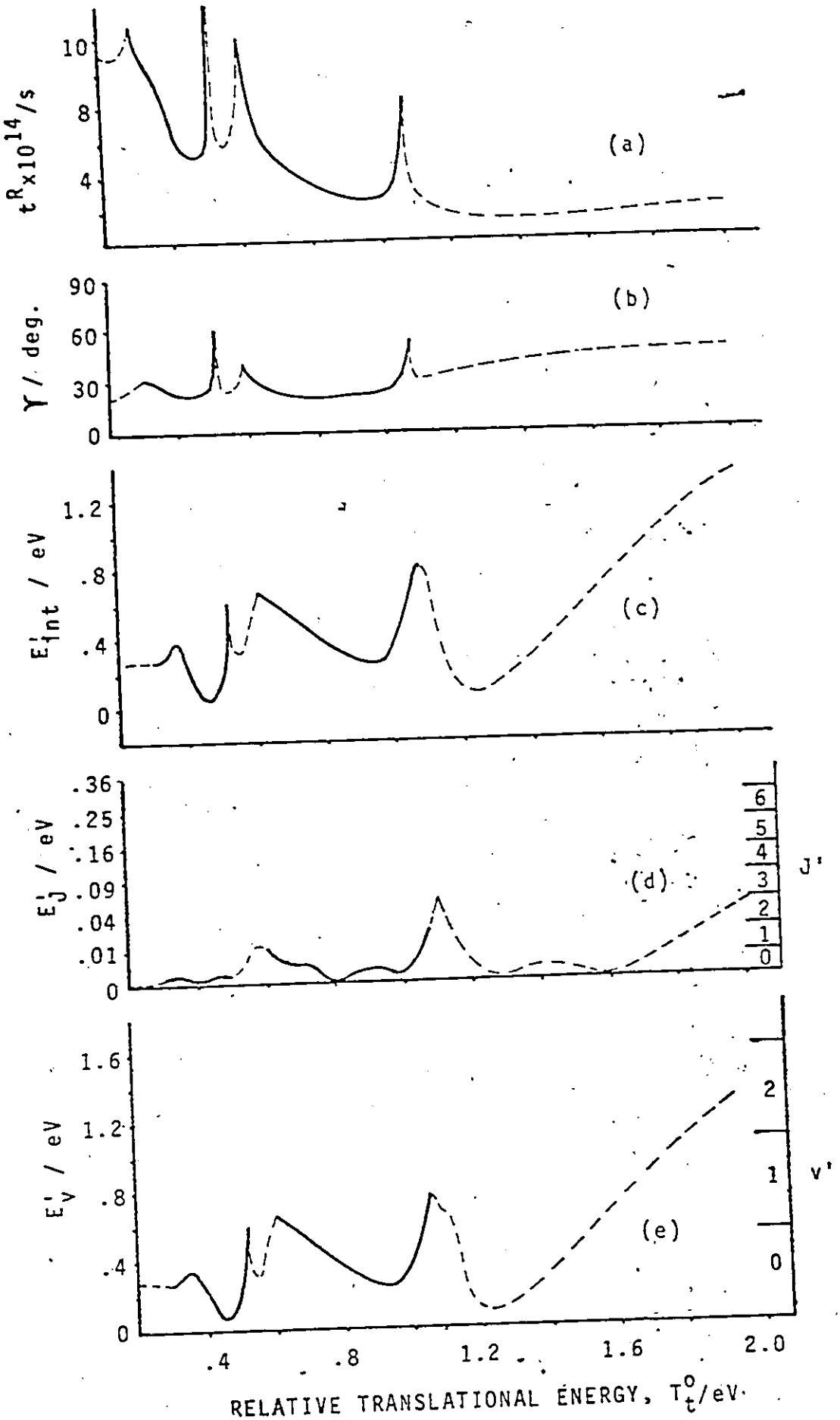
$t^R \times 10^{14}$/s
10
8
4
(a)
Υ / deg.
90
60
30
0
(b)
E'_{int} / eV
1.2
.8
.4
0
(c)
E'_J / eV
.36
.25
.16
.09
.04
.01
0
(d)
6
5
4
3
2
1
0
J'
E'_V / eV
1.6
1.2
.8
.4
0
(e)
2
1
0
v'
.4
.8
1.2
1.6
2.0
RELATIVE TRANSLATIONAL ENERGY, T^o_t/eV

The internal energy is plotted in the same way as before, but E'_J (d) and E'_v (e) are now plotted instead of J' and v', although these quantum numbers are still shown on the right-hand sides of the plots. If the E'_J axis is scaled in the non-linear way as shown in plot d ($\propto E'^{\frac{1}{2}}_J$), the J' axis on the right becomes roughly linear, and more details of the behavior of the E'_J curve at low J' become available. The E'_v curve (e) certainly shows more structure than the v' curves in the preliminary results (Sec. 4.3.1). This is especially true for the more general cases, where v' seldom reaches values of 2 and higher, and mostly remains zero.

To summarize, the following similarities to the 1-D results can be pointed out:

1. The T^o_t spectrum is usually divided into regions of different values.
2. The boundaries of these regions are clearly marked by t^R peaks and breakpoints in the other final parameter curves.
3. Not all t^R peaks, however, correspond to a band boundary, although they are usually related to the existence of such boundaries at slightly different initial conditions. Rounded peaks, shoulders and other irregularities in otherwise smooth portions of the t^R curve also belong in this category.
4. If these plots are arranged in sequence, with parameters ϕ^o, b or θ^o increasing, the variations of the band edges and characteristic structures of the final parameters are easily recognizable and generally very smooth.

B. Variations with ϕ^o.

The information gathered from a series of final parameter plots can now be represented in a more compact form, to show the variation of the band boundaries with another parameter such as ϕ^o. As in the 1-D case, two methods can be selected for this purpose.

1. The linear ϕ^o vs. T_t^o map can have the ϕ^o axis scaled to reflect the correct probability distribution function (see Sec. 2.6.5), to obtain reaction probabilities by graphical methods. It can also be used to display additional information such as product quantum numbers, angular distributions, statistical regions, etc. in the form of contour maps (see Fig.16a), and is in general the more accurate representation. In Fig.40a the ϕ^o vs. T_t^o band plot for the collinear calculations (v=0,J=0, b=0, ϕ^o=0^o) on the YL surface are compared to the one obtained using the SSMK surface (dashed lines, corrected for a reaction shell radius of 4 Å and a different barrier height of 0.477 eV, as discussed in Sec.2.6.5). The qualitative behavior of the reactivity bands is quite similar, although the fit would seem better if the SSMK results were shifted about 90^o downwards along the ϕ^o axis. The agreement of the reaction probability curves (P_{OT}^R) shown in Fig.40b, however,is very good, the major difference being a slightly higher reactivity of the SSMK surface (dashed line) and a higher cut-off energy. This is not surprising since the YL surface can be expected to be more similar to the SSMK surface scaled to a lower barrier height[38b,52], i.e. the QC* curve in Fig.14b. This was related to a slightly narrower reaction channel for the low barrier surfaces (see Sec.3.4.3)

Figure 40

(a) Linear reactivity map of ϕ^o vs. T_t^o, for collinear $H+H_2$ and a reaction shell radius (ρ^o) of 4 Å. (———) YL surface; (-------) SSMK surface.

(b) Total reaction probabilities P_{OT}^R, obtained by graphical summation from (a).

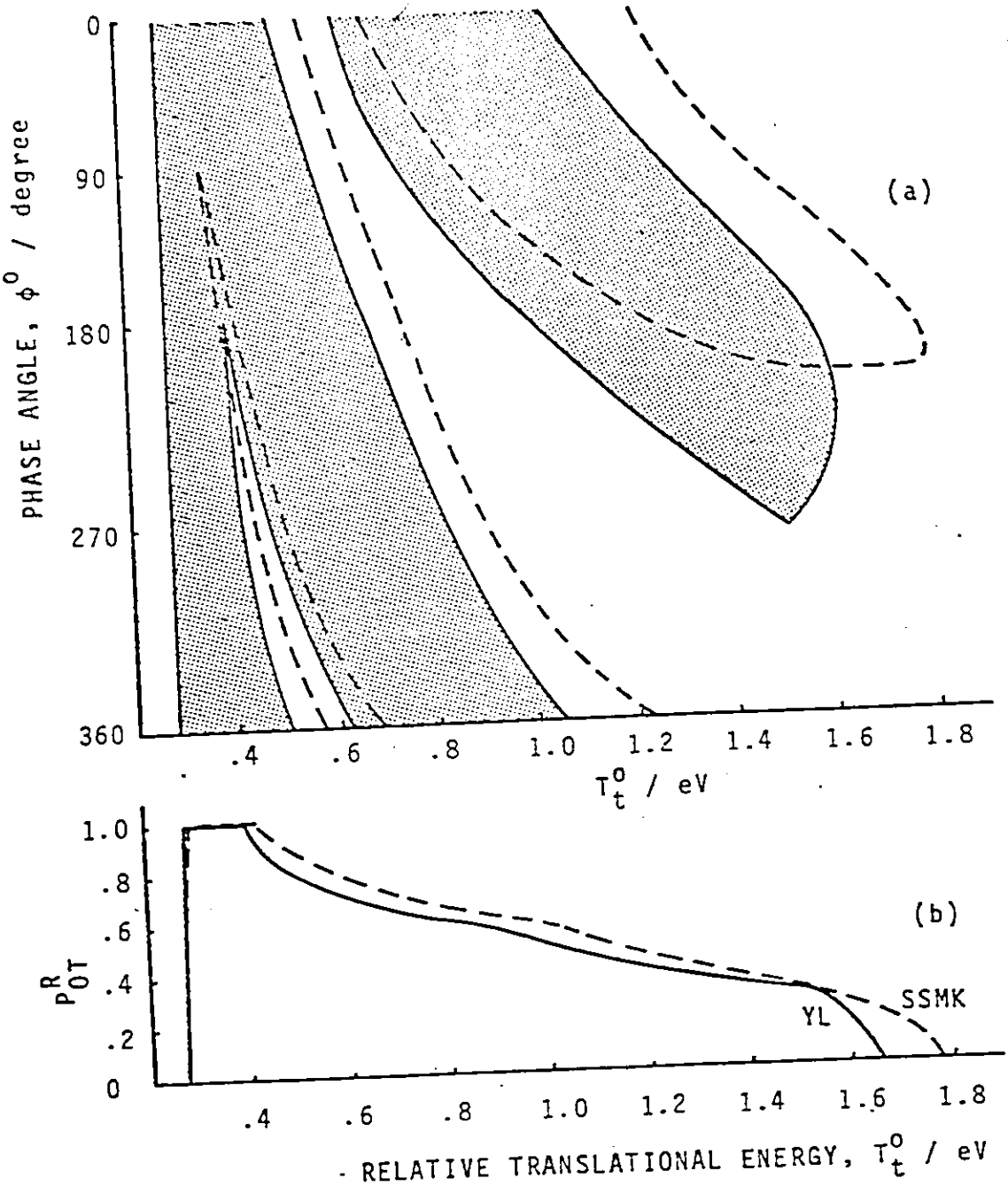
PHASE ANGLE, ϕ^o / degree
0
90
180
270
360
(a)
.4
.6
.8
1.0
1.2
1.4
1.6
1.8
T_t^o / eV
P_{OT}^R
1.0
.8
.6
.4
.2
0
(b)
SSMK
YL
RELATIVE TRANSLATIONAL ENERGY, T_t^o / eV

which is also evident from the slightly higher force constant for the symmetric stretch (A_S=0.32 a.u.) for the YL surface, compared to the value of 0.31 a.u. reported for the SSMK surface (see Table II).

2. The polar form of the ϕ vs. T_t^o map demonstrates the regularity and continuity of the bands much more clearly, and allows a more direct comparison between related but different cases (see Sec.3.3.2). In Fig.41a-d some such maps are displayed for the collinear (a; θ^o=0^o,b=0) and various non-linear results (b-d; θ^o=45^o, b=0,0.5,1.0 a.u.). Fig.41a does not provide much new information, since it is essentially the same as Fig.40a and very similar to other polar plots for collinear $H+H_2$ on the SSMK surface (Figs.15 and 24a). It serves to point out the essential features of 1-D results: the threshold (inner circle) is constant (0.28 $\pm$ 0.01 eV) at all ϕ^o; the band boundaries shift smoothly and continuously to higher T_t^o with increasing ϕ^o so that a characteristic spiral form is obtained; the unreactive branch of the spiral widens, contributing to a decrease in reactivity at high T_t^o and a cut-off in reactivity is observed. Fig.41b shows that under quite non-linear conditions (θ^o=45^o,b=0) a very similar behavior can be obtained. The main differences with plot a are a higher threshold (0.4-0.45 eV) which is no longer constant at all ϕ^o, resulting in an eccentric inner circle. The unreactive branch of the spiral still widens, but no cut-off is observed. This leads to the surprising result that the reaction probability increases with increasing deviation from collinearity.

Figure 41

Polar plot of reactivity for coplanar $H+H_2$. Angular coordinate: ϕ^o; radial coordinate: T_t^o. (a) J=0, $\theta^o=0^o$, b=0 (collinear case);

(b) J=0, $\theta^o=45^o$, b=0 a.u.;

(c) J=0, $\theta^o=45^o$, b=0.5 a.u.;

(d) J=0, $\theta^o=45^o$, b=1.0 a.u.

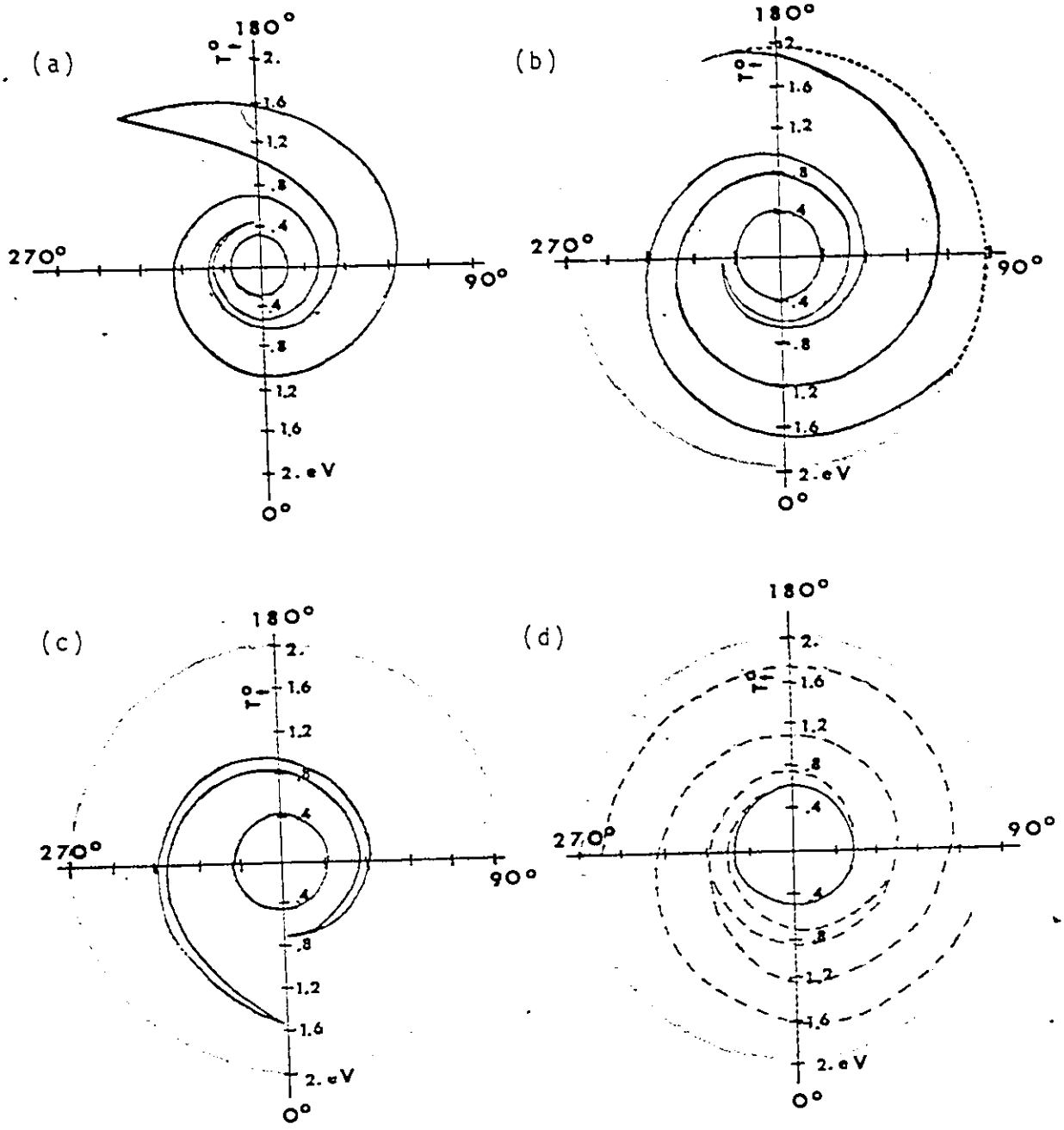
(a)
180°
0°
2.
1.6
1.2
.8
.4
270°
90°
.4
.8
1.2
1.6
2. eV
0°
(b)
180°
0°
2
1.6
1.2
.8
.4
270°
90°
.4
.8
1.2
1.6
2. eV
0°
(c)
180°
0°
2.
1.6
1.2
.8
.4
270°
90°
.4
.8
1.2
1.6
2. eV
0°
(d)
180°
0°
2.
1.6
1.2
.8
.4
270°
90°
.4
.8
1.2
1.6
2. eV
0°

These trends are continued into the next plot c, which is slightly less collinear (θ^o=45^o, b=0.5) than the previous case. The threshold has increased slightly in value and eccentricity (0.42-0.49 eV). The unreactive spiral first increases in width, but then narrows down again, to disappear near (ϕ^o=0^o,T_t^o=1.55 eV). An enormous reactivity is therefore predicted for this special case, over a wide range of energies. A continuation of these trends yields plot d (θ^o=45^o,b=1 a.u.), where the threshold is now between 0.52-0.62 eV, and the unreactive branch of the spiral has completely disappeared. The dashed-dotted lines show a variation of anomalous peaks with ϕ^o and T_t^o, indicating that although the unreactive band has disappeared through a variation of b at constant θ^o (45^o), some traces are left behind in the form of anomalous irregularities in the final parameter plots. These traces also correspond to remnants of unreactivity bands that might appear by varying θ^o at constant b (1 a.u.). The important point is that the plot shows that the characteristic features of the t^R curve still vary roughly in the prescribed manner (towards higher T_t^o with increasing ϕ^o), and that they can be used to determine the shifting patterns of the bands with other (b,θ^o) initial parameters. A continuation of the above trends to θ^o=45^o, b=1.5 a.u. (not shown) breaks down, as no reactivity is observed for this case at all. Anomalous unreactive time peaks are still observed and can be roughly related to the shifting pattern of the reaction threshold and to unreactive bands and reactive anomalous peaks at lower b values.

Figure 42

Polar ϕ^o vs. T_t^o plots of total reactivity.

(a) J=0, b=1.0 a.u., $\theta^o=0^o$;

(b) J=0, b=1.0 a.u., $\theta^o=30^o$;

(c) J=0, b=1.0 a.u., $\theta^o=60^o$;

(d) J=0, b=1.0 a.u., $\theta^o=90^o$;

(e) J=0, b=1.0 a.u., $\theta^o=120^o$;

(f) J=0, b=1.0 a.u., $\theta^o=135^o$.

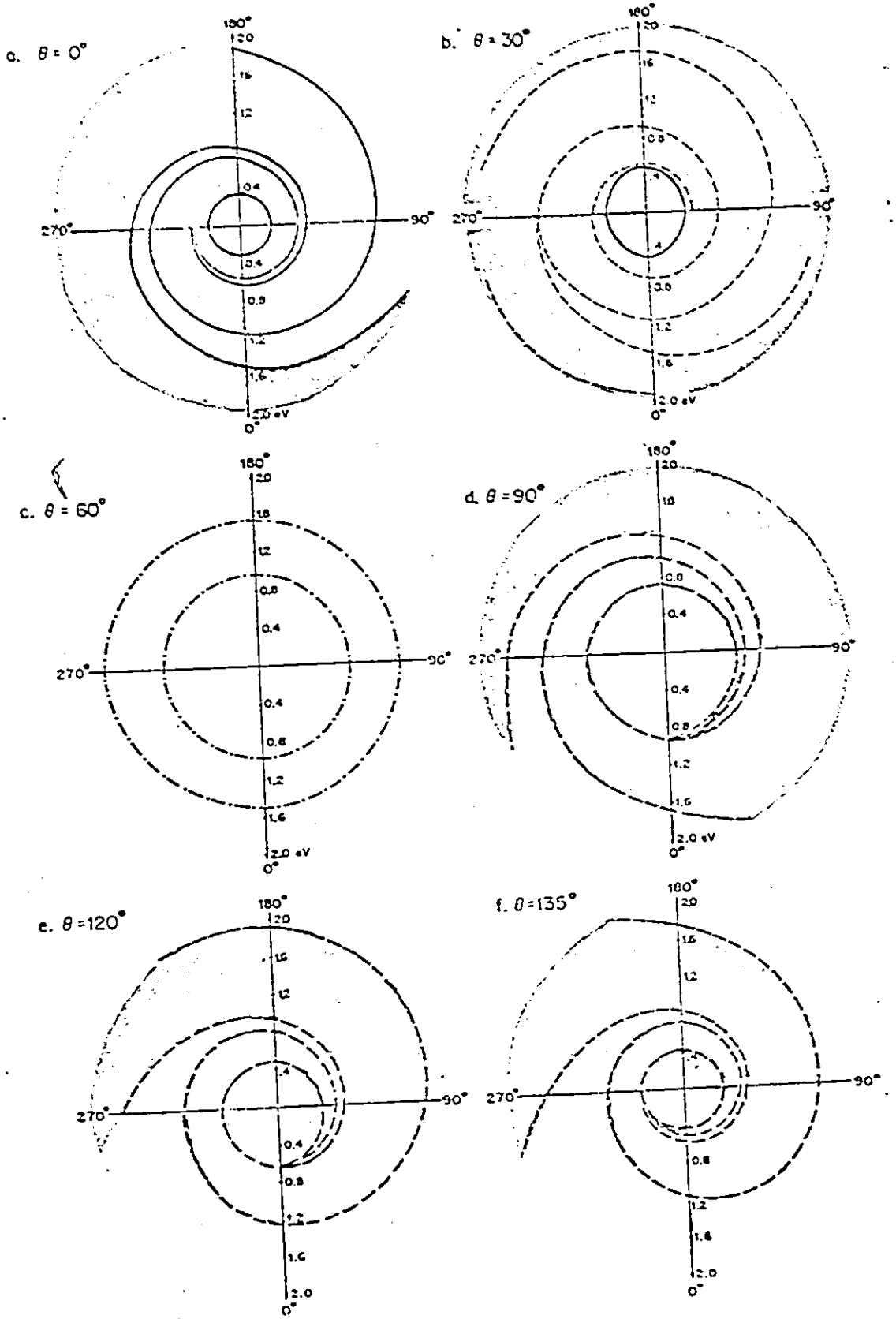
a. θ = 0°
b. θ = 30°
c. θ = 60°
d. θ = 90°
e. θ = 120°
f. θ = 135°
180°
270°
90°
0°
2.0 eV

Fig.42a-f also shows some polar ϕ^o vs. T_t^o plots, arranged in a different order (b=1 a.u., θ^o=0-135^o). In plot a the nearly collinear case (b=1,θ^o=0^o) again shows great similarity to 1-D behavior. The threshold is slightly higher, but quite constant at all ϕ^o (0.3 $\pm$ 0.01 eV; inner circle). The unreactive branch continuously widens, but again no cut-off is observed; reactivity is thus increased compared to the 1-D case. In plot b (θ^o=30^o) the same trend observed for increasing b at constant θ^o (Fig. 41b-d), but at a much accelerated pace, leads to the disappearance of the unreactive band and eccentricity of the threshold (0.42-0.47 eV). The variation of the anomalous reactive peaks are again shown (dashed lines). Similar to the behavior discussed under Fig.41, the next plot (Fig.42c, b=1, θ^o=60^o) is totally unreactive; only the location of the unreactive anomalous peaks are shown (dashed-dotted lines). It is convenient to regard these as asymptotic limits for the threshold (inner circle) and for the unreactive band (outer circle). The next plot d (θ^o=90^o) can then be explained from a reversal of the trends discussed above. The reaction channel has changed (χ=2) as indicated by the heavy dashed lines bordering the shaded areas; product AC+B is formed. The threshold has "decreased" (compared to the inner circle of plot c) and is quite eccentric (0.74-0.93 eV). An unreactive band starts right at the threshold near (ϕ^o=0^o,T_t^o =0.93 eV) and spirals out to higher energies with increasing ϕ^o, continuously widening, but not leading to a high-energy cut-off in reactivity. This trend is continued in plot e (θ^o=120^o), where the threshold is between 0.47 and 0.62 eV, and where the unreactive band shows

a behavior similar to the one in plot d. The overall reactivity (integral of the shaded area) slightly decreases compared to d, although it is difficult to measure by eye. For $\theta^0=135^0$ (f) the result is very similar to e. The threshold is lowered and less eccentric (0.42-0.48 eV), and the unreactive spiral also widens continuously, but seemingly at a lesser rate. This trend continues to $\theta^0 = 150^0$ (not shown), where the overall reactivity is definitely increasing, and to $\theta^0=180^0$ which is identical to $\theta^0=0^0$, except for the formation of a different product (x=2).

Because of the high symmetry of the present case ($H+H_2$, J=0), it must be realized that upon exchanging X = 1, 2:

a. at a single b value, the results obtained for θ^0 and $180^0+\theta^0$ will be identical;

b. combinations of positive b, θ^0 values will correspond to negative combinations ($-b$, $-\theta^0= 360^0- \theta^0$).

Thus, only positive values of b and θ^0 (between 0^0 and 180^0) need to be considered for a complete investigation of this case. This can be used to obtain a continuous picture from Fig.42, in the order c',d',e',f',a,b,c (240^0,270^0,300^0,315^0,0^0,30^0,60^0), where the results for $\theta^0=150^0$ ($\theta'^0=330^0$), with a threshold and a reactivity in between f and a, would nicely fit in. The behavior in 2-D is thus observed to be far more complicated than in 1-D, but seems to follow a consistent pattern. It is therefore of interest to explain these observations in a simple way.

Since no rotation is present in the reactant molecule, it is convenient to imagine the system as a single particle of

reduced mass sliding over three dimensional surfaces of the type shown in Fig.33a-c. The barrier height (i.e. the energy profile along the MERP) increases with increasing bending angle Γ (i.e the angle between the extension of r_{AB} and r_{BC} in the reactants), but the qualitative features and the location of the MERP and the saddlepoint are relatively constant. It is thus still appropriate to discuss reactant and product valleys, the bend in the transition state region connecting them, and the energy barrier, although in the actual case the system is not restricted to any particular surface at constant Γ, but is free to "jump" from surface to surface.

The most interesting result obtained thus far is that the reaction probability increases with decreasing collinearity, but then abruptly cuts off to become zero (see Figs.41,42, and discussions thereof). Since the reactivity in 1-D is limited by the brick wall effect, resulting in a relatively low energy limit for reactivity, these results must be attributed to the availability of alternative ways in 2-D for rounding the bend at the transition state. As A approaches BC, Γ is expected to increase slowly (out of geometrical considerations) if the initial configuration was not collinear. More translational energy is therefore consumed for non-collinear trajectories to climb the foot of the barrier and to climb to surfaces of higher Γ, at least during the first part of the approach. At lesser atom-molecule distances, the strong orientation effect will tend to decrease Γ again, so that the actual barrier height at the moment of closest approach is not excessively

high. This orientation effect decreases with increasing T_t^o, since less time is then available for it to take place. It also decreases with increasing deviation from collinearity, because A will pass farther away from either B or C, reducing the degree of interaction. Thus the non-linear trajectories seem to have the ability to adjust their approach in such a way that the barrier is scaled without a large amount of excess translational energy, eliminating the brick wall effect. If the deviation from collinearity becomes too large, however, this ability is lost as the short-range interaction decreases. Extremely high barriers are then encountered (Γ increases continuously during the approach), leading to a cut-off in reactivity.

Other features of interest are that the variation of the threshold generally follows the expansion and contraction of the reactive regions, and that it gives rise to an eccentrical ellipsoidal form at highly non-linear initial conditions. This is again understandable from the above arguments, where non-linear trajectories have to climb a steeper hill before the orientation effect can take place. More translational energy would be needed to start with, so that a point can be reached where short range interaction can occur, decreasing the barrier height from there on. The reactive threshold is therefore not a direct measure of the barrier height at the time of closest approach. The eccentricity of the reactive threshold further indicates an increased influence of ϕ^o in non-linear collisions,

at low T_t^o. Under these conditions, the extent of the orientation effect is very much dependent on the onset of short range interactions, and the greater dependence on ϕ^o can be understood. Thus, at a favorable ϕ^o, the AB or AC distance is short enough to induce the orientation effect when A still possesses some translational energy, enough to scale the now decreasing barrier. At less favorable ϕ^o, the same amount of T_t^o does not lead to reaction, because the orientation effect occurs too late. The atom A, having lost all its translational energy by climbing the steeper hill, slides back into the reactant valley. At low b and θ^o, the value of ϕ^o is not so critical since the slope of the barrier is more gentle, so that the arguments in the 1-D case (cf.Sec.3.4.3 C) apply.

It must further be realized that b and θ are closely related in that they constitute a measure of non-linearity. In fact, the angle η, which is used by many workers [45,46,71,107] instead of θ to describe the rotational phase, can be calculated from

$$\eta = \theta + \arcsin(b/R_{A,BC}), \qquad (106)$$

as is easily verified from Fig.30. It is therefore not very surprising that many similarities in the behavior patterns relating the individual plots in Figs.41 and 42 were detected. This might be an artifact of the rotationless case, where θ is relatively constant during a major portion of the approach. When initial rotational motion is present, the effect of θ^o on the outcome of the trajectories can be expected to be quite different from the present case, and from the dependence on b.

C. T_t^o vs. b Maps.

In Fig.43a-e the band edges are plotted as a function of b and T_t^o, at $\phi^o=0^o$ and several θ^o values. At $\theta^o=0^o$ (a) the B end is always closer to the incoming A atom, and because of the symmetry considerations as applied in the previous section the results for negative b values are identical with those at positive b. A narrow low-energy unreactive region is seen near 0.6 eV, extending from b=-1.5 to 1.5 a.u. At low impact parameters (less than 0.5 a.u.) a cut-off in reactivity is observed, indicating that the slope of the barrier along the approach coordinate is not steep enough to absorb excess translational energy, causing the brick wall effect. This cut-off region does not disappear completely until very high impact parameters; for b between $\pm$ 0.5 and $\pm$ 1.5 a.u. a high energy reactive region appears below 2.0 eV. This shows that a higher barrier is actually more favorable for reaction at high T_t^o, since the strong orientation effect is expected only to occur at lower T_t^o. At impact parameters between $\pm$ 1.5 to $\pm$ 1.7 no unreactive bands are observed above the threshold (0.44-0.5 eV) and below 2.0 eV. The reactivity (at constant b) then decreases until it completely disappears at the maximum impact parameter, b_{max} = 2.2 a.u. At $\theta^o=22.5^o$ (b) the symmetry of the plot has been slightly distorted, as if it were stretched towards high T_t^o and negative b, with the low-energy part of the plot reluctant to follow. The tip of a reactive region with χ=2 is beginning to show near b=1.25 a.u., T_t^o=2.0 eV. The maximum impact parameter is

Figure 43

Linear b vs. T_t^o maps of reactivity, at various θ^o values and J=0, $\phi^o=0^o$. The shaded reactive regions are bounded by solid lines for X=1 (product AB+C), and by dashed lines for X=2 (product AC+B).

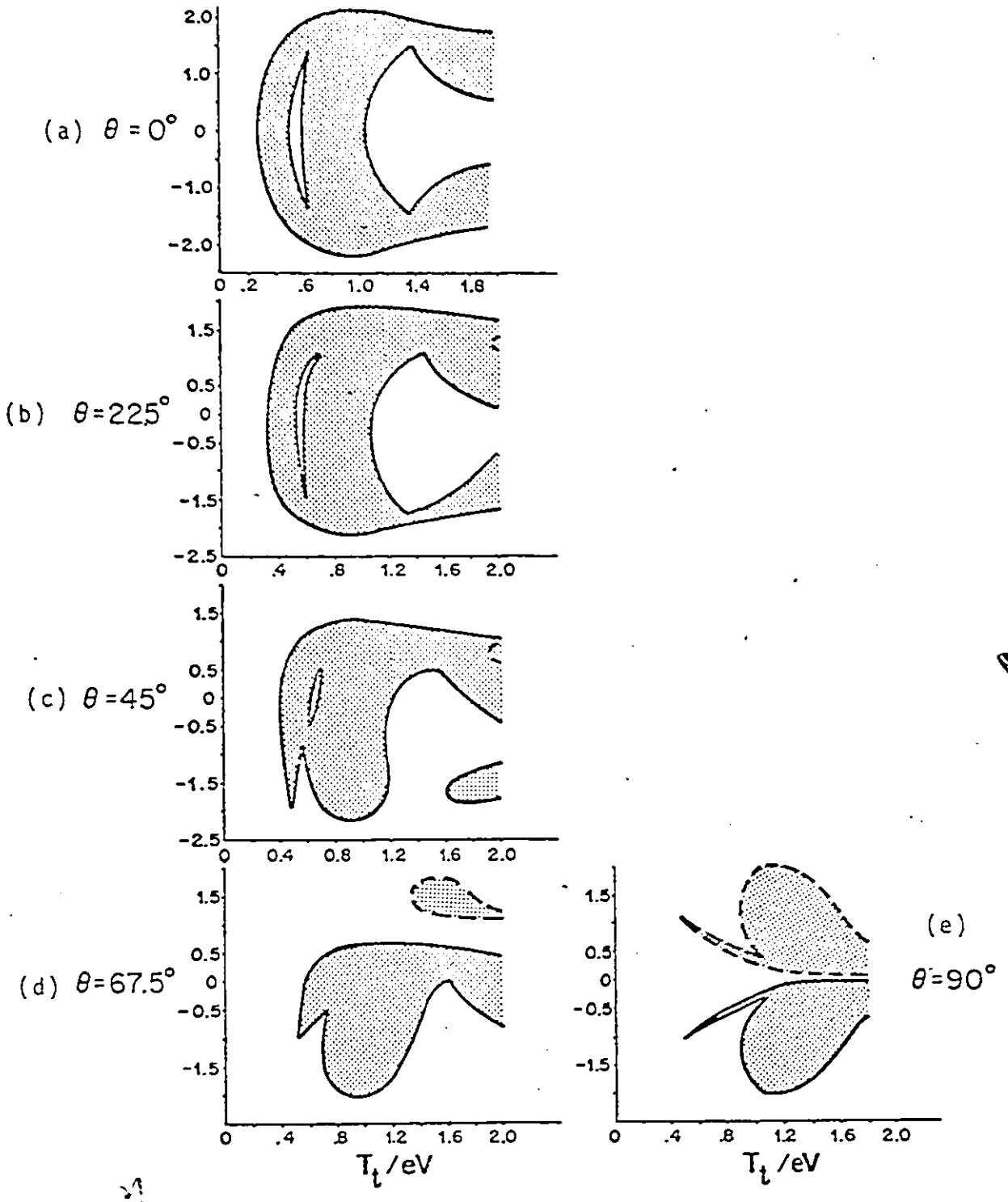
(a) θ = 0°
(b) θ = 22.5°
(c) θ = 45°
(d) θ = 67.5°
(e) θ = 90°
T_t / eV
T_t / eV

around 1.9 a.u. on the positive b side, but remains 2.2 a.u. on the negative b side. Otherwise the features described for plot a are qualitatively still recognizable. The trends above continue to plot c (θ^o=45^o), where the effects of the stretch are greatest in the high energy, highly negative b regions. The effect on the new reactive region (χ=2) is in an opposite direction; it seems to be pushed towards low energies, higher positive impact parameters. The plot has now split along the points of "highest stress", i.e. those points where the reactive regions (χ=1) were the thinnest. This causes the existence of three separated reactive regions at b between -1.2 to -1.8 a.u. The part of the plot on the positive b side is qualitatively unchanged compared to plot b, but the maximum impact parameter here has now dropped to 1.4 a.u. The b_{max} value on the negative side still remains at 2.2 a.u. The trend again continues into plot d (θ^o=67.5^o), where the low energy unreactive region and the high energy reactive region at negative b have completely disappeared because of the stretch. The new reactive region (χ=2) has now separated from the χ=1 region as a result of its opposite behavior. The maximum impact parameter for χ=1 is now 0.7 and -2.1 a.u. on the positive and negative side, but the b_{max} value for χ=2 (positive side only) is 1.8 a.u. Finally, plot e (θ^o=90^o) is evolved from this constantly shifting pattern with θ^o. The map is completely symmetric about the b=0 axis, except for the type of products formed (χ=1 for negative b, χ=2 for positive b). This is again understood from the symmetry considerations of the previous section, and the absence of any

reactivity at b=0 follows from the fact that since B and C are equidistant from A at all times, the orientation effect cannot take place and the unfavorable condition $\eta=90^{o}$ is encountered all along the approach coordinate. The fact that the reaction probability increases rapidly with slight deviations from b=0 indicates the significant role this orientation effect plays in the dynamics of the collisions, since without it the conditions along the approach coordinate would be just as unfavorable as for the b=0 case.

Again some consistent shifting patterns have been observed which need to be understood, at least qualitatively. Keeping the definitions of positive b and positive θ^{o} in mind (Fig.30), the decrease of the $\chi=1$ region on the positive b side can be related to an increasing AB distance at the moment of closest approach with increasing θ^{o}. At the same time, the deviation from collinearity must indeed be associated with less favorable reaction conditions, since the reactive region ($\chi=1$) also decreases with increasing θ^{o} for negative b values. The reactive region with $\chi=2$ increases with increasing θ^{o}, because at positive b values the incoming atom A will start to "see" the C end of the molecule coming out from behind B. At low θ^{o}, the A atom must have sufficient translational energy and relatively low impact parameter to be able to pass B without being scattered too far away from C, for reaction to take place. At high θ^{o} this becomes less of a problem since C emerges more and more from behind B. Reaction with C will thus become possible at lower T_t^{o} and a wider range

of b. The reaction probability will thus increase with θ^o, but even at $\theta^o=90^o$ it is still far from being at its maximum which occurs at $\theta^o=180^o$. The following generalizations can therefore be made:

1. The reactivity in 2-D is generally increased compared to 1-D, because a cooperation between a steeper approach and a strong collinear orientation effect at short distances will eliminate the brick wall effect, but not excessively increase the actual barrier height for reaction.
2. However, closely collinear initial conditions must still be considered to be most favorable for reaction, and by the same argument large deviations from collinearity are very unfavorable.
3. The atoms of the molecule should be assigned reactive and unreactive spheres of influence, beyond which no significant interaction with the translating atom can occur. The radii of these spheres will decrease with increasing (local) T_t, and are expected to depend also on the intramolecular distance at the moment of closest approach. The unreactive sphere of influence is larger than the reactive one, and will cause deflections of the translating atom, which will also depend on the impact parameter. More quantitative definitions are difficult to achieve, but these ideas are essential for a qualitative understanding of the results.
4. For the rotationless case discussions in terms of motion of a reduced mass over a series of three dimensional surfaces

was found to be helpful. Such a procedure may also be applied to the more general cases where rotational motion is present, but would be more difficult to follow because of more rapid upward and downward "jumping" of these surfaces.

D. Plots of θ^o vs T_t^o.

Since the parameter θ^o is a cyclic function similar to ϕ^o (indeed, θ^o can be regarded as the rotational phase angle), two methods can again be applied to map the reactivity bands as a function of θ^o and T_t^o. At an early stage of this investigation it was found that only a polar form of such maps can be obtained, because the band edges were oscillating wildly on a linear θ^o vs. T_t^o plot. Fig.44a-d shows the very peculiar and irregular form of even the polar plots, for $\theta^o=0^o$ and b=0,0.5,1.0,1.5 a.u. Fig.44a (b=0) is perfectly symmetric about the $\theta^o=0^o$ axis. Since the results at θ^o+180^o are identical except for $\chi=2$ instead of $\chi=1$, the plot is also symmetric about the $\theta^o= \pm 90^o$ axis. At low θ^o a low-energy unreactive region exists, and a cut-off in reactivity is observed. At high θ^o a high-energy reactive region appears, extending beyond 2 eV. The reactivity therefore increases between $\theta^o = 30^o$ and 70^o, but decreases again as a high energy cut-off appears beyond $\theta^o=70^o$, to become completely zero at $\theta^o=90^o$. Plot b (b=0.5 a.u.) is completely unsymmetric about the $\theta^o=0^o$ axis. A rotation of 180^o, however, would yield the reactive region with $\chi=2$. The behavior on the positive θ^o side is still roughly similar to that observed in plot a, except that zero reactivity is reached at $\theta^o=75^o$. The reactivity on the negative θ^o side also ceases at $\theta^o=180^o+75^o=255^o=-105^o$. This gives the appearance

Figure 44

Polar β^{o} vs. T_t^{o} maps at J=0, $\phi^{o}=0^{o}$, and various b values.

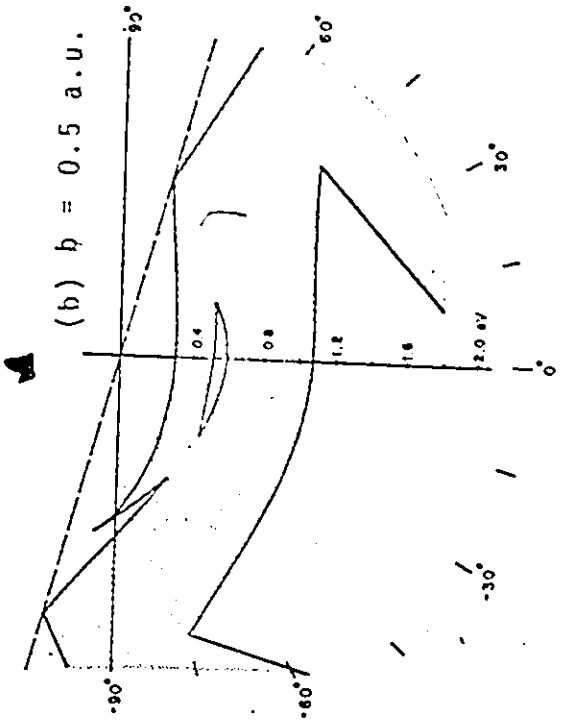
(b) b = 0.5 a.u.
90°
60°
30°
0°
-30°
-60°
-90°
0.4
0.8
1.2
1.6
2.0 eV

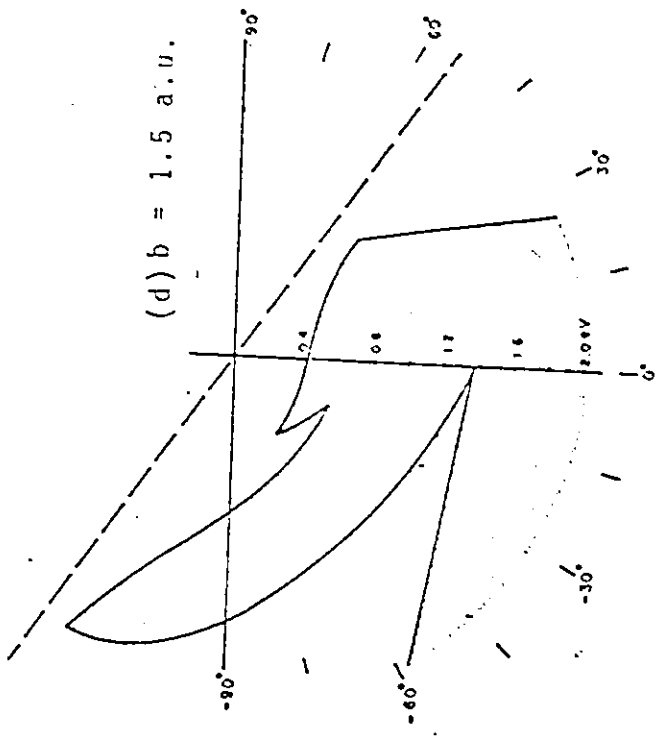
(d) b = 1.5 a.u.
90°
60°
30°
0°
-30°
-60°
-90°
0.4
0.8
1.2
1.6
2.0 eV

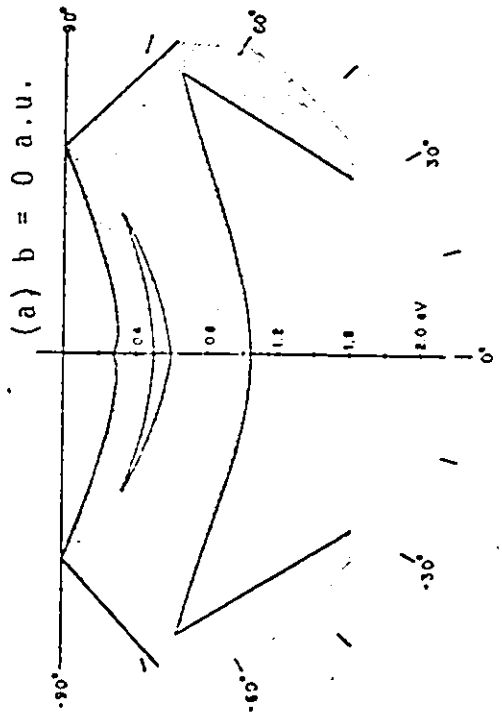
(a) b = 0 a.u.
90°
60°
30°
0°
-30°
-60°
-90°
0.4
0.8
1.2
1.6
2.0 eV

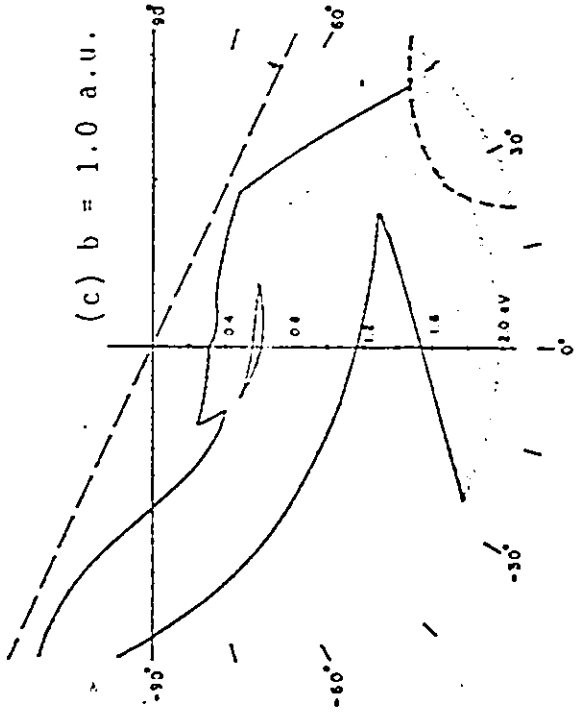
(c) b = 1.0 a.u.
90°
60°
30°
0°
-30°
-60°
-90°
0.4
0.8
1.2
1.6
2.0 eV

that plot a has been rotated by -15^{o} and distorted on the negative θ^{o} side, in a complicated way, to yield plot b. A further rotation and distortion then generates plot c (b=1.0 a.u.), where a high-energy reactive region with χ=2 has appeared between $\theta^{o} = 20^{o}$ and 50^{o}, and where the reactive region has shrunk away from the line separating the predominantly χ=1 and χ=2 regions, which is now located at θ^{o}=65^{o} (145^{o}). A continuation of these trends yields the next plot d (b=1.5 a.u.) where the χ=2 high energy region has disappeared again, and where the dividing line is shifted to θ^{o}= 55^{o} (235^{o}). The positive θ^{o} side now shows one continuous reactive region, extending to beyond 2 eV for low θ^{o} ($<25^{o}$). The map for b=2.0 a.u. is not shown, but reflects a continuation of this rotational pattern, where no reactivity is observed for positive θ^{o} and where the reactive region has shrunk to a narrow band between 0.7-1.2 eV and θ^{o}=-90^{o}→0^{o}. These seemingly very complicated behavior patterns can be qualitatively interpreted in much the same way as in the discussion of Fig.43. In fact, if the plots are closely examined a parallel behavior to the b vs.T_t^{o} maps can be detected. Towards the end of this investigation, after all other maps had been refined by numerous trajectory calculations at critical points, a linear form of the θ^{o} vs. T_t^{o} was again considered. The results are shown in Fig.45, which also summarizes the complete variation of the reactive regions with all initial parameters for the v=0,J=0 case. The individual graphs are linear θ^{o} vs. T_t^{o} maps, ordered horizontally with b increasing, and

vertically with ϕ^o increasing. All previously shown diagrams can be generated from this composite picture in a rough form. The individual θ^o vs. T_t^o plots have now taken on a very familiar form, reminiscent of the b vs. T_t^o plots shown in Fig.43. Even the variation of the plots with increasing b (horizontally) can be described in much the same way as a stretch towards high T_t^o and negative θ^o, although qualitative differences in the effects of such a stretch seem to exist in comparison to Fig.43. The disappearance of the reactive region with χ=2 at b=1.5 a.u. is not quite true, since identical plots with $\theta'^o=\theta^o+180^o$ and χ'=2 do exist but are not shown. The χ=2 region which started to appear at b=1.0 a.u. must have followed the trend predicted for such a region (toward higher positive θ, lower T_t^o; see previous section), and must have joined with the χ'=2 region not shown in these pictures. The variation of these plots with ϕ^o (vertically) can be easily described from the familiarity with ϕ^o vs. T_t^o diagrams in 1-D and 2-D: the variation is cyclic and the band edges shift towards higher T_t^o with increasing ϕ^o. This trend is clearly seen in the first column of Fig.45 (b=0) where the unreactive bands shift to higher T_t^o but a new unreactive band opens up at $\phi^o=270^o$ (bottom) to generate the plot at $\phi^o=0$ (top) by a further shift of the unreactive regions to higher T_t^o. As before (Fig.44a) the θ^o vs. T_t^o plots are symmetric about the $\theta^o=0^o$ axis (dashed lines), at all ϕ^o. The shifting behavior described above can also be observed at other b values, and the variation of the plots with increasing b at constant ϕ^o is quite consistent.

Figure 45

Linear θ^o vs. T_t^o maps of the reactivity bands for J=0, various b values (horizontally) and various ϕ^o values (vertically). The dashed lines indicate the $\theta^o=0^o$ axes.

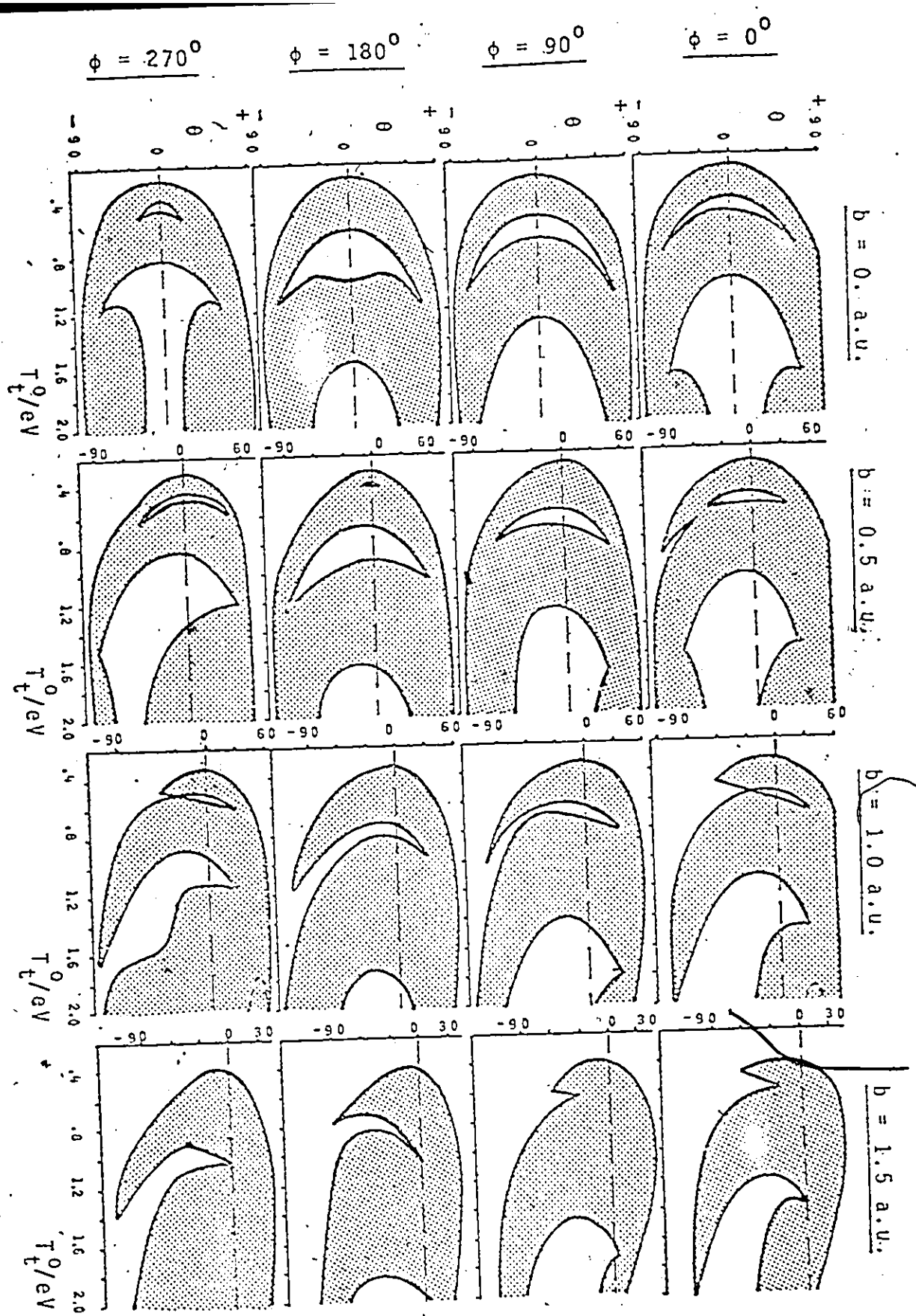
ϕ = 270°
ϕ = 180°
ϕ = 90°
ϕ = 0°
b = 0. a.u.
b = 0.5 a.u.
b = 1.0 a.u.
b = 1.5 a.u.
θ
T_t^o/eV

E. Reaction Probabilities.

The total reaction probability is most generally defined as the sum over the product of all normalized distribution functions F(i) and the individual reaction probability p^R. Here $p^R = 1$ if the outcome of the trajectory, at a particular combination of the free variables i, is reactive, and $p^R = 0$ if it is unreactive. Thus, in the 2-D case at constant v and J, the reaction probability as a function of T_t^o is:

$$P_{2D}^R(T_t^o) = \int_0^{b_{max}} \int_0^{2\pi} \int_0^{2\pi} db\, d\phi^o d\theta^o F(b) F(\phi^o) F(\theta^o) p^R \qquad (107)$$

The limits of integration also define the area of investigation, and reflect the exhaustive variation of the cyclic variables θ^o and ϕ^o (range: $0 \rightarrow 2\pi$). The variation of b must be limited by a maximum impact parameter b_{max}, beyond which no reactivity will be observed[65]. In order to obtain accurate results with fewer calculations, and to improve upon the statistics of Monte Carlo calculations, a smaller value b'_{max} can be chosen, where the reactivity has dropped to insignificant levels[46].

The order of integration is not critical and the most convenient sequence can be selected to evaluate the integral in a series of steps, e.g.:

$$p^R(\theta^o, b, T_t^o) = \int_0^{2\pi} p^R(\phi^o, \theta^o, b, T_t^o)\, F(\phi^o)\, d\phi^o \qquad (108)$$

$$p^R(b, T_t^o) = \int_0^{2\pi} p^R(\theta^o, b, T_t^o)\, F(\theta^o)\, d\theta^o \qquad (109)$$

$$p^R(T_t^o) = \int_0^{b_{max}} p^R(b, T_t^o)\, F(b)\, db \qquad (110)$$

The distribution of ϕ^o has been given in eq.(54), Sec.2.6.5, in terms of the double harmonic approximation, and can be normalized to yield:

$$F(\phi^o)\, d\phi^o = \sum_{i=l,r} \frac{\tau_i}{\pi\tau}\, d\phi_i^o \; ; \; (\phi_l^o = 0 \rightarrow \pi, \phi_r^o = \pi \rightarrow 2\pi) \qquad (111)$$

The distributions of b and θ^o in 2-D are uniform:

$$F(b)\, db = db/b_{max} \; ; \; (b = 0 \rightarrow b_{max}) \qquad (112)$$

$$F(\theta^o)\, d\theta^o = d\theta^o/(2\pi) \; ; \; (\theta^o = 0 \rightarrow 2\pi) \qquad (113)$$

where the limits of variation can be reduced to $\theta^o = 0 \rightarrow \pi$ for the highly symmetric $H+H_2$, J=0 case. The integration can also be carried out as a graphical summation with only the ϕ^o axis scaled to reflect a non-linear distribution. The most direct method is to construct θ^o vs. ϕ^o maps at many b, T_t^o values, and to cut out and weigh the reactive regions, to obtain $P^R(b,T_t^o)$.

In Fig.46 some of these $P^R(b,T_t^o)$ curves (solid lines) as a function of b are compared to the results of other workers. The results of Yates and Lester[58] (dashed-dotted) were obtained from 3-D Monte Carlo calculations on the surface used for the present investigation. Although the general forms of the curves are similar, the quantitative agreement is rather poor. The same can be said about the results of Karplus, Porter and Sharma (KPS)[65] from 3-D Monte Carlo calculations on the PK surface[59], as shown by the dotted line. Saxon and Light (SL)[108] carried out quantum-mechanical and quasi-classical 2-D calculations on a PK type of fit to the scaled SSMK surface[38b]. The classical calculations were quite limited in range and accuracy, so that

Figure 46

Reaction probability curves $P^R(b,T_t^o)$ for collinear $H+H_2$, at various T_t^o values, as a function of the impact parameter.

(———) the present work;

(- - - - -) Yates and Lester[58];

(· · · · · ·) Karplus, Porter and Sharma[65];

(------) Saxon and Light[108].

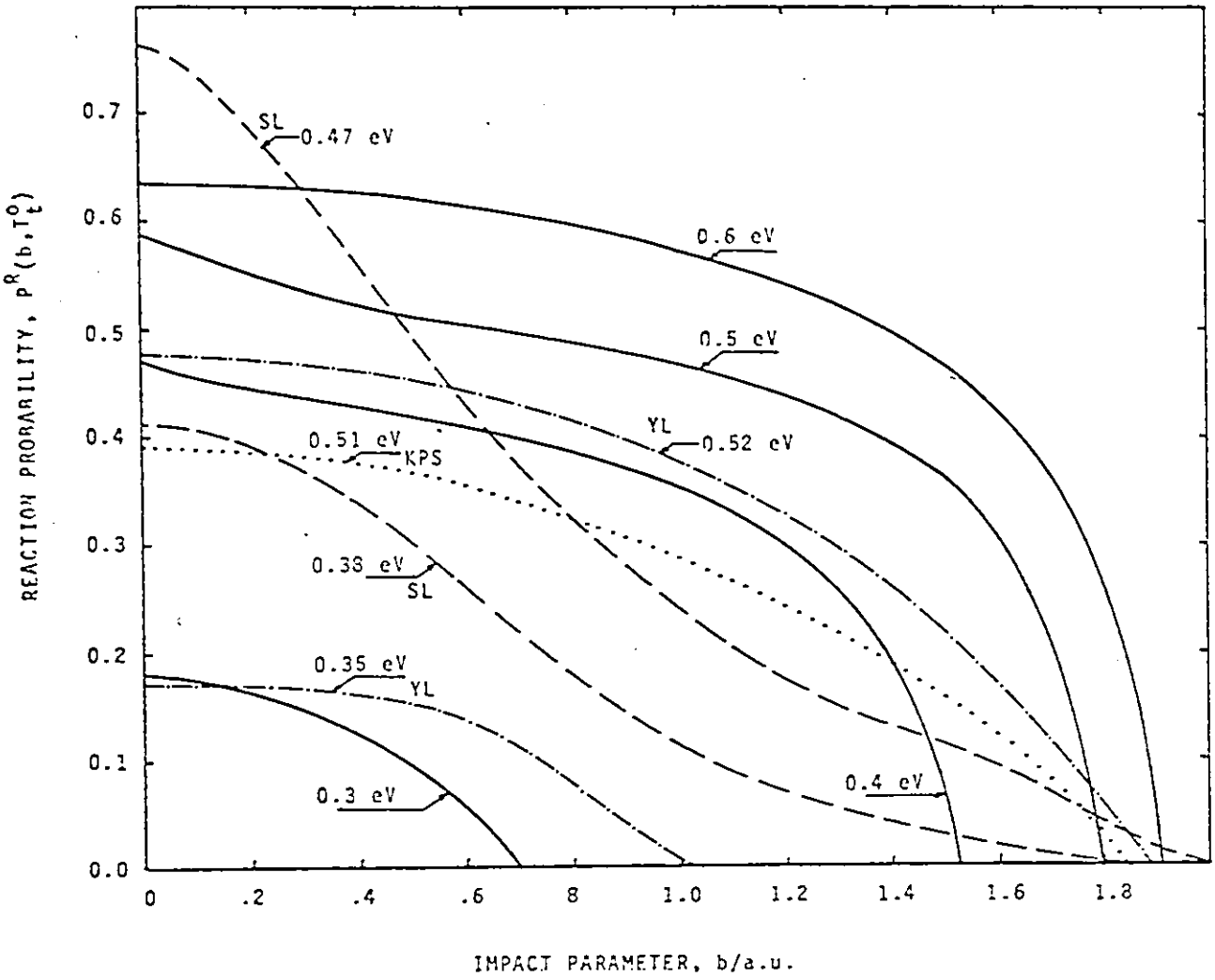
REACTION PROBABILITY, $P^R(b,T_t^o)$
IMPACT PARAMETER, b/a.u.
0.0
0.1
0.2
0.3
0.4
0.5
0.6
0.7
0
.2
.4
.6
8
1.0
1.2
1.4
1.6
1.8
SL
0.47 eV
0.6 eV
0.5 eV
YL
0.52 eV
0.51 eV
KPS
0.38 eV
SL
0.35 eV
YL
0.3 eV
0.4 eV

only the quantum-mechanical results are shown in Fig.46 (dashed lines). This time even the shapes of the curves are different from the results obtained in the present study. The classical points calculated by Saxon and Light would predict a slightly broader distribution, but no quantitative agreement would be obtained. In general the probability curves obtained in the present investigation are more square than the results obtained by others. The 2-D results seem definitely more reactive at low impact parameters, and the classical 2-D results show a steeper drop-off at higher impact parameters.

Purely numerical averaging methods were also tested, but were found to be less reliable, giving rise to less smooth behavior of the curves and a standard deviation from the results shown in the order of 2%, considered as the limit of accuracy. The band continuity property can in principle still be used to obtain more accurate results, using many more intermediate values of ϕ^o, θ^o and b. However, the graphical method would soon become tedious since many more maps will be needed. The numerical method would become feasible if the maps are fitted by analytical functions (e.g. splines), so that reliable interpolations and integrations can be carried out on the computer.

The $P^R(b,T_t^o)$ vs. b curves were graphically integrated to obtain $P^R(T_t^o)$. Eqs.(110) and (112) show that this normalized probability is inversely proportional to b_{max}. An absolute measure of the reactivity can be obtained by defining a "cross section" $S^R_{2D}(T_t^o) = b_{max} P^R(T_t^o)$ (a.u.), which is more suitable for comparison to other work. To allow qualitative comparisons

with 3-D calculations, the differences between 2-D and 3-D distribution functions must also be examined. Fig.47 shows the coordinate system for the description of a rotationless three particle system in 3-D. The parameters are similar to those used by Karplus et al.[65], except that θ is defined as an azimuthal angle, whereas the out of plane orientation of the molecule is measured by a polar angle ζ. A third (azimuthal) orientation angle was eliminated, since there is no initial rotational momentum vector (J=0) which need be defined. Atom A and the initial relative velocity vector V_R are in the X,Y plane, V_R is parallel to the Y axis, and the center-of-mass of B-C ($\overline{BC}$) is still located at the origin. The orientation angle θ is now the angle between the projection of the BC axis on the X,Y plane and the Y axis, ζ is the angle of the BC and Z axes. The impact parameter b is still the distance of A from the Y axis, and the maximum impact parameter b_{max} is also schematically indicated. The distribution functions of ϕ^o and θ^o as given by eqs.(111) and (113) remain unchanged. The ζ^o and b distributions are determined from the fraction of the target area (the sphere) covered by constant values of these parameters:

$$F(b)\,db = \frac{2\pi b\,db}{\pi b_{max}^2} = \frac{2b\,db}{b_{max}^2} \quad ; \quad (b=0\rightarrow b_{max}) \tag{114}$$

$$F(\zeta^o)\,d\zeta^o = \frac{2\pi R^2 \sin(\zeta^o)\,d\zeta^o}{4\pi R^2}$$

$$= \tfrac{1}{2}\sin(\zeta^o)\,d\zeta^o \quad ; \quad (\zeta^o=0\rightarrow\pi) \tag{115}$$

where the range of ζ^o can again be reduced to $0 \rightarrow \pi/2$ from

Figure 47

A coordinate system for the selection of initial conditions for 3-D trajectories. The motion of A is initially restricted to the X,Y plane, parallel to the Y axis. A cut-away view of the target sphere (shaded) of radius b_{max} is presented, to indicate how the probability distribution functions can be obtained. The orientation angle θ is measured in the X,Y plane, and the polar angle ζ defines the orientation of the BC molecular axis with respect to the Z axis.

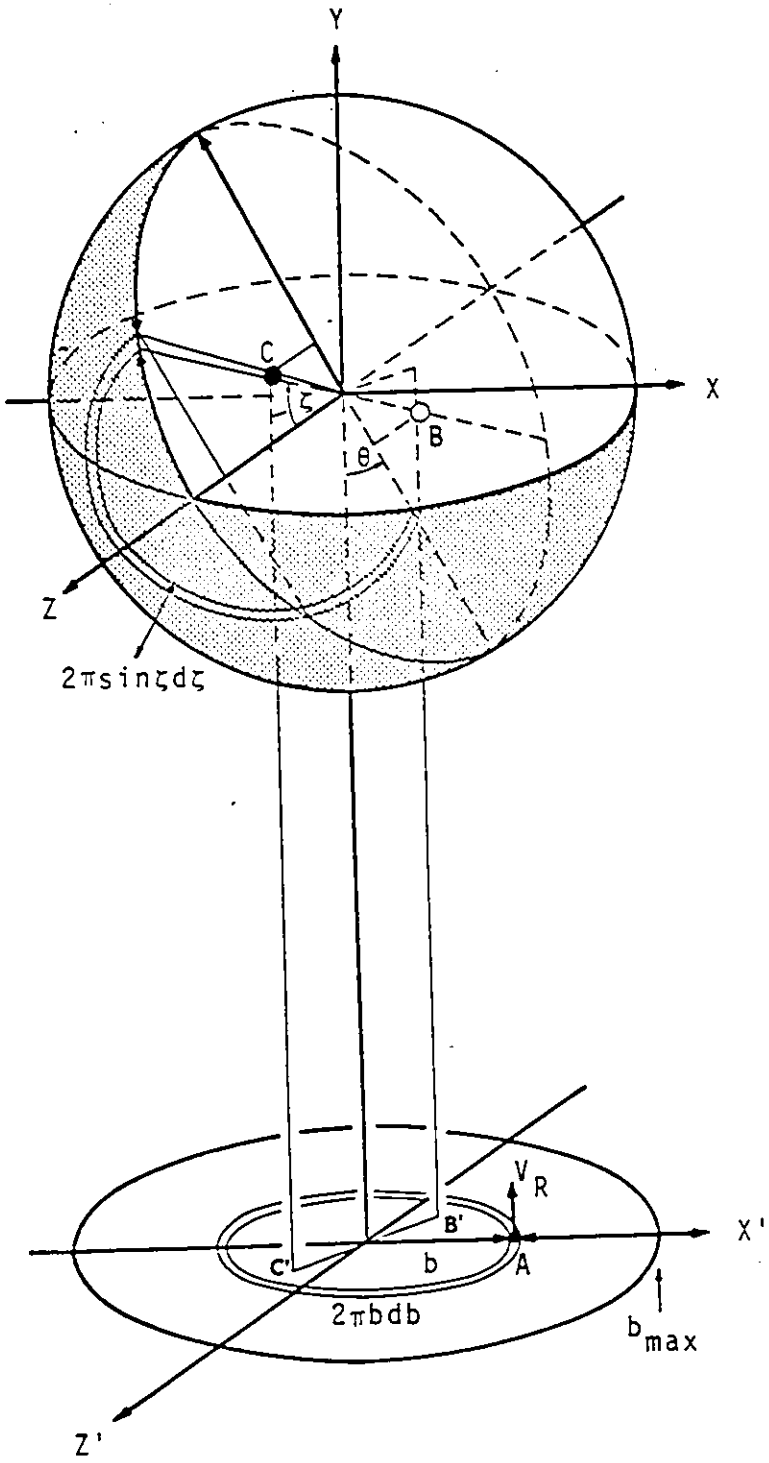

Fig.47: 3-D Coordinate System.

symmetry considerations. The 2-D results ($\gamma^o=90^o$) allow the evaluation of the "3-D" reaction probability, only up to

$$P^R_{"3D"} = P^R_{3D}(\gamma^o=90^o, T^o_t)$$
$$= \frac{2}{b^2_{max}} \int_0^{b_{max}} db\ P^R_{2D}(b, T^o_t)\ b. \qquad (116)$$

A more absolute measure of 3-D reactivity can again be obtained by the definition of the reactive cross section:

$$S^R(T^o_t) = \pi b^2_{max}\ P^R_{3D}(T^o_t) \quad (a.u.)^2, \qquad (117)$$

which might be interpreted as the effective size of the target area, but cannot be simply related to the actual size of the atom and molecule.

In Fig.48 the 2-D and "3-D" cross sections are compared to the results obtained by others. The 2D curve (solid line) was evaluated from the $P^R(b,T^o_t)$ vs. b diagrams, by means of graphical integration. To obtain the "3D" curve (dashed line) the $P^R(b,T^o_t)$ values were first multiplied by b, and then plotted against b and integrated. The final values were then multiplied by 2π to obtain the reactive cross section directly. The value b_{max} = 2.2 a.u., as determined from Fig.43 and from $P^R(b,T^o_t)$ vs. b plots, defines the limits of investigation, outside of which no reactivity was observed. The dashed-dotted line again represents the quantum-mechanical SL results[108] in 2-D, and the dotted curve shows the 3-D Monte Carlo KPS results[65], both for v=J=0. The scale for the 2-D cross sections is shown on the left hand side in units of length; the scale for the 3-D curves is on the right, in units of area. The agreement between the 2D and SL

Figure 48

Reactive cross sections as a function of T_t^o. The scale on the left is for 2D cross sections, the one on the right is for 3D results. All results are for J=0, v=0.

(———) the present work (2D);

(------) Saxon and Light[108], 2D quantum-mechanical results;

(------) the present work, assuming no dependence of the reaction probability on γ° for J=0;

(·····) Karplus, Porter and Sharma[65] (3D).

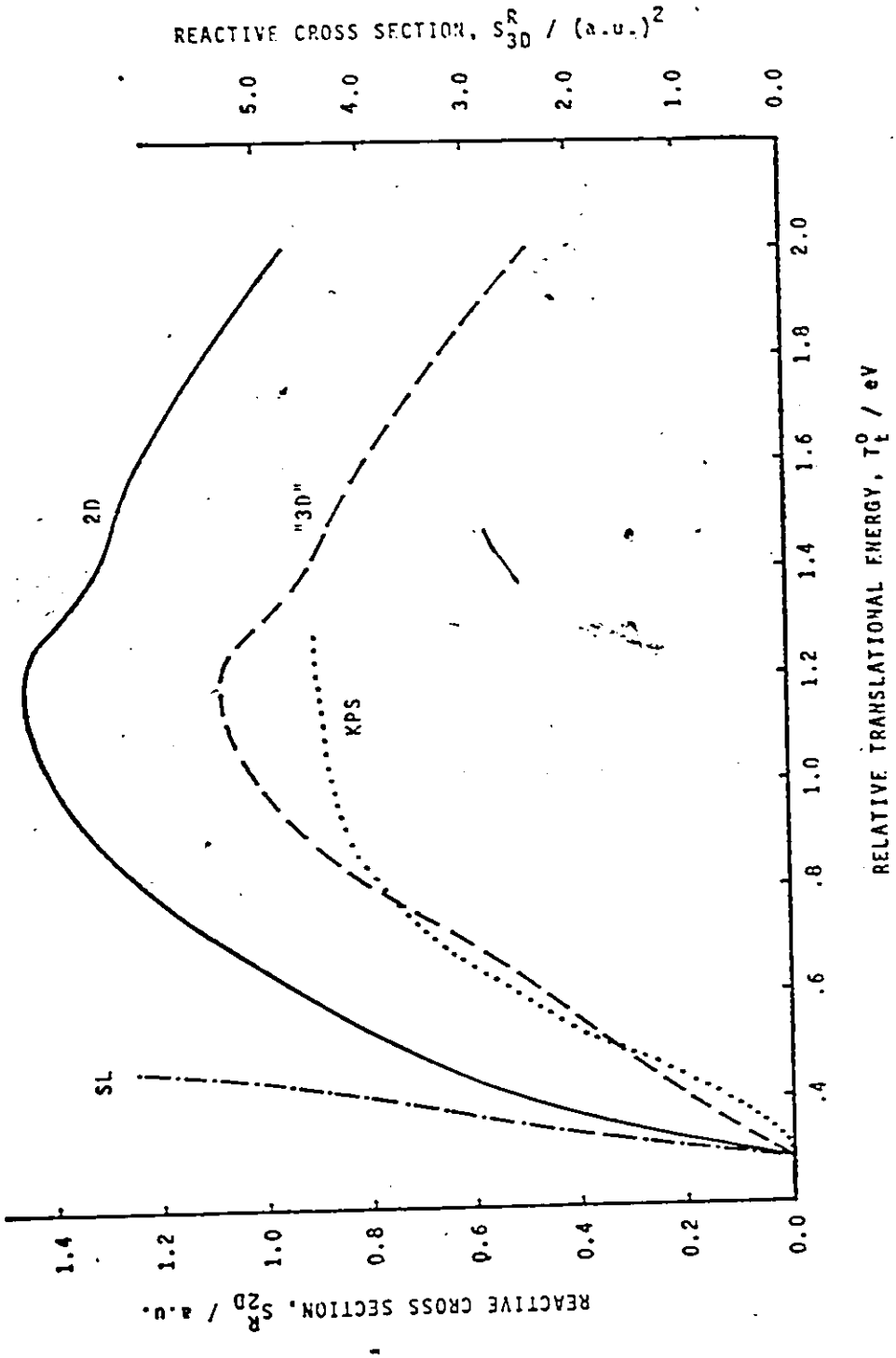
REACTIVE CROSS SECTION, S^R_{3D} / (a.u.)^2
5.0
4.0
3.0
2.0
1.0
0.0
2D
"3D"
KPS
SL
RELATIVE TRANSLATIONAL ENERGY, T^o_t / eV
.4
.6
.8
1.0
1.2
1.4
1.6
1.8
2.0
REACTIVE CROSS SECTION, S^R_{2D} / a.u.
0.0
0.2
0.4
0.6
0.8
1.0
1.2
1.4

curves, and between the "3D" and KPS results, can be termed satisfactory, considering the differences in methods and/or the dimensionality of the calculations. The differences of the surfaces used may also play an important role, but has partly been accounted for by adjusting the KPS results to reflect the lower barrier height (9.13 kcal/mole) of the PK surface (the YL and scaled SSMK surfaces have a barrier height of 9.8 kcal/mole). The SL result shows a very steep behavior at the threshold, more similar to classical 1-D results than to those expected for higher dimensions[65]. The KPS results on the other hand are in surprisingly good agreement with the "3D" curve, especially at low T_t^o. Karplus et al.[65] report that the S^R curve slowly decreases in 3-D for T_t^o in excess of 3 eV. The "3D" results are therefore seen to be too reactive between 0.3-0.5 eV and 0.8-1.5 eV, but not reactive enough between 0.5-0.8 and 1.5-2.0 eV, larger deviations occurring at higher energies.

A further extension of the 2-D results might be achieved by speculating about the dependence of $P_{3D}^R(\zeta^o, T_t^o)$ on ζ^o. If no dependence is assumed, i.e. $P_{3D}^R(\zeta^o, T_t^o) = \text{constant} = P_{"3D"}^R$

$$P_{3D}^R(T_t^o) = P_{"3D"}^R \int_0^{\pi/2} \sin(\zeta^o)\, d\zeta^o = P_{"3D"}^R \qquad (118)$$

Such an assumption is not very reasonable, because a deviation from $\zeta^o=90^o$ will introduce a further deviation from collinearity and will cause the passage of atom A further away from B and C (see Fig.47, where this is schematically indicated by the B'C' projection on the X'Y' plane). This would result in a steeper barrier along the approach coordinate and smaller b_{max} values

for $\zeta^o \neq 90^o$. The steeper threshold of the "3D" curve can then be attributed to a gentler slope of the barrier, and the less reactive regions (0.5-0.8 and 1.5-2.0 eV) to the absence of high energy cut-offs for less collinear initial configurations. The more reactive region (0.8-1.5 eV) must then be attributed to the larger b_{max} value for the coplanar case within this energy range (see Fig.43) which is exaggerated in the extension to "3D" by the multiplication of $P^R_{2D}(b,T^o_t)$ with b. These considerations are admittedly extremely speculative and based on the assumption that the comparison made between the "3D" and KPS curves in Fig.48 is valid. If no corrections had been made for the barrier height, the KPS curve would have been completely more reactive at low T^o_t, and a further shift of this curve towards higher energies would make it completely less reactive below 1.5 eV. The arguments can only be proven or disproven by a comparison to systematic 3-D calculations on the same surface, but can be regarded as a prediction of the results expected from such a calculation.

Further analysis of product energy distributions, scattering angles and rate constants are also possible from the results obtained. However, the restriction to the J=0 case is still too artificial to warrant comparison to experimental results. The real purpose of the study was to develop a feasible method for systematic calculations in higher dimensions, and at this point the need for more quantitative generalizations of the band-edge behavior was felt, in order to be able to reduce the computational requirements even further. Thus, with the present method,

a full 2-D investigation (v=0, J=0-5, T_t^o=0-2 eV , b =0-2 a.u., ϕ^o=0^o-270^o, θ^o=0^o-330^o; ΔJ=1, ΔT_t^o=0.05 eV, Δb=0.5 a.u., $\Delta\phi^o$=90^o, $\Delta\theta^o$=30^o) would require a minimum of about 50,000 trajectory calculations. In the most favorable case the additional 3-D parameters ζ^o=0^o-90^o, ι^o=0^o-180^o (orientation of rotational momentum vector) can be varied in steps of 30^o, leading to an estimated minimum of 1,000,000 trajectories for a full 3-D investigation. In comparison, Monte Carlo calculations require a minimum of 300 trajectories per (J,T_t^o) combination[65], so that 100,000 trajectories can be considered adequate for a full 3-D study. If the consistent shift of the band boundaries with the vibrational phase angle ϕ^o can be predicted quantitatively from basic surface and system parameters, a reduction by a factor of 4 could bring the systematical method into much closer competitition to the Monte Carlo technique. The investigations of the variation of the band boundaries with ϕ^o are further of interest in that the origin of the reactivity bands might be better understood. The trajectory calculations were therefore discontinued, and an attempt was made to develop a simple model which could quantitatively account for the behavior of the reactivity bands, at least for the 1-D case. A further reason for abandoning the trajectory calculations was the accumulation of a massive amount of data, which at the time could not be fully interpreted. Rather than adding to the otherwise quite interesting results, a better understanding of the dynamical behavior of reacting systems was sought, which could aid in future extensions of the study.

4.9. Discussion of the 2-D Results.

Although the comparison of the reaction probabilities of the present study to the results of other workers might be less than convincing (Figs.47 and 49), very good agreement with previous results (cf.Refs.45-54,62,65,81,93,100,107) was obtained in terms of predicted and observed dynamical behavior as a function of the reaction conditions. This is exemplified by the comparison to the systematic 2-D study by Wu and Marcus[107], based on an application of the vibrational-adiabaticity theory[71] and the use of action-angle variables[70] in a natural collisional coordinate system[71]. They examined the product energy distributions, and found that the 2-D trajectories are statistically more vibrationally adiabatic than 1-D trajectories. They deduce that the local (excess) T_t is less effective in exciting product vibration than in 1-D, and attribute this to the availability of more energy sinks in the higher dimension. This result has also been observed in the present study, where it was noted that the v' curves are very insensitive to changes in other product attributes, and generally retain low values. Apart from the fact that rotational excitation is much more effective in the competition for excess energy because of a closer spacing of its energy levels (actually more energy is usually being channeled into product vibration, but this does not show up in the quantum number v'), the excess translational energy is most effectively dissipated by climbing a steeper hill along the approach coordinate in non-linear collisions, so that in general

less local translational energy is available than in the 1-D case to excite product vibration.

Wu and Marcus further treat the collision as a continuous process, where reactant vibration is transformed into the symmetric stretch of the transition state and into product vibration, whereas reactant rotation is converted into the in plane bending mode of the activated complex and into product rotation. The coupling between orbital angular momentum (ℓ) and rotation is also treated in an analytical way, showing the possibility of rotation reversion at low T_t^o and low $J+\ell$. They argue that at high T_t^o the time of closest interaction is too short for the complex to execute a single bending vibration, and that at high $J+\ell$ the system cannot be deflected from a simple BC rotation. The observation of a reversal of rotational motion in Sec.4.8.2 of this study was related to the strong collinear orientation effect, and only observed under conditions which favored the kinematic stability of the collinear geometry, i.e. low b, J, and T_t^o, thus generally confirming Wu and Marcus's predictions. Many other similarities can be pointed out such as the existence of reactive and unreactive regions as a function of ϵ^o and the increase of the width of these regions with T_t^o followed by a drop off at higher T_t^o (see Fig.45), the observation of closely collinear configurations at the moment of closest approach, the treatment of initial vibrational and rotational "action" as constants of motion rather than the corresponding energies, etc.

This comparison shows that qualitatively similar results were obtained from two quite different methods of calculation,

although more quantitative comparisons cannot be made in a straightforward manner, because of the completely different coordinate systems used and the different presentation of the results. The present method can be regarded as more accurate, since no approximations are involved. A comparison of the computational requirements is also instructive. Wu and Marcus used $\Delta\theta^o=10^o-15^o$ and 24 values of ϕ^o for each θ^o. In the present study $\Delta\theta^o=30^o$ and $\Delta\phi^o=90^o$, an economy of a factor of 12, based on the variation of two parameters.

Finally, some inferences can be made about the influence of J by comparing the partial results presented in Fig.36 to Fig.43. Since rotational motion averages over all possible θ, comparison should be made to Fig.43c where $\theta^o=45^o$, and only to the positive b side. Despite the many differences, a remarkable similarity between the two plots is observed. The threshold at J=5,b=0 is only slightly higher than at J=0,b=0 (less than 0.01 eV), and both plots show a narrow low-energy unreactive region. The behavior of the maximum impact parameter as a function of T_t^o is also similar, but at J=5 the absolute value of b_{max} (1.0 a.u.) is lower than at J=0 (1.45 a.u.). Both plots further have a high-energy reactive region with different χ. The only real differences are that at J=5 this second reactive region is separated from the first by an unreactive region, and that it extends to the b=0 axis below 2.0 eV. On the other hand, the unreactive region associated with the brick wall effect for near collinear collisions has disappeared in Fig.36 (J=5). The high energy unreactive region has been shown to reflect the unfavorable

orthogonal geometry at the moment of closest approach (cf.Sec. 8.4.2), which might also be termed a brick wall effect, since a very steep barrier is encountered. These facts all point to the averaging over θ that takes place when $J \neq 0$, and might give some idea of what is to be expected in 3-D where an even more effective averaging process can occur. Other effects such as the influence of rotational momenta seem to play a lesser role, although they might also be responsible for the 2-D brick wall effect mentioned above, and the reduction of the absolute b_{max} value (in Sec.8.4.2 it was argued that the coupling between rotational and orbital momenta would tend to deflect A from its approach coordinate, so that it would pass further away from $\overline{BC}$ at the moment of closest approach, if the direction of rotation and the value of b are both positive or both negative).

In general then, the present 2-D study has been able to uncover many interesting features and to confirm many earlier observations. The results were obtained in a particularly comprehensive form, allowing a total view of the dynamic behavior as a function of various initial parameters to be presented in a single composite map (Fig.45). This has aided the interpretation of many old and new observations in a consistent manner, and the extension of many generalizations from 1-D to 2-D. The method has been shown to be quite economical, and capable of yielding very accurate results if full use of the band continuity property is made. As in the 1-D case the study has opened many possibilities for future extension, e.g. to full 3-D calculations, semi-classical studies, or studies related to energy transfer mechanisms.

CHAPTER 5: DEVELOPMENT OF SIMPLE MODELS

5.1 Introduction.

The systematic calculations revealed very consistent patterns of band behavior, which might be used to achieve further reductions of computational requirements by allowing quantitative a priori predictions to be made. Thus, the shift of the bands to higher energies with increasing vibrational phase angles is observed for all the cases studied so far. This is clearly indicative of some redundancy involved in calculations at many vibrational phase angles but otherwise constant conditions.

In the past, many simple models have been developed to allow the interpretation of dynamic behavior on the basis of system and potential-energy surface characteristics. The hard-sphere collisional models of Suplinskas[91] and Malcolme-Lawes[92] have been successfully applied to several hot-atom reactions. Many other models have been developed to predict energy transfer phenomena [109] and reactive behavior[43,47].

It would be of considerable interest and significance to design a simplified model which would reproduce the main results obtained with the collinear quasi-classical trajectory calculations. Such a model would not only eliminate the necessity of varying the vibrational phase angle, but would also throw some theoretical light on the origin of the reactivity bands. The inclined plane model of Chapuisat, Jean and Salem[110] showed that reactivity bands are generally expected if the vibrational energy

is varied at constant total energy. However, the banding observed in the present study, at constant vibrational phase angles and energies, but at varying translational energies, could not be accounted for. In this chapter, similar but more realistic models are developed on a sounder theoretical basis, in which previously discussed ideas and findings have been incorporated.

5.2 The Vibrational Adiabaticity Assumption.

In Sec.2.2 the separation of the kinetic energy into vibrational and translational terms has been discussed. In the analytical treatment by Marcus[71], translational motion is considered to take place along a curvilinear path, continuously leading from reactants to the transition state and to products (if reaction occurs). Vibrational motion is always normal to the translational path, and vibrational adiabaticity is defined as the adherence to a constant vibrational action variable (classical equivalent of the vibrational quantum number) during the course of the trajectory. The energy content of the vibrational mode then depends on the vibrational potential, which continuously changes along the reaction path. Thus, in fact, the vibrational adiabatic principle requires the transfer of exactly the right amount of energy between the translational and vibrational modes of motion, to keep the system in its correct vibrational level. Non-adiabatic energy transfer, as a rule, only takes place when the system is reflected by the highly curved portion of the reaction channel, i.e. in the vicinity of the transition state.

The translational path, at least along the approach coordinate, is usually taken as the vibrationally averaged reaction path (VARP) and its curvature and location depend on the initial relative translational energy. At low T_t^o it will closely adhere to the minimum energy reaction path (MERP), and at higher energies it will become more rectilinear, owing to a centrifugal force or bobsled effect. The centrifugal potential is dependent on the curvature of the VARP and the distance of the actually vibrating system from the VARP, and is included in the effective potential for vibration, which has a minimum at the VARP[54,71,81,82].

A simplification can be achieved by treating the reaction as a discontinuous process: from reactants up to the transition state (approach coordinate) and from the transition state down to the products (retreat coordinate)[43]. By use of the principle of microscopic reversibility[12,47], only one part of the trajectory need then be examined, with perhaps some overlap in the transition state region where non-adiabatic behavior is most likely to occur. Since the reactants always start out in a well defined vibrational level, whereas products are formed with all kinds of vibrational energy, it is reasonable to treat the problem from the reactant's point of view, i.e. along the approach coordinate. The vibrational adiabaticity principle can further be simplified by assuming that outside the transition state region, limited by the complex shell (see Sec.2.2), no energy transfer will occur between the translational and vibrational modes of motion. This means the assumption of a single

rectilinear translational path (independent on T_t^o), and constant vibrational potentials along this path, so that it can be characterized by the line $r_{BC}=r_e$ (equilibrium separation of BC). In the actual case it was found that an adequate simplification of the problem is achieved by requiring the vibrational period τ to be roughly constant up to the transition state. The vibrational motion can then be treated as a simple cyclic form of motion, described by a single parameter, time. Examination of many 1-D time vs. distance diagrams (not shown, but similar to Figs.37 and 38) indicated that the VARP's are essentially linear and that τ is quite constant, until $r_{AB}=r_{BC}<1.1$ Å, i.e. up to regions very near to the saddle point. The largest errors will therefore occur in the transition state region where the assumptions break down, and where non-adiabatic behavior is expected, but this region is treated somewhat differently.

5.3 Models Based on a Rectilinear Reaction Path.

5.3.1 A Simple Surface Model.

A. The Surface.

Several simple models have been based on a rectilinear reaction path, all hard-sphere models belong in the present category. Mahan[68], for example, discussed extrapolations of reactive behavior on the basis of skewed potential-energy surface models with hard-walled troughs instead of valleys. Tunneling corrections[103] are often based on a zero-curvature

reaction path, and Wu and Levine[81] performed quantum mechanical calculations on a surface where the curvature of the reaction path was artificially set to zero, to examine the effect of dynamic nonadiabaticity. Ogg, Evans and Polanyi[111] analyzed the dynamics on potential-energy surfaces on the basis of a series of rectilinear and perpendicular cuts along the reaction coordinate.

The only model pertaining to reactivity bands was developed by Chapuisat et al.[110] on the basis of some preliminary results of the present study[112] and of some of their own calculations[113]. This model consisted of an inclined plane, bordered by straight walls on either side with an exit located at some point along the slope, as shown in Fig.49a. They varied the vibrational energy and determined the reaction criteria analytically, and obtained qualitatively satisfactory agreement to the banding behavior observed in the dynamical treatment of the isomerization of cyclopropane[113]. The model predicted that no banding was expected for the variation of T_t^o at constant vibrational energy, unless an upper rigid wall is added, as indicated in Fig.49a. This sudden and dramatic change of slope reflects some of the more energetic trajectories back into the lower part of the surface. The same effect of lowering the reactivity above the threshold might also be achieved by introducing a more realistic "curved plane", i.e. a two-dimensional surface with zero curvature in one dimension, and a gradually increasing slope along the other dimension, perpendicular to the first one. The resulting model, in which the rigid walls and the exit were retained, is schematically shown

Figure 49

Simplified surface models:

(a) The inclined plane model of Chapuisat. Jean and Salem[110].

(b) The present "curved-plane" model.

The exit regions represent the transition region in terms of the actual potential-energy surface.

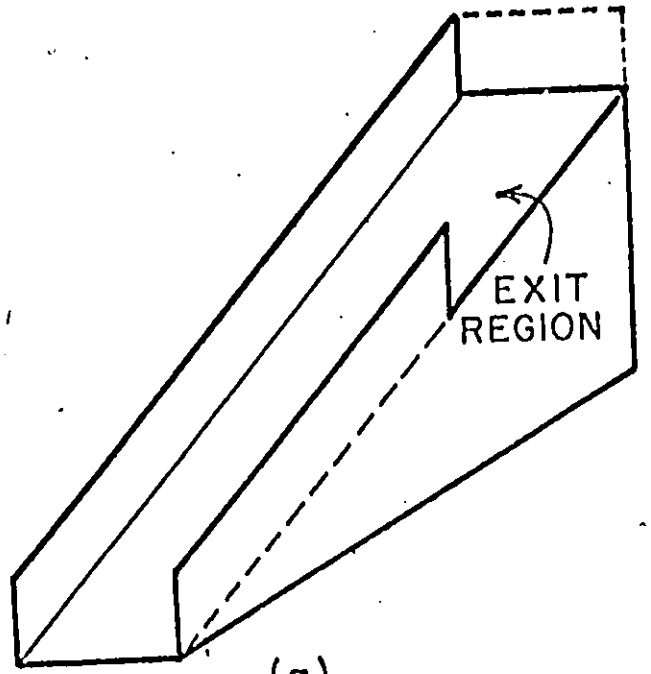

(a)

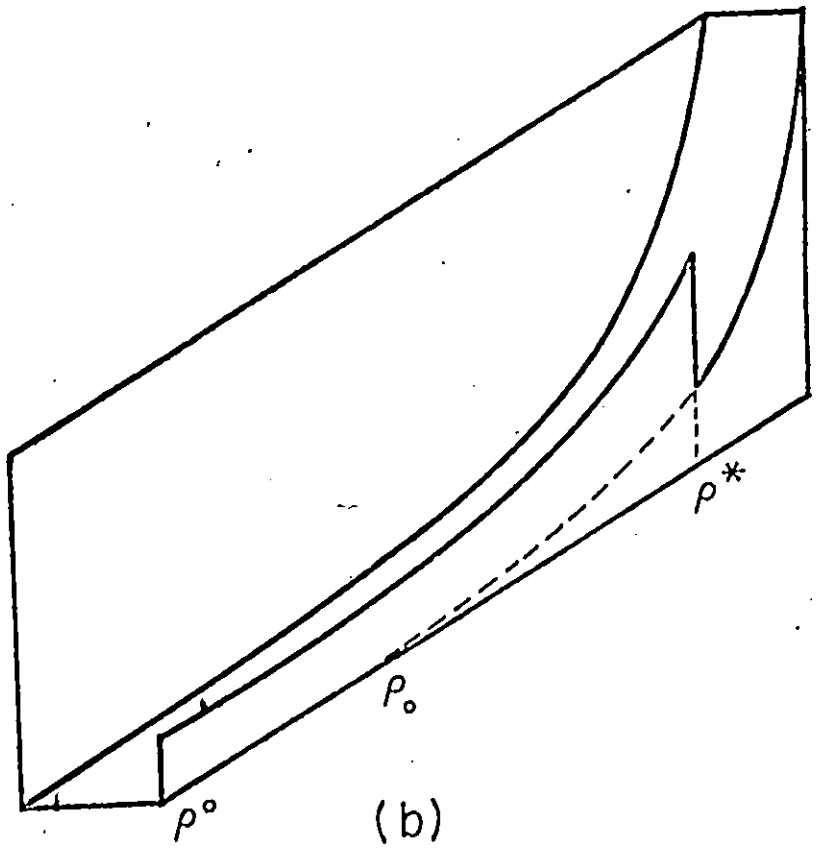

(b)

in Fig.49b, and can be derived from actual potential-energy surfaces using the more restricted vibrational adiabaticity approximation.

The first surface used was obtained by taking a cut through the collinear YL surface corresponding to $r_{BC}=r_e=1.406$ a.u., with $R_{A,BC}=$ 1.7 to 5.2 a.u. in steps of 0.1 a.u. At $R_{A,BC} = 5.3$ a.u. the potential energy becomes slightly negative, returning to a zero value for $R_{A,BC} > 9.7$ a.u. (see Sec.4.6); this portion of the curve was set to zero for the present purposes. The points obtained from this cut were fitted to a polynomial

$$V_a = \sum_{0}^{7} a_i (5.2-R_{A,BC})^i \quad ; \; (R_{A,BC} \leq 5.2 \text{ a.u.}). \qquad (119)$$

The energy profile along this path defines the curvature of the model surface I along the translational coordinate, and is shown as curve a in Fig.50. In this plot and in the subsequent discussion the variable $\rho = R_{A,BC}$ is used; the reaction shell is indicated by $\rho^o = 7.56$ a.u., and the curve is completely flat for $\rho > \rho_o = 5.2$ a.u. In terms of the potential-energy surface model, the exit region of the present model represents the transition state, which must be crossed in a direction towards the product side, for reaction to take place. The beginning of this exit region is marked by ρ^*, which roughly corresponds to the complex shell.

B. Trajectory Calculations.

The vibrational coordinate can be eliminated by using the time t as a basic variable. Since the vibrational motion is described by a constant vibrational period τ, between successive collisions on one wall, the width of the reactant channel is $\frac{1}{2}\tau$.

Figure 50

Model surface profiles:

a. The simple model surface (I), obtained from a cut through the YL potential-energy surface at $r_{BC} = r_e = 1.406$ a.u.

b'. The modified surface (II), where a platform corresponding to the zero-point energy of H_2 has been constructed along the minimum-energy reaction path.

b. The same surface b' lowered by 0.27 eV, the ZPE.

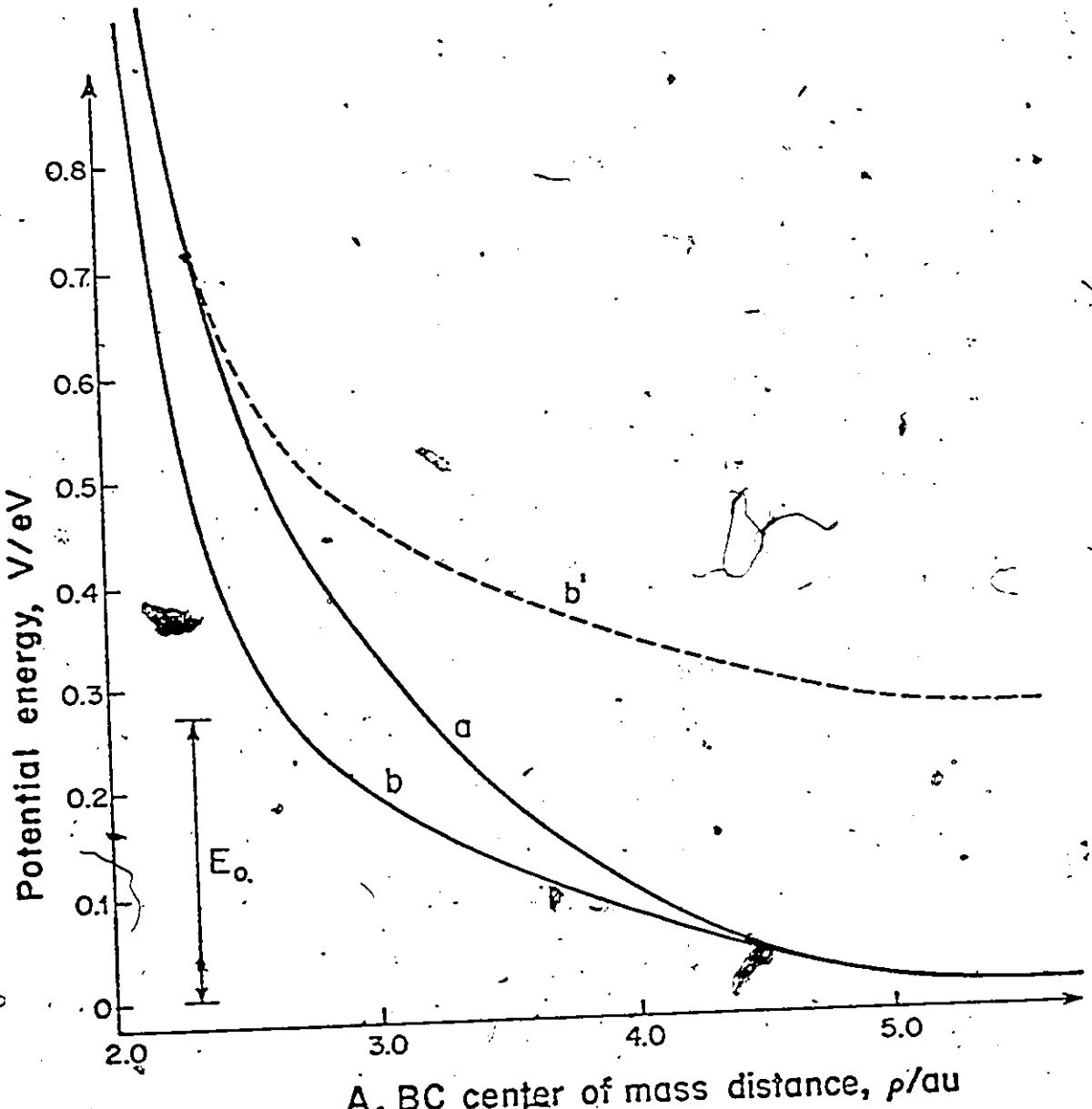
Potential energy, V/eV
0.8
0.7
0.6
0.5
0.4
0.3
0.2
0.1
0
2.0
3.0
4.0
5.0
A, BC center of mass distance, ρ/au
b'
a
b
E_0

The advantage of such a treatment is that only one complete set of translational trajectories has to be calculated, since the vibrational motion is completely defined by the common parameter t. The results can then be adjusted for any initial phase angle ϕ^o, if the relationship $\phi^o(t)$ is known, e.g. from the double harmonic approximation.

The surface is completely flat up to ρ_o, so that the time needed to go from ρ^o to ρ_o is

$$t_o = (\rho^o - \rho_o)/v_t^o, \tag{120}$$

where the initial velocity is constant in this interval:

$$v_t^o = (2T_t^o/\mu_{A,BC})^{\frac{1}{2}}. \tag{121}$$

The Newtonian equation of motion is

$$\mu_{A,BC}\,\ddot{\rho} = -\,dV/d\rho. \tag{122}$$

This can be integrated to

$$\tfrac{1}{2}\,\mu_{A,BC}\,\dot{\rho}^2 = T_t^o - V, \tag{123}$$

which reflects the law of conservation of energy. Because the non-linear form of eq.(123) (V is a polynomial in ρ), for $\rho<\rho_o$, a numerical integration is required to obtain the translational trajectory $\rho(t)$, a typical example of which is shown on the right hand side of Fig.51, corresponding to a particular T_t^o value. The numerical integration need only be done from ρ_o to the maximum, since the part up to ρ_o is linear and evaluated from eq.(120), and the right hand part, beyond the maximum, is obtained by symmetry. The actual motion up the surface, shown on the left hand side of the figure, can be related to the continuous translational

Figure 51

A typical translational trajectory to which $\Delta t^* < \tau$ applies with a R→U boundary at $\phi \geq 270^o$. The actual trajectories are shown for $\phi = 270^o$ (curve a) and $270^o < \phi < 360^o$ (curve b), demonstrating the adjustment of the time axis t'_ϕ. The inset below these trajectories define $\phi = 0^o, 90^o, 180^o, 270^o$ in terms of phase space and time shifts Δt_ϕ.

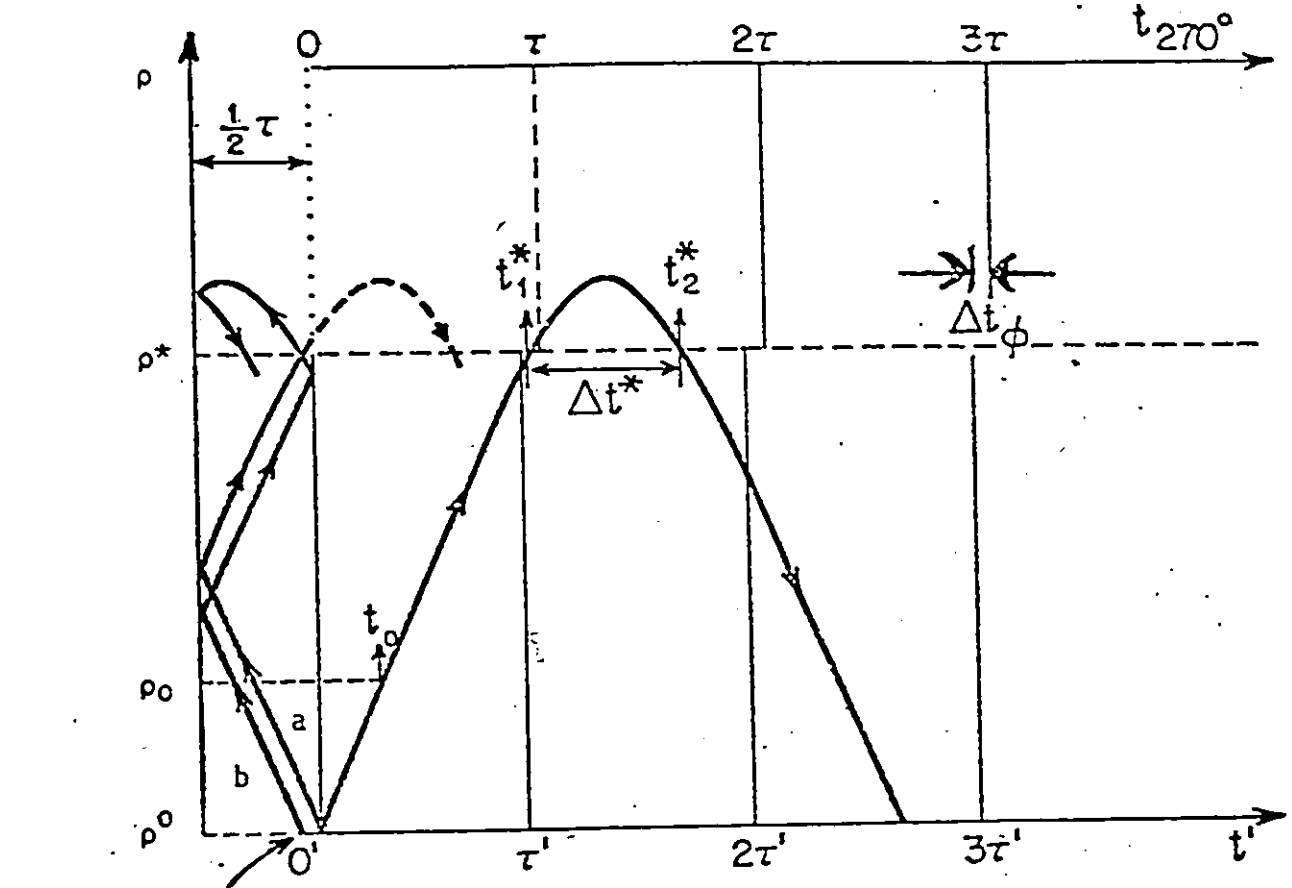

ϕ =	270°	0°	90°	180°	270°
Δt_ϕ =	0	$\frac{1}{2}\tau_r$	$\frac{1}{2}\tau$	$\frac{1}{2}\tau + \frac{1}{2}\tau_\ell$	0, (τ)

trajectory by the multiple reflection technique used by previous workers[114,115]. A necessary condition for reaction is that the exit region is reached, i.e. $T_t^o \geq V(\rho^*)$, where the reactive threshold corresponds to the potential energy $V(\rho^*)$ at the beginning of the exit area. The first time of arrival at ρ^* is denoted by t_1^*, and the second time (on the return trip) as t_2^*. The system thus spends a time period of $\Delta t^* = t_2^* - t_1^*$ in the exit region ($\rho \leq \rho^*$). Reaction can only take place if the extension of the right hand wall is crossed during this interval Δt^*. Reaction always occurs (at any ϕ^o) if $\Delta t^* \geq \tau$, since the system is bound to meet the right hand wall once in time τ. The total reaction probability P^R is unity for T_t^o values which satisfy this condition.

Reactivity bands will be observed if $0 < \Delta t^* < \tau$, since the system may have fallen below the ρ^* level before encountering the right-hand boundary. Reaction will thus occur for some ϕ^o, but not for others, and the reaction probability is given by $P^R = \Delta t^*/\tau$. The conditions can therefore be summarized as:

$$P^R = 0 \text{ , if } \Delta t^* = 0,\ T_t^o \geq V(\rho^*), \tag{124}$$

$$P^R = \Delta t^*/\tau, \text{ if } \Delta t^* < \tau, \tag{125}$$

$$P^R = 1 \text{ , if } \Delta t^* \geq \tau. \tag{126}$$

It follows that plots of P^R vs. T_t^o as found in Chapters 2 and 3, are essentially similar to plots of Δt^* vs. T_t^o, truncated at $\Delta t^* = \tau$ since P^R cannot exceed unity. This will provide a simple means of evaluating the present results, without going through the more complicated procedure of determining the band boundaries

as a function of ϕ^o and T_t^o, as described below.

C. Adjustments for Different Phase Angles.

Reactive and unreactive ϕ^o regions can be determined by superimposing the vibrational phase on the translational motion by following the actual zig-zag trajectory and introducing a shift in the time axis, as illustrated in Fig.51. The computed translational trajectory a corresponds to $\phi^o=270^o$ (see insert in the lower part of Fig.51), and the time scale at the top of the figures applies (t_{270^o}= 0 at the right hand wall).Suppose that instead the initial phase angle is somewhere between 270^o and 0^o, as in trajectory b shown in Fig.51. The time scale is then shifted to the left so that t'=0 corresponds to the beginning of the trajectory; this is shown on the scale at the foot of the figure. The points τ', $2\tau'$, etc. are all shifted equally to the left, as shown. The relationship between the required shift in the time axis, Δt_ϕ, and ϕ^o is shown in the insert at the bottom of the figure, and directly follows from the double harmonic approximation in eq. (42).

A reactive to unreactive (R→U) boundary, for increasing ϕ^o, is found when the actual trajectory hits the right hand wall at ρ^* on its upward path. This means that $t_1^*(\phi)$, which is $t_1^*(270^o)$ to which the correction Δt_ϕ^U has been added, must be an integral multiple of τ:

$$t_1^*(\phi) = t_1^*(270^o) + \Delta t_\phi^U = n_1\tau. \qquad (127)$$

Similarly, the U→R boundary is found when the trajectory hits the right-hand wall at ρ^* on the downward path, and this is

defined by

$$t_2^*(\phi) = t_2^*(270^o) + \Delta t_\phi^R = n_2\tau. \qquad (128)$$

To summarize the procedure: t_1^* and t_2^* are evaluated from the computed translational trajectory and a particular choice of ρ^*. The required time shift Δt_ϕ^{II} (or Δt_ϕ^R) is evaluated as the interval between t_1^* (or t_2^*) and the next larger integral multiple of τ. The band boundary is then determined from the phase angle-time relationship, e.g. eq.(42) for the double harmonic approximation with $\phi^o=270^o$.

D. Results.

Translational trajectories were calculated for surface I with T_t^o ranging from 0.2 to 2.1 eV in steps of 0.1 eV, $\rho^o=7.56$ and $\rho_o=5.2$ a.u. The family of curves thus obtained is shown in Fig.52. At low T_t^o the curves are very broad, narrowing down considerably, but not gaining much added height at higher T_t^o. The sharpness of the maxima is not merely a function of T_t^o but reflect the steepness of the slope of the surface near the turning point (if the surface were a simple inclined plane as in the model of Chapuisat et al., the curves would be parabolic with broader maxima at higher T_t^o). The "exit times" t_1^*, t_2^* and Δt^* can be evaluated from this graph for various ρ^*, but were computed using numerical interpolation formulae.

In Fig.53 plots of Δt^* against T_t^o for various exit positions are compared to the reaction probability curve (dashed line, truncated at $\Delta t^*=\tau$) obtained from quasi-classical computations on the YL surface. The exit locations are $\rho^* = 3.46$ (a),

Figure 52

The family of curves representing translational trajectories on the simple model.

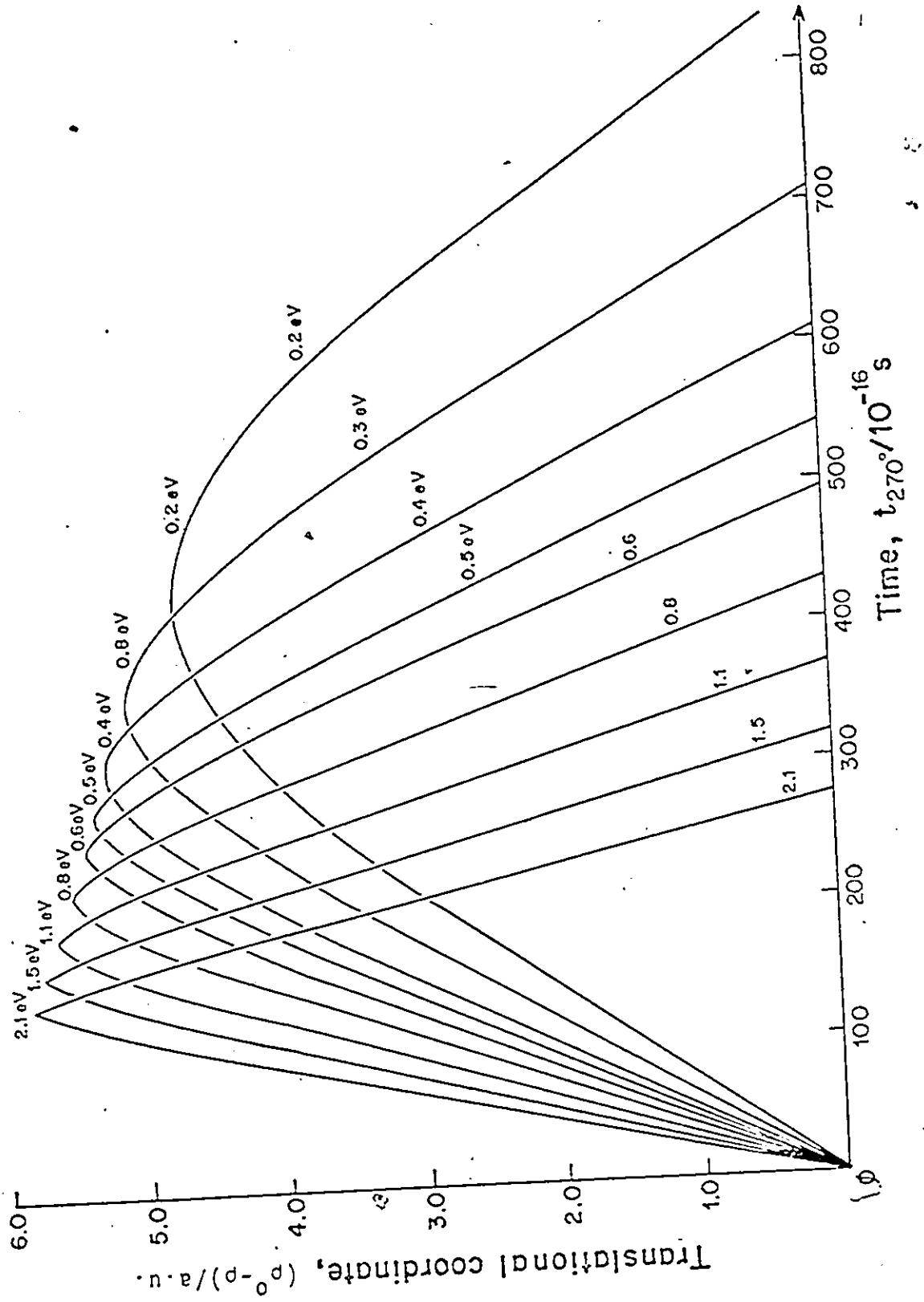
Translational coordinate, $(\rho^0-\rho)/a.u.$
Time, $t_{270°}/10^{-16}$ s
0
100
200
300
400
500
600
700
800
1.0
2.0
3.0
4.0
5.0
6.0
0.2 eV
0.3 eV
0.4 eV
0.5 eV
0.6
0.8
1.1
1.5
2.1
0.2 eV
0.4 eV
0.5 eV
0.6 eV
0.8 eV
1.1 eV
1.5 eV
2.1 eV

Figure 53

Plots of Δt^* against T_t^o for surface I and four different exit locations (curves a-d). The reaction probability curve (dashed line, truncated at $\Delta t^*=\tau$), obtained from quasi-classical calculations on the YL surface, is shown for comparison.

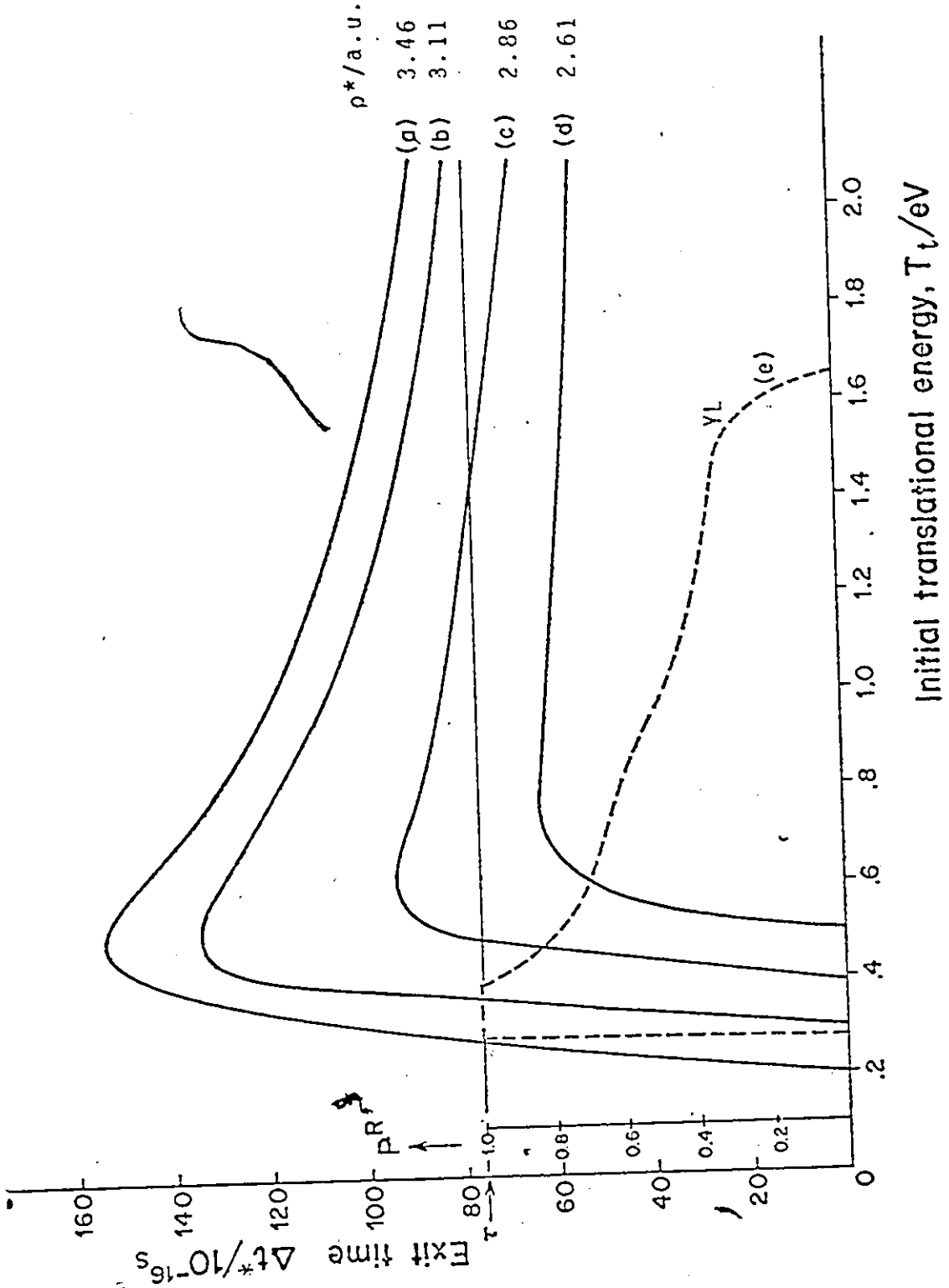
ρ*/a.u.
(a) 3.46
(b) 3.11
(c) 2.86
(d) 2.61
(e)
YL
Exit time Δt*/10⁻¹⁵s
Initial translational energy, T_t/eV
P^R
τ
0
20
40
60
80
100
120
140
160
.2
.4
.6
.8
1.0
1.2
1.4
1.6
1.8
2.0
0.2
0.4
0.6
0.8
1.0

3.11 (b), 2.86 (c) and 2.61 a.u. (d). It would be reasonable to assume that the exit occurs before the saddle point (r_{sp}=1.74, ρ_{sp}=1.5xr_{sp}=2.61 a.u.) is reached, but not much sooner, since at $r_{BC}=r_e$=1.4 a.u., ρ=2.61 would correspond to r_{AB}=1.91 a.u. which is already much larger than r_{sp}. In the absence of any other reference point, ρ^*=2.61 a.u. was thus deemed a reliable estimate for the exit location. Fig. 53 shows that at ρ^*=2.61 a.u. (curve d) $\Delta t^* < \tau$ at all energies, so that the model does lead to banding. The fit to the quasi-classical results (curve e), however, is far from satisfactory in the low-energy region, near the reactive threshold.

5.3.2 Improved Model Surface.

A. The Surface.

For the surface to reproduce the quasi-classical behavior more accurately, it is necessary for it to be less steep in the neighborhood of the exit and more steep later, so as to lower the threshold and increase the reactivity at low T_t^o, and to allow lack of reactivity at higher energies. The first requirement is satisfactorily achieved by simulating the procedure of Tweedale and Laidler[82], who constructed a floor on the potential energy surface, at a height corresponding to the zero-point energy (ZPE) of vibration normal to the MERP. Since the rectilinear path does not correspond to the MERP, it was argued that the potential-energy profile along the path would cross this floor when the deviation from the MERP becomes large enough, e.g. near the exit

location. The ZPE was therefore rather arbitrarily distributed between ρ = 5.2 and 2.6 a.u. by the formula

$$V' = V + ZPE \{1 - V(\rho)/V(2.6)\} \qquad (129)$$

which ensured a smooth curve, which can again be accurately described by the polynomial expression (119). The potential-energy profile thus obtained is shown as curve b' in Fig.50, and represents the curvature of model surface II. The energy is raised by 0.27 eV (ZPE) at the start, and by progressively smaller amounts as ρ decreases. The actual surface II is represented by curve b, where the energy of $H+H_2$ (including ZPE) has been set to zero.

The treatment of Tweedale and Laidler[82] is roughly equivalent to vibrationally averaged quasi-classical calculations, where the centrifugal potential has been neglected, and allows the difference in ZPE of the reactants and the transition state (symmetric stretch) to help the system cross the barrier. This contribution of ZPE to the asymmetric mode of motion is also allowed in exact quasi-classical treatments (see Sec.3.4.3 C and Refs.46-51,65,100), but the simple model made no provision for this. In the present model the total amount of the initial ZPE contributes to passage into the exit region, to compensate for the steeper slope encountered on a rectilinear path.

B. Results.

Fig.51 shows plots of Δt^* against T_t^o for ρ^* = 3.11 (a), 2.86 (b), 2.61 (c), and 2.46 a.u. (d), again compared to the

quasi-classical results (dashed line). For $\rho^* = 2.61$ a.u., the fit at low energies near the threshold has greatly improved, but at higher energies surface I gives slightly better results (cf. curve d in Fig.53).

Fig.55 shows a plot of the band boundaries as a function of ϕ^o and T_t^o, determined for $\rho^* = 2.61$ a.u. according to the procedure outlined in Sec.5.3.1 C. Superimposed on this diagram are the quasi-classical results for the YL surface (dashed lines). The qualitative similarity of the band behavior, shifting to higher T_t^o with increasing ϕ^o, is striking. The unreactive band also widens with increasing energy, but does not lead to a cut-off in reactivity.

5.4 Discussion.

Further improvements of the fit of the Δt^* curve to the quasi-classical results can be obtained by adjusting the "free" parameters $V(\rho)$, ρ^*, and by introducing a vertical wall above the exit. However, a high-energy cut-off cannot be generated by these means since the size of the exit must remain finite, so that $P^R = \Delta t^*/\tau$ would asymptotically approach a small but non-zero value. Other weaknesses of the model are that no reactivity is predicted for vibrationless trajectories, and that the second (high energy) reactive regions for higher mass combinations cannot be reproduced. It is instructive to analyze the shortcomings of the models and the effects of the artificial means introduced to improve the results.

Figure 54

A similar diagram to Fig.53 for the modified surface (II).

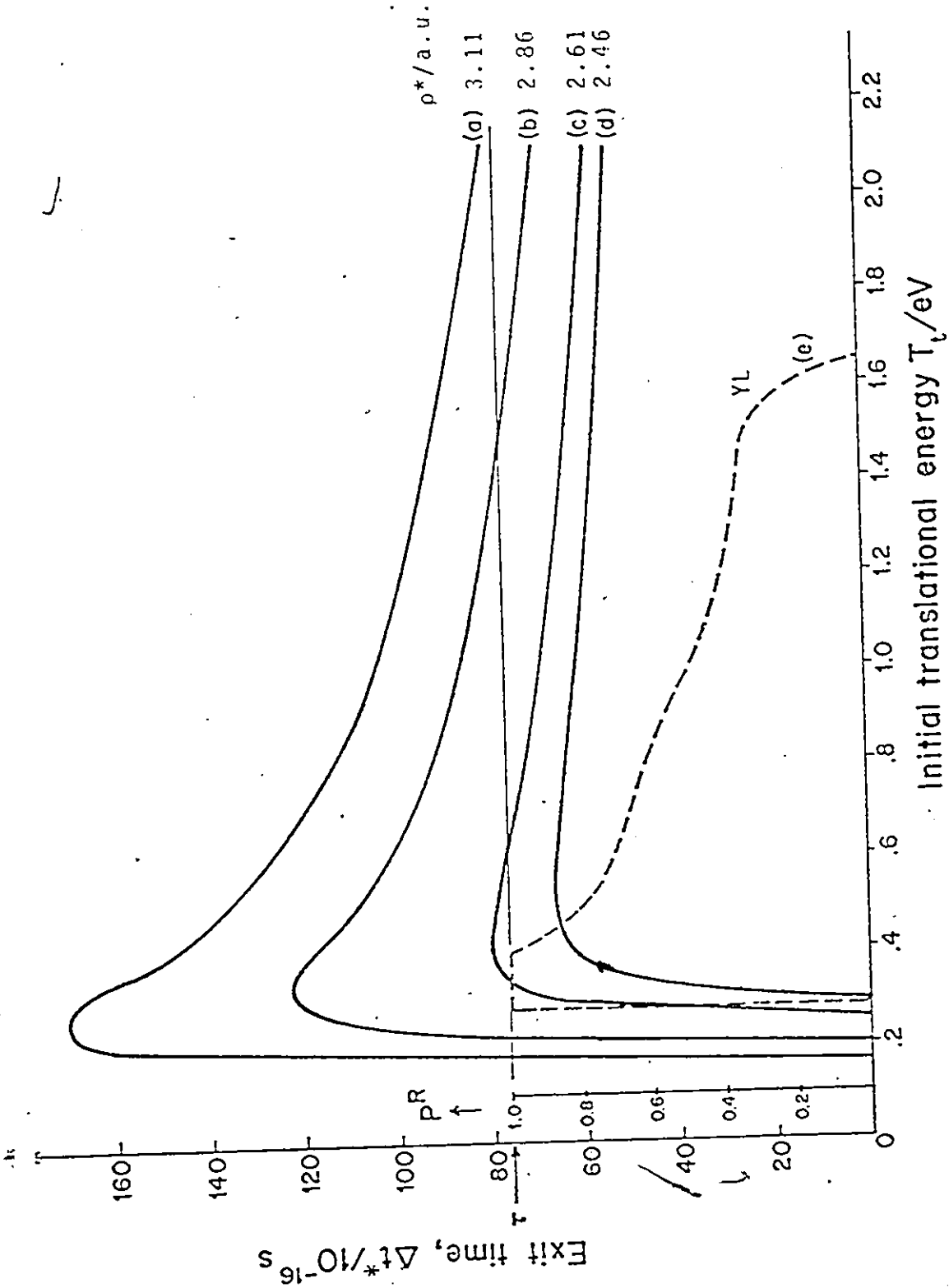
ρ*/a.u.
(a) 3.11
(b) 2.86
(c) 2.61
(d) 2.46
(e)
YL
P^R
Exit time, $\Delta t^*/10^{-16}$ s
Initial translational energy T_t/eV

Figure 55

Reactive (shaded) and unreactive regions as a function of and T_t^o for surface II with ρ^*=2.61 a.u. The boundaries obtained from the quasi-classical calculations are shown as dashed lines.

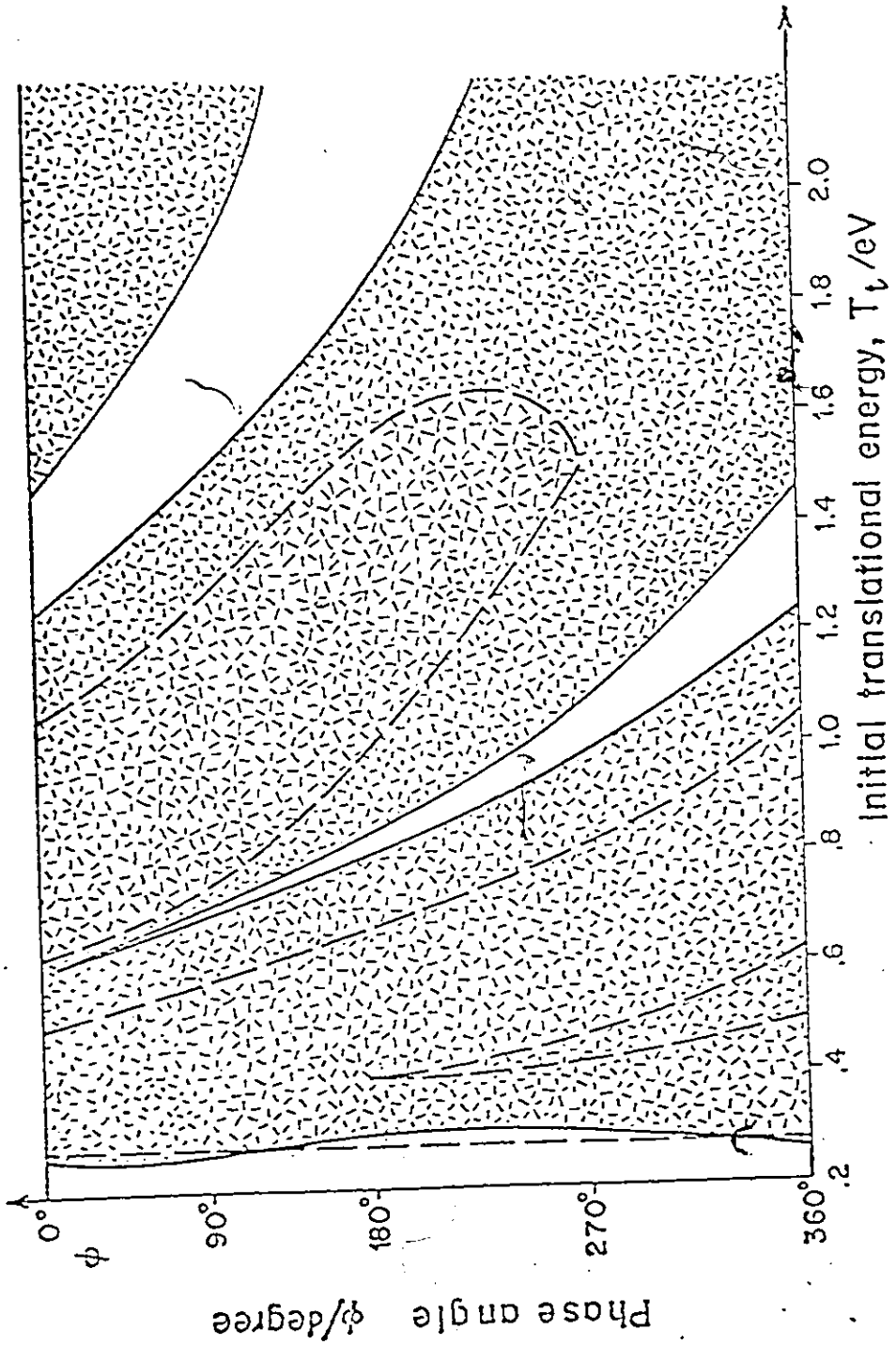
Initial translational energy, T_t/eV
.2
.4
.6
.8
1.0
1.2
1.4
1.6
1.8
2.0
Phase angle ϕ/degree
0°
90°
180°
270°
360°

The failure of the simple model to predict the correct threshold behavior is directly related to the steeper energy profile along the rectilinear cut compared to the actual barrier encountered on the MERP. The introduction of a vibrational floor above the actual surface cannot be fully justified in the present case, although it helps in keeping the vibrating system at roughly the same level as in the actual case, at low T_t^o. For higher energies, however, the inclusion of the centrifugal potential into the effective vibrational potential[54,71,81,82], would cause the original energy profile along the rectilinear cut to become more realistic, but not by much (compare curve c in Fig.53 to curve d in Fig.54). The major problem is that no single simplified surface is adequate to describe the dependence of the translational potential on T_t^o. The consideration of curvilinear reaction paths (actual VARP's) would overcome this deficiency, and would also allow reactivity for vibrationless trajectories.

The absence of a high-energy cut-off and second reactive regions for higher mass combinations must be associated with the neglect of the skew angle ξ (see Secs.3.3.4 and 3.3.5). This can be corrected for by introducing a vertical wall at a $(90^o-\xi)$ angle to the sides of the surface, at some point above the exit. However, individual trajectories must then be calculated separately at every ϕ^o, T_t^o combination, since such a reflecting wall would introduce non-adiabatic behavior, and the outcome of the trajectories would then depend on the point of reflection and the local direction of motion at that point. It would also invalidate

the expression $P^R = \Delta t^*/\tau$, since this was based on the assumption that adiabatic behavior continues in the exit region.

Further, the exit region was considered simply as an extension of the model surface, i.e. as an extension of the reactant channel, whereas the actual transition state includes a sizable portion of the product channel. The dilemma is to determine a suitable reaction criterion which takes into account the time spent in the exit area, the actual geometry of this region, the skew angle and possible non-adiabatic behavior. This problem seems insurmountable as yet, although a solution might be found by examining the energy content of the AB and BC entities in the transition-state region, as suggested for simple hard-sphere models[91,92]. The release and distribution of reactant vibrational energy in the transition-state region, as discussed in Sec.3.4.3 C, must thereby be taken into account.

The consideration of curvilinear reaction paths, on the other hand, does not pose too much of a problem, if it can be assumed that the vibrational and translational modes of motion can still be separated and superimposed , and that the period τ is still roughly constant up to regions near the saddle point. Vibrationless trajectories can then be calculated on the actual potential-energy surface, up to the dividing line (or the first turning point, i.e. $\rho = \rho_{min.}$, $V=T_t^o$), to obtain a rough estimate of the average time spent in the exit region, the energy distributions and local directions of motion. An advantage is that the only remaining free parameter ρ^* is then directly related to the

quasi-classical threshold, through $V(\rho^*) = T_t^{thld.}$. The significance of $T_t^{thld.}$ is then that it brings the system up to a point where pure vibrational motion can cause the system to cross the dividing line. The unsolved problem is again: where and how to evaluate the energy contents of AB and BC to obtain a realistic reaction probaility, and how to superimpose the vibrational motion to obtain the dependence on the initial positional parameters (ϕ^o and ρ^o).

To conclude, however, the simple models were quite successful not only in generating reactivity bands, but also in simulating their dependence on ϕ^o and T_t^o. This indicates that on the actual surface, as in the simplified models, the conditions encountered at the band edges must be essentially the same for any initial phase angle. The behavior of the bands can be rationalized in terms of the shifts of the time axis, Δt_ϕ, associated with each ϕ^o, as was shown in Fig.52, and the difference in T_t^o which will exactly compensate for these time shifts. This is most easily explained using the model. For a particular T_t^o value, a band boundary is encountered at ϕ_1^o if the right-hand wall is exactly met at ρ^*. For a higher phase angle ϕ_2^o, the time axis is shifted towards the left in Fig.51. The translational energy must therefore be increased if at ϕ_2^o the right-hand wall is again to be encountered exactly at ρ^*. In the actual case, a band boundary occurs if the system is reflected at a point of high curvature near the dividing line, with subsequent motion nearly parallel to the ridge separating reactants from products, as if it were

hesitating which side to remain on (see Sec.2.6.2). At a slightly larger initial phase angle, a band boundary is expected to occur if the very same spot was again hit, which by analogy to the model would require a slightly increased T_t^o.

It is therefore evident,that even for the simplest case, collinear $H+H_2$, the dynamic behavior is quite complicated and difficult to predict quantitatively on the basis of a priori considerations of basic surface and system parameters. The development of similar models for higher-dimensional reactions is naturally far more complicated, since the system is no longer restricted to a single three-dimensional potential-energy surface, and because of the larger number of available degrees of freedom. Exact quasi-classical calculations are therefore still the only means of achieving a quantitative understanding of molecular collision processes, with reasonable computational requirements. The band continuity property as a function of ϕ^o and T_t^o, however, has been shown to be quite predictable, qualitatively, since the two parameters are related through the common variable time. This band continuity property can thus be expected to persist in the 3-D case, and can be relied on for accurate interpolations as in the present method.

CLAIMS TO ORIGINAL RESEARCH

1. A method for systematic quasi-classical trajectory calculations has been developed, which offers a powerful alternative to Monte Carlo methods of calculation. The method is based on the observation that the outcome of individual collisions assumes the form of reactivity bands, i.e. regions of alternating reactivity, as a function of the relative translational energy, and that the boundaries of these bands are clearly marked by peaks in the otherwise smooth behavior of the reaction time. Other product attributes, such as internal energies and the scattering angle, show a very similar behavior to the reaction time. The band boundaries and the corresponding breakpoints in the final parameter curves vary in a consistent and continuous manner with individual initial parameter values, which allows complete maps of dynamic behavior to be obtained with relatively few trajectory calculations.

2. The collinear $H+H_2$ reaction and some of its isotopic analogues have been studied with this method over a wide range of energies: 0 to 2 eV. Many new features of interest, such as a high-energy cut-off in reactivity, second reactive regions of different reaction mechanism, the constancy of the threshold with varying mass combinations, and the consistent behavior patterns of the reactivity bands with varying initial parameters, have been observed. These and many previously reported phenomena have been interpreted in a consistent way, in terms of motion of a single particle of reduced mass over a skewed potential-energy surface.

3. Complete maps of reactive behavior have been obtained, and reaction probabilities as a function of the relative translational energy were determined. For collinear T+HT the extraordinary form of the probability curve, showing two reactive regions separated by a large region of zero reaction probability, has been noted. A similar and even more extreme behavior of the collinear D+HD reaction was confirmed.

4. A complete study of the coplanar $H+H_2$ reaction has been made for the case J=0, and the influence of rotational motion was briefly looked into. The persistence of the reactivity bands and their continuous variation with additional coplanar parameters was established. Many new features, such as the increase of reactivity for near collinear initial configurations, but the overall decrease in reactivity with increasing non-linearity, the existence of separate reactive regions where different products were formed, and clear evidence of the strong orientational effect at short atom-molecule distances, have been observed. Many generalizations have been extended from 1-D to 2-D, and most of the observations were interpreted, consistent with the 1-D interpretations, in terms of the motion of the system over a hypersurface.

5. Reaction probabilities and cross sections were calculated from the complete reactivity maps. For $H+H_2$ the effects of the reactivity bands in the cross section have largely disappeared, although the high-energy fall off in reactivity can be directly associated with the continuation of the large unreactive region, above the cut-off energy, to non-linear initial configurations. Rotational motion was seen to average over the non-rotating case.

6. A simplified surface model has been developed, which is capable of generating the reactivity bands and to simulate their dependence on the translational energy and vibrational phase angle in a qualitative way. Although quantitative a priori predictions could not be made on the basis of characteristic system and surface parameters, this part of the study has also contributed to a better insight of dynamical behavior on potential-energy surfaces, and has thrown some theoretical light on the origin of the reactivity bands.

7. The present study has opened up many alternative routes for future extensions to higher dimensional cases, different reaction systems, detailed energy-transfer studies and semi-classical calculations. The main advantage of the method is the clear and detailed relationship between initial and final reaction parameters that can be obtained in the form of reactivity maps. This feature is essential for a deeper understanding and a more detailed analysis of the dynamic behavior of reacting systems.

REFERENCES

1. S.Glasstone, K.J.Laidler and H.Eyring, The Theory of Rate Processes, (McGraw-Hill, New York, 1941).
2. K.J.Laidler, Theories of Reaction Rates, (McGraw-Hill, New York, 1969).
3. R.B.Bernstein and R.D.Levine, Molecular Reaction Dynamics, (Oxford University Press, New York, 1974).
4. H.S.Johnston, Gas Phase Reaction Rate Theory, (Ronald Press, New York, 1966).
5. W.Byers Brown and J.C.Polanyi (eds.), MTP International Review of Science, (Buttersworth, Oxford, 1972), Physical Chemistry, Series 1, Vols. 1 and 9.
6. J.Wm.McGowan and K.P.Lawley (eds.), Advances in Chemical Physics, Vols. 28 and 30 (1975).
7. Ch.Schlier (ed.), Molecular Beams and Reaction Kinetics, (Academic Press, New York, 1970).
8. H.Eyring, D.Henderson and W.Jost (eds.), Physical Chemistry - An Advanced Treatise, (Academic Press, New York, 1974), Vols. VIA and VIB.
9. W.H.Lester Jr. (ed.), Potential-Energy Surfaces in Chemistry, (IBM Research Lab., San Jose, 1971).
10. Discuss. Faraday Soc., Vols. 44 (1967) and 55 (1973).
11. R.N.Porter, Ann.Rev.Phys.Chem., 25, 317 (1974).
12. J.C.Polanyi, Acc.Chem.Res., 5, 161 (1972).
13. S.Arrhenius, Z.Physik.Chem. (Leipzig), 4, 226 (1889).

14. M. Trautz, Z. Anorg. Allgem. Chem., 96, 1 (1916).

15. W.C.McC. Lewis, J. Chem. Soc., 113, 471 (1918).

16. J.H. van 't Hoff, Etudes de Dynamique Chimique, (F.Muller and Company, Amsterdam, 1884).

17. H. Eyring, J. Chem. Phys., 3, 107 (1935).

18. M.G. Evans and M. Polanyi, Trans. Faraday Soc., 31, 875 (1935).

19. W.H. Miller, Acc. Chem. Res., 4, 161 (1971).

20. J.N.L. Connor, Chem. Soc. Rev., 5, 125 (1976).

21. H. Eyring, J. Walter, and E. Kimball, Quantum Chemistry, (John Wiley and Sons, New York, 1944).

22. R.C. Tolman, Statistical Mechanics, (Chemical Catalog Company, Inc., New York,1927).

23. H. Goldstein, Classical Mechanics, Addison Wesley, Reading, Mass., 1950).

24. E. Schroedinger, Ann. Physik, 79, 489 (1926); 80, 437 (1926); 81, 109 (1926).

25. H. Heitler and F. London, Z. Physik, 44, 455 (1927).

26. F. London, Z. Elektrochem., 35, 552 (1929).

27. H. Eyring and M. Polanyi, Z. Physik. Chem. (Leipzig), B12, 279 (1931); H. Eyring, Chem. Rev., 10, 103 (1932).

28. J.O. Hirschfelder, Ph.D. thesis, Princeton University, New Jersey (1935); J.O. Hirschfelder, H. Eyring and B. Topley, J. Chem. Phys., 4, 170 (1936).

29. M.G. Evans and M. Polanyi, Trans. Farday Soc., 35, 178 (1939).

30. H. Eyring, H. Gershinowitz, and C.E. Sun, J. Chem. Phys., 3, 786 (1935).

31. M.von Hartel and M.Polanyi, Z.Physik.Chem. (Leipzig), B11, 97 (1931); M.Polanyi, Atomic Reactions, (Williams and Northgate, London, 1932).

32. A.Marcelin, Ann.Physik, 3, 158 (1915).

33. T.H.Bull and P.B.Moon, Discuss.Faraday Soc., 17, 54 (1954).

34. E.H.Taylor and S.Datz, J.Chem.Phys., 23, 1711 (1955).

35. F.J.Lipscomb, R.G.W.Norrish and B.A.Thrush, Proc.Roy.Soc. (London), A233, 455 (1956); W.D.McGrath and R.G.W.Norrish, ibid., A242, 265 (1957); A254, 317 (1960).

36. J.K.Cashion and J.C.Polanyi, J.Chem.Phys., 29, 455 (1958); 30, 317, 1097 (1959); 35, 600 (1961); Proc.Roy.Soc.(London), A258, 529, 570 (1960).

37. F.T.Wall, L.A.Hiller Jr. and J.Mazur, J.Chem.Phys., 29, 255 (1958).

38. a) I.Shavitt, R.M.Stevens, F.L.Minn, and M.Karplus, J.Chem. Phys.,48, 2700 (1968); b) I.Shavitt, ibid., 49, 4048 (1968).

39. B.Liu, J.Chem.Phys., 58, 1925 (1973).

40. A.Kuppermann and G.C.Schatz, J.Chem.Phys., 62, 2502 (1975).

41 A.B.Elkowitz and R.E.Wyatt, J.Chem.Phys., 62, 2504 (1975).

42. D.L.Bunker, Methods Computational Phys., 10, 287 (1971).

43. J.C.Polanyi and J.L.Schreiber, in Ref.8.

44. J.O.Hirschfelder, H.Eyring and N.Rosen, J.Chem.Phys., 4, 121 (1936).

45. P.J.Kuntz, E.M.Nemeth, J.C.Polanyi and W.H.Wong, J.Chem. Phys.,52, 4654 (1970); P.J.Kuntz, M.H.Mok and J.C.Polanyi, ibid., 50, 4623 (1969); P.J.Kuntz, E.M.Nemeth and J.C.Polanyi, ibid., 50, 4607 (1969); K.G.Anlauf, J.C.Polanyi, W.H.Wong

and K.B.Woodall, ibid., 49, 5189 (1968); P.J.Kuntz, E.M. Nemeth, J.C.Polanyi, S.D.Rosner, and C.E.Young, ibid., 44, 1168 (1966); J.C.Polanyi and S.D.Rosner, ibid., 38, 1028 (1963).

46. C.A.Parr, J.C.Polanyi, and W.H.Wong, J.Chem.Phys., 58, 5 (1973); I.G.Czismadia, J.C.Polanyi, A.C.Roach, and W.H.Wong, Can.J. Chem., 47, 4097 (1969); M.H.Mok and J.C.Polanyi, J.Chem.Phys., 51, 1451 (1969); J.C.Polanyi and W.H.Wong, ibid.,51, 1439 (1969); N.H.Hijazi and J.C.Polanyi, ibid., 63, 2249 (1975).
47. See also contributions by J.C.Polanyi et al. in Refs.5 and 10.
48. P.N.Careless and D.Hyatt, Chem.Phys.Lett.,14, 358 (1972).
49. E.M.Mortensen, J.Chem.Phys., 49, 3526 (1968).
50. D.Russel and J.C.Light, J.Chem.Phys., 51, 1720 (1969).
51. K.P.Fong and D.J.Diestler, J.Chem.Phys., 56, 3200 (1972).
52. J.M.Bowman and A.Kuppermann, Chem.Phys.Lett.,12, 1 (1971); 19, 166 (1973); J.Chem.Phys., 59, 6524 (1973).
53. J.W.Duff and D.G.Truhlar, Chem.Phys.,4, 1 (1974).
54. S.F.Wu and R.A.Marcus, J.Chem.Phys., 53, 4026 (1970).
55. R.A.Marcus, Discuss.Farday Soc., 55, 7 (1973).
56. W.H.Miller, J.Chem.Phys., 53, 1949 (1970); Adv.Chem.Phys., 25, 5135 (1974), and references cited therein.
57. R.A.Marcus, Chem.Phys.Lett., 7, 525 (1970); J.Chem.Phys., 59, 5135 (1970), and references therein.
58. A.C.Yates and W.A.Lester Jr., Chem.Phys.Lett., 24, 305 (1974).
59. R.N.Porter and M.Karplus, J.Chem.Phys.,40, 1105 (1964).
60. J.T.Muckerman, Quantum Chemistry Program Exchange, Catalog X, Program#229 (1974); J.Chem.Phys., 54, 1155 (1971); 56, 2997 (1972).

61. F.T.Wall, L.A.Hiller Jr. and M.Mazur, J.Chem.Phys., 35, 1284 (1961).

62. F.T.Wall and R.N.Porter, J.Chem.Phys., 39, 3112 (1963).

63. F.T.Wall and R.N.Porter, J.Chem.Phys., 36, 3256 (1962).

64. S.Sato, J.Chem.Phys., 23, 592, 2465 (1955).

65. M.Karplus, R.N.Porter and R.D.Sharma, J.Chem.Phys., 43, 3259 (1965).

66. J.E.Hulse, B.Sc.(Hon.)-thesis, Carleton University, Ottawa (1972).

67. R.L.Jaffe, J.M.Henry and J.B.Anderson, J.Chem.Phys., 57, 1128 (1973); J.B.Anderson and R.T.V.Kung, ibid., 58, 2477 (1973); J.B.Anderson, ibid., 58, 4684 (1973); J.M.Henry, J.B.Anderson and R.L.Jaffe, Chem.Phys.Lett.,20, 138 (1973).

68. B.H.Mahan, J.Chem.Ed., 51, 308, 377 (1974).

69. E.A.McCullough Jr. and R.E.Wyatt, J.Chem.Phys., 54, 3592 (1971).

70. C.C.Rankin and W.H.Miller, J.Chem.Phys., 55, 3150 (1971).

71. R.A.Marcus, J.Chem.Phys., 45, 4493, 4500 (1966); 49, 2610, 2617 (1968).

72. J.O.Hirschfelder, Int.J.Quant.Chem., Vol.IIIs, 17 (1969).

73. J.E.Hulse, R.A.Jackson and J.S.Wright, J.Chem.Ed., 51, 78 (1974).

74. S.K.Gray and J.S.Wright, J.Chem.Phys., received August (1976).

75. G.Herzberg and L.L.Howe, Can.J.Phys., 37, 636 (1959); G.Herzberg and A.Monfils, J.Mol.Spectry., 5, 482 (1960).

76. G.Herzberg, Spectra of Diatomic Molecules, (Van Nostrand, Princeton, New Jersey, 1950).

77. H.Margenau and G.M.Murphy, The Mathematics of Physics and Chemistry, (Van Nostrand, Princeton New Jersey, 1956).

78. S.C.Leasure and J.M.Bowman, J.Chem.Phys., 64, 4229 (1975).

79. a. S.K.Gray, private communications; b. R.K.Preston and R.J.Cross, J.Chem.Phys., 59, 3616 (1973).

80. C.E.Froeberg, Introduction to Numerical Analysis, (Addison-Wesley, Don Mills, 1969).

81. S.F.Wu and R.D.Levine, Mol.Phys., 22, 881 (1971); S.F.Wu, B.R.Johnson and R.D.Levine, ibid., 25, 609, 839, 937 (1973); R.D.Levine and S.F.Wu, Chem.Phys.Lett., 11, 557 (1971).

82. A.Tweedale and K.J.Laidler, J.Chem.Phys., 53, 2045 (1970).

83. J.R.Stine and R.A.Marcus, Chem.Phys.Lett., 29, 575 (1974).

84. R.Wolfgang, Acc.Chem.Res., 3, 48 (1970).

85. R.D.Levine, Acc.Chem.Res., 3, 273 (1970).

86. P.Pechukas and F.J.McLafferty, J.Chem.Phys., 58, 1622 (1973).

87. D.G.Truhlar and A.Kuppermann, J.Chem.Phys., 52, 3841 (1970).

88. D.G.Truhlar and A.Kuppermann, J.Chem.Phys., 56, 2232 (1971).

89. J.S.Wright, K.G.Tan and K.J.Laidler, J.Chem.Phys., 64, 970 (1976).

90. J.S.Wright and K.G.Tan, J.Chem.Phys., received July (1976).

91. R.J.Suplinskas, J.Chem.Phys., 49, 5046 (1968); T.F.George and R.J.Suplinskas, ibid., 51, 3666 (1969); 54, 1037, 1046 (1971).

92. D.J.Malcolme-Lawes, J.C.S.Faraday II, 68, 1613, 2051 (1972).

93. M.D.Pattengill and J.C.Polanyi, Chem.Phys., 3, 1 (1974).

94. D.L.Thompson, J.Chem.Phys., 57, 4164 (1972); 56, 3570 (1972).

95. J.M.White and D.L.Thompson, J.Chem.Phys., 61, 719 (1975).

96. I.W.M.Smith, J.C.S.Faraday II, 71, 1970 (1975).

97. R.L.Wilkins, J.Chem.Phys., 59, 698 (1973); 63, 534 (1975).

98. J.M.Bowman, A.Kuppermann and G.C.Schatz, Chem.Phys.Lett., 19, 21 (1973).

99. D.J.Malcolme-Lawes, J.C.S.Faraday II, 70, 1942 (1974); 71, 1183 (1975).

100. I.W.M.Smith and P.M.Wood, Mol.Phys., 25, 441 (1973).

101. D.J.Diestler, J.Chem.Phys., 56, 2092 (1972).

102. W.H.Miller and T.F.George, J.Chem.Phys., 56, 5668 (1972); 57, 2458 (1972); J.D.Doll, T.F.George and W.H.Miller, J.Chem.Phys., 58, 1343 (1973).

103. D.G.Truhlar and A.Kuppermann, J.C.S.Faraday II, 93, 1840 (1971); Chem.Phys.Lett., 9, 269 (1971).

104. J.S.Wright, unpublished work.

105. B.P.Stoicheff, Can.J.Phys., 35, 730 (1951); Advan.Spectry., 1, 91 (1959).

106. J.C.Polanyi, IBM Publ.RA18, San Jose, California (1971).

107. S.F.Wu and R.A.Marcus, J.Chem.Phys., 56, 3519 (1972).

108. R.P.Saxon and J.C.Light, J.Chem.Phys., 56, 3885 (1972); 57, 2758 (1972).

109. E.E.Nikitin, in Refs.6 and 8.

110. X.M.Chapuisat, Y.Jean and L.Salem, Chem.Phys.Lett., 37, 119 (1976).

111. R.A.Ogg and M.Polanyi, Trans.Faraday Soc., 31, 604 (1935); M.G.Evans and M.Polanyi, ibid., 34, 11 (1938); 35, 178 (1939).

112. J.S.Wright, K.G.Tan, K.J.Laidler and J.E.Hulse, Chem. Phys. Lett., 30, 200 (1975).

113. X.M.Chapuisat and Y.Jean, J.Am.Chem.Soc., 97, 6325 (1975).

114. D.W.Jepsen and J.O.Hirschfelder, J.Chem.Phys., 30, 1032 (1975).

115. H.K.Shin, Chem.Phys.Lett., 34, 546 (1975).

116. R.N.Porter, L.M.Raff and W.H.Miller, J.Chem.Phys.,63, 2214 (1975).

117. W.H.Miller (ed.), Dynamics of Molecular Collisions Part B, (Plenum, New York, 1976).

118. A.Kuppermann, G.C.Schatz, and M.Baer, J.Chem.Phys., 65, 4596 (1976), G.C.Schatz and A.Kuppermann, ibid., 65, 4624, 4642, 4668 (1976).

119. D.G.Truhlar and R.E.Wyatt, Ann.Rev.Phys.Chem., 27, 1 (1976).

APPENDIX I: 1-D COMPUTER PROGRAM.

```
C
C     ***************************************************************
C     PROGRAM FOR DYNAMIC CALCULATIONS ON THE SSNK SURFACE.
C     ORIGINAL PROGRAM WRITTEN BY HULSE,JACKSON AND WRIGHT, OF.
C     J.E.HULSE, B.SC.THESIS,CARLTON UNIVERSITY,OTTAWA (1972)
C
C     CALCULATIONS ARE IN ATOMIC UNITS, EXCEPT FOR ENERGIES (EV).
C     INPUT/OUTPUT OF TIME IN 10**-16 SEC...., ANGLES IN DEGREES....
C     THE FOLLOWING DATA CARDS ARE READ:
C     1. TITLE, TO IDENTIFY THE SYSTEM AND CONDITIONS.
C     2. PROGRAM PARAMETERS: NRUN= # OF TRAJECTORIES
C                            NPRINT= # OF STEPS BETWEEN EACH PRINT OUT.
C                            NIT= MAXIMUM # OF STEPS.
C                            IE = FLAG FOR OPERATION MODE
C                            IE= 0 NORMAL MODE
C                            IE= 1 BACK INTEGRATION.
C                            IE= 2 WRITE OUTPUT FILE
C     3. SYSTEM PARAMETERS: AM,BM,CM, ARE THE ATOMIC MASSES
C                           EO = THE INITIAL VIBRATIONAL ENERGY
C                           DT = TIME STEP FOR INTEGRATION
C     4. VIBRATIONAL CONSTANTS: PHI = PHASE ANGLE
C                               AL,AR = AMPLITUDES
C                               RHO = REACTION SHELL RADIUS
C                               RE = EQUILIBRIUM SEPARATION
C     ***************************************************************
C
      IMPLICIT REAL*8 (A-H,O-Z)
      DIMENSION NAME(18),UM(2)
      COMMON Y(4),DY(4),U(2),BM,V,DX,IR,NSTEP
      F2=1.8562336869410-02
      F3=1.7453292520-02
      READ(5,500) NAME
      READ(5,501) NRUN,NPRINT,NIT,IE
      READ(5,502) AM,BM,CM,EO,DT
      READ(5,502) PHI,AL,AR,RHO,RE
      DX=DT*F2
      IR=0
      WRITE(6,600) NAME
    5 WRITE(6,601) NRUN,NPRINT,NIT,IE
      WRITE(6,602) AM,BM,CM,EO,DT
      WRITE(6,603) PHI,AL,AR,RHO,RE
C
C   INITIALIZE SURFACE PARAMETERS  AND CALCULATE MASS RATIOS.
C
      CALL POTIN
      U(1)=AM*BM/(AM+BM)
      U(2)=BM*CM/(BM+CM)
      UM(1)=AM*(BM+CM)/(AM+BM+CM)
      UM(2)=(AM+BM)*CM/(AM+BM+CM)
C
```

```
C     CALCULATE SKEW ANGLE (XSI) AND  REFERENCE POTENTIAL (VREF)
C
      XSI=DSQRT(U(1)/U(1))
      XSI=DARCOS(XSI)/1.3
      Y(1)=(RHO-U(2)*RE/BM
      Y(2)=RE
      CALL POTEN
      VREF=V
C
C     CALCULATE INITIAL COORDINATES AND VIBRATIONAL MOMENTUM (PV)
C
      AMP=AL
      IF(PHI.GT.100.000) AMP=AR
      Y(2)=RE-AMP*DSIN(PHI*1.3)
      Y(1)=(RHO-U(2)*Y(2))/BM
      CALL POTEN
      VVO=V-VREF
      Q1=Y(1)
      Q2=Y(2)
      TVO=EO-VVO
      IF(TVO.LT.0.000) TVO=1.D-40
      PV=DSQRT(2.000*U(2)*TVO)
      IF(DABS(PHI-180.000).GT.90.000) PV=-PV
      WRITE(6,604) XSI,VREF,Q1,Q2,PV
C
C     ********************************************************************
C     TRAJECTORY CALCULATIONS AT CONSTANT PHI AND VARYING TTO
C     ********************************************************************
C
      DO 100 K=1,NRUN
      TR=0.000
      NSTEP=0
      Y(1)=Q1
      Y(2)=Q2
      READ(5,503) TTO
      WRITE(6,605) K,TTO
      Y(3)=-DSQRT(2.0000*U(1)*TTO)
      Y(4)=Y(3)*U(2)/BM+PV
C
C     WRITE INITIAL COORDINATES AND MOMENTA
C
   10 CALL POTEN
      T=0.5000*(Y(3)*Y(3)/U(1)+Y(4)*Y(4)/U(2))-Y(3)*Y(4)/BM
      H=T+V
      WRITE(6,606) TR,Y,T,V,H
C
C     ********************************************************************
C     CALL INTEGRATION ROUTINE DDASH
C     ********************************************************************
   20 CALL DDASH
      TR=NSTEP*DT
C
C     ********************************************************************
C     CHECK FOR FINAL CONDITIONS AND CALCULATE ENERGIES
```

```
C    ***********************************************************************
       RF=Y(IR+1)+U(2-IR)*Y(2-IR)/BM
       IF(RF.GE.RHO.OR.NSTEP.GE.NIT) GOTO 40
C
C    PRINT INTERMEDIATE VALUES EVERY NPRINT STEP
C
       IF(MOD(NSTEP+1,NPRINT)-1) 20,10,20
  40   CALL POTEN
       T=0.5000*(Y(3)*Y(3)/U(1)+Y(4)*Y(4)/U(2))-Y(3)*Y(4)/BM
       TT=0.5000*Y(IR+3)*Y(IR+3)/UN(IR+1)
       TV=(T-TT)
       EV=TV*0-VREF
       H=T*0
       WRITE(6,607) TR,Y,T,V,H,TV,EV,IR
       IF(IE-1) 100,50,70
C
C    ***********************************************************************
C     BACK INTEGRATION
C    ***********************************************************************
  50   DX=-DX
       NC=NSTEP
       NSTEP=0
       DO 60 I=1,NC
  60   CALL DBASH
       TR=TR-I*DT
       WRITE(6,608) TR,Y
       GOTO 100
C
C    ***********************************************************************
C     WRITE OUTPUT FILE FOR STORAGE
C    ***********************************************************************
  70   WRITE(7,701) AM,PHI,TTO,TR,Y,EV,IR
 100   CONTINUE
C
C    ***********************************************************************
C     READ INITIAL CONDITIONS FOR NEXT BATCH
C    ***********************************************************************
       READ(5,504) NRUN,NPRINT,IE,PHI
       IF(NRUN.GT.0) GOTO 5
       STOP
 500   FORMAT(16A4)
 501   FORMAT(4I5)
 502   FORMAT(5F10.2)
 503   FORMAT(F10.2)
 504   FORMAT(3I5,F10.2)
 600   FORMAT(1H1,5(/),20X,16A4,5(/),20X,'INPUT DATA',//,20X,10('*'))
 601   FORMAT(///,20X,'PROGRAM PARAMETERS....:',//,25X,'NRUN',5X,
      1'NPRINT',5X,'NIT',5X,'IE',//,20X,I8,I11,I9,I7)
 602   FORMAT(///,20X,'SYSTEM PARAMETERS....:',//,25X,'MA',10X,'MB'
      1,10X,'MC',10X,'EO',10X,'DT',//,20X,F10.4,F11.4,F12.4,F12.4,F11.2)
 603   FORMAT(///,20X,'VIBRATIONAL PARAMETERS....:',//,25X,'PHI'
      1,9X,'AL',10X,'AR',10X,'RHO',9X,'RE',//,20X,F10.2,4F12.5)
 604   FORMAT(5(/),20X,'CALCULATED DATA:',//,20X,16('*'),//,22X,'XSI'
      1,6X,'VREF',6X,'RAB',6X,'RBC',6X,'PV',//,19X,5F9.5)
```

```
 605  FORMAT(1H1,5(/),20X,'TRAJECTORY #',I3,10X,'TTO =',F9.4,5(/),20X,
     1'INITIAL CONDITIONS....:')
 606  FORMAT(//,20X,'REACTION TIME:',F7.2,/,20X,'COORDINATES:',
     12F12.6,/,20X,'MOMENTA:',4X,2F12.6,/,20X,'KINETIC ENERGY:',
     2F12.6,/,20X,'POTENTIAL ENERGY:',F10.6,/,20X,'TOTAL ENERGY:',
     3F14.6)
 607  FORMAT(//,20X,'FINAL CONDITIONS....:',//,20X,'REACTION TIME'
     1,F7.2,/,20X,'COORDINATES:',2F12.6,/,20X,'MOMENTA:',4X,2F12.6
     2,/,20X,'KINETIC ENERGY:',F12.6,/,20X,'POTENTIAL ENERGY:',F10.6
     3,/,20X,'TOTAL ENERGY:',F14.6,/,20X,'KIN.VIB.ENERGY:',F12.6,/,20X,
     4'VIBRTL.ENERGY:',F13.6,/,20X,'REACTION CHANNEL:',I5)
 608  FORMAT(5(/),20X,'BACK INTEGRATION....:',//,20X,'REACTION TIME'
     1,F7.2,/,20X,'COORDINATES:',2F12.6,/,20X,'MOMENTA:',4X,2F12.6)
 701  FORMAT(6F10.4,I5)
      END
      BLOCK DATA
      IMPLICIT REAL*8 (A-H,O-Z)
      COMMON/COEFF/CC(9),C(28)
C
C     ***************************************************************
C       THE H2 FUNCTION CONSTANTS.
C     ***************************************************************
      DATA CC/2.2881106,-8.6064101,4.6016784,-2.3976518,-0.42034964,
     1     0.54761616,-0.24622333,0.046039649,-0.0043680049/
C
C     ***************************************************************
C       THE H3 FUNCTION CONSTANTS.   ALL CONSTANTS DEFINED HERE ARE
C       STORED IN LABELLED COMMON BLOCK/COEFF/.
C     ***************************************************************
      DATA C/0.17204175D00,-4.5584173D00,0.5386946D00,32.350972D00
     *-8.8025264D00,1.0203549D00,-80.772167D00,9.0971615D00,6.1798531D00
     *,-1.4533685D00,103.11613D00,-1.9957114D00,-8.5296565D00,
     *-0.63722732D00,0.55209203D00,-61.744419D00,-9.8121584D00,8.5460058
D00
     *D00,0.45704353D00,-0.1196757D00,-0.078315251D00,20.67282D00,-3.532
     *6727D00,3.8209212D00,-2.7667995D00,0.53396417D00,-0.034958722D00,
     *0.005669712D00/
      END
      SUBROUTINE POTIN
C
C     ***************************************************************
C      INITIALIZES SSMK SURFACE PARAMETERS, F1 IS ENERGY CONVERSION
C      FACTOR (EV/A.U.).
C     ***************************************************************
C
      IMPLICIT REAL*8 (A-H,O-Z)
      COMMON/COEFF/CC(9),C(28)
      COMMON Y(4),DY(4),U(2),BM,V,DX,IR,NSTEP
      COMMON/PARAM/ A,ALPHA,F1
      F1=27.211652D00
      A=1.32D00
      ALPHA=1.218D00
      EREF=-1.66959D00
      RETURN
```

```
      ENTRY POTEN
C
C     ***************************************************************
C      CALCULATES THE SSMK POTENTIAL ENERGY AS A FUNCTION OF THE INTER-
C      ATOMIC SEPARATIONS, WHERE RAB > RBC.
C     ***************************************************************
        IF(Y(IR+1).LT.Y(2-IR)) IR=IABS(IR-1)
        RAB=Y(IR+1)
        RBC=Y(2-IR)
C
C     ***************************************************************
C        THE H2 ENERGY
C     ***************************************************************
   10   H2SUM=CC(9)
        DO 12 K=1,8
   12   H2SUM=H2SUM*RBC+CC(9-K)
        EH2=H2SUM*DEXP(-A*RBC)
C
C     ***************************************************************
C        THE H3 ENERGY
C     ***************************************************************
        H3SUM=0.D00
        DO 14 I=1,7
        J=0
   15   J=J+1
        N=((I-1)*I)/2+J
        H3SUM=H3SUM+C(N)*RBC**(7-I)*RAB**(J-1)
        IF(I-J) 14,14,15
   14   CONTINUE
        E=EH2-.5+H3SUM*DEXP(-ALPHA*(RAB+RBC))
C       THE ENERGY SCALED WITH ZERO OF ENERGY  AT INFINITE
C       SEPARATION. . RETURNED IN EV.
        V=(E-EREF)*F1
        RETURN
        END
        SUBROUTINE DERIVE
C
C     ***************************************************************
C      CALCULATES THE TIME DERIVATIVES OF THE COORDINATES AND MOMENTA
C      ACCORDING TO HAMILTON'S EQUATIONS OF MOTION AND THE SSMK
C      POTENTIAL-ENERGY FUNCTION
C     ***************************************************************
C
        IMPLICIT REAL*8 (A-H,O-Z)
        COMMON/PARAM/ A,ALPHA,F1
        COMMON Y(4),DY(4),U(2),BM,V,DX,IR,NSTEP
        COMMON/COEFF/CC(9),C(28)
        DY(1)=Y(3)/U(1)-Y(4)/BM
        DY(2)=Y(4)/U(2)-Y(3)/BM
        IF(Y(IR+1).LT.Y(2-IR)) IR=IABS(IR-1)
        RAB=Y(IR+1)
        RBC=Y(2-IR)
C
C     ***************************************************************
```

```
C     THE H2 POWER SERIES.
C     EH2 W.R.T. RBC (TERM 1)
C    ***************************************************************
       A1=DEXP(-A*RBC)
       A2=DEXP(-ALPHA*(RAB+RBC))
       S1=CC(9)*RBC+CC(8)
       S2=8.000*CC(9)
       DO 12 K=2,8
       S1=S1*RBC+CC(9-K)
  12   S2=S2*RBC+CC(10-K)*(9-K)
       TERM1=A1*(S2-A*S1)
C
C    ***************************************************************
C     THE H3 POWER SERIES.
C     EH3 W.R.T. RAB (TERM3) AND W.R.T. RBC (TERM2)
C    ***************************************************************
       S3=0.
       S4=0.
       S5=0.
       DO 14  I=1,7
       J=0
  15   J=J+1
       N=((I-1)*I)/2+J
       S3=S3+C(N)*RBC**(7-I)*RAB**(J-1)
       S4=S4+C(N)*(J-1)*RBC**(7-I)*RAB**(J-2)
       S5=S5+C(N)*(7-I)*RBC**(6-I)*RAB**(J-1)
       IF(I-J) 14,14,15
  14   CONTINUE
       TERM2=A2*(S5-ALPHA*S3)
       TERM3=A2*(S4-ALPHA*S3)
C
C    ***************************************************************
C     .
C     P(RAB) IS TERM3
C     .
C     P(RBC) IS TERM1 + TERM2
C    ***************************************************************
       DERAB=TERM3
       DERBC=TERM1+TERM2
C
C    ***************************************************************
C     STORE INTO APPROPRIATE ELEMENTS OF  DERIVATIVE VECTOR.
C     NEGATIVE SIGN INTRODUCED FOR EQUATIONS OF MOTION
C    ***************************************************************
       DY(IR+3)=-DERAB*F1
       DY(4-IR)=-DERBC*F1
  90   RETURN
       END
       SUBROUTINE DBASH
C
C     ADAMS-BASHFORTH 4TH ORDER PREDICTOR-CORRECTOR ROUTINE, WITH A
C     THEREE-STEP RUNGE-KUTTA START-UP, AND A FIXED STEPSIZE (DX)
C    ***************************************************************
C
```

```
      IMPLICIT REAL*8 (A-H,O-Z)
      COMMON Y(4),DY(4),U(2),BM,V,DX,IR,NSTEP
      DIMENSION DIFF(4),ARRAY(4,4)
      NE=4
      IF (NSTEP.LT.3) GOTO  5
C     PREDICTOR COLLECTOR INTEGRATION
      DO 1 J=1,NE
      YPC=ARRAY(4,J)+DX*(2.2916666666667D00*DY(J)-2.4583333333333D00
     1*ARRAY(3,J)+1.5416666666667D00*ARRAY(2,J)-0.375D00*ARRAY(1,J))
      ARRAY(1,J)=ARRAY(2,J)
      ARRAY(2,J)=ARRAY(3,J)
      ARRAY(3,J)=DY(J)
      Y(J)=YPC-0.92962962962963D00*DIFF(J)
    1 DIFF(J)=YPC
      CALL DERIVE
      DO 2 J=1,NE
      YPC=ARRAY(4,J)+DX*(0.375D00*DY(J)+0.79166666666667D00*ARRAY(3,J)-
     10.20833333333333D00*ARRAY(2,J)+0.04166666666667D00*ARRAY(1,J))
      DIFF(J)=DIFF(J)-YPC
    2 Y(J)=YPC+0.07037037037037D00  *DIFF(J)
      CALL DERIVE
      NSTEP=NSTEP+1
    3 DO  4 J=1,NE
    4 ARRAY(4,J)=Y(J)
      RETURN
C
C   ***********************************************************************
C     RUNGE KUTTA INTEGRATION
C   ***********************************************************************
    5 IF (NSTEP.NE.0) GOTO 7
      CALL DERIVE
      DO 6 J=1,NE
    6 ARRAY(1,J)=DY(J)
    7 DO 26 I=1,4
      DO 14 J=1,NE
      GOTO (8,9,9,10),I
    8 DIFF(J)=Y(J)
      ARRAY(4,J)=-DY(J)
    9 YPC=2.D00
   10 ARRAY(4,J)=ARRAY(4,J)+YPC*DY(J)
      GOTO (13,13,12,11),I
   11 Y(J)=DIFF(J)+DX*ARRAY(4,J)/6.D00
      GOTO 14
   12 YPC=1.D00
   13 Y(J)=DIFF(J)+DX*DY(J)/YPC
   14 CONTINUE
      CALL DERIVE
   26 CONTINUE
      NSTEP=NSTEP+1
      DO 17 J=1,NE
      ARRAY(NSTEP+1,J)=DY(J)
   17 DIFF(J)=0.D00
      IF (NSTEP.LT.3) RETURN
      GOTO 3
      END
```

SAMPLE RUN.:O+HT. RHO = 7.56 A.U.

INPUT DATA
****

PROGRAM PARAMETERS....:

NRUN	NPRINT	NIT	IE
2	100	900	0

SYSTEM PARAMETERS....:

MA	VB	MC	EC	DT
2.0140	1.0030	3.0160	0.2200	2.00

VIBRATIONAL PARAMETERS....:

PHI	ML	AB	RHO	RE
0.0	0.10000	0.13300	7.56000	1.41000

CALCULATED DATA:
****

XSI	VREF	RAB	RBC	PV
44.97154	-0.00615	6.50320	1.41000	-0.57656

TRAJECTORY # 1 TTO = 1.0000

INITIAL CONDITIONS....:

```
REACTION TIME:    0.0
COORDINATES:     6.503201     1.410000
MOMENTA:        -1.638427    -1.804564
KINETIC ENERGY:     1.220000
POTENTIAL ENERGY: -0.008153
TOTAL ENERGY:       1.211847

REACTION TIME: 200.00
COORDINATES:     2.191252     1.364442
MOMENTA:        -1.306520    -1.358269
KINETIC ENERGY:     0.730962
POTENTIAL ENERGY:   0.480881
TOTAL ENERGY:       1.211843

REACTION TIME: 400.00
COORDINATES:     3.743216     1.206609
MOMENTA:         1.025064     1.649803
KINETIC ENERGY:     0.905705
POTENTIAL ENERGY:   0.306832
TOTAL ENERGY:       1.212537
```

FINAL CONDITIONS....:

```
REACTION TIME 592.00
COORDINATES:     6.780035     1.096892
MOMENTA:         1.118131     0.979040
KINETIC ENERGY:     0.478864
POTENTIAL ENERGY:   0.733756
TOTAL ENERGY:       1.212642
KIN.VIB.ENERGY:     0.013157
VIBRTL.ENERGY:      0.755068
REACTION CHANNEL:      0
```

TRAJECTORY # 2 TTO = 2.0000

INITIAL CONDITIONS....:

REACTION TIME: 0.0
COORDINATES: 6.503201 1.410000
MOMENTA: -2.317096 -2.313221
KINETIC ENERGY: 2.220000
POTENTIAL ENERGY: -0.008153
TOTAL ENERGY: 2.211847

REACTION TIME: 200.00
COORDINATES: 1.825555 1.382270
MOMENTA: 1.664976 0.965386
KINETIC ENERGY: 1.513668
POTENTIAL ENERGY: 0.698164
TOTAL ENERGY: 2.211832

FINAL CONDITIONS....:

REACTION TIME 362.00
COORDINATES: 6.266473 1.748910
MOMENTA: 2.192301 1.699442
KINETIC ENERGY: 1.792451
POTENTIAL ENERGY: 0.419326
TOTAL ENERGY: 2.211609
KIN.VIB.ENERGY: 0.002988
VIBRTL.ENERGY: 0.429579
REACTION CHANNEL: 0

APPENDIX II: 2-D COMPUTER PROGRAM.

```
C
C  ****************************************************************
C  SYSTEMATIC QUASI-CLASSICAL TRAJECTORY PROGRAM. THIS VERSION IS A
C  MODIFICATION OF THE MONTE CARLO  PROGRAM (QCPE 229) WRITTEN BY
C  J. T. MUCKERMAN.....METHOD BASED ON FORMULATION OF KARPLUS, PORTER,
C  AND SHARMA, J. CHEM. PHYS. 43, 3259 (1965), WITH SOME MODIFICATIONS.
C
C  THIS VERSION IS APPROPRIATE FOR THE 2D H+H-H SYSTEM ON THE YATES -
C  LESTER GENERALIZED POTENTIAL ENERGY SURFACE
C  EV,AU. UNITS ARE USED THROUGHOUT UNLESS OTHERWISE SPECIFIED.....
C  ****************************************************************
C
      IMPLICIT REAL*8 (A-H,O-Z)
      DIMENSION NAME(16),EM(3)
      COMMON XM,S(4,3),C,B,RO,RLO,RHI,Y(8),R(3),FF(8),DD(3),TERM,VREL,
     1RHO,HO,AVV,ANG,AMINT,AMTOT,XTER,ENFIN,ENTOT,T,H,EVIB,EROT,TAD,DIST
     2,NV,NJ,IREACT,KDQ,IDEX,IE
      COMMON/CONST/RAD,HBAR,PI
C
C  ****************************************************************
C  READ AND WRITE TITLE TO IDENTIFY SYSTEM AND ENERGY
C  ****************************************************************
      READ(1,500) NAME
      WRITE(6,600) NAME
C
C  ****************************************************************
C  RHO IS INITIAL A-BC DISTANCE, EM IS HYDROGEN MASS, HO IS STEP SIZE
C  IN NUMERICAL INTEGRATION.....NTOT IS THE NUMBER OF TRAJECTORIES TO
C  BE COMPUTED.....NV AND NJ ARE THE INITIAL VIBRATIONAL AND ROTATIONAL
C  QUANTUM NUMBERS OF THE REACTANT DIATOMIC MOLECULE.....IE DENOTES
C  CHOICE OF CONTROL OPTION.....
C     <0   BACK INTEGRATION OF EACH TRAJECTORY
C      0   NORMAL (NO BACK INTEGRATION), PRINTS COORDINATES EVERY NPRINT
STEP
C      1   CREATES DATA FILE (PUNCHED OUTPUT) CONSISTING OF CARTESIAN
C          COORDINATES OF EACH OF THE THREE PARTICLES (IN INTEGER FORMAT)
C
 TO
C          PRODUCE COMPUTER ANIMATED MOVIES OF SELECTED TRAJECTORIES.
C      2   ON LINE PLOT (INTERNAL COORDINATES)
C
C  READ AND WRITE THIS GROUP OF  PARAMETERS
C  ****************************************************************
      READ(1,501) RHO,EM,HO,RLO,RHI,EOJ,NTOT,NPRINT,IE,NV,NJ
      IV = NV
      IJ = NJ
      WRITE(6,601) NTOT,EM(1),EOJ,RHO,NPRINT,EM(2),IV,RLO,IE,EM(3),IJ,
     1RHI,HO
C
C  ****************************************************************
C  SET UP MASS RATIO ARRAYS
```

```
C    ***************************************************************
       XM=EM(1)+EM(2)+EM(3)
       DO 10 I=1,3
       S(1,I)=EM(I)/(EM(1)+EM(2))
       S(2,I)=EM(I)/(EM(1)+EM(3))
       S(3,I)=EM(I)/(EM(2)+EM(3))
       S(4,I)=EM(I)/XM
    10 CONTINUE
       RME=XM*S(4,1)*(1.D00-S(4,1))
C
C   ***************************************************************
C   CHANNEL NUMBERS ARE ASSIGNED AS FOLLOWS.....
C      0   NO REACTION (PRODUCT BC)
C      1   PRODUCT AB
C      2   PRODUCT AC
C      3   DISSOCIATION
C
C
C   THE FOLLOWING CALLS TO SUBROUTINES INITIALIZE CONSTANTS  IN THESE
C   ROUTINES OR ALLOW DATA TO BE READ BY THESE ROUTINES.....ALL ARGUMENTS
C   ARE TRANSFERED THROUGH BLANK COMMON.
C   ***************************************************************
       CALL FMOMIN
       CALL DFFOTI
       CALL RESLVI
       CALL ANGLIN
       CALL FSTART
       CALL FENGIN
  400  CALL FARMIN
C
C   ***************************************************************
C   TRAJECTORIES ARE COMPUTED IN THE FOLLOWING LOOP
C   ECOL IS THE C.M. COLLISION ENERGY IN EV. DEC = THE INCREMENT FOR ECOL
C   ***************************************************************
       READ(1,504) ECOL,DEC
       IF(IE.EQ.1) WRITE(7,701) NTOT,IJ,RLO,RHI,EOJ,ECOL,DEC
       DO 300  ITRAJ=1,NTOT
       CALL SECOND(TAD)
       T=0.
       IREACT=0
       NV=IV
       NJ=IJ
       WRITE(6,614) ITRAJ,ECOL
       VREL=DSQRT(2.D00*ECOL/RME)
C
C   ***************************************************************
C   INITIALIZE COORDINATES AND MOMENTA
C
       CALL FARMO
C
C   RECORD INITIAL RELATIVE VELOCITY VECTOR
C
       CALL ANGLST
C
C   COMPUTE INITIAL ANGULAR MOMENTA
```

```
C
      CALL FMOM
C
C  COMPUTE INITIAL ENERGIES
C
      CALL FENGY
C
C  ***************************************************************************
C  WRITE INITIAL VALUES OF TOTAL ENERGY (ENTOT), TOTAL ANGUALR MOMENTUM
C  (AMTOT), INTERNAL ENERGY (ENFIN), INTERNAL ANGULAR MOMENTUM (AMINT),
C  AND POTENTIAL ENERGY (XTER)
C  ***************************************************************************
      WRITE(6,602) ENTOT,AMTOT,ENFIN,AMINT,XTER
C
C  CALL TRAJECTORY CONTROL ROUTINE MASTER
C
      CALL MASTER(NPRINT)
C
C  COMPUTE FINAL ENERGIES IN FENGY
C
      CALL FENGY
C
C  COMPUTE FINAL ANGULAR MOMENTA IN FMOM
C
      CALL FMOM
C
C  COMPUTE FINAL RELATIVE VELOCITY AND SCATTERING ANGLE IN ANGLE
C
      CALL ANGLE
      ANG=ANG*RAD
C
C  ***************************************************************************
C  WRITE COLLISION TIME (T), REACTION CHANNEL (IREACT), SCATTERING ANGLE
C  (ANG), AND FINAL VALUES OF RELATIVE VELOCITY (AVV), TOTAL ENERGY,
C  TOTAL ANGULAR MOMENTUM, INTERNAL ENERGY, AND INTERNAL ANGULAR
C  MOMENTUM.
C  ***************************************************************************
      CALL RESLVE
      WRITE(6,603) T,ENTOT,AMTOT,AMINT,IREACT,ANG,XTER,ENFIN,EVIB,NV,
     1EROT,NJ
C
C  ***************************************************************************
C  CONTROL OPTION (IE) DETERMINES IF BACK-INTEGRATION IS TO BE PERFORMED
C  BACK INTEGRATION CONTROLLED BY REMAST
C  ***************************************************************************
      IF(IE.LT.0) CALL REMAST
      IF(IE.EQ.1) WRITE(7,702) T,IREACT,ANG,EVIB,EROT,NV,NJ
      IF(IABS(IE).EQ.2) CALL OLPT
  300 ECOL=ECOL+DEC
      READ(1,505) NTOT,NPRINT,IE
      IF(NTOT.LE.0) GOTO 999
      WRITE(6,604)NTOT,NPRINT,IE
      GOTO 400
  999 STOP
  500 FORMAT(16A4)
```

```
  501 FORMAT(8F10.3,/,5I5)
  504 FORMAT(2F10.6)
  505 FORMAT(3I5)
  600 FORMAT(1H1,5(/),20X,16A4)
  601 FORMAT(5(/),20X,'INPUT DATA....:',///,20X,'NTOT  =',I5,'  MA =',
     1F7.3,'  EOJ=',F7.3,'   RHO =',F8.4,/,20X,'NPRINT=',I5,'  MB ='
     2,F7.3,'  NV =',I3,7X,'RLO =',F8.4,/,20X,'IE    =',I5,'  MC ='
     3,F7.3,'  NJ =',I3,7X,'RHI =',F8.4,/,20X,'DT   =',F6.2)
  602 FORMAT(///,20X,'INITIAL ENERGIES....:',10X,'ANGULAR MOMENTA....:',
     1/,20X,'TOTAL     (H) =',F11.6,5X,'TOTAL W(L+J) =',E15.6,/,20X,
     2'INTERNAL  (E) =',F11.6,5X,'INTERNAL W(J)=',E15.6,/,20X,'POTENTIAL
     3 (V) =',F11.6)
  603 FORMAT(///,20X,'FINAL CONDITIONS....:',/,20X,'COLLISION TIME:'
     1,F20.2,/,20X,'TOTAL ENERGY :',F21.6,/,20X,'TOTAL ANG.MOMENTUM:'
     2,E20.6,/,20X,'INT.ANG.MOMENTUM:',E22.6,/,20X,'REACTION CHANNEL:'
     3,I15,/,20X,'SCATTERING ANGLE:',F15.2,/,20X,'POTENTIAL ENERGY:'
     4,F19.6,/,20X,'INTERNAL ENERGY:',F20.6,/,20X,'VIBRATIONAL ENERGY:'
     5,F17.6,10X,'NV=',I6,/,20X,'ROTATIONAL ENERGY:',F18.6,10X,'NJ=',I6)
  604 FORMAT(10(/),20X,'NEXT CALCULATIONS....:',/,20X,'NTOT,NPRINT,IE:'
     1,3I6)
  614 FORMAT(1H1,20X,14HTRAJECTORY NO.,I5,9X,' TT =',F10.2,'  EV')
  701 FORMAT(2I5,5F10.5)
  702 FORMAT(F5.1,I5,3F10.5,2I5)
      END
      BLOCK DATA
      IMPLICIT REAL*8 (A-H,O-Z)
      COMMON/CONST/RAD,HBAR,PI
      DATA RAD,HBAR,PI/57.29577951308D00,0.1221806962679D00,
     *3.14159265359D00/
      END
      SUBROUTINE DFPOTI
C
C   ***************************************************************
C  FOR INTERATOMIC DISTANCES R(I), CALCULATED IN RVECT.
C  CALCULATES THE POTENTIAL ENERGY ACCORDING TO THE YATES-LESTER FUNCTIO
N,
C  TWO ENTRY POINTS: DERIVE(MM) CALCULATES THE POTENTIAL ENERGY AND THE
C  DERIVATIVES (MM=2), OR ONLY THE POTENTIAL ENERGY (MM=1);  FPOTN
C  CALCULATES THE  H2 ENERGY FROM THE MORSE FUNCTION.
C  ***************************************************************
C
      IMPLICIT REAL*8 (A-H,O-Z)
      REAL*8  J4,J
      DIMENSION S(3),SS(3),Q(3),DEL(3),DS(3),DQ(3),J(3),AS(3),AJ(3)
     1,DDEL(3)
      COMMON XM,U(4,3),C,B,RO,RLO,RHI,Y(8),R(3),FF(8),DD(3),TERM,VREL,
     1RHO,HO,AVV,ANG,AMINT,AMTOT,XTER,ENFIN,ENTOT,T,H,EVIB,EROT,TAD,DIST
     2,NV,NJ,IREACT,KDQ,IDEX,IE
      READ (1,60)C,RO,B,AK,AL,DI,AE
      WRITE(6,61) C,AK,RO,AL,B,DI,AE
   61 FORMAT(10(/),20X,'YATES-LESTER SURFACE PARAMETERS:',//,20X,
     1'DE   =',F10.5,4X,'KAPPA   =',F11.5,/,20X,'RE    =',F10.5,4X,
     2'LAMBDA  =',F11.5,/,20X,'BETA =',F10.5,4X,'DELTA   =',F11.5,/,
     320X,'(MORSE CONSTANTS)',' EPSILON =',F11.5)
      GOTO 900
```

```
      ENTRY DERIVE(MM)
     DO 30 K=1,3
     RK=R(K)
     EX=DEXP(-B*(RK-RO))
     ES=C*EX*(EX-2.D00)
     Z=1.D00+AK*DEXP(-AL*RK)
     ZR=Z*RK
     S(K)=(1.D00+ZR*(1.D00+ZR/3.D00))*DEXP(-ZR)
     SS(K)=S(K)*S(K)
     Q(K)=(1.D00+SS(K))*ES/2.D00
     DEL(K)=DI*(1.D00+1.D00/RK)*DEXP(-2.D00*RK)
     IF(MM.EQ.1)GOTO 30
     DES=-2.D00*B*C*EX*(EX-1.D00)
     DZ=AL*(1.D00-Z)
     DS(K)=-ZR*(1.D00+ZR)*(Z+RK*DZ)*DEXP(-ZR)/3.D00
     DQ(K)=(1.D00+SS(K))*DES/2.D00+S(K)*DS(K)*ES
     DDEL(K)=-DI*(2.D00+(2.D00+1.D00/RK)/RK)*DEXP(-2.D00*RK)
30   CONTINUE
     QU=Q(1)+Q(2)+Q(3)
     S4=1.D00-S(1)*S(2)*S(3)
     J4=QU+AE*(S4-1.D00)
     J(1)=Q(1)+SS(1)*(DEL(2)+DEL(3))
     J(2)=Q(2)+SS(2)*(DEL(1)+DEL(3))
     J(3)=Q(3)+SS(3)*(DEL(1)+DEL(2))
     AS(1)=SS(2)-SS(3)
     AS(2)=SS(3)-SS(1)
     AS(3)=SS(1)-SS(2)
     AJ(1)=J(2)-J(3)
     AJ(2)=J(3)-J(1)
     AJ(3)=J(1)-J(2)
      C1=S4*S4-(AS(1)*AS(1)+AS(2)*AS(2)+AS(3)*AS(3))/2.D00
     C2=-S4*J4+(AS(1)*AJ(1)+AS(2)*AJ(2)+AS(3)*AJ(3))/2.D00
     C3=J4*J4-(AJ(1)*AJ(1)+AJ(2)*AJ(2)+AJ(3)*AJ(3))/2.D00
     E=-(C2+DSQRT(C2*C2-C1*C3))/C1
     XTER=E+C
     IF(MM.EQ.1)GOTO 900
     DO 31 K=1,3
     L=K+1-(K/3)*3
     M=L+1-(L/3)*3
     DSS=S(K)*DS(K)*2.D00
     DS4=-S(L)*S(M)*DS(K)
     DJK=DQ(K)+DSS*(DEL(L)+DEL(M))
     DJL=SS(L)*DDEL(K)
     DJM=SS(M)*DDEL(K)
     DC1=2.D00*S4*DS4-DSS*(AS(M)-AS(L))
     DC2=-S4*(DQ(K)+AE*DS4)-J4*DS4+(DSS*(AJ(M)-AJ(L))+DJK*(AS(M)-AS(L))
    1+DJL*(AS(K)-AS(M))+DJM*(AS(L)-AS(K)))/2.D00
     DC3=2.D00*J4*(DQ(K)+AE*DS4)-(DJK*(AJ(M)-AJ(L))+DJL*(AJ(K)-AJ(M))+
    1DJM*(AJ(L)-AJ(K)))
     DD(K)=0.5D00*(E*E*DC1+2.D00*E*DC2+DC3)/DSQRT(C2*C2-C1*C3)
31   CONTINUE
900  RETURN
     ENTRY FPOTN
     RK=DMIN1(R(1),R(2),R(3))
     IF(RK.GT.RHI+0.5D00*RHO) GOTO 210
```

```
      EX=1.D00-DEXP(-B*(RK-RO))
      TERM=C*EX*EX
      GOTO 900
  210 TERM=0.D00
      GOTO 900
   60 FORMAT(7F10.2)
      END
      SUBROUTINE RESLVI
C
C  ***************************************************************
C  ROUTINE RESOLVES THE FINAL INTERNAL ENERGY INTO ITS VIBRATIONAL AND
C  ROTATIONAL COMPONENTS.....ALSO CALCULATES NEAREST INTEGER VALUES FOR
C  THE VIBRATIONAL AND ROTATIONAL QUANTUM NUMBERS.....TWO ENTRY POINTS
C  .....RESOLVI INITIALIZES SPECTROSCOPIC CONSTANTS.....RESOLVE USES
C  METHOD DESCRIBED BY J. T. MUCKERMAN, J.C.P. 54, 1155 (1971) AND
C  J.C.P. 56, 2997 (1972) TO DO CALCULATION
C  ***************************************************************
C
      IMPLICIT REAL*8 (A-H,O-Z)
      COMMON XM,S(4,3),C,B,RO,RLO,RHI,Y(8),R(3),FF(8),DD(3),TERM,VREL,
     1RHO,HO,AVV,ANG,AMINT,AMTOT,XTER,ENFIN,ENTOT,T,H,EVIB,EROT,TAD,DIST
     2,NV,NJ,IREACT,KDQ,IDEX,IE
      COMMON/CONST/RAD,HBAR,PI
      EMU0=XM*S(4,2)*S(3,3)
      EMU1=XM*S(4,2)*S(1,1)
      EMU2=XM*S(4,1)*S(2,3)
      OE0=B*HBAR*DSQRT(2.D00*C/EMU0)
      OE1=B*HBAR*DSQRT(2.D00*C/EMU1)
      OE2=B*HBAR*DSQRT(2.D00*C/EMU2)
      OEXE0=(HBAR*HBAR*B*B)/(2.D00*EMU0)
      OEXE1=(HBAR*HBAR*B*B)/(2.D00*EMU1)
      OEXE2=(HBAR*HBAR*B*B)/(2.D00*EMU2)
      BE0=HBAR*HBAR/(2.D00*EMU0*RO*RO)
      BE1=HBAR*HBAR/(2.D00*EMU1*RO*RO)
      BE2=HBAR*HBAR/(2.D00*EMU2*RO*RO)
      AE0=6.D00*(DSQRT(OEXE0*BE0**3)-BE0**2)/OE0
      AE1=6.D00*(DSQRT(OEXE1*BE1**3)-BE1**2)/OE1
      AE2=6.D00*(DSQRT(OEXE2*BE2**3)-BE2**2)/OE2
      DE0=4.D00*BE0**3/OE0**2
      DE1=4.D00*BE1**3/OE1**2
      DE2=4.D00*BE2**3/OE2**2
   10 RETURN
      ENTRY RESLVE
C
C  ***************************************************************
C  RESOLVES INTERNAL ENERGY (ENFIN) AND INTERNAL ANGULAR MOMENTUM
C  (AMINT) IN CHANNEL DESIGNATED BY IREACT INTO VIBRATIONAL ENERGY
C  (EVIB), ROTATIONAL ENERGY (EROT), VIBRATIONAL QUANTUM NUMBER (NV),
C  ***************************************************************
C
      TJ=(AMINT/HBAR)**2
      NJ=DSQRT(TJ)
      NN=IREACT+1
      GO TO (1,4,7,11),NN
    1 CONTINUE
```

```
      MM=0
      EROT=TJ*BE0
      EVIB=ENFIN-EROT
      TER=0.D00
      TEV=0.D00
    2 CONTINUE
      ARG=(OE0/OEXE0)**2-4.D00*EVIB/OEXE0
      IF(ARG) 21,22,22
   21 CONTINUE
      ARG=0.D00
      WRITE(6,61)
   22 CONTINUE
      TV=(OE0/OEXE0-DSQRT(ARG))/2.D00
      BV=BE0-TV*AE0
      EROT=TJ*BV-TJ*TJ*DE0
      EVIB=ENFIN-EROT
      IF(DABS(EROT-TER).GT.DABS(EROT)*1.D-03) GOTO 3
      IF(DABS(EVIB-TEV).GT.DABS(EVIB)*1.D-03) GOTO 3
      NV=TV
      GO TO 10
    3 CONTINUE
      IF(MM.GT.50) GO TO 12
      TER=EROT
      TEV=EVIB
      MM=MM+1
      GO TO 2
    4 CONTINUE
      MM=0
      EROT=TJ*BE1
      EVIB=ENFIN-EROT
      TER=0.D00
      TEV=0.D00
    5 CONTINUE
      ARG=(OE1/OEXE1)**2-4.D00*EVIB/OEXE1
      IF(ARG) 51,52,52
   51 CONTINUE
      ARG=0.D00
      WRITE(6,61)
   52 CONTINUE
      TV=(OE1/OEXE1-DSQRT(ARG))/2.D00
      BV=BE1-TV*AE1
      EROT=TJ*BV-TJ*TJ*DE1
      EVIB=ENFIN-EROT
      IF(DABS(EROT-TER).GT.DABS(EROT)*1.D-03) GOTO 6
      IF(DABS(EVIB-TEV).GT.DABS(EVIB)*1.D-03) GOTO 6
      NV=TV
      GO TO 10
    6 CONTINUE
      IF(MM.GT.50) GO TO 12
      TER=EROT
      TEV=EVIB
      MM=MM+1
      GO TO 5
    7 CONTINUE
      MM=0
```

```
      EROT=TJ*BE2
      EVIB=ENFIN-EROT
      TER=0.D00
      TEV=0.D00
    5 CONTINUE
      ARG=(OE2/OEXE2)**2-4.D00*EVIB/OEXE2
      IF(ARG) 81,82,82
   81 CONTINUE
      ARG=0.D00
      WRITE(6,61)
   82 CONTINUE
      TV=(OE2/OEXE2-DSQRT(ARG))/2.D00
      BV=BE2-TV*AE2
      EROT=TJ*BV-TJ*TJ*DE2
      EVIB=ENFIN-EROT
      IF(DABS(EROT-TER).GT.DABS(EROT)*1.D-03) GOTO 9
      IF(DABS(EVIB-TEV).GT.DABS(EVIB)*1.D-03) GOTO 9
      NV=TV
      GO TO 10
    9 CONTINUE
      IF(MM.GT.50) GO TO 12
      TER=EROT
      TEV=EVIB
      MM=MM+1
      GO TO 8
   11 CONTINUE
      EROT=0.D00
      EVIB=0.D00
      GO TO 10
   12 CONTINUE
      WRITE(6,60)
      EROT=0.D00
      EVIB=0.D00
      GO TO 10
   60 FORMAT(50H ITERATIVE DECONVOLUTION OF INTERNAL ENERGY FAILED)
   61 FORMAT(20H ARG WAS SET TO ZERO)
      END
      SUBROUTINE DBASH
C
C     ***************************************************************
C     ADAMS-BASHFORTH FOURTH-ORDER PREDICTOR-CORRECTOR ROUTINE, WITH A
C     THREE-STEP RUNGE-KUTTA STARTUP AND A FIXED STEP SIZE (DX).
C     ***************************************************************
C
      IMPLICIT REAL*8 (A-H,O-Z)
      COMMON XM,S(4,3),C,B,RO,RLO,RHI,Y(8),R(3),DY(8),DD(3),TERM,VREL,
     1RHO,HO,AVV,ANG,AMINT,AMTOT,XTER,ENFIN,ENTOT,T,DX,EVIB,EROT,TAD,DIS
T
     2,NV,NJ,IREACT,KDQ,NSTEP,IE
      DIMENSION DIFF(8),ARRAY(4,8)
      NE=8
      IF (NSTEP.LT.3) GOTO  5
      DO 1 J=1,NE
      YPC=ARRAY(4,J)+DX*(2.29166666666667D00*DY(J)-2.45833333333333D00
     1*ARRAY(3,J)+1.54166666666667D00*ARRAY(2,J)-0.375D00*ARRAY(1,J))
```

```
      ARRAY(1,J)=ARRAY(2,J)
      ARRAY(2,J)=ARRAY(3,J)
      ARRAY(3,J)=DY(J)
      Y(J)=YPC-0.92962962962963D00*DIFF(J)
    1 DIFF(J)=YPC
      CALL F
      DO 2 J=1,NE
      YPC=ARRAY(4,J)+DX*(0.375D00*DY(J)+0.79166666666667D00*ARRAY(3,J)-
     10.20833333333333D00*ARRAY(2,J)+0.04166666666667D00*ARRAY(1,J))
      DIFF(J)=DIFF(J)-YPC
    2 Y(J)=YPC+0.0703703703703 7D00  *DIFF(J)
      CALL F
      NSTEP=NSTEP+1
    3 DO  4 J=1,NE
    4 ARRAY(4,J)=Y(J)
      RETURN
C
C   ***************************************************************************
C     RUNGE KUTTA INTEGRATION
C   ***************************************************************************
C
    5 IF (NSTEP.NE.0) GOTO 7
      CALL F
      DO 6 J=1,NE
    6 ARRAY(1,J)=DY(J)
    7 DO 26 I=1,4
      DO 14 J=1,NE
      GOTO (8,9,9,10),I
    8 DIFF(J)=Y(J)
      ARRAY(4,J)=-DY(J)
    9 YPC=2.D00
   10 ARRAY(4,J)=ARRAY(4,J)+YPC*DY(J)
      GOTO (13,13,12,11),I
   11 Y(J)=DIFF(J)+DX*ARRAY(4,J)/6.D00
      GOTO 14
   12 YPC=1.D00
   13 Y(J)=DIFF(J)+DX*DY(J)/YPC
   14 CONTINUE
      CALL F
   26 CONTINUE
      NSTEP=NSTEP+1
      DO 17 J=1,NE
      ARRAY(NSTEP+1,J)=DY(J)
   17 DIFF(J)=0.D00
      IF (NSTEP.LT.3) RETURN
      GOTO 3
      END
      SUBROUTINE PARMIN
C
C   ***************************************************************************
C   VARIABLE INITIALIZATION ROUTINE.....TWO ENTRY POINTS.....MONTIN
C   CALCULATES CONSTANTS AND READS CHOICE OF DIATOMIC TURNING POINT FOR
C   FIRST TRAJECTORY.....MONTE INITIALIZES ALL MONTE CARLO VARIABLES
C   ***************************************************************************
C
```

```
      IMPLICIT REAL*8 (A-H,O-Z)
      COMMON XM,S(4,3),C,B,RO,RLO,RHI,Y(8),R(3),FF(8),DD(3),TERM,VREL,
     1RHO,HO,AVV,ANG,AMINT,AMTOT,XTER,ENFIN,ENTOT,T,H,EVIB,EROT,TAD,EOJ
     2,NV,NJ,IREACT,KDO,IDEX,IE
      COMMON/CONST/RAD,HBAR,PI
C
C     BPM = IMPACT PARAMETER
C  PHI=PHASE ANGLE, THETA IS ORIENTATION PARAMETER,RLO IS INNER TURNING
C  POINT(PHI=90), RHI IS OUTER TURNING POINT (PHI=270) AND EOJ IS THE
C  ENERGY FOR THE APPROPRIATE (NV,NJ) LEVEL.
C
      READ(1,501) PHI,THETA,BPM
      WRITE (6,601)PHI,THETA,BPM
      PHI=PHI/RAD
      THETA=THETA/RAD
      EM=XM*S(4,2)*S(3,3)*2.D00
      TJSQ=NJ*(NJ+1)
      ST=DSIN(THETA)
      CT=DCOS(THETA)
      AMP=RO-RLO
      IF(PHI.GT.PI) AMP=RHI-RO
      RR=RO-AMP*DSIN(PHI)
      PEQ=DSQRT(TJSQ)*HBAR/RR
      EPX=1.D00-DEXP(-B*(RR-RO))
      EPR=PEQ*PEQ/EM+C*ERX*EPX
      IF(EOJ.LT.EPR) EOJ=EPR
      PRAD=DSQRT(EM*(EOJ-EPR))
      IF(DABS(PHI-PI).GT.PI/2.D00)PRAD=-PRAD
      IF(IE.EQ.1) WRITE(7,701) PHI,THETA,BPM
  701 FORMAT(3F10.5)
  100 RETURN
      ENTRY PARMO
C
C   ***************************************************************
C  INITIALIZE CO-ORDINATES
C   ***************************************************************
      Y(1)=RR*ST
      Y(2)=RR*CT
      Y(3)=BPM
      Y(4)=-DSQRT(RHO*RHO-BPM*BPM)
C
C   ***************************************************************
C  INITIALIZE MOMENTA
C   ***************************************************************
      Y(5)=-PEQ*CT+PRAD*ST
      Y(6)=PEQ*ST+PRAD*CT
      Y(7)=0.D00
      Y(8)=XM*S(4,1)*(1.D00-S(4,1))*VREL
      IF(IABS(IE).EQ.1) WRITE(7,600)RHO,RR,NV,NJ,PHI,THETA,BPM
C
C   ***************************************************************
C  WRITE INITIAL VALUES OF COORDINATES AND MOMENTA
C   ***************************************************************
      WRITE(6,602) T,Y
      GO TO 100
```

```
501   FORMAT(3F10.6)
600   FORMAT(' R(A-BC)=',D15.6,'  R(B-C)=',D15.6,'  (CM)     ',/,10X,
     1'NV=',I5,'   NJ=',I5,'   PHI=',F10.2,/,10X,'THETA=',F10.2,'   B=',
     2D15.6)
 601 FORMAT(/,20X,' INITIAL PARAMETERS....:  PHI,THETA,BPM '/20X3F12.6)
 602 FORMAT(///,20X,'REACTION TIME:',F10.2,/,20X,'COORDINATES:',4F12.6,
     1/,20X,'MOMENTA:',4X,4F12.6)
      END
      SUBROUTINE OLPT
C
C   ***************************************************************
C  ON-LINE PLOTTING ROUTINE FOR TIME VS. DISTANCE DIAGRAMS
C   ***************************************************************
C
      IMPLICIT REAL*8 (A-H,O-Z)
      INTEGER*2 SB,IP(126),NX
      COMMON/PLT/X,Y,Z,A,B,NP,NS,NT
      DIMENSION XS(30),YS(30),ZS(30),ALP(30),BET(30),NX(9),NA(7)
      DATA SB,NX,NA/' ',0,1,2,3,4,5,6,7,0,30,60,90,120,150,180/
      DO 10 J=1,126
   10 IP(J)=SB
      WRITE(6,500) NX,NA
      WRITE(6,501)
      IF(NP.EQ.0) NP=1
      NN=50/NP
      WRITE(6,504) NX(1)
      DO 1 I=1,NP
      IX=XS(I)+1.5D00
      IY=YS(I)+1.5D00
      IZ=ZS(I)+1.5D00
      IA=ALP(I)/3.+66
      IB=BET(I)/3.+66
      IC=258-IA-IB
      IP(IX)=NX(2)
      IP(IY)=NX(3)
      IP(IZ)=NX(4)
      IP(IA)=NX(5)
      IP(IB)=NX(6)
      IP(IC)=NX(7)
      WRITE(6,503) IP
      IP(IX)=SB
      IP(IY)=SB
      IP(IZ)=SB
      IP(IA)=SB
      IP(IB)=SB
      IP(IC)=SB
      NC=(I-1)*NT/NP
      WRITE(6,504) NC
      DO 1 J=1,NN
    1 WRITE(6,502)
      WRITE(6,501)
      WRITE(6,505) NX,NA
  500 FORMAT(1H1,40X,'R ( A.U    )',60X,'ANGLE (DEGREE)',/,5X,
     118(I1,6X),1X,4(8X,I2),3(7X,I3),/)
  501 FORMAT(5X,7('+------'),'+',14X,6('+----+----'),'+')
```

```
502  FORMAT(5X,'[',63X,'[')
503  FORMAT(1H+,4X,126A1)
504  FORMAT(1H+,I3,62X,I3)
505  FORMAT(5X,8(I1,6X),1X,4(8X,I2),3(7X,I3),//,15X,'TIME          VS
     1        DISTANCE',30X,'TIME          VS          MOLECULAR ANGLE')
 900 RETURN
     ENTRY PLOT
     XS(NP)=X*7.
     YS(NP)=Y*7.
     ZS(NP)=Z*7.
     ALP(NP)=A
     BET(NP)=B
     GOTO 900
     END
     SUBROUTINE ANGLIN
C
C   ***************************************************************************
C   ROUTINE CALCULATES SCATTERING ANGLE AND FINAL RELATIVE VELOCITY.....
C   THREE ENTRY POINTS.....ANGLIN INITIALIZES CONSTANTS.....ANGLST STORES
C   INITIAL RELATIVE VELOCITY VECTOR.....ANGLE PERFORMS CALCULATION
C   ***************************************************************************
C
      IMPLICIT REAL*8 (A-H,O-Z)
      COMMON/CONST/RAD,HBAR,PI
      COMMON XM,S(4,3),C,B,RO,RLO,RHI,Y(8),R(3),FF(8),DD(3),IERM,VREL,
     1RHO,HO,AVV,ANG,AMINT,AMTOT,XTER,ENFIN,ENTOT,T,H,EVIB,EROT,TAD,DIST
     2,NV,NJ,IREACT,KDQ,IDEX,IE
      DIMENSION VO(2),V(2)
      RM1=XM*S(4,1)*(1.D00-S(4,1))
      RM2=XM*S(4,3)*(1.D00-S(4,3))
      RM3=XM*(1.D00-S(4,3))*(1.D00-S(4,1))
      RM4=XM*S(4,2)*(1.D00-S(4,2))
      RM5=XM*(1.D00-S(4,2))*(1.D00-S(4,1))
 100  RETURN
      ENTRY ANGLST
C
C   ***************************************************************************
C   STORE RELATIVE VELOCITY VECTOR IN VO(3) AND ITS MAGNITUDE IN AVVO
C   ***************************************************************************
C
      DO 110  I=1,2
      VO(I)=Y(I+6)/RM1
 110  CONTINUE
      AVVO=VREL
      GO TO 100
      ENTRY ANGLE
C
C   ***************************************************************************
C   CALCULATES FINAL RELATIVE VELOCITY AND SCATTERING ANGLE USING INITIAL
C   AND FINAL RELATIVE VELOCITY VECTORS
C   ***************************************************************************
C
      DOTPR=0.D00
      AVV=0.D00
      DO 600  I=1,2
```

```
      NN=IREACT+1
      GO TO(200,300,400,200),NN
  200 CONTINUE
      V(I)=Y(I+6)/RM1
      GO TO 500
  300 CONTINUE
      V(I)=Y(I+6)/RM3-Y(I+4)/RM2
      GO TO 500
  400 CONTINUE
      V(I)=Y(I+4)/RM4+Y(I+6)/RM5
  500 CONTINUE
      DOTPR=DOTPR+V(I)*VO(I)
      AVV=AVV+V(I)*V(I)
  600 CONTINUE
      AVV=DSQRT(AVV)
      IF(DABS(DOTPR).LE.1.D-20) GOTO 700
      D=AVVO*AVV/DOTPR
      D=DSQRT(D*D-1.D00)
      ANG=DATAN(D)
      GO TO 100
  700 ANG=PI/2.D00
      GO TO 100
      END
      SUBROUTINE MASTER(NPRINT)
C
C  ***************************************************************
C  ROUTINE CONTROLS CALCULATION OF TRAJECTORY.....TWO ENTRY POINTS.....
C  MASTER CALCULATES STANDARD TRAJECTORY.....REMAST CONTROLS BACK-
C  INTEGRATION OF EACH TRAJECTORY IF IE=1 OR 2.....IF IE=1  MASTER
C  CREATES PUNCHED OUTPUT FILE CONSISTING OF THE CARTESIAN COORDINATES
C  OF EACH ATOM AT EACH FIFTEENTH POINT IN THE INTEGRATION.....ONE CARD
C  IN INTEGER FORMAT AT EACH POINT PUNCHED
C  ***************************************************************
C
      IMPLICIT REAL*8 (A-H,O-Z)
      COMMON/FACT/F(4)
      COMMON XM,S(4,3),C,B,RO,RLO,RHI,Y(8),R(3),FF(8),DD(3),TERM,VREL,
     1RHO,HO,AVV,ANG,AMINT,AMTOT,XTER,ENFIN,ENTOT,T,H,EVIB,EROT,TAD,DIST
     2,NV,NJ,IREACT,KDQ,IDEX,IE
      COMMON/PLT/XS,YS,ZS,ALPHA,BETA,NP,NS,NT
      COMMON/CONST/RAD,HBAR,PI
      DIMENSION NCD(6)
      H=HO*1.856233688694D-02
      KDQ=1
      NP=0
      IDEX=0
C
C  CALCULATE QUANTITIES USED IN END TEST OF TRAJECTORY
C
      RTEST=RHO+.5D00*RHI
      NMAX=(RHI-RLO)/VREL/H
      IF(IABS(IE)-1) 100,90,140
   90 CONTINUE
      TF1=S(4,1)/S(3,1)
      TF2=-S(3,3)
```

```
      TF3=-S(4,1)
      TF4=S(3,2)
      GOTO 140
  100 CONTINUE
C
C   CHECK FOR END OF TRAJECTORY ONLY AFTER TAKING NMAX STEPS
C
      IF(KDQ.LT.NMAX) GO TO 120
C
C   CHECK FOR END OF TRAJECTORY.....IS ONE INTERNUCLEAR DISTANCE GREATER
C   THAN RTEST
C
      IF(R(1).GT.RTEST) GO TO 200
      IF(R(2).GT.RTEST) GO TO 300
      IF(KDQ.GT.1000) GOTO 500
  120 CONTINUE
C
C   INTEGRATE EQUATIONS OF MOTION ONE STEP
C
      CALL DBASH
      T=T+HO
      KDQ=KDQ+1
C
C   TEST TO SEE IF COORDINATES SHOULD BE PUNCHED OUT
C
      IF(MOD(KDQ,NPRINT).NE.1) GOTO 100
  140 CONTINUE
      NP=NP+1
      NT=T+0.5D00
      IF(IABS(IE)-1)  110,130,150
  110 CALL FENGY
      WRITE(6,50) T,R,ENFIN,XTER,ENTOT
      GOTO 100
  130 CONTINUE
      DO 160 J=1,2
      NCD(J)=TF1*Y(J+2)*1.D14
      NCD(J+2)=(TF2*Y(J)+TF3*Y(J+2))*1.D14
      NCD(J+4)=(TF4*Y(J)+TF3*Y(J+2))*1.D14
  160 CONTINUE
      WRITE(7,40) NCD,NT,NP
      GOTO 100
  150 CONTINUE
      XS=R(1)
      YS=R(2)
      ZS=R(3)
      D=2.D0*R(2)*R(3)/(R(2)*R(2)+R(3)*R(3)-R(1)*R(1))
      DA=DABS(D*D-1.D00)
      DA=DSQRT(DA)
      ALPHA=DATAN(DA)*RAD
      D=2.D00*R(1)*R(3)/(R(1)*R(1)+R(3)*R(3)-R(2)*R(2))
      DA=DABS(D*D-1.D00)
      DA=DSQRT(DA)
      BETA=DATAN(DA)*RAD
      CALL PLOT
      GO TO 100
```

```
  200 CONTINUE
C
C   TEST FOR A SECOND INTERNUCLEAR DISTANCE GREATER THAN RTEST.....ASSIGN
C   CHANNEL NUMBER (IREACT)
C
      IF(R(2).GT.RTEST) GO TO 310
      IF(R(3).GT.RTEST) GO TO 320
      GO TO 120
  300 CONTINUE
      IF(R(3).GT.RTEST) GO TO 330
      GO TO 120
  310 CONTINUE
      IREACT=2
      GO TO 500
  320 CONTINUE
      IREACT=0
      GO TO 500
  330 CONTINUE
      IREACT=1
  500 CONTINUE
      KNG=KDQ-1
      CALL SECOND(CPTIME)
      CPTIME=CPTIME-TAD
C
C   WRITE NUMBER OF INTEGRATION STEPS TAKEN AND REAL ELAPSED TIME FOR THE
C   COMPUTATION OF TRAJECTORY
C
      WRITE(6,10) KNG,CPTIME
C
C   WRITE SIMULATED TIME FOR COLLISION PROCESS AND FINAL VALUES OF THE
C   COORDINATES AND MOMENTA
C
      WRITE(6,20) T,Y
  700 RETURN
      ENTRY REMAST
C
C   BEGIN BACK-INTEGRATION
C
      H=-H
      IDEX=0
      DO 600  KDQ=1,KNG
      CALL DBASH
      T=T-HO
  600 CONTINUE
C
C   WRITE FINAL SIMULATED TIME AND COORDINATES AND MOMENTA FROM BACK-
C   INTEGRATION.....THESE SHOULD BE IDENTICAL TO THE INITIAL VALUES
C
      WRITE(6,20) T,Y
      GO TO 700
   10 FORMAT(//,20X,'NUMBER OF STEPS =',I6,5X,'CPU TIME =',F10.3)
   20 FORMAT(///,20X,'REACTION TIME:',F10.2,/,20X,'COORDINATES:',4F12.6,
     1/,20X,'MOMENTA:',4X,4F12.6)
   30 FORMAT(1H ,20X,4D15.6)
   40 FORMAT(10I8)
```

```
   50 FORMAT(20X,F10.2,3F15.6,5X,'TV=',F15.6,5X,'V(H2)=',F15.6,5X,'H=',
     1F15.6)
      END
      SUBROUTINE FSTART
C
C  ***************************************************************
C  ROUTINE FOR HAMILTON'S EQUATIONS OF MOTION.....TWO ENTRY POINTS.....
C  FSTART INITIALIZES CONSTANTS.....F CALCULATES TIME DERIVATIVES OF
C  COORDINATES AND MOMENTA
C  ***************************************************************
C
      IMPLICIT REAL*8 (A-H,O-Z)
      COMMON/FACT/FC(4)
      COMMON XM,S(4,3),C,B,RO,RLO,RHI,Y(8),R(3),FF(8),DD(3),TERM,VREL,
     1RHO,HO,AVV,ANG,AMINT,AMTOT,XTER,ENFIN,ENTOT,T,H,EVIB,EROT,TAD,DIST
     2,NV,NJ,IREACT,KDQ,IDEX,IE
      W=1.D00/S(3,2)/S(4,3)/XM
      Z=1.D00/S(4,1)/(1.D00-S(4,1))/XM
      W1=S(3,2)
      W2=S(3,3)
  100 RETURN
      ENTRY F
C
C  ***************************************************************
C  TIME DERIVATIVES OF COORDINATES AND MOMENTA ARE CALCULATED AT POINT
C  SPECIFIED BY Y(12) AND ARE STORED IN FF(12)
C  ***************************************************************
C
      DO 200  J=1,2
      FF(J)=W*Y(J+4)
      FF(J+2)=Z*Y(J+6)
  200 CONTINUE
      CALL RVECT
      CALL DERIVE(2)
      DO 300  I=1,3
  300 DD(I)=DD(I)/R(I)
      DO 400  I=1,2
      PAR1=(W2*Y(I)+Y(I+2))*DD(1)
      PAR2=(W1*Y(I)-Y(I+2))*DD(3)
      FF(I+4)=-W2*PAR1-DD(2)*Y(I)-W1*PAR2
      FF(I+6)=PAR2-PAR1
  400 CONTINUE
      GO TO 100
      END
      SUBROUTINE RVECT
C
C  ***************************************************************
C
C  INTERNUCLEAR DISTANCES ARE CALCULATED FROM GENERALIZED COORDINATES
C  (FIRST SIX ELEMENTS IN Y(12)) AND ARE STORED IN R(3)
C
C  ***************************************************************
C
      IMPLICIT REAL*8 (A-H,O-Z)
      COMMON XM,S(4,3),C,B,RO,RLO,RHI,Y(8),R(3),FF(8),DD(3),TERM,VREL,
```

```
     .1RHO,HO,AVV,ANG,AMINT,AMTOT,XTER,ENFIN,ENTOT,T,H,EVIB,EROT,TAD,DIST
     2,NV,NJ,IREACT,KDQ,IDEX,IE
      W1=S(3,3)
      W2=S(3,2)
      W3=W1*Y(1)+Y(3)
      W4=W1*Y(2)+Y(4)
      R1=DSQRT(W3*W3+W4*W4)
      R2=DSQRT(Y(1)*Y(1)+Y(2)*Y(2))
      W3=W2*Y(1)-Y(3)
      W4=W2*Y(2)-Y(4)
      R3=DSQRT(W3*W3+W4*W4)
      R(1)=R1
      R(2)=R2
      R(3)=R3
      RETURN
      END
      SUBROUTINE FMOMIN
C
C     ***************************************************************
C     ROUTINE FOR CALCULATING TOTAL AND INTERNAL ANGULAR MOMENTA.....TWO
C     ENTRY POINTS.....FMOMIN INITIALIZES CONSTANTS.....FMOM PERFORMS
C     CALCULATION
C     ***************************************************************
C
      IMPLICIT REAL*8 (A-H,O-Z)
      COMMON XM,S(4,3),C,B,RO,RLO,RHI,Y(8),R(3),FF(8),DD(3),TERM,VREL,
     1RHO,HO,AVV,ANG,AMINT,AMTOT,XTER,ENFIN,ENTOT,T,H,EVIB,EROT,TAD,DIST
     2,NV,NJ,IREACT,KDQ,IDEX,IE
      C1=S(1,2)/(1.D00-S(4,1))
      C2=S(1,2)*S(3,3)/(1.D00-S(4,1))
      C3=S(1,1)*S(3,3)
      C4=S(1,1)
      C5=S(2,3)/(1.D00-S(4,1))
      C6=-S(2,2)*S(3,3)/(1.D00-S(4,1))
      C7=S(2,1)*S(3,2)
      C8=-S(2,1)
   10 RETURN
      ENTRY FMOM
C
C     ***************************************************************
C     TOTAL ANGULAR MOMENTUM (AMTOT) AND INTERNAL ANGULAR MOMENTUM (AMINT)
C     IN CHANNEL DESIGNATED BY IREACT ARE CALCULATED
C     ***************************************************************
C
      NN=IREACT+1
      GO TO(200,300,300,200),NN
  200 CONTINUE
      AX=Y(1)*Y(6)-Y(2)*Y(5)
      AXT=AX+Y(3)*Y(8)-Y(4)*Y(7)
      AMINT=DABS(AX)
      AMTOT=DABS(AXT)
      IF(IREACT.EQ.3) GO TO 500
      GO TO 100
  300 CONTINUE
      AX1=Y(3)*Y(8)-Y(4)*Y(7)
```

```
      AX2=Y(1)*Y(8)-Y(2)*Y(7)
      AX3=Y(1)*Y(6)-Y(2)*Y(5)
      AX4=Y(3)*Y(6)-Y(4)*Y(5)
      IF(IREACT.EQ.2) GO TO 400
      AX=C1*AX1+C2*AX2+C3*AX3+C4*AX4
  350 CONTINUE
      AMINT=DABS(AX)
      AXT=AX3+AX1
      AMTOT=DABS(AXT)
      GO TO 100
  400 CONTINUE
      AX=C5*AX1+C6*AX2+C7*AX3+C8*AX4
      GO TO 350
  500 CONTINUE
      AMINT=0.D00
  100 RETURN
      END
      SUBROUTINE FENGIN
C
C  ***************************************************************************
C  ROUTINE FOR CALCULATING TOTAL AND INTERNAL ENERGIES.....TWO ENTRY
C  POINTS.....FENGIN INITIALIZES CONSTANTS.....FENGY PERFORMS
C  CALCULATION
C  ***************************************************************************
C
       IMPLICIT REAL*8 (A-H,O-Z)
       COMMON XM,S(4,3),C,B,RO,RLO,RHI,Y(8),R(3),FF(8),DD(3),TERM,VREL,
      1RHO,HO,AVV,ANG,AMINT,AMTOT,XTER,ENFIN,ENTOT,T,H,EVIB,EROT,TAD,DIST,
      2,NV,NJ,IREACT,KDQ,IDEX,IE
       RED1=1.D00/(2.D00*XM*S(3,2)*S(4,3))
       RED2=S(1,1)/(2.D00*XM*S(4,2))
       RED3=S(1,2)/(2.D00*XM*S(4,1)*(1.D00-S(4,1))**2)
       RED4=1.D00/(XM*(1.D00-S(4,3))*(1.D00-S(4,1)))
       RED5=S(2,1)/(2.D00*XM*S(4,3))
       RED6=S(2,3)/(2.D00*XM*S(4,1)*(1.D00-S(4,1))**2)
       RED7=-1.D00/(XM*(1.D00-S(4,2))*(1.D00-S(4,1)))
       RED8=RED1
       RED9=1.D00/(2.D00*XM*S(4,1)*(1.D00-S(4,1)))
   10 RETURN
      ENTRY FENGY
C
C  ***************************************************************************
C  CALCULATE TOTAL ENERGY (ENTOT) AND INTERNAL ENERGY (ENFIN) IN
C  CHANNEL DESIGNATED BY IREACT
C  ***************************************************************************
C
       CALL RVECT
       CALL FPOTN
       CALL DERIVE(1)
       PP1=Y(5)*Y(5)+Y(6)*Y(6)
       PP2=Y(7)*Y(7)+Y(8)*Y(8)
       PP3=Y(5)*Y(7)+Y(6)*Y(8)
       ENKT=RED8*PP1+RED9*PP2
       NN=IREACT+1
       GO TO(30,40,50,30),NN
```

```
 30 CONTINUE
    TINTF=RED1*PP1
    ENFIN=TINTF+TERM
    IF(ENFIN.GE.C)     GO TO 60
    ENTOT=ENKT+XTER
    GO TO 10
 40 CONTINUE
    TINTF=RED2*PP1+RED3*PP2+RED4*PP3
    ENFIN=TINTF+TERM
    IF(ENFIN.GE.C)     GO TO 60
    ENTOT=ENKT+XTER
    GO TO 10
 50 CONTINUE
    TINTF=RED5*PP1+RED6*PP2+RED7*PP3

    ENFIN=TINTF+TERM
    IF(ENFIN.GE.C)     GO TO 60
    ENTOT=ENKT+XTER
     GO TO 10
 60 CONTINUE
    IREACT=3
    ENFIN=0.D00
    ENTOT=ENKT+XTER
    GO TO 10
    END
    SUBROUTINE SECOND(SEC)
    IMPLICIT REAL*8 (A-H,O-Z)
    CALL TIMER(INT)
    SEC=INT*26.014660D-06
    RETURN
    END
```

SAMPLE RUN: D+H2, NJ=NV=0,PHI=90,THETA=0,B=1.5 AU.

INPUT DATA....:

```
NTOT   =     5   MA =   2.014   ECJ=   0.2e9    RHO =   7.5600
NPRINT= 1000     MB =   1.008   NV =   0         RLO =   1.2074
IE     =    0    MC =   1.008   NJ =   0         RHI =   1.6600
DT     =  2.00
```

YATES-LESTER SURFACE PARAMETERS:

```
DE    =    4.72703     KAPPA   =     3.12796
RE    =    1.40631     LAMBDA  =     0.96131
BETA  =    1.07366     DELTA   =    55.25083
(MORSE CONSTANTS)  EPSILON =  -79.13556
```

INITIAL PARAMETERS....: PHI,THETA,BPM

```
  90.000000     0.0          1.500000
```

TRAJECTORY NO. 1 TT = 0.25 EV

```
REACTION TIME:        0.0
COORDINATES:    0.0          1.207433     1.500000    -7.409696
MOMENTA:        0.0          0.0          0.0          0.709753
```

INITIAL ENERGIES....:

```
TOTAL     (H) =   0.514192
INTERNAL  (E) =   0.267639
POTENTIAL (V) =   0.264192
```

ANGULAR MOMENTA....:

```
TOTAL M(L+J) =   0.1064630 01
INTERNAL M(J)=   0.0
```

```
NUMBER OF STEPS =   490     CPU TIME =     6.077
```

```
REACTION TIME:      980.00
COORDINATES:   -1.065523     1.115021     7.561140    -5.198216
MOMENTA:        0.307703    -0.297835     0.639349    -0.295339
```

FINAL CONDITIONS....:

```
COLLISION TIME:                 980.00
TOTAL ENERGY :                  0.514201
TOTAL ANG.MOMENTUM:             0.1064630 01
INT.ANG.MOMENTUM:               0.2574540-01
REACTION CHANNEL:                  0
SCATTERING ANGLE:               65.21
POTENTIAL ENERGY:                0.066120
INTERNAL ENERGY:                 0.269137
VIBRATIONAL ENERGY:              0.268811      NV=     0
ROTATIONAL ENERGY:               0.000326      NJ=     0
```

```
TRAJECTORY NO.     2          TT =       0.50  EV

REACTION TIME:          0.0
COORDINATES:      0.0          1.207433     1.500000    -7.409696
MOMENTA:          0.0          0.0          0.0          1.003743

INITIAL ENERGIES....:                ANGULAR MOMENTA....:
TOTAL      (H) =    0.764192         TOTAL W(L+J) =    0.1505610 01
INTERNAL   (E) =    0.267639         INTERNAL W(J)=    0.0
POTENTIAL  (V) =    0.264192

NUMBER OF STEPS =    331       CPU TIME =       4.013

REACTION TIME:        662.00
COORDINATES:     -7.578418     3.708110     5.034746    -1.697445
MOMENTA:         -0.680654     0.241934     0.451428     0.009708

FINAL CONDITIONS....:
COLLISION TIME:                  662.00
TOTAL ENERGY :                 0.764187
TOTAL ANG.MOMENTUM:            0.1505610 01
INT.ANG.MOMENTUM:              0.2327890 00
REACTION CHANNEL:                    1
SCATTERING ANGLE:              75.34
POTENTIAL ENERGY:               0.145325
INTERNAL ENERGY:                0.164631
VIBRATIONAL ENERGY:             0.164516          NV=      0
ROTATIONAL ENERGY:              0.020115          NJ=      1

TRAJECTORY NO.     3          TT =       0.75  EV

REACTION TIME:          0.0
COORDINATES:      0.0          1.207433     1.500000    -7.409696
MOMENTA:          0.0          0.0          0.0          1.229329

INITIAL ENERGIES....:                ANGULAR MOMENTA....:
TOTAL      (H) =    1.014192         TOTAL W(L+J) =    0.1843990 01
INTERNAL   (E) =    0.267639         INTERNAL W(J)=    0.0
POTENTIAL  (V) =    0.264192

NUMBER OF STEPS =    270       CPU TIME =       3.530

REACTION TIME:        540.00
COORDINATES:     -6.755765     5.029632     4.658944    -1.727421
MOMENTA:         -0.928316     0.192480     0.124659    -0.373492

FINAL CONDITIONS....:
COLLISION TIME:                  540.00
TOTAL ENERGY :                 1.014183
TOTAL ANG.MOMENTUM:            0.1843990 01
INT.ANG.MOMENTUM:              0.2669930 00
REACTION CHANNEL:                    1
SCATTERING ANGLE:              69.05
POTENTIAL ENERGY:               0.045555
INTERNAL ENERGY:                0.270924
VIBRATIONAL ENERGY:             0.244635          NV=      0
ROTATIONAL ENERGY:              0.026289          NJ=      2
```

TRAJECTORY NO. 4 TT = 1.00 EV

REACTION TIME: 0.0
COORDINATES: 0.0 1.207433 1.500000 -7.409696
MOMENTA: 0.0 0.0 0.0 1.419507

INITIAL ENERGIES....:
TOTAL (H) = 1.264192
INTERNAL (E) = 0.267839
POTENTIAL (V) = 0.264192

ANGULAR MOMENTA....:
TOTAL w(L+J) = 0.212926D 01
INTERNAL w(J)= 0.0

NUMBER OF STEPS = 265 CPU TIME = 3.360

REACTION TIME: 530.00
COORDINATES: -8.209843 1.911856 5.322567 -0.870553
MOMENTA: -0.587097 0.023986 0.369470 0.022048

FINAL CONDITIONS....:
COLLISION TIME: 530.00
TOTAL ENERGY : 1.264194
TOTAL ANG.MOMENTUM: 0.2129260 01
INT.ANG.MOMENTUM: 0.7249700-01
REACTION CHANNEL: 1
SCATTERING ANGLE: 89.37
POTENTIAL ENERGY: 0.229009
INTERNAL ENERGY: 0.356792
VIBRATIONAL ENERGY: 0.354865 NV= 0
ROTATIONAL ENERGY: 0.001927 NJ= 0

TRAJECTORY NO. 5 TT = 1.25 EV

REACTION TIME: 0.0
COORDINATES: 0.0 1.207433 1.500000 -7.409696
MOMENTA: 0.0 0.0 0.0 1.587057

INITIAL ENERGIES....:
TOTAL (H) = 1.514192
INTERNAL (E) = 0.267839
POTENTIAL (V) = 0.264192

ANGULAR MOMENTA....:
TOTAL w(L+J) = 0.238059D 01
INTERNAL w(J)= 0.0

NUMBER OF STEPS = 247 CPU TIME = 3.047

REACTION TIME: 494.00
COORDINATES: -8.636657 4.279173 3.209751 -1.640115
MOMENTA: -0.761246 -0.140482 0.639455 -0.977955

FINAL CONDITIONS....:
COLLISION TIME: 494.00
TOTAL ENERGY : 1.514197
TOTAL ANG.MOMENTUM: 0.2380580 01
INT.ANG.MOMENTUM: 0.8671030 00
REACTION CHANNEL: 1
SCATTERING ANGLE: 72.13
POTENTIAL ENERGY: 0.242154
INTERNAL ENERGY: 0.661975
VIBRATIONAL ENERGY: 0.394541 NV= 0
ROTATIONAL ENERGY: 0.267434 NJ= 7

APPENDIX III: Glossary

A. Abbreviations:

1-D	One dimensional (collinear).
2-D	Two dimensional (coplanar).
3-D	Three dimensional (spatial).
C	Classical.
EQ	Exact quantum.
FD	Fong and Diestler[51].
KPS	Karplus, Porter and Sharma[65].
LEP	London-Eyring-Polanyi surface[27].
LEPS	London-Eyring-Polanyi-Sato surface[64].
MERP	Minimum energy reaction path.
PK	Porter-Karplus surface[59].
QC	Quasi classical
QM	Quantum mechanical.
SL	Saxon and Light[108].
SSMK	Shavitt, Stevens, Minn and Karplus surface[38].
VA	Vibrational adiabaticity.
VARP	Vibrationally averaged reaction path.
WP	Wall-Porter surface[63].
YL	Yates-Lester surface[58].
ZPE	Zero-point energy.

B. Subscripts:

a	A+BC configuration.
b	A···B···C (1-D), or AC+B (2-D) configuration.
c	AB+C configuration.
d	A+B+C configuration (2-D).
l	Vibrational compression phase.
r	Vibrational extension phase.
r	rotational mode.
t	translational mode.
v	vibrational mode.
int	internal mode (vibration + rotation).
orb	orbital mode.
A	Asymmetric stretching mode.
S	Symmetric stretching mode.
T	Total.

C. Superscripts:

o	Initial values.
'	Final values.
·	Time derivatives.
*	Values at the exit location (Chapter 5).

D. Symbols:

A Amplitudes of vibration (A_l,A_r) or force constants (A_S,A_A).

b Impact parameter; b_{max} = maximum impact parameter.

c Velocity of light.

D_e Dissociation energy.

E_i Energy of mode i; E_a = barrier height; E_c = calculated minimum potential-energy for H_2.

F(i) Probability distribution function.

f_{vib} Fraction of total energy which is product vibrational energy.

H Hamiltonian, or total energy, $\hbar$ = Planck's constant/2π.

J Rotational quantum number.

k Force constant; k = rate constant.

M Total mass of the ABC system.

m_i Mass of the i^{th} atom.

n Product vibrational box.

p^R_{vn} Reaction probability; p^R = outcome of trajectory.

P_i Momenta conjugate to the relative coordinates Q_i or R_i.

p_i Momenta conjugate to the internal coordinates q_i or r_i; or momenta corresponding to mode i.

R_i Relative coordinates corresponding to configuration i.

r_i Internal coordinates corresponding to configuration i.

Q_i Relative coordinates used in computation, i = 1-4.

q_i Internal coordinates used in computation. i = 1,2.

S^R Reaction cross section.

T_i Kinetic energy of mode i.

t Time.

t^R Reaction time.

Δt^* Time spent in the exit region.

Δt_ϕ Shift in the time axis corresponding to a shift

V_i Potential energy of mode i.

V_{ref} Minimum of vibrational potential at the reaction shell.

x,y,z Cartesian Coordinates.

B_e, B_v, D_e, D_v, r_e Spectroscopic constants[76].

$\overline{ABC}$ Center-of-mass of the ABC system.

$\overline{AB}$, $\overline{AC}$, $\overline{BC}$ Center-of-mass of the AB, AC, BC entities.

A,$\overline{BC}$-Pertaining to motion of A relative to $\overline{BC}$.

E. Greek symbols:

β Morse constant (exponential factor).

γ Scattering angle (P_t, P_t').

Γ Bending angle $(180^o - ABC)$.

ζ 3-D orientation angle (z, r_{BC}).

η 2-D configuration angle (R_i, r_i)

θ 2-D and 3-D orientation angle or rotational phase (y, r_{BC}).

μ Reduced mass, e.g. $\mu_{A,BC} = m_A(m_B+m_C)/M$; $\mu_{AB} = m_A m_B/(m_A + m_B)$.

ξ Skew angle of the r_{AB} and r_{BC} coordinate axes.

ρ $R_{A,BC}$, e.g. ρ^o = reaction shell radius;

ρ = translational coordinate (Chapter 5);

ρ_o = limit of flat part of surface (Chapter 5);

ρ^* = exit location.

τ Classical period of vibration.

ϕ Vibrational phase angle.

χ Reaction channel: $\chi = 0$, unreactive, product A+BC;

$\chi = -1$, reactive , product AB+C;

$\chi = 2$, reactive , product AC+B;

$\chi = 3$, dissociation, product A+B+C.

ω Angular momentum, e.g. ω_T, ω_{int}, ω_{orb}.

α_e, β_e, ω_e Spectroscopic constants[76].